

## ABSTRACT

Title of Document: Investigation of Colorless Distributed Combustion (CDC) with Swirl for Gas Turbine Application

Ahmed Essam EIDin Khalil Hasan, PhD, 2013

Directed By: Dr. Ashwani K. Gupta  
Distinguished University Professor  
Department of Mechanical Engineering

Colorless Distributed Combustion (CDC) with swirl is investigated for gas turbine engine applications due to its benefits for ultra-low pollutants emission, improved pattern factor and thermal field uniformity, low noise emission, and stable combustion with the alleviation of combustion instabilities. Adequate and fast mixing between the injected air and internally recirculated hot reactive gases to form hot and diluted oxidant is critical for CDC, followed by rapid mixing with the fuel. This results in distributed reaction zone instead of a concentrated thin flame front as observed in conventional diffusion flames, leading to avoidance of hot spot regions and providing reduced  $\text{NO}_x$  and CO emissions. The focus of this dissertation is to develop and demonstrate CDC in a cylindrical combustor for application to stationary gas turbine combustors. The dissertation examines the sequential development of ultra-low emission colorless distributed combustor operating at a nominal thermal intensity of  $36\text{MW/m}^3\text{-atm}$ . Initially, the role of swirl is evaluated through comparing the performance of swirling and non-swirling configurations with focus on pollutants emission, stability, and isothermal flowfield through particle image velocimetry. Different fuel injection locations have also been examined, and based on performance a swirling configuration have been down selected for further investigations demonstrating emissions as low as

1 PPM of NO with a 40% reduction compared to non-swirling configuration. Further investigations were performed to outline the impact of inlet air temperature and combustor pressure on reaction distribution and combustor performance.

Next, Fuel flexibility has been examined with view to develop CDC combustors that can handle different gaseous and liquid fuels, both traditional and renewable. These fuels included diluted methane, hydrogen enriched methane, propane, ethanol, kerosene, JP-8, Hydrogenated Renewable Jet fuel, and novel biofuel. Swirling CDC combustor demonstrated emissions below 7.5 PPM of NO regardless of the fuel used, with emissions below 40PPM of CO for liquid fuels and 10 PPM for gaseous fuels.

Further enhancement of swirling CDC combustor was sought next. Various fuel injection techniques have been examined, outlining the importance of fuel injection location with respect to air and hot reactive gases recirculation. The impact of air injection velocity on combustor performance have been examined in terms of increased recirculation (via isothermal flow field characterization using PIV) and enhanced performance with lower pollutants emission leading to 45% reduction in NO emissions with no impact on CO emissions. The impact of fuel dilution on mixing and performance has been also examined as a method to enhance mixing due to the increased fuel jet momentum. Dual air and fuel injection have been explored to outline the impact of multi injection on combustor performance for scaling up of the combustor.

Planar Laser Induced Fluorescence technique was used to evaluate the reaction behavior and its distribution in the combustor through detection of activated OH radicals at different activation lines in different configurations.

The different investigations performed (experimentally and numerically) have been compiled and analyzed with view to develop a “Distribution Index” that evaluated the reaction distribution in a given combustor based on certain parameters. These parameters include, but no limited to, hot reactive gases recirculation (entrainment) rate, air injection velocity, mixing between air and fuel, and operational equivalence ratio and inlet air temperature. The developed distribution index, DI, will be a valuable tool for future combustor design.

Investigation of Colorless Distributed Combustion (CDC) with Swirl for Gas  
Turbine Application

By

Ahmed Essam EIDin Khalil Hasan

Dissertation submitted to the Faculty of the Graduate School of the  
University of Maryland, College Park, in partial fulfillment  
of the requirements for the degree of  
Doctor of Philosophy  
2013

Advisory Committee:

Professor Ashwani K. Gupta, Chair

Professor Kenneth T. Kiger

Associate Professor Kenneth H. Yu. (Dean's Representative)

Associate Professor Peter B. Sunderland

Associate Professor Bao Yang

© Copyright by  
Ahmed Essam EIDin Khalil Hasan  
2013

# **Dedication**

To My Mum

## **Acknowledgements**

The work presented in this dissertation is the result of my experience at the University of Maryland Combustion Laboratory. I am grateful to Prof. Gupta for offering me the opportunity to work at UMCL on one of the topics that interest me the most. As my mentor and advisor, Prof. Gupta provided me with continuing support and advice that helped shaping my research. He has motivated me to believe in the value of hard work, persistence and dedication to achieve excellence. I would also like to thank my dissertation committee members, Prof. Kenneth Kiger, Assoc. Prof. Kenneth Yu, Assoc. Prof. Peter Sunderland and Assoc. Prof. Bao Yang for their efforts, insights, advice and support.

I thank my family for their unwavering support and encouragement. I am especially thankful to my mother and sister for their everlasting support and my father for encouraging me to pursue my graduate degrees. My gratitude to my mother, father, sister and uncle cannot be expressed in words. They all deserve all the credit for my achievements.

I would like to extend my gratitude to my former and current colleagues (the Combustion Lab Crew) at UMCL; Vaibhav Arghode, Islam Ahmed, Hatem Selim, Vivek Shirsat, Henry Molintas, Ryan James, Ajay Singh, Salisu Ibrahim, Aaron Leyko, Teresa Wierzbicki, Richard Scenna and Jonathan Brooks for providing great advice, making the work environment enjoyable, and helping inside and outside the lab. I would like to specifically thank Vaibhav, Islam, Hatem and Vivek for their valuable insights and advice regarding my work. I would also like to thank my undergraduates

and high school interns for their help with the experiments, namely, Max Frantz, Laura Stinnet, Harsha Cuttari, Eric Yoo, Tony Perez, and Miles Robinson.

Finally, I would like to extend my thanks to my friends and all of those who helped me and supported me along the path. I'm blessed to have you all. No words would be enough to thank you properly.

I wish to express my sincere gratitude to Office of Naval Research (ONR) program managers, Dr. Gabriel D. Roy and Dr. Clifford Bedford, for providing the financial support that made this research possible. The support from DLA is also highly appreciated.

# Table of Contents

Dedication .....	2
Acknowledgements .....	3
Table of Contents .....	5
List of Tables.....	10
List of Figures .....	11
1. Chapter One: Introduction .....	1
1.1. Background and Objective.....	1
1.2. Gas Turbine Combustor Design Considerations.....	4
1.2.1. High Combustion Efficiency .....	4
1.2.2. Low Pollutant Emission.....	5
1.2.3. High Thermal Intensity .....	6
1.2.4. Stable Combustion.....	7
1.2.5. Low Pressure Loss .....	7
1.2.6. Wide Operational Limit .....	8
1.2.7. Uniform Pattern Factor .....	8
1.2.8. Fuel flexibility.....	9
1.3. Pollutant Formation .....	10
1.3.1. Oxides of Nitrogen.....	10
1.3.2. CO Formation .....	15
1.3.3. Unburned Hydrocarbons (UHC) Formation .....	16
1.3.4. Soot Formation.....	16
1.4. NO <sub>x</sub> Abatement Strategies .....	17
1.4.1. Injection of Diluents .....	18
1.4.2. Exhaust Clean-up.....	18
1.4.3. Limiting NO <sub>x</sub> Formation.....	19
1.5. Objective.....	23
2. Chapter Two: Literature Review .....	25
2.1 Furnace Application.....	28
2.2 Gas Turbine Application.....	39
2.3. High Temperature Air Combustion (HiTAC).....	50
2.3.1. Concept of HiTAC.....	50
2.3.2. Benefits of HiTAC.....	55
2.3.3. HiTAC Investigations .....	58
2.4. Colorless Distributed Combustion.....	64
2.5. Dissertation Outline .....	68
3. Chapter Three: CDC Design Considerations.....	72

3.1.	Reactive Gas Recirculation.....	72
3.2.	Swirling Flows.....	74
3.3.	Ignition Delay.....	75
3.4.	Fuel/Oxidizer Mixing.....	77
3.4.1.	Jet Decay in Cross-Flow.....	77
3.4.2.	Turbulent Mixing Time.....	78
3.5.	Pressure Loss.....	78
3.6.	Thermal Intensity and Flow Configuration.....	79
4.	Chapter Four: Swirling Colorless Distributed Combustor Design.....	82
4.1.	Numerical Modeling.....	82
4.1.1.	Combustor Exit Configuration.....	82
4.1.2.	Inlet Air Angle.....	86
4.2.	Experimental Investigations (swirling vs. non-swirling).....	87
4.2.1.	Combustor Fabrication.....	88
4.2.2.	Emission Measurements.....	89
4.2.3.	Cases Investigated.....	90
4.2.4.	Results and Discussion.....	91
4.3.	Extended Axial Exit Configuration.....	97
4.4.	Flowfield Characterization using PIV.....	102
4.4.1.	PIV Setup Arrangement.....	102
4.4.2.	Numerical Predictions.....	105
4.4.3.	Normal exit arrangement for combustion gases.....	105
4.4.4.	Axial exit arrangement for combustion gases.....	109
4.4.5.	Axially extended exit arrangement for combustion gases.....	113
4.4.6.	Summary.....	115
4.5.	Other Geometrical Parameters.....	117
4.6.	Temperature and Pressure Effects.....	118
4.6.1.	High Temperature Experiments.....	119
4.6.2.	Elevated Pressure Experiments.....	122
4.6.3.	Preheated Air and Elevated Pressure Experiments.....	125
4.7.	Summary.....	129
5.	Chapter Five: Fuel Flexible CDC.....	130
5.1.	Low Calorific Value Fuel (Diluted Methane).....	133
5.1.1.	Experimental Conditions.....	135
5.1.2.	Results and Discussion.....	136
5.1.3.	Summary.....	146
5.2.	Hydrogen Enriched Methane.....	148
5.2.1.	Experimental Conditions.....	152
5.2.2.	Results and Discussion.....	152
5.2.3.	Summary.....	161
5.3.	Heavier Fuels.....	163
5.3.1.	Fuels Examined.....	163
5.3.2.	Liquid Fuel Introduction.....	166

5.3.3.	Experimental Conditions .....	167
5.3.4.	Results and Discussion .....	167
5.3.5.	Summary .....	175
5.4.	Biofuels for Energy.....	177
5.4.1.	Droplet Size and Atomization.....	180
5.4.2.	Experimental Conditions .....	183
5.4.3.	Results and Discussion .....	185
5.4.4.	Summary .....	188
6.	Chapter Six: Injection Design.....	189
6.1.	Fuel Injection Location.....	189
6.1.1.	Geometries Examined.....	190
6.1.2.	Numerical Investigations .....	192
6.1.3.	Results and Discussion .....	193
6.1.4.	Summary.....	198
6.2.	Injector Shape .....	201
6.2.1.	Experimental Conditions .....	202
6.2.2.	Results and Discussion .....	203
6.2.3.	Summary .....	206
6.3.	Air Injection Velocity .....	207
6.3.1.	Experimental Parameters .....	208
6.3.2.	Isothermal Flowfield.....	209
6.3.3.	Pollutants Emission Results and Discussion.....	212
6.3.4.	Summary.....	219
6.4.	Air Dilution.....	220
6.4.1.	Experimental Investigations.....	221
6.4.2.	Results and Discussion .....	223
6.4.3.	Summary .....	226
6.5.	Dual Injection.....	226
6.5.1.	Experimental Facility.....	228
6.5.2.	Experimental Investigations.....	230
6.5.3.	Results and Discussion .....	230
6.5.4.	Dual injection under non-premixed combustion.....	234
6.5.5.	Summary.....	235
7.	Chapter Seven: Planar Laser Induced Fluorescence.....	237
7.1.	Planar Laser Induced Fluorescence Technique.....	237
7.1.1.	Mechanics of LIF.....	238
7.1.2.	Detection of the OH Radical.....	240
7.2.	PLIF System Setup .....	240
7.2.1.	Dye Laser system.....	241
7.2.2.	System Optics .....	242
7.2.3.	Data Acquisition System.....	244
7.2.4.	System Tuning .....	245
7.2.5.	Combustor Setup.....	247

7.3.	OH-PLIF Concentration Experiments .....	248
7.3.1.	Initial Experiments.....	248
7.3.2.	OH-PLIF Concentration.....	250
7.3.3.	OH* Chemiluminescence .....	258
7.3.4.	Fluorescence vs. Chemiluminescence .....	260
7.4.	Temperature Measurement with PLIF .....	263
7.4.1.	Q <sub>2</sub> (11), R <sub>2</sub> (5) Signal.....	265
7.4.2.	Q <sub>1</sub> (11), Q <sub>1</sub> (1) Signal.....	265
7.4.3.	Analysis for Temperature plots.....	267
7.5.	Other Configurations .....	270
7.6.	Summary .....	271
8.	Chapter Eight: Towards Distributed Combustion.....	272
8.1.	Summary .....	272
8.2.	Colorless Distributed Combustion.....	273
8.2.1.	Reactive Gas Recirculation.....	274
8.2.2.	Air Injection Velocity .....	275
8.2.3.	Fuel Injection Location .....	276
8.2.4.	Ignition Delay .....	277
8.3.	Distribution Index .....	279
8.3.1.	Combustion Geometry .....	279
8.3.2.	Air Injection Velocity .....	282
8.3.3.	Fuel Injection Location.....	285
8.3.4.	Equivalence Ratio .....	288
8.3.5.	Inlet Air Temperature .....	290
8.3.6.	DI Equation.....	293
9.	Chapter Nine: Conclusions and Recommendations for Future Work .....	294
9.1.	Conclusions.....	294
9.1.1.	Effect of Flowfield Configuration .....	294
9.1.2.	Effect of Fuel Injection Location.....	295
9.1.3.	Temperature and Pressure Effect.....	295
9.1.4.	Fuel Flexibility.....	296
9.1.5.	Injector Shape .....	297
9.1.6.	Air Injector Velocity.....	297
9.1.7.	Fuel Dilution Effects.....	298
9.1.8.	Dual Injection.....	298
9.1.9.	PLIF Experiments .....	299
9.1.10.	Distribution Index .....	299
9.2.	Recommendations for Future Work.....	300
9.2.1.	Examination of the Role of Hot Recirculated Reactive Gases .....	300
9.2.2.	Detailed Species and Temperature Distribution .....	300
9.2.3.	Quantification of Relevant Time Scales .....	301
9.2.4.	Improved Fuel/Oxidizer Mixing.....	301
9.2.5.	Characterization of Dynamic Performance.....	302

9.2.6.	Multi-injection and Scaling of CDC Combustor .....	302
9.2.7.	Elevated Pressure Operation .....	302
9.2.8.	Part Load Operation .....	303
	Appendix A: List of Papers.....	304
A.1	Published Journal Papers .....	304
A.2	Journal Papers Under Review/In preparation .....	305
A.3	Peer Reviewed Conference Papers .....	305
	Appendix B: Combustor Assembly .....	307
B.1	Schematic of the Combustor .....	307
B.2	Stainless Steel assembly.....	308
B.3	Insulation.....	309
B.4	Extended Axial Exit.....	310
B.5	Injectors and Exit Assembly .....	311
	Appendix C: Geometrical Variations.....	312
C.1	Combustor Length Variation.....	312
C.2	Combustor Exit Clearance .....	314
C.3	Injection Plane Location.....	316
C.4	Combustor Diameter Effect .....	318
	Appendix D: Novel Mixing for Ultra-High Thermal Intensity.....	320
D.1	Geometry.....	321
D.2	Numerical.....	322
D.3	Experimental .....	323
D.4	Results and Discussion.....	326
D.4.1	Flow field and mixing .....	326
D.4.2	Premixed and Non-Premixed Operation .....	329
D.4.3	Novel Mixture Preparation.....	332
D.5	Conclusions .....	335
	References .....	337

## List of Tables

Table 1-1 Typical parameters for land based and aviation gas turbine combustor .....	3
Table 4-1 Experimental parameters investigated.....	91
Table 4-2 PIV Parameters .....	104
Table 5-1 Experimental Parameters for Methane Dilution.....	136
Table 5-2 Experimental Parameters for Hydrogen Enrichment .....	152
Table 5-3 Hydrogen enrichment amount and adiabatic flame temperature.....	153
Table 5-4. Experimental parameters for Different Fuels .....	167
Table 5-5 Properties of Bio-Fuels.....	180
Table 5-6 Average diameters for Butyl Nonanoate and JP-8 .....	181
Table 5-7 Average diameters for fuel mixture and JP-8.....	182
Table 5-8 Bio-Fuels Examined .....	184
Table 6-1 Fuel Injection Scenarios .....	192
Table 6-2 Elliptical Nozzles Experimental Parameters .....	202
Table 6-3 Experimental Parameters for Different Injection Velocities .....	208
Table 6-4 Experimental parameters for air dilution.....	222
Table 6-5 Different scaling approaches .....	227
Table 6-6 Experimental parameters for dual injection .....	230
Table 7-1 Wavelength spectra for laser absorption fluorescence .....	239
Table 7-2 Excited OH states .....	246
Table 7-3 PLIF system parameters .....	249
Table D-1 Different cases presented ( $\Phi = 0.8$ , heat load = 6.25 kW, $T_{top} = 600$ K, $T_{cross} = 300$ K) .....	325

## List of Figures

Figure 1-1 Gas turbine operation principle.....	1
Figure 1-2 Pollutant trade-off. ....	6
Figure 1-3 NO <sub>x</sub> formation mechanisms.....	11
Figure 1-4 NO formation via thermal Zeldovich mechanism, NO formation rate (left) and NO formed (right) [1].....	13
Figure 1-5 Effect of premixing on NO <sub>x</sub> emissions.....	19
Figure 1-6 Lean premixed combustion (left) as opposed to conventional non-premixed combustion (right).....	20
Figure 1-7 Rich-quench-lean combustion [3].....	21
Figure 1-8 Catalytic combustion vs. premixed and conventional combustion.....	22
Figure 2-1 NO <sub>x</sub> emission from different gas turbines.....	26
Figure 2-2 Thermal intensities for furnaces.....	27
Figure 2-3 Thermal intensities for combustors.....	28
Figure 2-4 NO <sub>x</sub> emissions for furnaces.....	29
Figure 2-5 CO emissions for furnaces.....	30
Figure 2-6 NO emissions for different combustors.....	40
Figure 2-7 CO emissions for different combustors.....	41
Figure 2-8 Potential applications of high temperature air combustion, including applications already developed or at present being developed [21]. ....	51
Figure 2-9 Mixing and combustion in furnace [21].....	52
Figure 2-10 Conceptual temperature histories and fluctuation intensity [21].....	55
Figure 2-11 Preheated air temperature on NO <sub>x</sub> emission [21].....	56
Figure 2-12 Oxygen concentration at peak point and distribution of temperature of flame on burner center axis [21].....	57
Figure 2-13 Jet in cross flow of high temperature and diluted air.....	61
Figure 2-14 Jet in co-flow of flue gases.....	62
Figure 2-15 Effect of fuel mixing.....	63
Figure 2-16 Thermal intensity and length scale for various CDC combustors investigated previously.....	65
Figure 2-17 NO and CO emissions for various CDC combustors investigated previously.....	66
Figure 3-1 Ignition delay variation with air temperature and oxygen concentration [2]. ....	76
Figure 3-2 Pressure loss for different injection velocities.....	79
Figure 4-1 Schematic of the combustor for different models.....	83
Figure 4-2 Numerical model of the combustor.....	83
Figure 4-3 Velocity contours for normal exit (left) and axial exit (right). ....	85
Figure 4-4 Effect of air inlet angle on velocity field.....	86
Figure 4-5 Recirculation ratio vs. inlet air angle.....	87
Figure 4-6 Schematic of the combustor for different experimental configurations....	88
Figure 4-7 Assembled combustor for experimental investigations.....	89
Figure 4-8 NO and CO emissions for "N" exit arrangement.....	92
Figure 4-9 OH* chemiluminescence intensity distribution for "N" exit arrangement. ....	93

Figure 4-10 NO and CO emissions for "A" exit arrangement .....	94
Figure 4-11 OH* chemiluminescence intensity distribution for "A" exit arrangement .....	96
Figure 4-12 Schematic diagram of different exit arrangements and fuel injection locations. ....	97
Figure 4-13 NO and CO emissions for different exit configurations (non-premixed) .....	99
Figure 4-14 NO and CO emissions for different exit configurations (Premixed) ....	100
Figure 4-15 OH* chemiluminescence intensity distribution for "AT" exit arrangement .....	101
Figure 4-16 Schematic diagram for the PIV setup used .....	103
Figure 4-17 Experimental Particle Image Velocimetry setup.....	104
Figure 4-18 Velocity vectors (a), Urms (b), and Vrms (c) for configuration "N" ....	106
Figure 4-19 Velocity vectors, experimental (a) and numerical (b) along with normalized tangential velocity profiles (c) for configuration "N" .....	108
Figure 4-20 Velocity vectors (a), Urms (b), and Vrms (c) for configuration "A" ....	109
Figure 4-21 Velocity vectors, k-ε model (a) and RSM model (b) along with normalized tangential velocity profiles (c) for configuration "A" .....	112
Figure 4-22 Velocity vectors (a), Urms (b), Vrms (c) for configuration "AT" .....	113
Figure 4-23 Normalized tangential velocity profiles for different arrangements for L1, L2 and L3 lines .....	114
Figure 4-24 Global flame images for normal "N" (left), axial exit with tube "AT" (right). ....	116
Figure 4-25 Pollutants emission for non-premixed combustion mode with fuel injection at location one for different air inlet temperatures. (Left) NO, (Right) CO .....	120
Figure 4-26 Pollutants emission for premixed combustion mode for different air inlet temperatures. (Left) NO, (Right) CO.....	121
Figure 4-27 OH* chemiluminescence intensity distribution under preheated air. ...	122
Figure 4-28 Pollutants emission for non-premixed combustion mode for normal and elevated combustor pressure. (Left) NO, (Right) CO.....	123
Figure 4-29 Pollutants emission for premixed combustion mode for normal and elevated combustor pressure. (Left) NO, (Right) CO.....	124
Figure 4-30 OH* chemiluminescence intensity distribution under elevated pressure condition. ....	125
Figure 4-31 Pollutants emission for non-premixed combustion mode for different operational conditions. (Left) NO, (Right) CO.....	126
Figure 4-32 Pollutants emission for premixed combustion mode for different operational conditions. (Left) NO, (Right) CO.....	127
Figure 4-33 OH* chemiluminescence intensity distribution under elevated temperature and pressure. ....	128
Figure 5-1 Schematic diagrams of the Combustor used .....	131
Figure 5-2 Adiabatic flame temperature (Tad) and laminar flame speed (S) for different dilution percent (by volume) at stoichiometric mixtures .....	134
Figure 5-3 Laminar flame speed at different equivalence ratios for different dilution percent (by volume) .....	135

Figure 5-4 NO and CO emissions at different equivalent fuel calorific value under non-premixed conditions .....	137
Figure 5-5 NO and CO emissions for non-premixed combustion mode at different equivalent fuel calorific value with inlet air preheated to 600K.....	138
Figure 5-6 NO and CO emissions for premixed combustion mode with pure methane and 50-50 (vol.) mixture of methane and nitrogen. ....	140
Figure 5-7 NO and CO emissions for premixed combustion mode with pure methane and 50-50 (vol.) mixture of methane and nitrogen with 600K preheated inlet air ...	140
Figure 5-8 OH* chemiluminescence intensity distribution for premixed cases for pure methane (top) and for 50-50 (vol.) mixture of methane and nitrogen (bottom) .....	141
Figure 5-9 OH* chemiluminescence intensity distribution for premixed cases for pure methane (top) and for 50-50 mixture of methane and nitrogen (bottom) with 600K preheated air temperature.....	142
Figure 5-10 NO and CO emissions for non-premixed combustion mode with pure methane and 50-50 (vol.) mixture of methane and nitrogen.....	143
Figure 5-11 NO and CO emissions for non-premixed combustion mode with pure methane and 50-50 (vol.) mixture of methane and nitrogen with 600K preheated inlet air .....	144
Figure 5-12 OH* chemiluminescence intensity distribution for non-premixed cases for pure methane (top) and for 50-50 mixture of methane and nitrogen (bottom) ...	145
Figure 5-13 OH* chemiluminescence intensity distribution for non-premixed cases for pure methane (top) and for 50-50% mixture of methane and nitrogen (bottom) with 600K preheated air temperature.....	145
Figure 5-14 NO and CO emissions with different amounts of hydrogen addition (by mass) to methane fuel (left: premixed, right: non-premixed). ....	154
Figure 5-15 OH* chemiluminescence intensity distribution for different H <sub>2</sub> enrichment.....	155
Figure 5-16 Instantaneous OH* chemiluminescence intensity distribution for different H <sub>2</sub> enrichment .....	156
Figure 5-17 Global images for different H <sub>2</sub> enrichment.....	157
Figure 5-18 NO and CO emissions at different equivalence ratios .....	158
Figure 5-19 OH* chemiluminescence intensity distribution under premixed combustion.....	159
Figure 5-20 Instantaneous OH* chemiluminescence intensity distribution under premixed combustion.....	159
Figure 5-21 Calculated NO emissions using GRI 3.0 (CHEMKIN-PRO) .....	160
Figure 5-22 NO emissions from experimental and numerical work.....	161
Figure 5-23 Calculated adiabatic flame temperature for the different fuels used....	168
Figure 5-24 Laminar flame speed for the different fuels used.....	169
Figure 5-25 NO emission for the different fuels used .....	170
Figure 5-26 CO emission for the different fuels used.....	171
Figure 5-27 OH* chemiluminescence for methane and diluted methane flames .....	173
Figure 5-28 OH* chemiluminescence for the hydrogen enriched methane flame ...	173
Figure 5-29 OH* chemiluminescence for the propane flame.....	174
Figure 5-30 OH* chemiluminescence for ethanol and kerosene flames .....	175

Figure 5-31 PDPA arrangement with spray nozzle .....	181
Figure 5-32 Number diameter distribution for JP-8 (left) and Butyl Nonanoate (right) .....	182
Figure 5-33 Number diameter distribution for JP-8 (left) and fuel mixture (right)..	183
Figure 5-34 Schematic of the experimental combustion facility for biofuel .....	184
Figure 5-35 NO emissions for Butyl Nonanoate and JP-8 .....	185
Figure 5-36 CO emissions for Butyl Nonanoate and JP-8.....	186
Figure 5-37 NO and CO emissions for Butyl Nonanoate, JP-8, and HRJ .....	187
Figure 5-38 OH* chemiluminescence for JP-8 and Butyl Nonanoate flames .....	188
Figure 6-1 Schematic diagram of different fuel introduction scenarios, end cross-sectional view at middle location of the combustor.....	191
Figure 6-2 NO and CO emissions for different injection arrangements .....	194
Figure 6-3 OH* chemiluminescence intensity distribution for different injection arrangements .....	196
Figure 6-4 Temperature distribution obtained numerically at the air/fuel injection plane for the different cases .....	197
Figure 6-5 Methane mass fraction distribution at the air/fuel injection plane for the different cases .....	198
Figure 6-6 combustor with different injection locations.....	200
Figure 6-7 NO emissions for different configurations at $\phi=0.6$ .....	200
Figure 6-8 NO and CO emissions for elliptical injectors under premixed conditions .....	203
Figure 6-9 NO and CO emissions for elliptical injectors under non-premixed conditions.....	204
Figure 6-10 NO and CO emissions for different aspect ratios under premixed combustion.....	205
Figure 6-11 NO and CO emissions for different aspect ratios under non-premixed combustion.....	206
Figure 6-12 Velocity vectors (a), $U_{mean}$ (b), and $V_{mean}$ (c) for configuration ATP-31.....	209
Figure 6-13 Velocity vectors (a), $U_{mean}$ (b), and $V_{mean}$ (c) for configuration ATP-24.....	210
Figure 6-14 Velocity fluctuations ( $U_{rms}$ ) at the jet entry region .....	211
Figure 6-15 NO emissions for different injection velocities. Inlet air temperature =300K .....	212
Figure 6-16 CO emissions for different injection velocities. Inlet air temperature =300K .....	213
Figure 6-17 NO emissions for different injection velocities. Inlet air temperature =600K .....	214
Figure 6-18 CO emission for different injection velocities. Inlet air temperature =600K .....	215
Figure 6-19 OH* chemiluminescence for cases ATP-T-31 and ATP-T-20 .....	216
Figure 6-20 NO emissions for different injection velocities, non-premixed. Inlet air temperature=600K .....	217

Figure 6-21 CO emission for different injection velocities, non-premixed. Inlet air temperature =600K .....	218
Figure 6-22 Pressure loss percentage for different air injection velocities.....	219
Figure 6-23 Schematic of the air dilution experimental facility .....	222
Figure 6-24 NO emission for premixed, non-premixed, and air dilution case .....	224
Figure 6-25 CO emission for premixed, non-premixed, and air dilution case .....	224
Figure 6-26 OH* chemiluminescence intensity distribution for both non-premixed and dilution cases .....	225
Figure 6-27 Schematic diagram of the combustor with extended axial exit “at” (left: top section at mid location, and right: combustor interior).....	229
Figure 6-28 Colorless combustion with dual injection combustor .....	229
Figure 6-29 NO emissions for single and dual injection cases .....	231
Figure 6-30 OH* chemiluminescence intensity distribution for premixed single and dual injection.....	232
Figure 6-31 NO emissions for fuel distribution variation dual injection cases .....	233
Figure 6-32 OH* chemiluminescence intensity for dual injection fuel distribution variation cases.....	234
Figure 7-1 Laser induced excitation followed by spontaneous emission .....	238
Figure 7-2 PLIF System at UMD Combustion Lab.....	242
Figure 7-3 Optical arrangement for laser beam .....	243
Figure 7-4 Formed UV laser sheet.....	243
Figure 7-5 PLIF system timing sequence .....	245
Figure 7-6 OH-PLIF signal for Q <sub>1</sub> (6) excitation.....	247
Figure 7-7 Combustor with PLIF laser .....	248
Figure 7-8 OH signal, unactivated (left) and activated using Q <sub>1</sub> 6 line (right), with the combustor in the background.....	250
Figure 7-9 OH-PLIF Signal for non-premixed (left) and premixed (right) for an equivalence ratio of 0.7.....	251
Figure 7-10 OH-PLIF Signal for non-premixed (left) and noise signal recorded with a shift of 0.07 A .....	252
Figure 7-11 OH-PLIF instantaneous and average shots .....	253
Figure 7-12 OH-PLIF intensity distribution for Q <sub>1</sub> (5) line under non-premixed combustion mode.....	254
Figure 7-13 OH-PLIF intensity distribution for Q <sub>1</sub> (5) line under premixed combustion mode.....	254
Figure 7-14 Signal distribution for Q <sub>1</sub> (5) vs. equivalence ratio.....	255
Figure 7-15 OH-PLIF intensity distribution for Q <sub>1</sub> (6) line under non-premixed combustion mode.....	256
Figure 7-16 OH-PLIF intensity distribution for Q <sub>1</sub> (6) line under premixed combustion mode.....	256
Figure 7-17 Signal distribution for Q <sub>1</sub> (6) vs. equivalence ratio.....	257
Figure 7-18 OH Chemiluminescence signal .....	259
Figure 7-19 OH-PLIF Signal and chemiluminescence signal for non-premixed combustion at equivalence ratio of 0.7. ....	260

Figure 7-20 OH-PLIF Signal and chemiluminescence signal for premixed combustion at equivalence ratio of 0.7 .....	261
Figure 7-21 Signal distribution for $Q_1(5)$ and chemiluminescence .....	262
Figure 7-22 Signal ratio, $Q_1(11)/Q_1(1)$ (left) and $Q_2(11)/R_2(5)$ (right).....	264
Figure 7-23 OH-PLIF signal for $Q_1(1)$ activation line.....	265
Figure 7-24 OH-PLIF signal for $Q_1(11)$ activation line.....	266
Figure 7-25 $Q_1(11)/Q_1(1)$ ratio at $\phi=0.6$ .....	267
Figure 7-26 Temperature plot based on $Q_1(11)$ and $Q_1(1)$ ratio .....	268
Figure 7-27 Error in ratio due to reflected laser .....	270
Figure 8-1 Effect of entrainment on temperature and oxygen concentration .....	280
Figure 8-2 Effect of air injection velocity on NO emission.....	284
Figure 8-3 NO emission under different fuel injection locations .....	285
Figure 8-4 NO emissions for different fuel injection locations .....	286
Figure 8-5 Normalized NO emission vs. air and fuel separation distance.....	287
Figure 8-6 NO emission vs. Equivalence ratio .....	288
Figure 8-7 Experimentally measured NO emission as compared to the obtained equation.....	289
Figure 8-8 NO emission vs. inlet air temperature.....	290
Figure 8-9 Experimentally measured NO emission as well as emission obtained from the developed relation .....	291
Figure 8-10 . Contribution of thermal NO as a percent of total NO, CHEMKIN-PRO .....	292
Figure B-1 Schematic of the assembled Combustor.....	307
Figure B-2 Cut section into the combustor assembly .....	308
Figure B-3 End-Plates dimensions.....	308
Figure B-4 Stainless Steel pipe dimensions.....	309
Figure B-5 Inner insulation with extended axial exit at center.....	310
Figure C-1 Schematic of the Combustor with depth change (8D).....	313
Figure C-2 NO and CO emissions for different combustor depth.....	314
Figure C-3 NO and CO emissions for different exit clearances and air intake temperature of 600K .....	315
Figure C-4 OH* Chemiluminescence for 1D exit clearance and the base case for premixed combustion with air preheat temperature of 600K .....	316
Figure C-5 Air/Fuel injection plane location .....	316
Figure C-6 NO and CO emissions for different injection planes.....	317
Figure C-7 OH* Chemiluminescence for 2D injection plane and the base case for premixed combustion with air preheat temperature of 600K .....	318
Figure C-8 NO and CO emissions for different combustor diameters .....	319
Figure D-1 Ultra-high thermal intensity CDC combustor (a) schematic, (b) non-premixed mode, and (c) premixed mode .....	321
Figure D-2 Ultra-high intensity CDC (a) experimental facility, (b) CDC combustor, and (c) the combustor optical access. ....	324
Figure D-3 Velocity magnitude contours at the symmetrical plane for various cases presented .....	327

Figure D-4 Methane mass fraction contours at the symmetrical plane for various cases presented .....	329
Figure D-5 NO, CO, and unburned hydrocarbons emission for premixed and non-premixed combustion modes with methane as the fuel .....	330
Figure D-6 OH* distribution (equivalence ratio = 0.8) for premixed and non-premixed mode with methane as the fuel. ....	331
Figure D-7 NO and CO emission for different mixing cases, normalized by premixed emissions (Non P = non-premixed, P = premixed).....	333
Figure D-8 OH* distribution (equivalence ratio = 0.8) for different cases presented .....	334

# 1. Chapter One: Introduction

## 1.1. Background and Objective

The present dissertation focuses on the development of colorless distributed combustion (CDC) with swirl for fuel flexible land based and aviation gas turbine combustors. Gas turbines engines follow Brayton cycle arrangement as shown in Figure 1-1. In an ideal Brayton cycle, air is isentropically compressed (1-2) followed by constant pressure heat addition (2-3) then the high temperature and high pressure gases are expanded isentropically in turbine (3-4) followed by heat rejection (4-1). The objective of a gas turbine combustor is to increase the temperature of gases at constant pressure as shown in path 2-3 in Figure 1-1. Gas turbine combustors operate at elevated pressure and the inlet temperature of gases is governed by the pressure ratio in the compressor or by the efficiency of recuperator if any exists. Generally, the operational pressure of a land based gas turbine combustor is about 16atm and inlet temperature is about 700K.

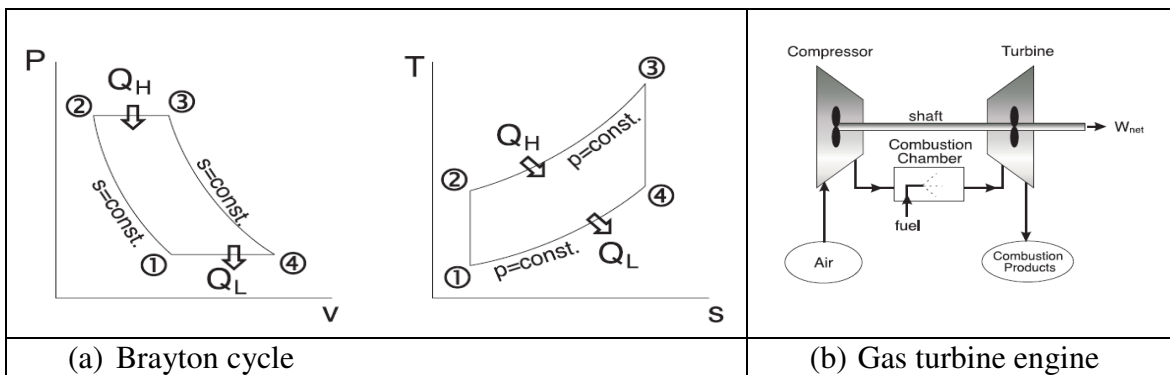


Figure 1-1 Gas turbine operation principle

Gas turbines can be powered by either gaseous or liquid fuels. Natural gas is one of the major fuels used for land based power plants, with liquid fuels being essentially

used for aviation purposes due to its high storage density. Though the U.S. Energy Information Administration (EIA) projects that Coal remains the dominant fuel for electricity generation, its share is expected to decline significantly. In 2010, coal accounted for 45 percent of total U.S. generation; in 2020 and 2035 its projected share of total generation is 39 percent and 38 percent, respectively. Competition from natural gas and renewables is a key factor in the decline. Overall, coal-fired generation in 2035 is 2 percent higher than in 2010 but still 6 percent below the 2007 pre-recession level. Generation from natural gas grows by 42 percent from 2010 to 2035, and its share of total generation increases from 24 percent in 2010 to 28 percent in 2035. The relatively low cost of natural gas makes the dispatching of existing natural gas plants more competitive with coal plants and, in combination with relatively low capital costs, makes natural gas the primary choice to fuel new generation capacity. The EIA also expects that Natural-gas-fired plants will account for 60 percent of capacity additions between 2011 and 2035, compared with 29 percent for renewables, 7 percent for coal, and 4 percent for nuclear power plants [1]. The major constituent of natural gas is methane and hence for the present investigation methane is used as fuel to simulate operation of gas turbine combustor with natural gas. Liquid fuels such as JP-8, Jet-A and others which are derivatives of petroleum fuels are mostly used for aircraft engines and will be used to examine the combustor fuel flexibility. Typical operation parameters for land based gas turbines and aviation gas turbines combustors are listed in Table 1-1 [2].

Table 1-1 Typical parameters for land based and aviation gas turbine combustor

	Land based gas turbine combustor	Aircraft gas turbine combustor
Length	60inch	10inch
Residence time	20ms	2-3ms
Thermal intensity	15MW/m <sup>3</sup> -atm	150MW/m <sup>3</sup> -atm
Fuel	Natural gas	Kerosene based liquid fuel
Pressure ratio	15	10 (cruise),40 (takeoff)
Flame stabilizer	Swirler	Swirler
Fuel introduction	Lean premixed	Liquid fuel atomization

The focus of this dissertation is on development of advanced combustion technology called colorless distributed combustion (CDC) for land based and aviation gas turbine application with fuel flexibility. CDC combustor employs direct injection of both air and fuel in the combustor without any need for a flame stabilizer. Air is injected tangentially to impart swirling motion without the use of any swirlers, typically used in conventional gas turbine combustors. The benefits of CDC technology are ultra-low pollutant emission, improved pattern factor, low noise emission, stable combustion and low pressure drop across the combustor. Thermal intensity of interest is about 20 MW/m<sup>3</sup>-atm operating on natural gas for land based operation with possible extension to high thermal intensity aircraft application using liquid fuel and much higher heat release intensities. The next section describes basic gas turbine design considerations.

## 1.2. Gas Turbine Combustor Design Considerations

The basic considerations for designing a gas turbine combustor can be summarized as follows [3]:

- High combustion efficiency
- Low emissions of pollutants and smoke
- Reliable and smooth ignition with relevance to aircraft engines
- Wide operational and stability limits
- Low pressure loss
- An outlet temperature distribution (pattern factor) that is tailored to maximize lives of turbine blades
- Freedom from pressure pulsation and other manifestations of combustion induced instabilities
- Multi-fuel capability
- Design for minimum cost and ease of manufacturing
- Durability
- Maintainability

The most important considerations are discussed briefly in the following subsections.

### 1.2.1. High Combustion Efficiency

Combustion efficiency of gas turbine combustors are almost 100%. This high combustion efficiency is mandated by fuel cost savings and low unburned hydrocarbons (UHC) emissions. The higher the combustion efficiency is, the less fuel

is consumed to reach the desired load conditions. Obtaining such high combustion efficiency might be a challenge when operating under ultra lean conditions, where incomplete CO to CO<sub>2</sub> conversion might occur, leading to a rise in carbon monoxide (CO) and UHC.

### 1.2.2. Low Pollutant Emission

Pollutants emission reduction as dictated by stringent regulations and environmental concerns has governed the design and development of land based gas turbine combustors to a large extent. Recently, these regulations have been extended to govern emissions from aviation gas turbines, especially during taxiing, take-off and landing. Figure 1-2 shows typical trade-off for NO<sub>x</sub> and CO/UHC for a gas turbine combustor. Higher CO emissions are observed at both low and high equivalence ratios and NO<sub>x</sub> emissions are high at higher equivalence ratios up to stoichiometry and decreases in fuel rich condition. The CO emission can be explained by the lack of excess oxygen for complete CO to CO<sub>2</sub> conversion and dissociation of CO<sub>2</sub> to CO and O<sub>2</sub> at the rich side, while at the lean side, the flame temperature is not high enough for complete CO to CO<sub>2</sub> conversion [4]. On the Other hand, NO<sub>x</sub> is a strong function of the flame temperature, consequently NO<sub>x</sub> is at its maximum around stoichiometry, where the maximum flame temperature occurs, and decreases at both sides of the stoichiometry as seen in Figure 1-2. Hence there is a small operational window where both NO<sub>x</sub> and CO emissions are in acceptable range. Soot, which is mostly carbon particles, is formed in fuel rich condition and is hard to eliminate once it is formed. The regulations from EPA restricts the NO<sub>x</sub> emissions for a land based gas turbine combustor burning natural

gas to be less than 15PPM for units > 250MW, less than 25PPM for units in range of 15-250MW and less than 42PPM for units <15MW [5].

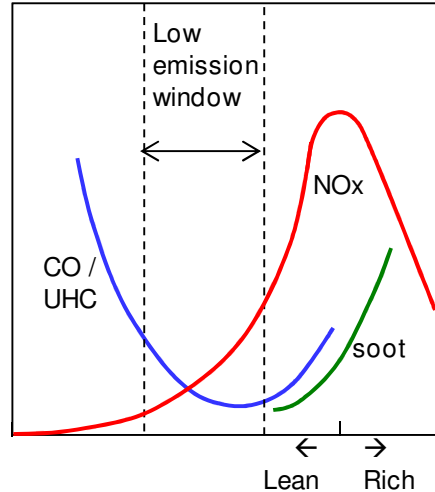


Figure 1-2 Pollutant trade-off.

### 1.2.3. High Thermal Intensity

The generally accepted definition of thermal intensity in literature is the amount of heat energy released per unit time in a unit volume of combustor scaled by the operating pressure [6]. Land based gas turbine combustors operate at thermal intensity range of 5-50MW/m<sup>3</sup>-atm [6]. The state of the art GE DLN 2.6 combustor which is widely used in popular gas turbine engines such as GE-7FA operates at thermal intensity of about 15MW/m<sup>3</sup>-atm [7]. Higher thermal intensity would result in smaller combustor volume for the same thermal load; hence higher thermal intensity is desired to reduce space as well as the weight of the gas turbine engine and hence reduce the hardware costs. Thermal intensity becomes more critical for aviation purposes, where the combustor size and weight are desired to be at minimum. Aviation gas turbines, in general, operate at a thermal intensity ten folds that of stationary gas turbines.

#### 1.2.4. Stable Combustion

As shown in section 1.2.2, it is desirable to operate gas turbine combustor at that narrow window of low emissions. It is desirable to operate in ultra-lean premixed mode to avoid hot spot regions and minimize the NO<sub>x</sub> emissions. However, near the lean operational limit, the combustor is susceptible to combustion instabilities. Combustion instabilities are large amplitude pressure oscillations due to coupling between oscillatory heat release process (unsteady combustion) and a natural acoustic mode of the combustor. Combustion instability in gas turbine combustor is one of the active topics for combustion research mostly for ultra-lean premixed combustors [8]. Combustion instabilities are undesirable because they may induce stress due to fatigue on the combustor components, and may result in thermal stress to the components. More importantly they may result in flame flashback or blow off. It is desirable to design a combustor which results in very small pressure oscillations. Industrially accepted value for pressure fluctuations (root mean square) is 1.5%rms.

#### 1.2.5. Low Pressure Loss

Gas turbine combustors operate at the high pressure side of the Brayton cycle, it is of great importance to minimize the pressure drop through the combustor, as such pressure drop will reflect in a loss of available energy to be extracted through the turbine. Overall pressure loss is defined by the ratio of total pressure drop across the combustor to the inlet total pressure and is given by equation 1.1 below. Pressure loss in the combustor is directly related to the total efficiency of the gas turbine cycle hence

minimum pressure loss is desirable. Generally, overall pressure loss across a gas turbine combustor range from 4-8% [3], calculated in cold flow condition.

$$\text{Overall pressure loss} = \frac{P_{in}^{total} - P_{out}^{total}}{P_{in}^{total}} \quad (\text{Equation 1-1})$$

Estimate of pressure drop due to combustion for a constant area duct is given by equation 1.2 below.

$$\text{Combustion pressure drop} = \Delta P_{combustion}^{total} = P_{in}^{dynamic} \times \left( \frac{T_{out}}{T_{in}} \right) (\text{Equation 1-2})$$

For practical combustors combustion pressure drop is about 0.5-1% of the inlet total pressure [3].

#### 1.2.6. Wide Operational Limit

Wide operational limit is of critical importance for gas turbine combustors, it is desired to furnish the operator with the ability to operate the gas turbine at different loads with high efficiency. The state of the art combustors operate at 50-100% load without influencing the emission profiles [7]. Higher pollutants emission is expected at conditions outside these loads such as part loading <50%. For aircraft engines the flexibility is even more desirable as the power requirements vary significantly (factor of 2-3) during taxi, take-off and cruise.

#### 1.2.7. Uniform Pattern Factor

A uniform temperature distribution at the combustor outlet is critical to maximize the turbine blade life and minimize thermal stresses in the blades [3]. Pattern factor quantifies the variation in temperature distribution at the combustor exit and is given by the following equation 1.3.

$$\text{Pattern factor} = \frac{T_{max}^{out} - T_{avg}^{out}}{T_{avg}^{out} - T_{avg}^{in}} \quad (\text{Equation 1-3})$$

As the pattern factor goes near zero, the maximum combustor outlet temperature will approach the average combustor outlet temperature. This allows for reducing cooling air requirements, as the blades will not be subjected to the same high amount of thermal stresses and temperature variations. Reduction in cooling air requirements reflects in increased efficiency and costs saving as more air will be available for energy conversion.

#### 1.2.8. Fuel flexibility

With increasing fuel costs, depletion of fossil fuels, concerns about energy security, and calls to move to a more sustainable energy sources such as bio-derived fuels, it is desirable to design gas turbine combustors for fuel flexible operation. This will allow the unit to operate with different kinds of fuel depending on availability and economics of operation. Generally natural gas is used for land based gas turbines. However, syngas produced from gasification plants, and low calorific value fuels can also be utilized in the gas turbine combustors as in Integrated Gasification Combined Cycle plants (IGCC). Aircraft engines generally use kerosene based liquid fuels such as Jet-A or JP-8. Flexibility to burn alternative fuels such as Hydrogenated Renewable Jet (HRJ) fuel and other viable biofuels will also be required in future with continuous depletion of petroleum resources.

In the next section, minimizing pollutants emissions, one of the most important design criteria, is discussed. Firstly, different pollutant formation mechanisms are described followed by discussion on the abatement strategies used in the industry.

### 1.3. Pollutant Formation

Pollutant emissions from different combustion processes have become of great concern due to their harmful impact on health and the environment. These concerns led to ever increasingly stringent regulations concerning pollutants emission from different kinds of engines including gas turbines. To design gas turbine combustor that surpasses current and near future emission requirements, an understanding for different pollutants formation mechanisms is critical. The main pollutants emitted by gas turbine combustions are as follows; oxides of nitrogen, carbon monoxides, unburned hydrocarbons, particulate matter (carbon / soot), and oxides of sulfur.

#### 1.3.1. Oxides of Nitrogen

Oxides of Nitrogen, or “NO<sub>x</sub>”, are considered of the most important pollutants emitted from gas turbines that have influenced the development of gas turbine combustors significantly [9]. The importance of oxides of nitrogen is related to their harmful effects such as contribution to photochemical smog formation, acid rain and ozone layer depletion [3]. Stricter emission regulations have pushed the gas turbine combustor development towards ultra low NO<sub>x</sub> emissions, specifically for large gas turbines (>250 MW) as specified by EPA [5]. NO<sub>x</sub> is mostly mixture of nitric oxide (NO) and nitrogen dioxide (NO<sub>2</sub>). NO at lower temperature can oxidize to NO<sub>2</sub>, however, NO forms major portion (about 90%) of NO<sub>x</sub> mixture and hence the formation mechanisms of NO are discussed here. NO<sub>2</sub> is formed in the post flame zone due to further oxidation of formed NO. NO could be formed by oxidation of atmospheric nitrogen with oxygen at high temperatures (thermal mechanisms) or via

other chemical kinetic pathways involving fuel chemistry. Different NO formation mechanisms that involve nitrogen from the air are thermal (or Zeldovich) mechanism, Fenimore (or prompt) mechanism and the N<sub>2</sub>O intermediate mechanism. The thermal mechanism dominates in high temperature combustion over a fairly wide range of equivalence ratios. The Fenimore mechanism is of more importance in rich combustion. The N<sub>2</sub>O intermediate mechanism plays an important role in the production of NO at very lean, low temperature combustion processes. In addition to that, NO can be formed if the fuel contains Nitrogen (Fuel NO). Figure 1-3 summarizes NO<sub>x</sub> formation mechanisms.

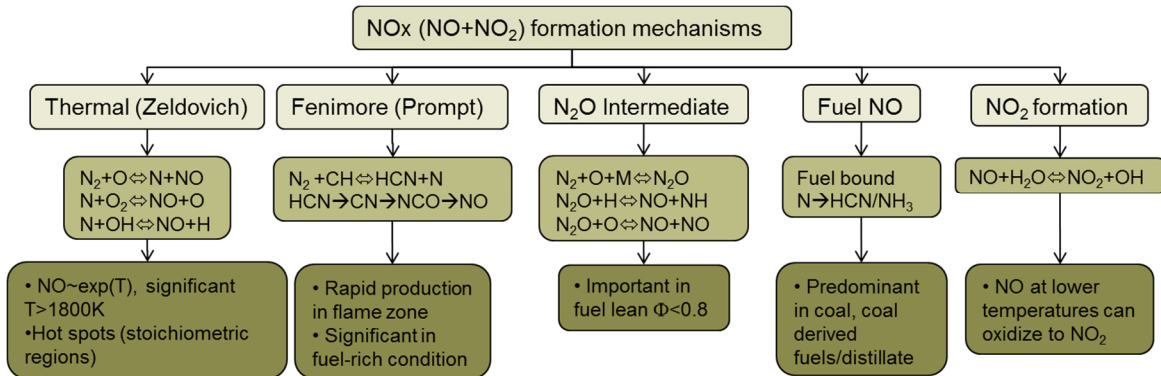


Figure 1-3 NO<sub>x</sub> formation mechanisms

Various researchers have investigated the contribution of each of those mechanisms on total NO<sub>x</sub> emissions, either in premixed flames [10] or in diffusion flames [11]. It was concluded that the main contributor to NO<sub>x</sub> formation is the thermal mechanism in premixed flames. It was also concluded that the main source of NO formation is thermal when velocity gradient is small and shifts to Fenimore as velocity gradient is increased [12]. Each of these mechanisms is described next.

### 1.3.1.1. Thermal (Zeldovich) mechanism

Thermal or Zeldovich mechanism for NO formation consists of two chain reactions with an additional reaction which is referred to the extended Zeldovich mechanism.



The rate constants for these equations (forward and reverse) can be found in the literature [13]. This mechanism is essentially coupled with fuel combustion chemistry through the O<sub>2</sub>, O and OH species. However, in case of complete fuel combustion before NO formation, the two processes can be uncoupled. NO is formed due to oxidation of atmospheric nitrogen. N<sub>2</sub>, O<sub>2</sub> and O are considered to be in equilibrium and N atoms are assumed to be at steady state. The rate of formation of NO is significant at high temperatures only because the fixation of nitrogen requires the breaking of strong N<sub>2</sub> triple bonds as seen in the high activation energy of the first equation of the Zeldovich mechanism. On the other hand, the activation energy for nitrogen oxidation is relatively small. Consequently, whenever oxygen is available, the rate of consumption of nitrogen atoms will be equal to that of its formation leading to a steady state. This assumption is valid except in fuel-rich combustion conditions.

Figure 1-4 shows the NO formation rates at different operating temperatures and oxygen concentrations as well as NO emission at various residence times [2]. It can be seen that NO formation rate increases exponentially at temperatures above 1850K. Consequently, the avoidance of hot spots is of critical importance to achieve ultra-low

NO emissions. Also, NO increases linearly with residence time, however the NO levels are much below the equilibrium value for a typical gas turbine combustor due to slower rate of NO formation and insufficient time to achieve equilibrium [2].

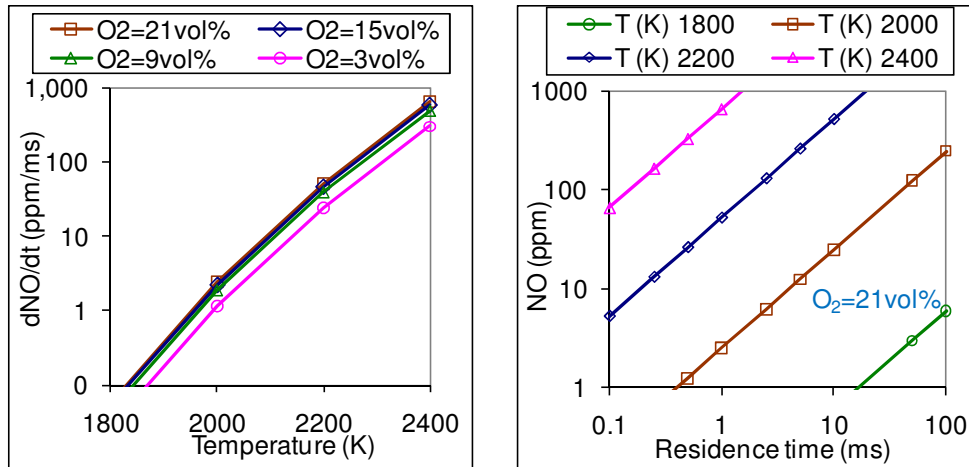


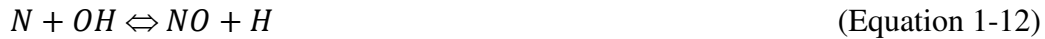
Figure 1-4 NO formation via thermal Zeldovich mechanism, NO formation rate (left) and NO formed (right) [2]

In flame zone, equilibrium assumption is not valid, super equilibrium (O, OH atoms) concentration of radicals can be several order of magnitude greater than equilibrium concentration. This can greatly increase the NO formation rates [4]. Thermal NO has been found to be not only sensitive to the combustion temperature and residence time but also to the inlet air temperature [3].

#### 1.3.1.2. Prompt (Fenimore Mechanism)

Prompt NO is directly linked to combustion chemistry of hydrocarbons. Fenimore [14] found that NO is rapidly produced in the flame zone of laminar premixed flames long before there would be time to form thermal NO (hence the name “prompt” or Fenimore). Nitrogen forms HCN by reacting with CH radical and follows the prompt

route  $\text{HCN} \rightarrow \text{CN} \rightarrow \text{NCO} \rightarrow \text{NO}$  to form prompt NO for equivalence ratios less than 1.2 as follows [4].



For higher equivalence ratios, richer than 1.2, the reaction proceeds in other routes and the chemistry become more complex. However, these equivalence ratios are relatively high compared to gas turbine operating conditions.

#### 1.3.1.3. $\text{N}_2\text{O}$ intermediate Mechanism (Nitrous oxide)

$\text{N}_2\text{O}$  intermediate mechanism is important in fuel lean combustion ( $\Phi < 0.8$ ) combustion specifically at low temperature conditions. Initially  $\text{N}_2\text{O}$  is formed with reaction of O radical with nitrogen then  $\text{N}_2\text{O}$  gets further oxidized to form NO [4].



#### 1.3.1.4. Fuel NO

In this mechanism NO is formed mostly due to oxidation of fuel bound nitrogen and this mechanism is dominant in coal and coal derived fuels, as well as liquid distillate fuel, where the fuel bound nitrogen can reach up to 2% by mass. The fuel bound nitrogen rapidly converts to hydrogen cyanide, or ammonia. Then the remaining steps follow the prompt NO mechanism [4]. However contribution of fuel NO is negligible for natural gas combustion for gas turbine application.

#### 1.3.1.5. *Fuel NO<sub>2</sub> Formation*

Nitric oxide ultimately oxidizes to form nitrogen dioxide, which is important to the formation of acid rain and photochemical smog. NO<sub>2</sub> can form a significant fraction from the total NO<sub>x</sub> emitted. The formation of NO<sub>2</sub> from NO prior exhausting the combustion products is highly dependable on the HO<sub>2</sub> radical at low temperature regions [4].

#### 1.3.2. CO Formation

Carbon monoxide is essentially formed in fuel-rich pockets in the combustion zone due to the lack of available oxygen for complete CO to CO<sub>2</sub> conversion. Also, carbon monoxide can be present due to dissociation of carbon dioxide at high temperatures especially at stoichiometric and moderately lean conditions. In practice, CO concentrations can be found to be higher than values predicted from equilibrium calculations especially at low equivalence conditions. This is related to the incomplete combustion of fuel that may result from inadequate mixing and burning rate between air and fuel, or quenching of post flame products [3]. Good fuel/air mixing, avoidance of fuel rich pockets and hot stoichiometric regions will result in reduction of carbon monoxide levels.

CO emissions are highly influenced by equivalence ratio, where rich conditions foster CO emissions due to high temperature dissociation of carbon dioxide. CO emission also increases at low equivalence ratio (ultra lean) due to incomplete combustion resulting in a small low CO emissions window [15].

CO is also influenced by operating pressure and inlet air temperature, where an increase in any of them (or both) at lean conditions leads to a decrease in CO emission. This is related to the increased reaction rates resulting from the increase in pressure/temperature [3] [15]. At lean condition, residence time plays an important role in complete conversion of carbon monoxide to carbon dioxide.

If the reaction rates are slow enough such that the reactions are not complete during the residence time inside the combustor, high CO emissions will result due to incomplete combustion. Gas turbine combustors operate at lean condition hence the role of residence time on CO conversion is important to consider while designing the combustor.

#### 1.3.3. Unburned Hydrocarbons (UHC) Formation

Unburned hydrocarbons include fuels or species that emerge from the combustor without being completely converted to carbon dioxide. These emissions are normally associated with poor atomization, improper mixing with air, and stoichiometric variation leading to very rich burning conditions. The kinetics of UHC are relatively complicated compared to CO. Generally, UHC is considered to be governed by the same parameters that affect carbon monoxide [3]. UHC can contain extremely dangerous emissions. Consequently, the reduction of UHC is valuable to minimize pollution to the environment and to extract that remaining energy in that unburned fuel.

#### 1.3.4. Soot Formation

Soot (sometimes referred to as smoke) is formed in fuel-rich zones due to insufficient mixing between fuel and air. Soot consists mainly of carbon (about 96%)

along with hydrogen, oxygen, and other elements that exist in the fuel [3]. Increasing the combustor pressure increases soot emissions particularly with sprays as the pressure affects the cone angle of the spray [3]. However, these effects are less dominant in air blast atomizers [16]. Soot formation also depends on fuel type. Physical fuel properties affect fuel atomization and/or mixing. On the other hand, fuel chemical properties govern carbon formation. Soot tendency was found to depend on ASTM smoke point, offering better prediction of soot formation behavior of a certain fuel [17]. Mostly to prevent soot formation, avoidance of formation of fuel-rich pockets is considered to be an effective way.

$\text{NO}_x$  is one of the most important pollutants and it has driven the design of gas turbine combustors to a large extent. The next section discusses  $\text{NO}_x$  abatement strategies used in industry including gas turbines, furnaces as well as boilers.

#### **1.4. $\text{NO}_x$ Abatement Strategies**

Several  $\text{NO}_x$  abatement strategies exist to ensure compliance with emissions regulations. These strategies can be classified into three main categories. These are injection of diluents, exhaust gas clean up, and  $\text{NO}_x$  formation prevention. These methods try to eliminate  $\text{NO}_x$  formation either by lowering combustion chamber temperature (thermal  $\text{NO}_x$  prevention) or by enhancing mixing to avoid stoichiometry variation, except for exhaust gas clean up where  $\text{NO}_x$  is dealt with after being formed. These strategies are summarized next.

#### 1.4.1. Injection of Diluents

Diluents are injected into the combustion chamber to lower the temperature and prevent thermal  $\text{NO}_x$  formation. Water or steam injection has been implemented to reduce the reaction zone temperature and hence to reduce the  $\text{NO}$  formation rate in the reaction zone [18]. However, there are many drawbacks of this technology, such as higher capital cost, higher fuel consumption, cost associated with water treatment and potential for corrosion and maintenance. Due to lower temperatures,  $\text{CO}$  and  $\text{UHC}$  emissions are higher with use of this technique [3]. Exhaust gases can play the same role as water/steam injection. Exhaust gas recirculation have been used in internal combustion engines with significant emission reduction [19]. However application to gas turbines is not straight forward due to the requirement of a heat exchanger between exhaust and inlet to extract useful heat before recirculating. Little combustor development is required, however, this technology can only be used with very clean fuel to avoid fouling [3].

#### 1.4.2. Exhaust Clean-up

In this technique the  $\text{NO}_x$  in gas turbine exhaust is converted to molecular nitrogen and water vapor using ammonia. This method is also known as Selective Catalytic Reduction (SCR). The catalyst is also helpful in oxidizing some of  $\text{CO}$  and  $\text{UHC}$  present in the exhaust gases leading to an overall emission reduction. The most widely used catalyst is Vanadium Pentoxide. However, SCR is intolerant to sulfur-bearing fuels, resulting in more complicated operation for such fuels. The SCR is very successful with natural gas leading to 90%  $\text{NO}_x$  removal [3]. Major problem with this

technique is the requirement of feedback control loop system to furnish the required amount of ammonia according to the gas turbine loading conditions and emission reduction performance.

### 1.4.3. Limiting NO<sub>x</sub> Formation

Other than injecting diluents to lower combustion temperature, or after treatment of the formed NO<sub>x</sub>, several techniques are in use to manipulate the combustion process inside the combustor. These techniques focus on better reactants mixture to avoid variable stoichiometry, and on operating outside the NO<sub>x</sub> formation window.

#### 1.4.3.1. *Lean premixed (pre-vaporized) combustion:*

Low-emission combustors rely on near perfect mixing of fuel and air before combustion to avoid any stoichiometry variation and hot spot regions formation [3]. The combustor is operated in low emission window at temperatures less than 1850K such that NO<sub>x</sub> formed through thermal (Zeldovich) mechanism is almost nonexistent. To achieve ultra low emissions, premixing air and fuel is critical. The emissions are reduced significantly with the extent of mixing as shown in Figure 1-5 [20].

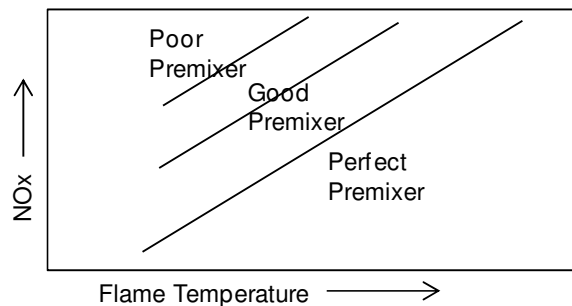


Figure 1-5 Effect of premixing on NO<sub>x</sub> emissions

A schematic of lean premixed combustor is shown in Figure 1-6 as compared to a conventional combustor. This technology is now widely used in land based gas turbine combustor and it has demonstrated single digit  $\text{NO}_x/\text{CO}$  emission levels [7].

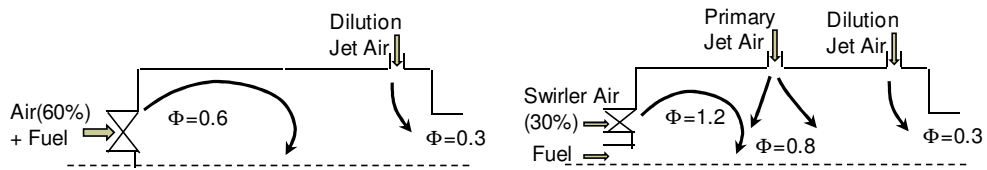


Figure 1-6 Lean premixed combustion (left) as opposed to conventional non-premixed combustion (right)

However, lean premixed combustion suffers from the problem of combustion instability and blowout due to their mode of operation near the flammability lean limit. Such instabilities may cause flame flashback in low velocity regions, such as boundary layers, leading to the reaction moving upstream towards the premixer which can be very dangerous in practical systems. Another problem is the difficulty of turn down of the combustor for part loading. One method to overcome this is to employ a non-premixed burner for part loading then move to a lean premixed burner as the load increases [7]. However, this will result in high emissions for part loading.

#### 1.4.3.2. *Lean direct injection*

Lean direct injection combustor operates in non-premixed combustion mode. Fuel is injected into air with focus on fast mixing between fuel and air such that they essentially burn in a local lean premixed mode producing low  $\text{NO}_x$ . Multipoint fuel injection systems have been investigated to achieve low  $\text{NO}_x$  emissions and each fuel injection system has a swirler to ensure fast turbulent mixing and gas recirculation for flame stabilization. The challenge is to achieve sufficiently fast turbulent mixing at

large length scales and elevated pressure conditions. This method have been also used in reciprocating engines where the piston head is designed to enhance turbulent mixing prior to combustion

1.4.3.3. *Rich-burn, quick-quench, lean-burn (RQL):*

In this technique, combustion occurs at both sides of the  $\text{NO}_x$  formation (high temperature) window. First, the reaction is initiated in a fuel-rich primary zone (equivalence ratio between 1.2-1.6) where  $\text{NO}_x$  formation rates are lower due to lack of oxygen and lower temperature. This zone also results in high CO and UHC production. Afterwards, rapid mixing and quenching occurs by additional combustion air to prevent combustion from happening near stoichiometric regions where  $\text{NO}_x$  formation rates are very high. This air addition leads to an overall lean mixture, in which the reaction is re-initiated, where  $\text{NO}_x$  formation rates are lower due to lower associated flame temperature. The operational equivalence ratio in this region is about 0.5-0.7, temperatures are maintained low enough so as to reduce thermal  $\text{NO}_x$  but high enough to convert CO and UHC emissions.

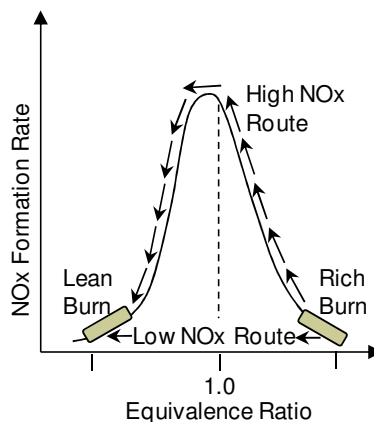


Figure 1-7 Rich-quench-lean combustion [3]

One critical factor concerning RQL combustion is the quenching process. Very fast cooling rates are essential to move from the rich regime to the lean regime without going through the high temperature high  $\text{NO}_x$  route. This adds to the complexity of the combustor as any deviation from the designed route will result in high pollutants emission.

#### 1.4.3.4. Catalytic combustion

Catalytic combustion is a process where a catalyst is used to initiate and promote chemical reactions at conditions in which the reaction is unsustainable. This allows stable combustion at ultra-lean conditions that are outside the flame flammability limits at lower operating temperatures. Catalytic combustor can operate at lower temperature because activation energy barrier is lower as compared to the homogeneous gas phase reactor. Combustion at such reduced temperatures dramatically decreases the production of thermal  $\text{NO}_x$ . The problem associated with catalytic reactor is to sustain high activity of the catalyst for a long period of time and to achieve large operational range. The second reactor is thermal reactor which raises the temperature of gases to turbine inlet temperature and reduces CO and UHC.

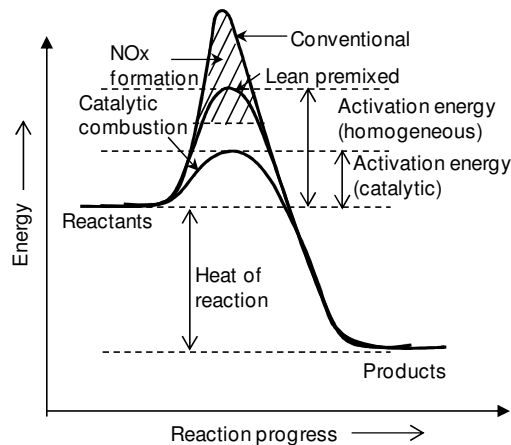


Figure 1-8 Catalytic combustion vs. premixed and conventional combustion

### 1.5. Objective

The objective of this present work is the development of Colorless Distributed Combustion technology for gas turbine applications at a thermal intensity, ranging from 5 to 50 MW/m<sup>3</sup>-atm. (commensurable to stationary gas turbines [6] ) and higher as compared to furnaces which operate at thermal intensity of less than 1MW/m<sup>3</sup>-atm.

High thermal intensity requires smaller confinement volume for the same thermal load. Such smaller volume results in higher velocities, lower residence time and difficulty in containing and stabilizing flame. Smaller confinement volume also affects the gas recirculation and air jet profiles. The objective of the present work is the development of high thermal intensity CDC combustor with careful control of different critical parameters. The major investigations reported in this dissertation are listed below.

1. Numerical investigation of gas recirculation and fuel/air mixing characteristics for different flow configurations employing swirling motion and the use of this information to improve design of CDC combustor.
2. Numerical examination of the residence time distribution characteristics inside the CDC combustor to achieve optimum performance.
3. Experimental evaluation of the flowfield of swirling CDC combustor under isothermal conditions using Particle Image Velocimetry
4. Experimental evaluation of different air and fuel injection configurations and their impact on pollutants emission using swirling CDC combustor.
5. Experimental evaluation of the impact of inlet air and combustor operating pressure on pollutants emission

6. Experimental evaluation of the swirling CDC combustor fuel flexibility using a wide range of fuels
  - Diluted methane
  - Hydrogen Enriched methane
  - Propane
  - Ethanol
  - Kerosene
  - JP-8
  - Hydrogenated Renewable Jet Fuel
  - Butyl Nonanoate
7. Experimental investigation of the effect of air injection diameter (air injection velocity) on performance of CDC combustor in terms of isothermal flowfield and pollutants emission.
8. Experimentally evaluating the impact of using multiple air/fuel injection on the combustor behavior.
9. Investigation of OH radical distribution using Planar Laser Induced Fluorescence technique with comparison to OH\* chemiluminescence.
10. Development of “Distribution Index” for colorless distributed combustion.

In the following chapter, different combustion technologies and combustor designs are discussed with emphasis on state of the art ultra-low emission combustion and high performance.

## **2. Chapter Two: Literature Review**

In this chapter, the previous work done by different researchers to achieve ultra-low emissions combustion is reviewed. Focus is on combustion technologies and combustors which employ discrete and direct injection of fuel and air in a confined chamber at high velocity so as to avoid flame stabilization. Under this criterion, several groups have demonstrated success in achieving their goal of low emission using their different techniques such as; High Temperature Air Combustion (HiTAC) [21] [22] [23] Flameless Oxidation (FLOX) [24] [25] [26] [27] [28], Moderate and Intense Low Oxygen Dilution (MILD) combustion [29] [30] [31], High Intensity Low Emission (HILE) burner [32], Stagnation Point Reverse Flow (SPRF) combustor [33] [34], and finally Colorless Distributed Combustion [2] [35] [36] [37] which is the main focus of this dissertation .

It may be noted that in stagnation point reverse flow combustor the fuel was injected coaxially with air and not discretely, however this investigation is also included in the consideration as conventional flame stabilization is avoided by high velocity of air injection. Other interesting combustor concepts that aim for low emissions include Trapped Vortex Combustor (TVC) [38] [39] [40]. TVC involves direct injection of fuel in the combustion recirculation zone, hence the name trapped vortex. This concept (TVC) was further developed to what is known as Ultra Compact Combustor (UCC) dedicated for aviation jet engines [41]. Princeton Asymmetric Whirl Combustor (PAWC) [42], where fuel is directly injected in very strong swirling fluid, has demonstrated low emissions. Jet Stirred Reactor (JSR) [43] is another combustor

design concept that is being investigated where premixed air and fuel is injected in a very small scale combustor.

All of the above combustors and combustion concept are in research phase either on a lab scale or as a prototype. Lefebvre gave a detailed description of currently used gas turbines and their combustor design [3]. These combustors are generally termed DLE combustors (Dry Low Emissions) and include Solar Turbines, Siemens hybrid burner, GE DLN (Dry Low NO<sub>x</sub>) and LM combustors, ABB EV burner, Allison combustors and others. These gas turbines have achieved low emissions (<100 PPM of NO<sub>x</sub>) using water/steam injection, emissions below 50 PPM of NO<sub>x</sub> have been shown with lean premixed combustion. Environmental Protection Agency has compiled the emissions of these gas turbine combustors [44] with some of these gas turbine emissions shown in Figure 2-1. NO<sub>x</sub> emissions were as low as 9 PPM for lean premixed combustion with CO emissions below 50 PPM, both corrected to 15% O<sub>2</sub>.

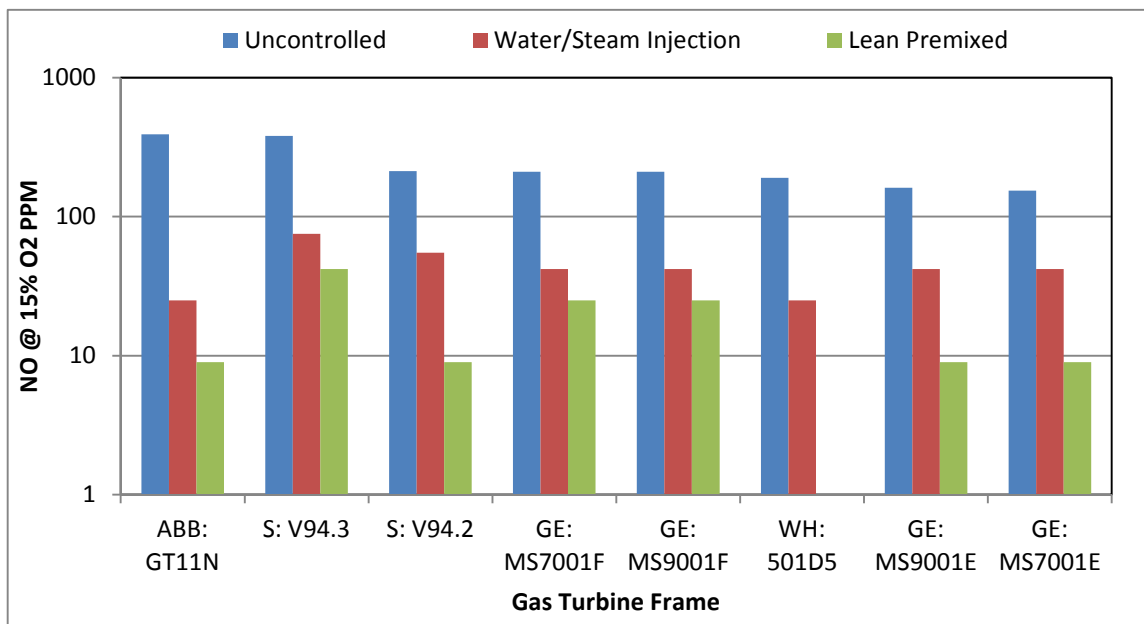


Figure 2-1 NO<sub>x</sub> emission from different gas turbines

Among these gas turbines, GE gas turbines with DLN 2.6 combustors have demonstrated the lowest emissions (9 PPM of NO<sub>x</sub> and 9 PPM of CO) [7] [44]. It may be noted that the DLN technology uses lean premixed combustion to minimize NO<sub>x</sub> emission. Fuel staging is used to operate the combustor at part load conditions under non-premixed conditions resulting in somewhat higher emissions at part loading. The combustor results in single digit NO<sub>x</sub> and CO emissions for 50-100% load condition at elevated pressure of about 16atm at firing temperature (combustor exit temperature) of 1561K operating at a thermal intensity of 15 MW/m<sup>3</sup>-atm [7] .

Figure 2-2 shows thermal intensities of combustors designed for furnace applications including the work of Weber [31], Colorado [25], Gupta, [21], Wunning [24], Sobiesiak [45], He [46], Yetter [42], Mi [47], Dally [48], Xing [49], and Szego [50]. Generally combustors having thermal intensity less than 1MW/m<sup>3</sup>-atm are intended for furnace application and thermal intensity greater than 10MW/m<sup>3</sup>-atm are intended for gas turbine combustor application [6]. Thermal intensity between 1-10MW/m<sup>3</sup>-atm [28] [32] are intended for high thermal intensity furnace application.

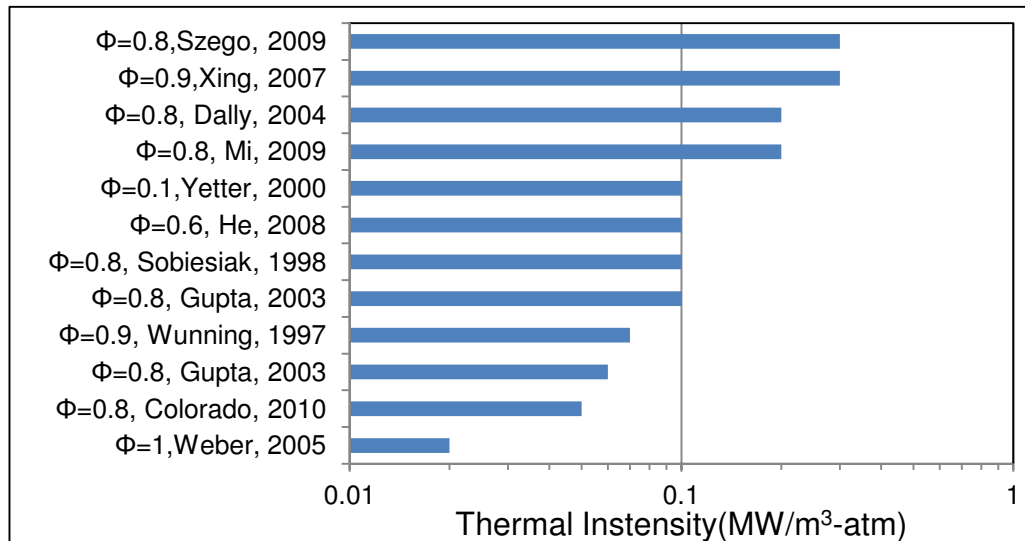


Figure 2-2 Thermal intensities for furnaces

Figure 2-3 shows the thermal intensities of combustors designed for gas turbine applications including the work of Verissimo [28], Kumar [32], Lukerath [26], Vanderbort [7], Bobba [33], Starub [40], Melo [39], and Hsu [38]. It can be seen that aside from Hsu work, most of the research for gas turbine combustors have been done in intensities ranging between 10 and 30 MW/m<sup>3</sup>-atm. Also, as we move to higher thermal intensities the combustor operates in a lean regime (low equivalence ratios) as compared to furnace applications as shown in Figure 2-3.

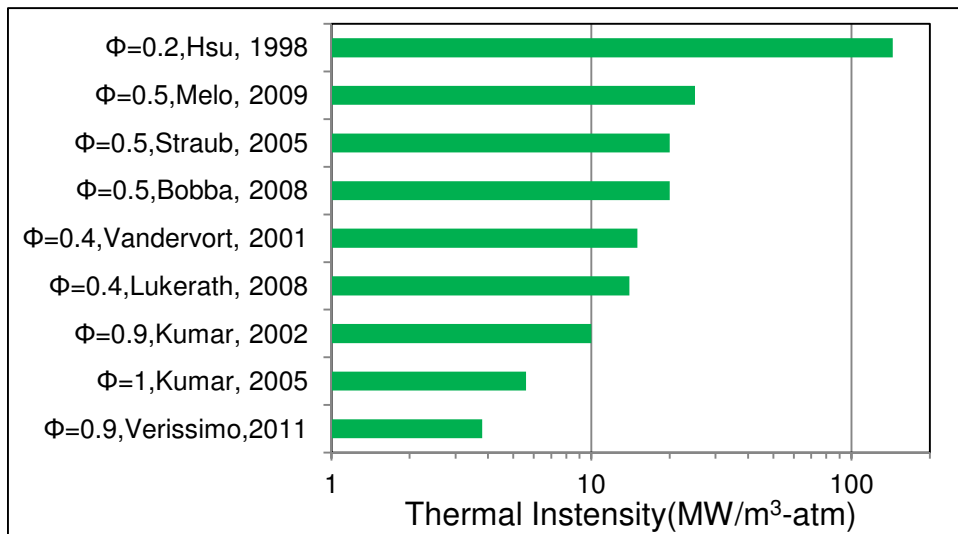


Figure 2-3 Thermal intensities for combustors

Following this categorization, these combustors will be discussed next in terms of design and resulting emissions.

## 2.1 Furnace Application

Low emission combustors have been developed to achieve low emission in furnaces which are characterized by low thermal intensity as opposed to gas turbines (< 1 MW/m<sup>3</sup>-atm.). In other words, the volume available for combustion is rather large, not

only to allow for complete combustion, but also to allow for heating/processing of different products. Consequently the length scales of these combustors are rather large. The air injection temperature is also much higher than the ambient temperature as it is thought that the temperature of air is required to be above the auto ignition temperature of fuel to achieve low emissions [21].

Figure 2-4 shows the NO<sub>x</sub> emissions for different furnace configurations while Figure 2-5 shows the corresponding CO emissions. It can be observed that the CO emissions for these combustors are generally about 10PPM, however, large variation in NO emissions has been reported. It can also be noted that the air and fuel injection velocities are about 100m/s for these combustors so that a conventional diffusion flame cannot be stabilized and lower emissions could be achieved. It is noteworthy that all the combustors intended for furnace application operate at atmospheric pressure condition.

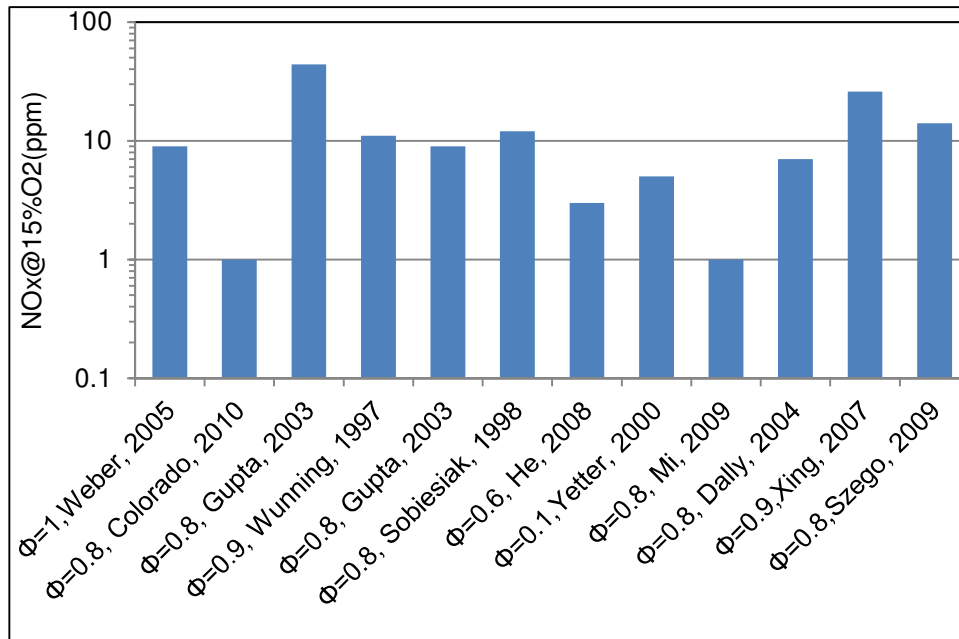


Figure 2-4 NO<sub>x</sub> emissions for furnaces

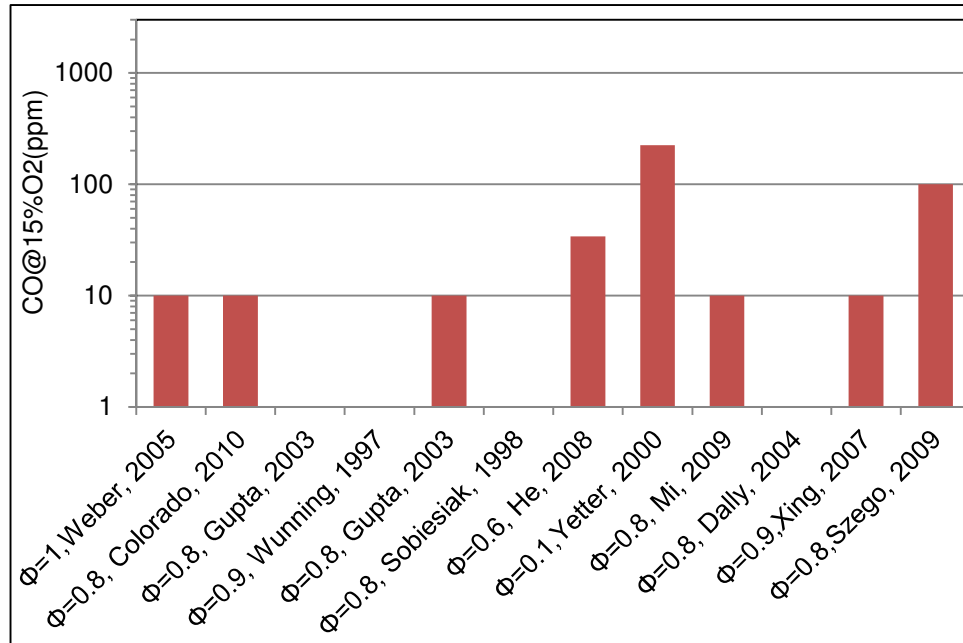


Figure 2-5 CO emissions for furnaces

Weber *et al.* [31], investigated MILD combustion at thermal intensity of  $0.02\text{MW}/\text{m}^3\text{-atm}$  for a range of gaseous, liquid and solid fuels including natural gas, heavy and light fuel oil and coal. The furnace had a very large length scale of about 246 inches and large air and fuel injection diameters resulted in much higher turbulent mixing time scales (1.46ms for air). Preheated air was supplied using a pre combustion chamber and very high preheat temperature of about 1600K was used. Oxygen was added at the combustor inlet to have 21% O<sub>2</sub> at the main combustor inlet. The furnace operated in forward flow configuration with fuel injected from same side of air injection. NO<sub>x</sub> at the inlet of combustion chamber was about 110PPM and at the exit was about 140PPM resulting in about 9PPM of net NO emission at 15% O<sub>2</sub> level. It is noteworthy that for furnaces application, emissions are corrected to 3% O<sub>2</sub> rather than 15%. However for ease of comparison, all emissions are corrected to 15% O<sub>2</sub>. No

detectable level of CO was found at the combustor exit. Uniform heat flux was observed in the furnace suggesting homogeneous combustion process.

Colorado *et al.* [25], investigated combustion of lower heating value fuels such as biogas (60% CH<sub>4</sub> and 40% CO<sub>2</sub>) as well as natural gas (97% CH<sub>4</sub>) in a self-recuperative reverse flow FLOX furnace at thermal intensity of 0.05MW/m<sup>3</sup>-atm. The furnace was about 53 inches in length. For both fuels, very uniform temperature profile was observed with flameless mode with temperature standard deviation of 10K as compared to temperature standard deviation of 114K for conventional mode suggesting very uniform temperature field inside the combustor. The reverse flow geometry resulted in very low NO<sub>x</sub> (1PPM) and CO (<10PPM) emissions. The air preheat temperature was 810K which is lower than the auto ignition temperature of natural gas suggesting that very high temperature is not necessary to achieve low emissions. It was observed that fuel dilution (with carbon dioxide in this case) had minimal effect on NO<sub>x</sub> and CO emissions. In flameless mode, the heat transfer efficiency was observed to be much higher as compared to the conventional mode (70% as compared to 40%) and this increase in efficiency was attributed to the recuperative system used for the flameless mode. In recuperative burner the heat is transferred continuously between the hot flue gases and combustion air by a heat exchanger. Recuperative system used in this work was a honeycomb made of cordierite which is used to extract heat from hot exhaust gases and transfer it to the combustion air. It may be noted that even though the mixing time scale for air injection was on higher side (0.309ms) very low NO<sub>x</sub> and CO emissions were obtained from this burner.

The previous work was performed in the early 2000's. Starting from mid-1990's Gupta *et al.* [23], and Tsuji *et al.* [21], investigated a 58kW regenerative HiTAC burner with elliptical air nozzles and circular fuel nozzles. The concept of HiTAC will be discussed in more details in later sections. Fuel nozzles were positioned around the air injector to operate in a forward flow configuration using natural gas as the fuel. The furnace was about 39 inch in length. It may be noted that, in a regenerator, heat is absorbed by a heat storing media such as ceramic monoliths by passing flue gas through it and then heat is recovered from the heat storage media by passing the combustion air through it and this cycle repeats alternately. Four burners were used with two burners operating simultaneously and switching with other two burners on the other side every 30s. The NO<sub>x</sub> emissions decreased from 210PPM to 44PPM when the combustion mode changed from ordinary combustion to distributed mode. This transition happened when the furnace temperature exceeded 1123K. In ordinary combustion usual flame was observed, however, in distributed mode flame in the furnace was very difficult to observe near the burner but in the area between fuel nozzles slightly blue color light was observed suggesting decomposition and ignition of fuel. Different cases were investigated and it was observed that NO<sub>x</sub> emissions were affected more by air jet velocity as compared to fuel jet velocity. The difference between maximum and minimum temperature was only 69K in distributed mode suggesting a uniform temperature field in the furnace.

Around the same time, in 1997, Wunning, J. A. and Wunning J. G. [24], introduced the name flameless oxidation (FLOX) as a technique to suppress thermal NO<sub>x</sub> by avoiding hot spot regions in the furnace. Under the conditions of internal gas

recirculation, combustion was observed without any visible or audible flame and hence it was named as flameless oxidation (FLOX). It was suggested that air preheat is not a strict requirement to achieve flameless oxidation; however in this study high air preheat temperatures were used (about 1100K). It was also mentioned that flameless mode can be achieved not only by discrete injection of fuel and air but also by common injection as well as in premixed mode. The flameless mode resulted in about 16dB noise reduction as compared to the flame mode. Both regenerative as well as recuperative burners were successfully demonstrated.  $\text{NO}_x$  emission of about 11PPM was reported with air preheat temperature of about 1100K and thermal intensity of  $0.07\text{MW}/\text{m}^3\text{-atm}$  at length scale of 92 inches.

Tsuji, Gupta, and Hasegawa [21], investigated a 350kW furnace operating in forward flow configuration with fuel injected from same side (denoted as “FS”) as well as opposite side (denoted as “FO”) of air injection to study the effect of fuel-air nozzle configuration. The thermal intensity for this furnace was  $0.1\text{MW}/\text{m}^3\text{-atm}$  and length scale of 150 inches. The combustion air was preheated to 1400K using regenerator with switching cycle of 30s. The “FO” flow configuration was expected to have enhanced dilution of fuel and air stream. The difference between maximum and minimum temperature was 80K for “FS” configuration however it decreased to 20K for “FO” configuration suggesting more uniform thermal field for configuration “FO”. The difference was about 120K for the conventional combustion mode. The furnace also achieved waste heat recovery in regenerator up to 77% and this directly relates to significant energy saving. Performance with respect to  $\text{NO}_x$  and CO emissions was similar for both “FS” and “FO” configurations with  $\text{NO}_x$  emission of about 9PPM as

compared to 128PPM in conventional mode. CO emissions were about 10PPM in both the HiTAC configurations and conventional combustion configuration. Visually low luminosity flames were observed in major part of the combustion volume simulating well stirred reactor features without actually having high agitating momentum.

Sobiesiak *et al.* [45], investigated a Fuel/Oxidant Direct Injection (FODI) burner which operated in forward flow mode. Plurality of air and fuel injection ports were used and air and fuel were injected at an angle so as to delay the fuel air mixing and enhance the recirculation and mixing of product gases before ignition. The burner was designed based on the calculation from solution of strong-jet/weak-jet (SJWJ) system investigated by Grandmaison *et al.* [51]. These calculations provided results for entrainment rates as well as the point of confluence of fuel jet with the air jet for different injection schemes. The fuel jet was considered the weak jet and air jet was considered as the strong jet based on the momentum ratio between the two jets. The NO<sub>x</sub> emission for this burner was 12PPM at thermal intensity of 0.1MW/m<sup>3</sup>-atm and furnace length scale of 118 inches. The air preheat temperature was 650K which is much lower than the auto ignition temperature of the fuel. The turbulent mixing time scale was also high with value of about 0.131ms for the air jet.

He [46], investigated a Strong-Jet/Weak-Jet furnace having a single air and fuel injection port. The higher momentum flux air jet was termed as Strong-Jet and the fuel jet was termed as Weak-Jet. The strategy to directly inject air and fuel inside the chamber was termed as FODI (fuel/oxidant direct injection). The combustor had reverse flow geometry and resulted in very low NO<sub>x</sub> (3PPM) and CO (34PPM) emissions at thermal intensity of 0.1MW/m<sup>3</sup>-atm. The length scale of the combustor

was 63 inches. Effect of fuel/air momentum flux, fuel/air nozzle separation and fuel injection angle was investigated in detail. Lower injection angle was observed to result in lower NO<sub>x</sub> emission and higher fuel injection velocity was observed to result in higher dilution of fuel jet before combustion and hence resulted in lower NO<sub>x</sub> emissions.

An interesting whirl combustor (PAWC) was investigated by Yetter *et al.* [42], where normal temperature air was injected tangentially and the product gases exits axially from the combustor. The swirl number for this combustor was very high (about 17) suggesting very strong tangential momentum as compared to axial momentum. Typical swirl number for conventional swirl stabilized combustor is about 0.5-0.7. The combustor operated at thermal intensity of 0.1MW/m<sup>3</sup>-atm and length scale of the combustor was 24 inch. Two types of fuel injection schemes were investigated, in the first scheme fuel was injected axially along the combustor centerline (symmetric) and in the second case fuel was injected near the air injection location in strong cross-flow (asymmetric). The fuel injection near the air jet in strong cross-flow resulted in favorable emission characteristics. For this combustor unusual stability limit below equivalence ratio of 0.1 was observed due to high temperature central region that supplies high temperature gases as well as radicals. Very low NO<sub>x</sub> emission of about 5PPM and CO emission of about 225PPM were reported for the asymmetric case. It may be noted that for this geometry the turbulent mixing time for air jet was high with a value of about 0.659ms, even then the NO<sub>x</sub> emission level was very low. For this combustor the NO<sub>x</sub> emission level increased to about 25PPM and CO emission level decreased to less than 10PPM at equivalence ratio of 0.4.

Mi *et al.* [47], investigated a small scale (23inch) furnace for the effect of air and fuel injection momentum as well as air/fuel premixing in a recuperative furnace. The thermal intensity was  $0.2\text{MW}/\text{m}^3\text{-atm}$  with air preheat temperature of 723K and normal temperature of fuel injection. The fuel nozzle was injected coaxially and not discretely in this furnace. The fuel nozzle was in the shape of a bluff body which is used to stabilize conventional combustion by protruding the nozzle inside the furnace. When the furnace temperature was above 1073K the nozzle is retracted to transition the reaction regime to MILD combustion. Effect of premixing was investigated by further retracting the fuel nozzle inside the air supply tube. The retraction increased the mixedness of fuel and air; however it also led to decrease in the jet momentum. The  $\text{NO}_x$  emission increased by retraction of fuel jet probably due to the more dominant effect of lowering of jet momentum while retracting the fuel nozzle. Hence the case when fuel nozzle is flush mounted with the combustion chamber gave the best results. It was also concluded that there is critical momentum required for air jet to sustain MILD combustion. Above the critical momentum both mixedness and jet momentum had minimal effect. Fully premixed mode also resulted in very low  $\text{NO}_x$  emissions (about 1PPM).

Dally *et al.* [48], investigated a MILD combustion furnace at thermal intensity of  $0.2\text{MW}/\text{m}^3\text{-atm}$  in reverse flow configuration. The furnace had length scale of 19 inches. Firstly, the furnace is heated up to 1073K using premixed mixture of methane and air and then fuel is introduced to make transition to MILD combustion. They observed that dilution of fuel with  $\text{CO}_2$  or  $\text{N}_2$  reduced the  $\text{NO}_x$  emissions significantly and resulted in invisible flame. Diluting methane up to fuel mass fraction of 0.15

resulted in NO<sub>x</sub> emission of less than 1PPM even in non-premixed mode. Greater reduction in NO<sub>x</sub> emission was observed with CO<sub>2</sub> dilution. Higher NO<sub>x</sub> emissions were observed with 100% propane (25PPM) and 100% ethylene (42PPM) as compared to methane fuel. They concluded that dilution with inert gases delays the ignition of fuel and allows fuel to mix with more recirculated gases before reaction and hence suppresses the NO<sub>x</sub> formation. They suggested that premixing the fuel stream with exhaust gases can result in lower NO<sub>x</sub> emissions.

Xing *et al.* [49], investigated flameless combustion by injecting normal temperature air in the furnace. The operating thermal intensity was about 0.3MW/m<sup>3</sup>-atm and length scale was 118 inch. The furnace operated in forward flow mode with coaxial injection of fuel and air instead of discrete injection. Initially, a diffusion flame was stabilized at lower flow rates. The flameless mode was achieved by increasing the flow rate (hence velocity) of natural gas where the flame zone was observed to become invisible. However, this furnace resulted in high NO<sub>x</sub> levels (26PPM) but low CO levels (<3PPM). This also suggests that even with coaxial injection higher level of NO<sub>x</sub> could be produced.

Szego *et al.* [50], investigated stability characteristics of a MILD combustion burner which operates in reverse flow configuration where the exit ports are located between the air and fuel injection ports. The air preheat temperature was of 723K, thermal intensity was about 0.3MW/m<sup>3</sup>-atm and length scale was about 23 inch. For the baseline case NO<sub>x</sub> emission was about 14PPM. Effect of air preheat temperature was investigated and it was observed that NO<sub>x</sub> emissions decrease from 14PPM at air preheat temperature of 723K to about 12PPM for air preheat temperature of 300K.

Amount of heat extracted had significant effect on NO<sub>x</sub> emissions as the emission level decreased to 7PPM from 14PPM by increasing heat extraction from 25% to 42%. Peculiar trend was observed with increase in equivalence ratio where increase in equivalence ratio from 0.8 to 0.9 resulted in decrease in NO<sub>x</sub> emission to 8PPM from 14PPM. Fuel dilution with CO<sub>2</sub> or N<sub>2</sub> (up to 76% by mass) resulted in significant reduction in NO<sub>x</sub> emission (up to 48%). It was postulated that the fuel jet momentum controls the stability of the system and lower fuel jet momentum results in lower penetration and hence lowers entrainment of the burned gases and hence a minimum fuel jet momentum (fuel/air momentum ratio=0.006) is required to achieve combustion in MILD regime.

Li *et al.* investigated the impact of using oxy-combustion under MILD conditions in a furnace at a heat release intensity of about 0.3 MW/m<sup>3</sup>-atm using natural gas, liquefied petroleum gas and ethylene [52]. It has been demonstrated that the MILD oxy-combustion can be achieved using the three fuels, even with pure oxygen as oxidant. When the MILD oxy-combustion is established, quite a uniform temperature distribution and very low emissions of NO<sub>x</sub> and CO are obtained. They demonstrated that the fuel-jet momentum rate is generally the most critical parameter for establishing the MILD oxy-combustion. In the present furnace system, both the use of a smaller diameter of the fuel nozzle and the fuel dilution by CO<sub>2</sub> result in a higher fuel-jet momentum rate and thus promote the occurrence of MILD combustion. Similarly, without any dilution, MILD combustion develops more easily when burning NG than using LPG and C<sub>2</sub>H<sub>4</sub> due to a higher momentum of the NG jet.

Relatively low NO<sub>x</sub> and CO emissions have been demonstrated at a similar heat release intensity using liquid hydrocarbons using double injection under MILD conditions [53]. However, it was concluded that using different fuels leads to different emission results, requiring adjustments to maintain these low emissions with various fuels.

## **2.2 Gas Turbine Application**

Different techniques and geometries have demonstrated low pollutants emission for furnace application with low heat release intensity. As we move towards the gas turbine combustors requirements, the heat release intensity is increased and the residence time is decreased. This limits the available time for mixing of the fresh reactants, as well as the time available for complete combustion for low CO emissions.

Figure 2-6 shows the NO<sub>x</sub> emissions for different combustor configurations discussed herein. It can be observed that the NO emissions for these combustors are generally below 10 PPM. Lower NO emissions have been demonstrated for combustors with intensity lower than 20 MW/m<sup>3</sup>-atm. Higher NO emission were shown for higher heat release intensities that are more suitable for gas turbine applications. It can also be noted that the air and fuel injection velocities are about 100m/s for these combustors so that a conventional diffusion flame cannot be stabilized and lower emissions could be achieved. Lower residence time demonstrated in gas turbine combustors lead to lower NO emissions, as the time available inside the combustor prevent the reaction from reaching equilibrium stage where high NO emissions are demonstrated.

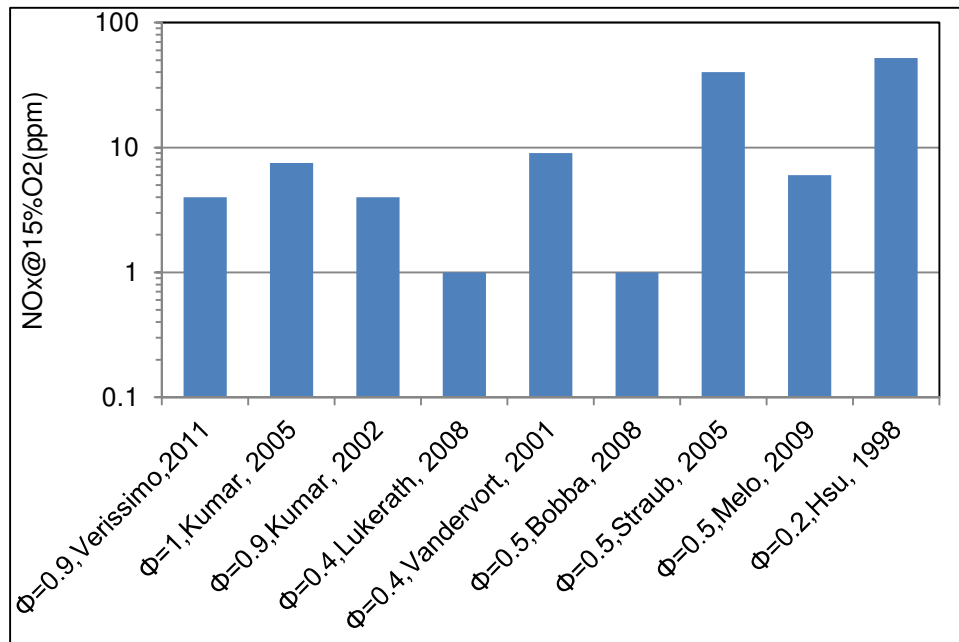


Figure 2-6 NO emissions for different combustors

Figure 2-7 shows the corresponding CO emissions for the same combustors. It can be seen that CO emissions varied substantially between different designs. 10 PPM of CO have been demonstrated, especially for combustors operating at higher pressures. On the other hand, high CO emissions have been encountered with some of the low heat release intensity configurations, requiring further understanding of the combustion behavior in each case. As the residence time is decreased, as compared to furnaces, CO emissions are expected to drastically increase as the time available for complete combustion is shortened.

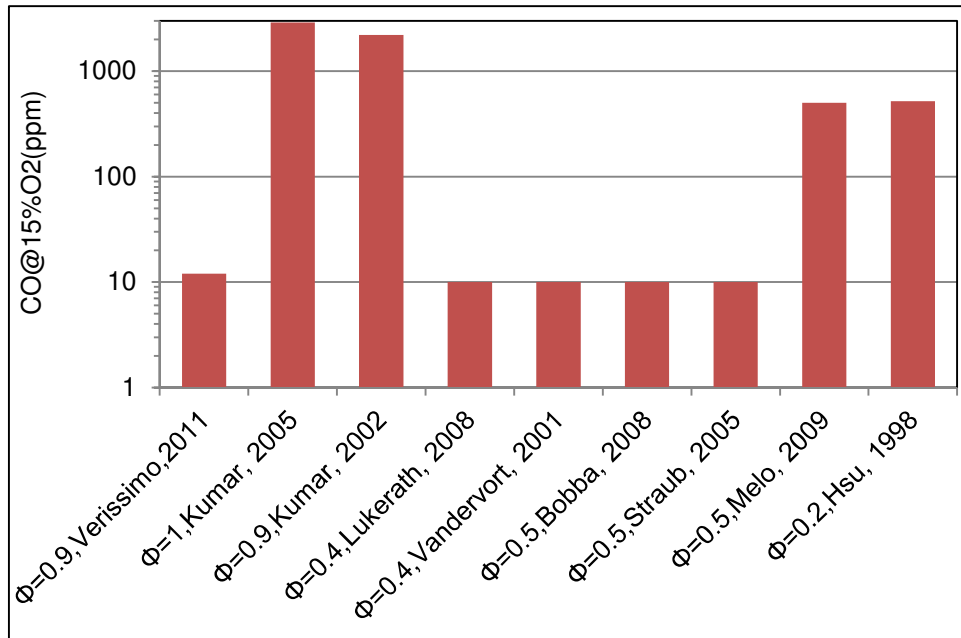


Figure 2-7 CO emissions for different combustors

Verissimo, A. S., *et al.*, [28], investigated a forward flow flameless combustor at thermal intensity of  $3.8\text{MW/m}^3\text{-atm}$  which represents high thermal intensity furnace application. The length scale of this combustor was small with length scale of 13.4 inch. Very low  $\text{NO}_x$  of about 4PPM and low CO of about 12PPM were observed for this combustor at equivalence ratio of 0.9. The air preheat temperature was 973K and turbulent mixing time scale for air injection was 0.104ms. An interesting trend was observed for this combustor, when air flow rate was increased at constant fuel flow rate to change the equivalence ratio the reaction zone was observed to move towards the air injection location. This was postulated to be because of faster entrainment and mixing of fuel jet in the higher momentum air jet resulting in shifting of reaction zone towards the air injection location.

Kumar, S., *et al.*, [32] investigated high intensity low emission combustor focused on high thermal intensity furnace application. The thermal intensity was  $10\text{MW/m}^3\text{-atm}$  as opposed to  $<1\text{MW/m}^3\text{-atm}$  demonstrated in previous studies at that time. This combustor had a frustum of a cone inside the combustion chamber to aid in recirculation of the gases. The combustor achieved 10-15dB reduction in noise level. In this work it was reported that high air preheat temperature is not a pre-requisite to achieve low emissions and in this work fuel and air were used at ambient temperature condition as opposed to use of recuperator/regenerator system used in previous studies. MILD combustion was defined in this work as having normalized spatial temperature variation of less than 15%. Experimentally very weak and barely visible flame was observed in MILD combustion mode. Even though low  $\text{NO}_x$  emissions of about 4PPM was obtained, high levels of CO emissions (2300PPM) were registered even after using staged air (10% excess) to oxidize CO.

Kumar, S., *et al.*, [54], examined the scaling criteria for MILD combustion burners and different strategies were discussed to scale the burner from 3kW to 150kW. Different approaches such as keeping the inlet velocity constant (CV), keeping the residence time constant (CRT) were considered. Keeping the velocity constant led to increase in mixing time ( $D/U$ , as  $D$  is increased) as well as decrease in the thermal intensity and keeping the residence time constant (constant thermal intensity) resulted in significantly higher velocities leading to unacceptable pressure drop. A different approach was successfully demonstrated where the burner major dimensions were scaled based on the CRT approach to keep the thermal intensity constant, however number of air and fuel injection ports were increased to result in similar mixing time

scale ( $D/U$ ). The air and fuel injection velocities were similar to maintain the pressure drop across the combustor to approximately same level. Air and fuel injection diameter were also kept similar by increasing the number of air and fuel injection ports. It was suggested in this work that the mixing time scale ( $D/U$ ) should be less than 0.086ms for the burner to effectively operate in MILD combustion regime. The burner was operated with both LPG (45MJ/kg) and producer gas (4.5 MJ/kg). It was observed that the scaled burner resulted in 8dB noise reduction as compared to conventional flame, and very uniform temperature and species field. For the scaled burner the CO emission level was quite high (2900PPM) however low NO level was achieved (8PPM). With producer gas the NO level was very low of about 1PPM and CO level was about 630PPM.

Luckerath, R., *et al.*, [26], investigated flameless combustion in forward flow configuration for application to gas turbine combustors. At the time of investigation this was the first study at elevated pressure for flameless combustion and the combustor was operated at pressure of 20atm. The fuel was introduced in the combustor by injecting the fuel coaxially with respect to high velocity air jet. The fuel nozzle was retracted so as to achieve some degree of partial premixing. This feature might also be responsible to achieve very low  $\text{NO}_x$  emissions of about 1PPM and CO emissions of less than 10PPM at equivalence ratio of 0.4 from the combustor even at elevated pressure. The thermal intensity of the combustor was  $14\text{MW}/\text{m}^3\text{-atm}$  and length scale was about 8inch. Very large nozzle velocity of about 160m/s was employed so that the turbulent mixing time for the air jet was very low with value of about 0.028ms. It was observed that nozzle velocity had significant effect on the mixing process and low

emission window was significantly extended by increasing the nozzle velocity and more distributed reaction zone was observed. Effect of hydrogen addition on flameless combustion condition was investigated and it was found that addition of hydrogen increases the NO<sub>x</sub> emission but extends the lean operational limit so that the combustor can be operated leaner to give lower NO<sub>x</sub> emissions. It was observed that decreasing the equivalence ratio makes the reaction zone more homogeneous. This combustor design has been patented [55].

Schutz, H., *et al.*, [56], analyzed pollutant formation for the FLOX combustor investigated by Luckerath, R., *et al.*, [26] using numerical simulation with optimized IGDIS code combined with GRI 3.0 reaction mechanism for chemical kinetic simulation. It was concluded that the thermal Zeldovich mechanism contributed about 41% of total NO<sub>x</sub> formed and prompt Fenimore mechanism and intermediate N<sub>2</sub>O mechanism contributed 27% and 32% respectively. They suggested that in flameless regime all three mechanisms contribute significantly to total NO<sub>x</sub> formed.

It may be noted that the state of the art gas turbine combustor (DLN-2.6) for land based power generation system operates at thermal intensity of about 15MW/m<sup>3</sup>-atm and the length scale of this combustor was 60inch. This combustor produced less than 9PPM of NO<sub>x</sub> as well as CO emissions for 50-100% load condition [Vandervort, C. L., [7]]. The inlet temperature is about 631K and outlet temperature is 1561K with operating pressure of 16atm.

Gopalakrishnan, P., [57] and Bobba, M. K., [58], investigated reverse flow geometry to achieve very low NO<sub>x</sub> (1PPM) and CO (<10PPM) emissions in both premixed and non-premixed conditions. This combustor operated at thermal intensity of 20MW/m<sup>3</sup>-

atm at equivalence ratio of 0.5 and combustor length scale was about 12inch. In this geometry the fuel was injected coaxially with air and this surrounding air acted as a shield from the hot product gases that prevented fuel from igniting prior to proper mixing with air and hence the combustor gives performance close to premixed combustion even in the non-premixed mode of operation. Liquid Jet-A fuel was also tested and it also resulted in very low emission levels (less than 10PPM for both NO and CO). Liquid Jet-A was injected directly and coaxially inside the combustor without any atomizer. The combustor was observed to be stable very close to the lean flammability limit of methane and this was postulated to be the reason for such low emissions. It was observed that the combustion is stabilized near the stagnation region opposite to the air injection location having low velocities and high turbulence levels. It was observed that the flame was in thin reaction zone regime. It was noted that the product gas entrainment does not have significant effect on the combustor performance and the lower emission levels are due to the ability of combustor to operate stably at lean condition. This combustor design has been patented [59].

Another interesting design is a trapped vortex combustor technology where fuel is injected in a vortex that is trapped between two plates or in a cavity in the path of combustion air flow to enhance flame stability. These combustors demonstrated exceptional lean operational limits of overall equivalence ratio less than 0.2 due to much richer burning reaction zone in a small cavity associated with the trapped vortex which serves as a continuous ignition source for combustion. The mixture in the trapped vortex is generally rich so that the hot gases produced are highly reactive for ignition of mixture in the main combustion chamber.

Straub, D. L., *et al.*, [40], investigated rich-burn, quick-mix, lean-burn (RQL) trapped vortex combustor at operating pressure of 10atm. The length scale of this combustor was 8inch. RQL concept has been used in conventional gas turbine combustor designs by axially staging air and having two different combustion zones in rich and lean regime to minimize NO<sub>x</sub> emission by avoiding near stoichiometric combustion, however, in TVC concept the air is radially staged. In trapped vortex combustor concept a cavity having high temperature circulating gases is used to stabilize combustion and the cavity region is the fuel rich region. The cavity flow was not observed to be affected by the main air flow rate. Cavity equivalence ratio of about 1.5 resulted in favorable emission profiles. Increasing the residence time in the cavity resulted in lower NO<sub>x</sub> emissions. Very low CO emissions of less than 10PPM were obtained however high NO<sub>x</sub> emissions were registered (about 40PPM).

A novel combustor model for application to gas turbine combustor was investigated by Melo, M. J., *et al.*, [39], by establishing large recirculation zone in the combustion chamber. The length scale of this combustor was 5.5inch. Fuel was injected in the recirculation zone which consists of hot and diluted mixture of combustion air and product gases which is above the auto ignition temperature of fuel. The combustor resulted in low NO<sub>x</sub> levels (6PPM) however much higher CO emission levels (500PPM) at equivalence ratio of 0.5.

Lammel, O., *et al.*, [27], investigated FLOX combustion at high power density of about 68MW/m<sup>3</sup>-atm and achieved low NO<sub>x</sub> and CO levels (<10PPM) at equivalence ratio of 0.63. Air and fuel were injected in forward flow premixed mode at elevated pressure of 7atm. It may be noted that this combustor was advancement to the

combustor investigated by Luckerath, R. *et al* [26], which operated at low thermal intensity of  $14\text{MW}/\text{m}^3\text{-atm}$ . In this combustor the air injection diameter was increased to 12mm from 4.5mm to allow more air flow as well as to reduce the pressure drop across the combustor. The length was reduced to 6.7inch from 8inch that was used by Luckerath. An advanced mixer was designed to premix air and fuel to a desirable degree before injecting the mixture in the combustor as opposed to partially premixing air and fuel as investigated by Luckerath. The combustor was also tested with propane and hydrogen-natural gas mixture fuel. It was observed that with addition of hydrogen the  $\text{NO}_x$  levels increased at a given equivalence ratio, however it decreased with operation of combustor at leaner mixtures and less than 10PPM  $\text{NO}_x$  was achieved for 50% hydrogen content fuel. In this investigation it was suggested that the power density with respect to the dome area is also important and it was mentioned that for gas turbine application power density in excess of  $10\text{MW}/\text{m}^2\text{-atm}$  is required for satisfactory performance.

Jet stirred reactor having reverse flow geometry and operating in premixed mode was investigated by Shuman, T. R., [60]. The reactor was very small (0.8inch in length) and the investigation was focused on the effect of residence time, pressure and inlet temperature on combustion characteristics of lean premixed combustion. Very low residence time of about 0.5ms was also investigated. This combustor operated at thermal intensity of  $90\text{MW}/\text{m}^3\text{-atm}$ . It was observed that  $\text{NO}_x$  was lowest at intermediate residence time suggesting no clear trends could be concluded with respect to residence time for  $\text{NO}_x$  emissions. At lower residence time it was observed that the free radicals, such as O, OH and CH fill the combustion volume causing high formation

rates of  $\text{NO}_x$ . It was observed that increasing inlet temperature and operating pressure tend to reduce  $\text{NO}_x$  emissions. It was concluded that the reactions occurs in chemical rate limiting regime due to fast turbulent mixing. This combustor was mostly intended for fundamental flame studies for conventional gas turbine application instead of actual implementation and development of distributed combustion technology. The turbulent mixing time for air jet was very small for this reactor (about 0.018ms) to provide intense mixing condition. A conceptual Time-Optimized Flame Cavity (TOFC) which is a jet-stirred reactor inside primary combustion zone was also discussed that could be implemented in a gas turbine combustor. The basic idea is to have optimal residence time to minimize  $\text{NO}_x$  emissions and it was postulated that the combustor could yield  $\text{NO}_x$  as low as 3PPM.

Very high intensity trapped vortex combustor has been developed at air force research laboratory (AFRL). Hsu, K. Y., *et al.*, [38], investigated a conceptual trapped vortex combustor where the vortex is trapped between a fore-body disc and an after-body disc and the blockage ratio was about 76%. The thermal intensity of this combustor was  $144\text{MW}/\text{m}^3\text{-atm}$  with very small length scale of 1.6inch. Air was injected in the cavity so as to reinforce the vortex in the cavity. The after-body diameter of about 0.73 times the fore-body diameter and cavity length of about 0.59 times the fore-body diameter was found to give favorable results of low pressure drop as well as stable flame. For the reacting flow condition very low pressure drop of about 1.5% was observed. Very low lean blowout equivalence ratio of 0.05 was obtained suggesting highly effective stabilizing influence of the trapped vortex. However, very high  $\text{NO}_x$  emission of about 52PPM and high CO emission of about 520PPM were reported at

overall equivalence ratio of 0.2. For this combustor the turbulent mixing time was about 0.048ms.

Advanced vortex combustor based on the concept of trapped vortex combustor was investigated by Edmonds, R. G., *et al.*, [61] at the National Energy Technology Laboratory. Ultra low NO<sub>x</sub>, CO and UHC emissions (4, 4, 0PPM) were obtained at equivalence ratio of 0.55 with very low pressure drop of 1.75% as the combustor did not require any swirl vanes to stabilize the flame. The combustor was tested at elevated pressure of 10atm. Very low pressure fluctuations of less than 0.15%rms were achieved which was an order of magnitude lower than industrial accepted level of 1.5%rms. This combustor design has been patented [62].

Ultra Compact Combustor, seen as a development of TVC, is being developed with military aviation application in view. Current investigations focus on the location of intermediate combustion products location and how that is affected by operational conditions and flow rates [63]. The reaction zone and pressure drop of UCC have been investigated to minimize Rayleigh pressure loss [64]. For these investigations, CO emissions were a main concern due to the small combustor size with relevance to combustion efficiency and thrust.

A summary of other relevant details of the discussed combustors performance operating in various configurations reported are available in the literature [2].

## 2.3. High Temperature Air Combustion (HiTAC)

### 2.3.1. Concept of HiTAC

Colorless distributed combustion (CDC), which is the focus of this dissertation, is based on the concept of high temperature air combustion (HiTAC) and in this section the features of HiTAC technology are discussed. HiTAC technology is now recognized as an advanced combustion technique for the combustion of fossil or derived fuels with simultaneous achievements of significant energy savings and pollution reduction (about 25%) [21] [65]. This technology is mostly focused on application for furnaces which operate at relatively lower thermal intensity ( $<1\text{MW}/\text{m}^3\text{-atm}$ ) as compared to gas turbine combustors ( $5\text{-}50\text{MW}/\text{m}^3\text{-atm}$ ) [6]. HiTAC is particularly attractive for processes that require uniform thermal field, higher and uniform heat flux distribution in the combustion zone, and compact size of the equipment [22] [23]. Controlled flame behavior results in uniform thermal field in the entire flame zone (less than about 50K [65]), significantly reduced pollutants emission (about 25%) and combustion noise (more than 7dB). Much of the experience with HiTAC has been on combustors for use in furnaces and boilers. The flow dynamics is much different under HiTAC conditions as compared to normal air case or normal air preheated to high temperatures.

The benefits of HiTAC technique has not been fully realized yet. Multiple fields and applications can greatly benefit from such a technique as it can be used in almost all kinds of combustion, power and propulsion systems. Figure 2-8 shows the possible applications of HiTAC, ranging from heating and high intensity combustion to thermal

destruction. Some of these fields have not been thoroughly investigated yet, while others are currently under investigation.

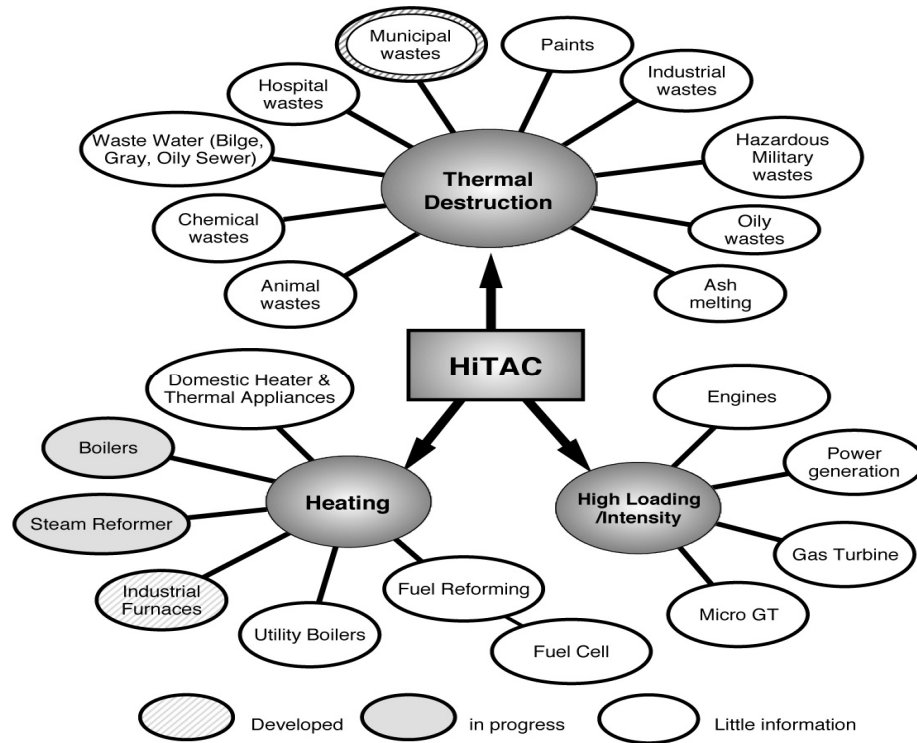


Figure 2-8 Potential applications of high temperature air combustion, including applications already developed or at present being developed [21].

In high-temperature air combustion (HiTAC) technology, high temperature combustion air in a low oxygen concentration is used in the combustion chamber. High temperature of the air is obtained by preheating the air with the exhaust gases from a furnace or reactor. The peak temperature in the flame zone is much reduced with the use of diluted low oxygen concentration combustion air even though the air is preheated to high temperatures. This low oxygen concentration or diluted air is obtained from the exhaust gases by recirculating part of the combustion products into the incoming hot combustion air. Internal heat circulation relies on heat convection and species

circulation so that pool of hot and active radicals in reaction zone can be maintained, which also assists in flame stabilization. The external circulation methods use heat exchanger to transfer the thermal energy via conduction between combustion products and solid media so that heat can be exchanged to the cool reactants. Most of the enthalpy contained in hot combustion products can be recirculated back to the combustion process. This allows one to utilize much of the waste energy for flame stabilization, reaction process control, and achieve desirable composition [22]. The combustion air is preheated to temperatures in excess of 1273°K, depending on the application, using honeycomb-type or ceramic ball-type heat exchangers.

For the furnaces area, HiTAC technology has shown revolutionary demonstration of energy conservation, reduction of pollution generation including NO<sub>x</sub> and CO<sub>2</sub>, uniform thermal field and higher heat flux than previously possible, to give superior quality product [21]. Higher heat flux is due to increase of both convective and radiative heat transfer. The concept of HiTAC is illustrated in Figure 2-9, in comparison with the concept of conventional furnace combustion. High temperature flames are usually generated in furnaces, if direct combustion between fuel and high temperature fresh air occurs.

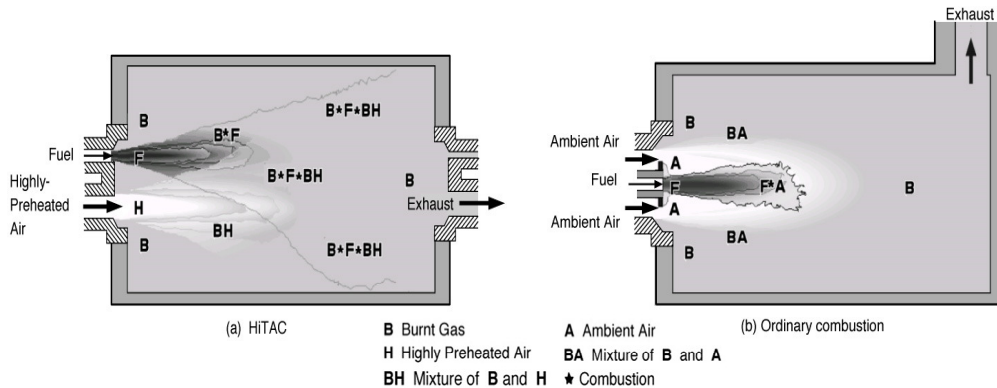


Figure 2-9 Mixing and combustion in furnace [21]

As a result of the new concept implementation, not only extinction of base flames occurs by the shear motion of high velocity inlet air but also the dilution of air with burned gas (BH) must occur prior to combustion by separating fuel and air inlets. Note that those are the conditions in which ordinary combustion cannot be sustained with ambient temperature air. In addition, the fuel injected separately into the furnace also entrains burned gas in the furnace, and some changes in the fuel, such as pyrolysis, decomposition, and vaporization of liquid fuel, if any, occur during this preparation period. Weak combustion reactions may occur between fuel and entrained products (B\*F) and the main combustion follows in the mixing zone of fuel and diluted air with a large amount of burned gas (B\*F\*BH). The change of flame due to a low concentration of oxygen caused by the high rate of recycling of burned gas probably yields a broadened reaction zone, where relatively slow reactions may be taking place. In established combustion without preheated air, direct combustion between fuel and fresh air (F\*A) occurs in the near-field of the burner. Thereafter, some combustion in diluted condition with burned gases may follow in the downstream portion of the flame because of the entrainment of recirculated burned gas by the incoming combustion air. Combustion (F\*A) in the vicinity of the burner shows the maximum temperature in the furnace, and most of the nitric oxides emitted from the furnace are formed there. However, combustion in this region is essential to sustain the combustion in the furnace, and whole flame cannot exist if extinction occurs in this portion.

Figure 2-10 shows conceptual temperature histories along streamlines passing through and by the flame zone. The former experiences near-stoichiometric flame temperature, which is slightly below the theoretical adiabatic temperature,  $T_{ad}$ , and the

latter rises only as mixing progresses. Turbulent mixing between the two produces large temperature fluctuations that can usually be observed in ordinary turbulent flames. If combustion air is preheated, it forces up all temperature profiles to some extent, with the same degree of fluctuations exceeding the theoretical adiabatic temperature of ordinary combustion  $T_{ad}$ , as shown in Figure 2-10(b). This is a well-known feature of the preheated air combustion (PAC) achieved by use of a recuperator. However, once the preheating temperature exceeds the auto-ignition temperature of the fuel, HiTAC becomes possible. Then, as shown in Figure 2-10(c), the temperature history along the streamline passing through the reaction zone shows a relatively mild temperature rise due to slow heat release in a low oxygen concentration atmosphere compared with those in previous cases. The other extreme indicates a temperature profile along the streamline outside the reaction zone, and it rises only with the progress of mixing between preheated combustion air and burned gas recirculating in the furnace. Accordingly, temperature fluctuations generated between these two are very small compared with the previous cases. In spite of the use of highly preheated air, the mean temperature as well as the instantaneous peak temperature is considerably lower in HiTAC than in ordinary combustion.

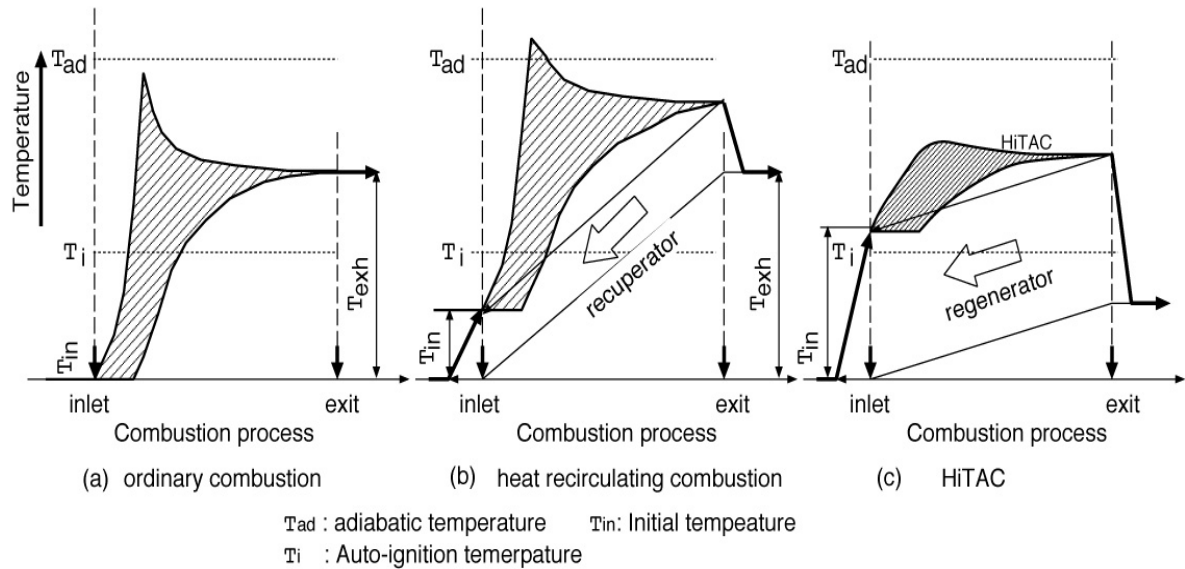


Figure 2-10 Conceptual temperature histories and fluctuation intensity [21]

### 2.3.2. Benefits of HiTAC

#### 2.3.2.1. *Energy Savings*

High-temperature air combustion technology uses regenerative heat exchangers to extract thermal energy from the waste gases in the combustion products. Exhaust gases from industrial furnaces and processes represent one of the major heat losses from the system. The regenerative media used in the HiTAC devices recovers large amounts of thermal energy from the exhaust gases and transports it back to the combustion zone. The amount of energy recovered translates directly into fuel saving which has been successfully demonstrated with savings up to 30% [21] [66].

### 2.3.2.2. *CO<sub>2</sub> Minimization*

The demands for reduced CO<sub>2</sub> emissions are increasing to prevent further global warming as the role of CO<sub>2</sub> is widely recognized in that aspect. Good correlation between fuel consumption and CO<sub>2</sub> production suggests that CO<sub>2</sub> reduction should be nearly the same as energy saving [21].

### 2.3.2.3. *NO<sub>x</sub> Reduction*

The temperature of the combustion air is one of the influencing factors on nitric oxides emission from combustion systems. The influence of inlet air temperature on nitric oxides emissions from a prototype furnace is shown in Figure 2-11.

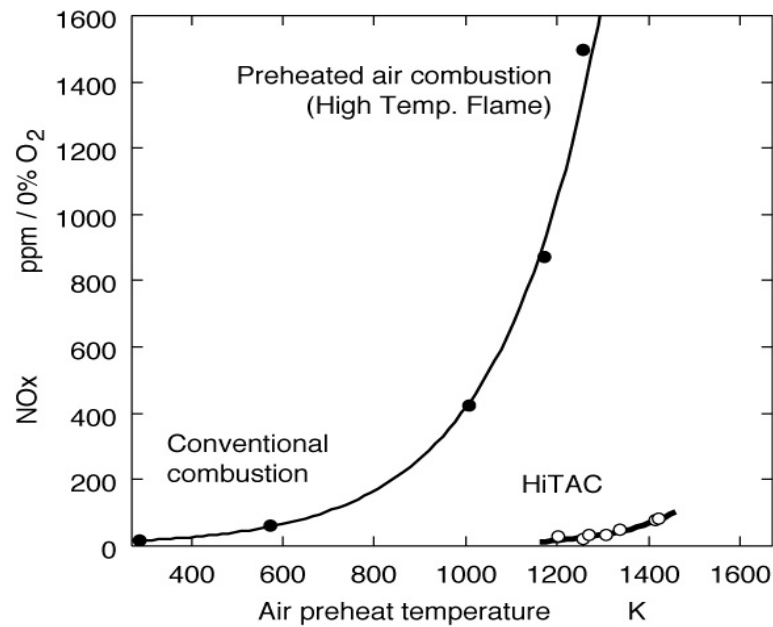


Figure 2-11 Preheated air temperature on NO<sub>x</sub> emission [21]

On the same figure, NO<sub>x</sub> emissions dependency on air inlet temperature for HiTAC technique is also shown. The dramatic decrease in NO<sub>x</sub> emissions can be seen as

counter intuitive. However, a detailed inspection showed that under HiTAC, unexpected low flame temperatures were seen as shown in Figure 2-12.

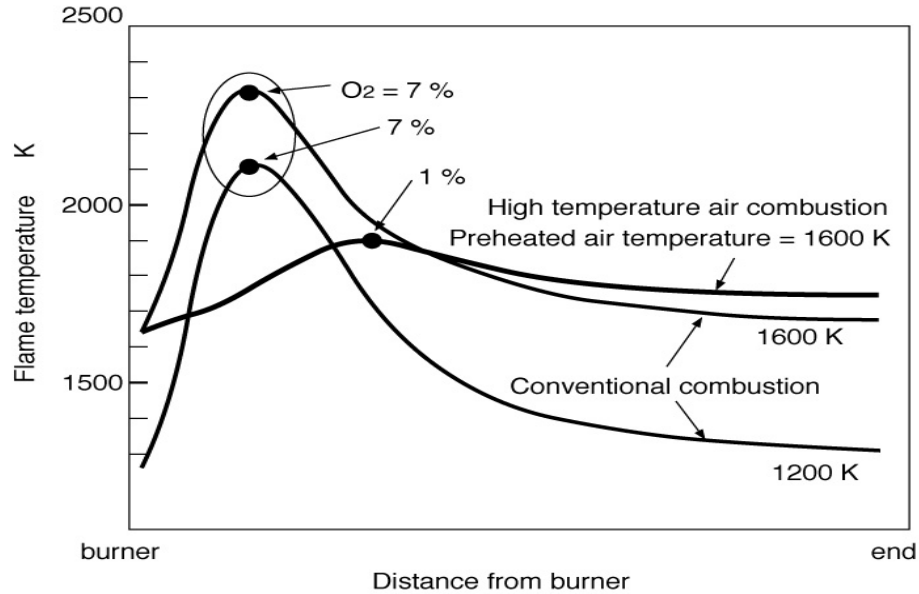


Figure 2-12 Oxygen concentration at peak point and distribution of temperature of flame on burner center axis [21]

This is caused by a combination of high preheating of reactants and the dilution by a large amount of inert gases. Consequently, the local reaction rate becomes small in diluted circumstances. Increased volume of the reaction zone (as combustion occurs in diluted circumstances) results in burning fuel at the same rate as the ordinary combustion, hence the same total heat release rate in the furnace is achieved. The same trend was seen in other demonstrations, where a drastic decrease of  $\text{NO}_x$  was obtained even in high air temperature by decreasing the oxygen concentration. The reduction in  $\text{NO}_x$  was reported to be about 50% [67].

#### 2.3.2.4. *Thermal Field Uniformity*

Under HiTAC conditions, the low oxygen concentration air at high temperatures is used for combustion and the temperature of combustion gases in the furnace or reactor is only about 50 to 100°C above the incoming high temperature combustion air. The oxygen concentration in the combustion air is very low (only about 2 to 5% by volume, depending on the application). Under these conditions the thermal field in the combustion zone is very uniform [68]. The peak temperatures in the combustion zone are suppressed to result in very low NO<sub>x</sub> emission levels.

From above discussion it can be noted that key features of HiTAC flames are discrete and direct injection of air and fuel and operation at elevated temperature and low oxygen concentration condition and these features will be incorporated while designing a CDC combustor. HiTAC technology has been successfully demonstrated and implemented for furnaces and its application can be extended to higher thermal intensity gas turbine combustors. It has been recognized that high temperature air is not essential to achieve low emissions and henceforth, we call the technology as colorless distributed combustion (CDC) focused on application to gas turbine combustors.

The high temperature air combustion work shares similar concepts with other combustion techniques such as Flameless Oxidation (FLOX) [24] and MILD combustion [29].

#### 2.3.3. HiTAC Investigations

Gupta, A. K., [22], investigated the characteristics of gaseous flames using high temperature air. The fuel was injection is cross flow from a 1mm diameter hole and air

preheat temperature above 1300K was used. The momentum ratio was kept constant in this study. Air was preheated using honeycomb regenerator and diluted with inert gas to simulate low oxygen concentration condition (up to 2%). It was observed that flames with high air preheat temperature were more stable and homogeneous both temporally and spatially. Temperature fluctuations (root mean square) decreased significantly from 197K to 4K with increase in air preheat temperature from 308K to 1473K and reduction in oxygen concentration from 21% to 4%. It was noted that HiTAC flames resulted in more uniform heat flux due to thermal field uniformity and hence resulted in more efficient heating in furnaces. Flame volume was observed to increase with decrease in oxygen concentration. Colorless flame was observed for oxygen concentration below 2% with methane fuel and this was termed as colorless combustion. The visible emission from flame was observed to be shifted towards green due to dominance of  $C_2$  radical under HiTAC condition. It was noted that the flame stability was infinite under HiTAC condition due to temperature of oxidizer being higher than the auto ignition temperature of fuel.

Gupta, A. K., *et al.*, [23], investigated the flame structure and emission characteristics for the effect of air preheat temperature and oxygen concentration in cross flow mode shown in Figure 2-13. It was suggested that at high temperature and low oxygen concentration condition the mixing time is higher, however, the increase in chemical time is much more leading to decrease in Damkohler number. With decrease in oxygen concentration the flame color was observed to change from yellow to blue to bluish green to green color and at very low oxygen concentration of less than 2% no color was observed and this was termed as colorless combustion. At lower

oxygen concentration (<5%) green color flame was observed due to domination of C<sub>2</sub> radical emission. With increase in air temperature the light intensity was observed to increase. Ignition delay time was calculated from flame standoff distance and it was observed that with increase in air temperature the ignition delay time decreases significantly. Mortberg, M., *et al.*, [69], investigated flow field features of HiTAC flames using particle image velocimetry technique for jet in cross flow configuration. It was observed that the fuel jet penetration was higher in high temperature air and turbulence level was lower. Mortberg, M., [70], observed significantly enlarged reaction zone (via OH\* chemiluminescence imaging) at high temperature and low oxygen concentration oxidizer condition and attributed it to low oxygen concentration which reduces the reaction rates and hence larger volume is required for combustion. In this work ignition delay time was estimated from the standoff distance of reaction zone from fuel jet injection and it was observed that the ignition delay time decreases with increase in air preheat temperature. Ignition delay time was observed to be significantly greater for lower calorific value fuel. Mortberg, M., *et al.*, [71], investigated flowfield and combustion features of methane and a low calorific value fuel (12% CH<sub>4</sub> in N<sub>2</sub>). The fuel jet velocity was about 25m/s and the cross flow velocity was 0.9m/s. For low calorific value fuel case almost colorless flames were observed. They observed higher turbulence and vorticity for low calorific value fuel case as compared to methane. Lower calorific value fuel revealed smaller penetration in cross flow, higher ignition delay time and uniform distribution of radicals as compared to methane fuel.

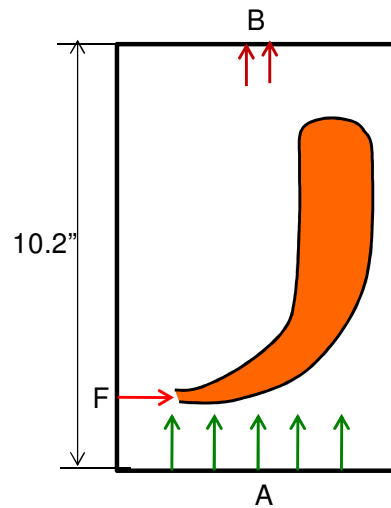


Figure 2-13 Jet in cross flow of high temperature and diluted

Lille, S., *et al.*, [72], investigated jet in co-flow configuration as shown in Figure 2-14. Hot flue gases from another burner were used instead of high temperature air from regenerator that was used in jet in cross-flow investigation shown in Figure 2-13. The air preheat temperature was about 1150K and O<sub>2</sub> concentration varied from 6-21%. Fuel/air velocity was kept constant in this investigation and fuel (propane) was injected from a 0.5mm diameter hole. The flue gas velocity was about 1m/s and fuel injection velocity was 26m/s. It was observed that with decrease in oxygen concentration in co-flowing gases the flame luminosity decreases and its size increases, similar to the observations made for jet in cross-flow experiments. At oxygen concentration lower than 10% no flame was visible. Yang, W. and Blasiak, W., [73], investigated the effect of oxygen concentration and temperature of co-flowing air, see Figure 2-14, on the flame size and they observed that flame length significantly increased with decrease in oxygen concentration. They suggested that at low oxygen

concentration condition the combustion phenomenon is very similar to well stirred reactor condition with volumetric combustion instead of a flame front. Increase in temperature of co-flowing gases was observed to increase the flame length slightly and the reason was attributed to lower mixing due to smaller density of oxidizer and higher temperature.

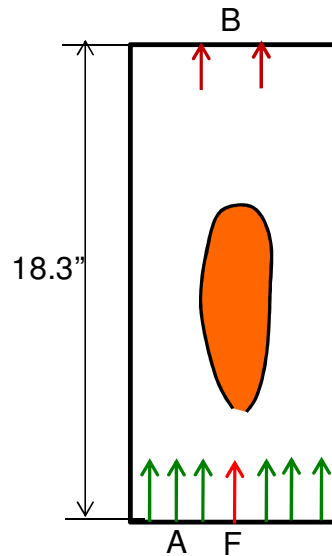


Figure 2-14 Jet in co-flow of flue gases.

Dally, B. B., *et al.*, [74], investigated jet in hot co-flow in geometry similar to that shown in Figure 2-14. The fuel jet diameter was 4.25mm and co-flow diameter was 82mm. The temperature of co-flowing gas was 1300K with oxygen concentration of 3%, 6% and 9%. 50% $H_2$ +50% $CH_4$  was used as the fuel. It was observed that with low oxygen concentration the visible emissions were low and the reason was attributed to suppression of radicals at low oxygen concentration. The peak temperature was significantly lower for low oxygen concentration condition. The OH radical concentration and CO levels was almost 3times less at 3% $O_2$  as compared to 9% $O_2$

with very wide reaction zone of 6mm. Much smaller NO levels were observed for low O<sub>2</sub> level.

Choi, G. M., and Katsuki, M., [75], investigated the effect of fuel injection location, simulating different fuel mixing conditions. Air was heated up to temperature of 1423K from an alternating-flow regenerative preheater. Fuel was injected from four locations as shown in Figure 2-15 and significant variation in NO was observed for different cases. Minimum NO was observed for fuel location “F4” due to uniform mixing of fuel and suggested distributed combustion. NO emission was found to be independent of temperature and equivalence ratio for this case. Very high NO was observed for fuel injection location “F2” due to fuel injection in recirculating flow and accumulation of fuel in the central region with lower mixing.

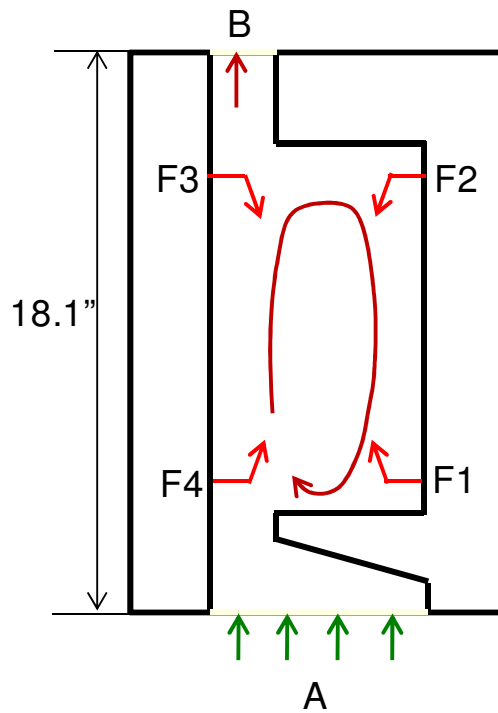


Figure 2-15 Effect of fuel mixing

As discussed earlier, very few studies have been reported at thermal intensity higher than  $25\text{MW}/\text{m}^3\text{-atm}$ . FLOX combustor [27] operates at thermal intensity of  $68\text{MW}/\text{m}^3\text{-atm}$ ., however, the fuel and air are well premixed before introduction in the combustor. Jet stirred reactor [60] operates at thermal intensity of  $90\text{MW}/\text{m}^3\text{-atm}$  but it also operates in premixed flow mode. This combustor had a very small length scale (0.8inch in length) and was used for fundamental flame investigation instead of application of technology to practical combustors. Trapped vortex combustor [38] operates at very high thermal intensity of  $144\text{MW}/\text{m}^3\text{-atm}$  in non-premixed mode, however, it resulted in very high  $\text{NO}_x$  (52PPM) and CO (520PPM) emission levels. It can also be noted that the combustors reported in literature operate in various fuel and air injection configurations such as forward flow (F) reverse flow (R) with fuel injection from same side (S), opposite side (O) or in premixed (P) mode with respect to air injection. Colorless Distributed Combustion is being developed with heat release intensities that span a wide range from  $20\text{MW}/\text{m}^3\text{-atm}$  up to  $400\text{MW}/\text{m}^3\text{-atm}$ . In the following section, CDC will be discussed in detail.

#### **2.4. Colorless Distributed Combustion**

The development of Color Distributed Combustion has been the main focus of the ongoing research at the combustion laboratory, university of Maryland. Development of colorless distributed combustion (CDC) for gas turbine application requires careful examination on the role of various input and operational parameters to achieve ultra-low  $\text{NO}_x$  emission and stable combustion operating at ultra-high thermal intensity. Various flowfield configurations have been previously investigated, such as forward

flow, reverse flow with fuel injection from same side of air injection, opposite side of air injection, in cross flow and premixed flow modes were investigated for a range of thermal intensity extending from 5 to 198MW/m<sup>3</sup>-atm starting from 2007 until 2011.

Figure 2-16(a) shows the thermal intensities and Figure 2-16(b) shows the length scale of selected combustors that have been previously investigated with the range of thermal intensity investigated extending from 5 to 170MW/m<sup>3</sup>-atm. [2]. It may be noted that for operation at ultra-high thermal intensity (156-198MW/m<sup>3</sup>-atm) the most desirable operational point was at equivalence ratio of 0.6 at thermal intensity of 170MW/m<sup>3</sup>-atm. The flowfield configuration as well as the corresponding equivalence ratio is also included in the graph. Both non-premixed and premixed flow modes are included in the plots. The length scale of the investigated combustors varies from 9inch for low thermal intensity (5MW/m<sup>3</sup>-atm) combustor to 1.5inch for ultra-high thermal intensity (156-198MW/m<sup>3</sup>-atm) combustor [2].

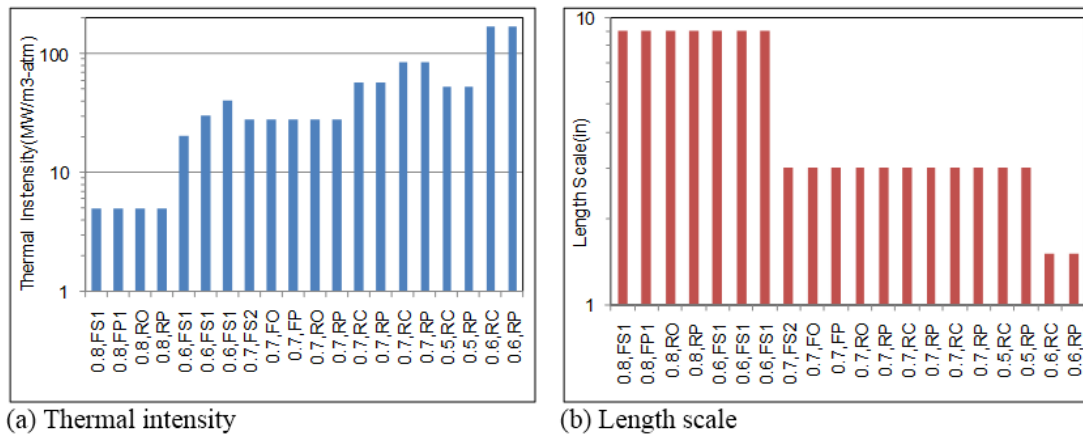


Figure 2-16 Thermal intensity and length scale for various CDC combustors investigated previously

Figure 2-17 shows the NO and CO emission level for the selected combustors. It can be observed that ultra-low NO emissions (about 1PPM) were observed for

premixed mode and the non-premixed combustion modes also reveal single digit NO emissions. CO emissions for most of the combustor geometries and configuration are less than 100PPM [2].

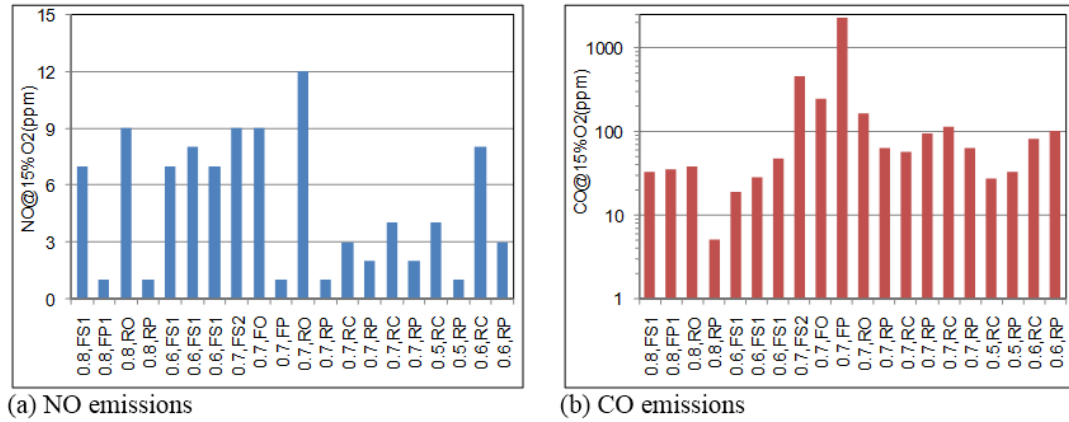


Figure 2-17 NO and CO emissions for various CDC combustors investigated previously

Initially investigations were performed at thermal intensity of  $5\text{MW}/\text{m}^3\text{-atm}$ . It was found from numerical investigation that reverse flow configuration resulted in higher fraction of gases having higher residence time even though the average residence time was noted to be independent of the flow configuration. This was supported by experimental investigation that revealed that reverse flow configuration resulted in lower CO emission levels on premixed flow mode. Effect of air and fuel injection diameter was investigated for a forward flow configuration “FS1” at thermal intensity of  $5\text{MW}/\text{m}^3\text{-atm}$  and it was observed that the fuel injection diameter had minimal effect on NO and CO emissions. However, with increase in air injection diameter, both the NO and CO emissions increased significantly suggesting that the air jet is the dominant jet and governs the flowfield and mixing inside the combustor as increase in air injection diameter considerably increases the mixing time scales ( $D/U$ ).

The thermal intensity was increased for forward flow configuration “FS1” and investigations were performed at thermal intensity of 20, 30 and 40MW/m<sup>3</sup>-atm. It was observed numerically that operation of combustor at higher thermal intensity (20-40MW/m<sup>3</sup>-atm) results in lower residence time and lower gas recirculation and hence it poses problem of stabilizing combustion and results in higher CO emissions with increase in thermal intensity. This was also supported by experimental investigation where higher CO emissions were observed at higher thermal intensity. A simpler combustor having only one air and fuel injection port was investigated at thermal intensity of 28MW/m<sup>3</sup>-atm in both non-premixed and premixed modes.

The thermal intensity was then increased to 57MW/m<sup>3</sup>-atm and reverse cross-flow configuration was observed to give most desirable performance. Fuel injection in cross-flow resulted in faster mixing between fuel and oxidizer and hence this resulted in lower NO and CO emissions. Further reduction in volume resulted in thermal intensity of 85MW/m<sup>3</sup>-atm. At thermal intensity of 85MW/m<sup>3</sup>-atm the effect of hydrogen addition to methane fuel was investigated and it was observed that with addition of hydrogen, the NO emission increased slightly, CO emissions decreased significantly and the lean stability limits were extended.

The selected geometry which operated in reverse cross-flow configuration at thermal intensity range of 53-85MW/m<sup>3</sup>-atm was further investigated. In non-premixed mode this configuration resulted in very low NO (about 4PPM) and CO (about 30PPM) as well as less than 5% pressure loss across the combustor. In premixed flow mode this configuration resulted in only 1PPM of NO and about 30PPM of CO emissions. Almost colorless reaction zones were observed in both non-premixed and premixed flow modes

and the reaction zone was observed to be present in cross flow near the fuel injection location in non-premixed mode. The thermal intensity at the most desirable operational point was  $53\text{MW/m}^3\text{-atm}$ .

Further reduction in volume of the combustor in reverse cross-flow configuration resulted in ultra-high thermal intensity range of  $156\text{-}198\text{MW/m}^3\text{-atm}$  and combustor operated at thermal intensity of  $170\text{MW/m}^3\text{-atm}$  at desirable operating point with NO emissions of 8PPM and 3PPM in non-premixed and premixed mode respectively. CO emission level was about 100PPM in both the modes. Dilution of fuel with inert gas as well as air resulted in significant reduction in NO emissions in non-premixed mode (from 8PPM to 2PPM). This geometry was also tested with liquid fuel (ethanol) and very low NO emission of 6PPM in direct-injection mode and 2PPM in premixed-pre-vaporized mode was obtained. CO emission level was 200PPM in both the modes. This shows promise for extension of this technology to aircraft engine application utilizing liquid fuel. Complete details of the investigations summarized herein are available in the literature [2].

## **2.5. Dissertation Outline**

The objective of this dissertation is investigation of the features of different flow configurations as well as development of high thermal intensity combustor with careful consideration of different parameters for CDC combustor. Key emphasis is on swirl generation and swirling motion to promote recirculation within the combustor to aid in achieving distributed reaction conditions. The dissertation elaborates sequential development of swirling high thermal intensity CDC combustor up to thermal intensity

of 105MW/m<sup>3</sup>-atm. The focus here is on land based gas turbine application. Various flowfield configurations including reverse flow geometry and swirling geometry as well as different combinations of fuel injection schemes has been investigated at range of thermal intensities in the dissertation.

In Chapter three, the design criteria for CDC are listed with emphasis on reactive gas recirculation and recirculation enhancement, swirl generation, ignition delay to ensure proper mixing prior to combustion. The mixing process is also discussed with relevance to jet in cross flow configuration. The importance of pressure loss elimination for power generation is also discussed

In Chapter four, investigations of the combustor flowfield, numerically and experimentally, are presented with comparison of different flow field configurations. Both premixed and non-premixed flow modes were investigated. The combustor operated at thermal load of 6.25kW with emphasis on the difference between three flow configurations covering both 2D like flow and 3D like flow. This chapter also includes velocity flowfield characterization using particle image velocimetry under isothermal conditions to evaluate flow recirculation under different conditions. Velocity flowfield coupled with measured pollutants emission provided a basis of comparison through which a final geometry was selected. Other geometrical parameters have been investigated to identify the most favorable swirling combustor design. These investigations are presented in the appendices. The performance of the geometry has been also evaluated under elevated temperature and pressure conditions.

In Chapter Five, fuel flexibility of the selected geometry is evaluated. The examined fuels included diluted methane, hydrogen enriched methane, propane, kerosene,

ethanol, JP-8, and renewable fuels. Emphasis is on the combustor fuel flexibility and low emissions regardless of the fuel used. The Impact of methane dilution was studied in details to evaluate the possibility of flame flashback or blow off. Similar analysis was performed with hydrogen enriched methane, where flame flashback is a possible hazard to the combustor due to the higher flame speed attributed to hydrogen combustion. Heavier hydrocarbons were used to evaluate the performance of the combustor in terms of pollutants emission and stability without the use of spray or atomizers. A novel biofuel was also examined to ensure that the discussed swirling CDC combustor demonstrate fuel flexibility over a wide range of fuels.

In Chapter six, further development of the combustor have been done in an effort to further reduce the resulting pollutants emissions. These developments included coaxial injection of fuel in air, and other non-premixed combustion configurations. The air injector shape was also examined, where the standard round injector was replaced with an elliptical injector with various aspect ratios and orientation. The third examined parameter was the air injection velocity. Three different velocity were examined under standard air temperature combustion. At first, isothermal velocity field was characterized using particle image velocimetry, then reacting flow experiments were performed to evaluate the pollutants emissions under these conditions. Another three air injection velocity were examined under preheated air condition in terms of pollutants emissions. For all these velocities, the pressure drop across the combustor was measured to quantify the impact of increased air velocity on pressure drop. The impact of air dilution on swirling CDC combustor was also examined. Air dilution has been studied as a means to reduce pollutants emission through diluting the fuel jet with

air, increasing its momentum, to result in better mixing. This technique have demonstrated success in ultra high thermal intensity up to  $430 \text{ MW/m}^3\text{-atm}$  and this demonstration is included in the appendix D. The impact of dual injection on the combustor performance have been studied. Scaling of the combustor requires the use of multiple injectors to maintain reasonable injection velocities in the combustor. The impact of dual injection on pollutants emission, as a step towards multiple injection, has been evaluated with focus on reaction distribution and reaction zone location.

Chapter 7 discusses the use of Planar Laser Induced Fluorescence to qualitatively outline the distribution of OH radicals inside the combustor. Various OH activation lines were examined with emphasis on OH distribution. The OH-PLIF data is compared to OH\* chemiluminescence to outline the difference between both techniques. A ratio between two activation lines was obtained in an effort to measure the temperature inside the combustor non-intrusively.

The experimental and numerical work is summarized in chapter 8, with focus on developing a “Distribution Index” that defines the amount of reaction distribution within the combustor based on a set of variables including geometrical and operational parameters. Chapter 9 focuses on the conclusions from present work and recommendations for future work.

### 3. Chapter Three: CDC Design Considerations

Colorless Distributed Combustion shares some of its key features with HiTAC technology which is discussed earlier. Key factors for CDC combustor or discussed in this chapter. These factors shall be taken into consideration while designing CDC combustor for ultra low emissions. These factors include internal reactive gases recirculation, high thermal intensity, air/fuel/recirculated reactive gases mixing and flow configuration.

#### 3.1. Reactive Gas Recirculation

Entrainment of hot reactive gases from within the combustor into the injected fresh air jet is critical to raise its temperature and reduce the oxygen concentration (to form hot and diluted oxidizer). Entrainment of jets has been studied heavily, where the recirculation ratio (ratio of entrained flow mass to the jet flow mass) was measured. Several correlations are available in the literature that describes the behavior of jet entrainment; among them is the work of Ricou and Spalding [76]. The correlation is for a non-reacting variable density free air jet, injected in a quiescent medium and is given below in equation 3-1.

$$\text{Recirculation ratio} = \frac{\dot{m}_{rec}}{\dot{m}_{jet}} = C_e \frac{X}{D^*} - 1 \quad (\text{Equation 3-1})$$

$$\dot{m}_{rec} = \text{recirculated mass flux}$$

$$\dot{m}_{jet} = \text{initial jet mass flux}$$

$$C_e = 0.32$$

$$X = \text{distance along the jet centerline}$$

$$D^* = D \left( \frac{\rho_{jet}}{\rho_{rec}} \right)^{1/2}$$

$D$  = jet diameter

$\rho_{jet}$  = injected jet density

$\rho_{rec}$  = recirculated gas density

Han and Mungal have quantified the effect of different parameters on jet entrainment such as heat release and buoyancy relating to reacting cases with view to predict NO<sub>x</sub> emission in a lifted jet flame [77]. It may be noted that the entrainment rate in a reacting jet is lower than a non-reacting jet. For free reacting jet the constant,  $C_e=0.13$  as compared to 0.32 for non-reacting jet [77]. Yang and Blasiak suggested that for lower oxygen concentration oxidizer the constant  $C_e$  increases and it lies closer to non-reacting value of 0.32, where the oxygen concentration is less than 5% [78]. However, considering that hot reactive gases entrainment is to be achieved prior to ignition, correlation for a variable density, non-reacting jet can be used. Moreover, the variation of recirculation ratio with jet diameter as well as the temperature of the injected air can be beneficial to understand the effect of these parameters that will be useful to design a combustor.

In a gas turbine the temperature of combustion air will increase with increase in pressure ratio due to near isentropic heating in the compressor. The variation of recirculation ratio with injected air temperature has been studied previously where it was observed that recirculation ratio increases, for higher air injection temperature (recirculation ratio  $\sim T_{air}^{1/2}$ ) [2]. Also the recirculation ratio was found to increase with injection air diameter decrease [2].

To achieve higher product gas recirculation, smaller air injection diameter is desired, however, smaller air injection diameter will result in higher air injection velocity and hence increased pressure drop. The injected air temperature as well as the product gas density will mostly be fixed based on the compressor pressure ratio as well as the overall operating equivalence ratio. However, when the air jet is enclosed in the combustor, the entrainment rate is expected to be different as the surrounding cannot be considered as a free stream anymore. Also, this expression only considers jet entrainment without considering any recirculated mass flow rate due to the combustor geometry. One common practice used to create recirculation and stabilize combustion is with swirl flow that entrains and recirculates a portion of the hot combustion species back to the root of the flame, which will be discussed next.

### **3.2. Swirling Flows**

Swirl flows have been widely investigated for several decades with different swirler arrangements and swirl numbers [79] [80]. Experiments in swirl flows have been carried varying from basic isothermal flow to reacting flows for low, moderate and strong swirl conditions. Experimental results have established the general characteristics of swirl flows that reveal the important effects of swirl on promoting flame stability, increasing combustion efficiency and controlling emission of pollutants from combustion [79].

Another method to create recirculation zone involves the use of cyclone like configuration. Cyclone combustion chambers have been reported in many forms [79]. The key factors associated with such arrangement can be summarized as follows.

1. Longer residence time inside the combustor.
2. Recirculation zones and turbulence are generated internally by shear between differing fluid
3. Large toroidal recirculation zone with high level of turbulence are generated for center exit configuration

Other beneficial aspects of such flow configuration and detailed description of their application can be found in the literature [79].

In these arrangements, the recirculation of hot active species is achieved through two key features. The first is the air jet entrainment, where the inlet air jet entrains flow from the surrounding as discussed earlier. The second is the recirculated gases due to the geometry of the combustor itself.

### **3.3. Ignition Delay**

It is of critical importance that the combustion does not occur until adequate mixing between fresh reactants and the hot recirculated reactive gases occur. Short ignition delay will result in a reaction that is rather concentrated resulting in hot spots formation. As recirculation ratio increases, the mixture temperature will increase and the oxygen concentration will decrease. With increase in the temperature of the oxidizer the ignition delay time of fuel will decrease so as to achieve conditions of spontaneous ignition. Arghode showed that for recirculation ratio in the range of 2-3, the temperature of oxidizer is about 1530-1655K with oxygen concentration of 9.4-8 % by volume [2]. These values (temperatures and oxygen concentration) have been used to estimate the ignition delay using the correlation below [81]

$$\text{Ignition delay} = t_{ig} = \frac{2.9 \times 10^{-13} [O_2]^{-1}}{T^{-0.31} \exp(-\frac{12000}{T})}, T \leq 1300K \quad (\text{Equation 3-2})$$

$$\text{Ignition delay} = t_{ig} = 6.25 \times 10^{-16} [O_2]^{-1} \exp(\frac{23000}{T}), T \geq 1400K$$

units = seconds,  $\frac{\text{moles}}{\text{cm}^3}$ , K

The ignition delay time decreases exponentially with increase in temperature and increases linearly with decrease in oxygen concentration. Figure 3-1 shows ignition delay time variation with oxygen concentration and temperature of oxidizer using both correlation and CHEMKIN-PRO simulations [2]. While designing a CDC combustor it should be noted that to achieve distributed reactions ignition delay time should be greater than the mixing time of fuel in oxidizer however, to achieve complete combustion the ignition delay time should be much less than the residence time in the reactor.

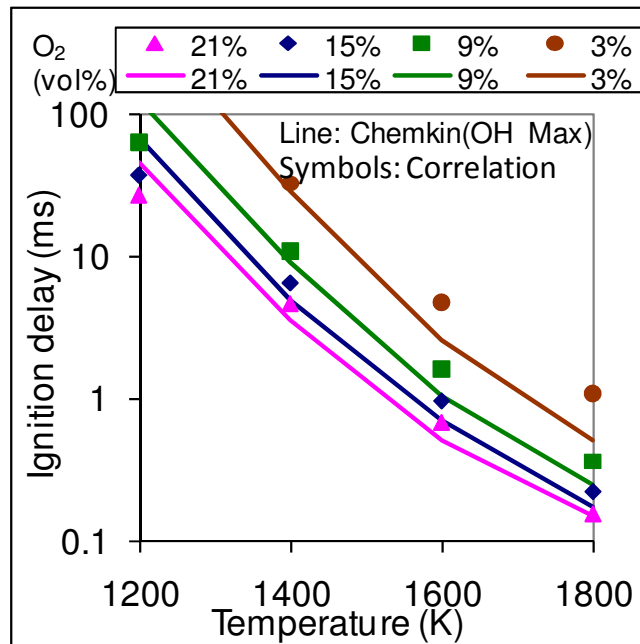


Figure 3-1 Ignition delay variation with air temperature and oxygen concentration [2].

### 3.4. Fuel/Oxidizer Mixing

#### 3.4.1. Jet Decay in Cross-Flow

In non-premixed combustion, fuel oxidizer mixing is generally governed by “jet in cross flow” mode where the fuel jet experiences cross flowing oxidizer stream to form a reactive mixture. Fast fuel/oxidizer mixing is desired such that a uniform reactive mixture is formed prior to ignition to result in distributed reactions. The behavior of jets in cross flow has been extensively studied. Pratte and Baines have introduced a correlation describing the behavior of such jets [82]. The correlation is given below in equation 3-3.

$$\frac{y}{rd} = A \left( \frac{x}{rd} \right)^B \quad (\text{Equation 3-3})$$

$$r = \left( \frac{\rho_i \times v_i^2}{\rho_c \times v_c^2} \right)^{\frac{1}{2}}$$

$$A = 2.05, B = 0.28$$

Further studies using planar laser induced fluorescence (PLIF) for acetone have been done to fully describe jet in cross flow by smith and Mungal for different cross flow velocities with r varying between 5 and 25. It was concluded that the higher the r ratio, the higher the jet penetration and that as the r ratio changes, different mixing regimes exist between the jet and the cross flow governing shape of the wake formed behind the jet [83]. Andreopoulos and Rodi investigated the behavior of jets in a cross flow for lower r values between 0.5 and 2. They concluded that for low r values, the turbulence of the cross flow jet plays an important role in the mixing process [84]. In general, for a jet in cross flow, as the cross flow velocity increases ( or fuel jet velocity

decreases), the  $r$  value drops, leading to less jet penetration and faster jet decay, which may or may not lead to good mixing depending on the flowfield geometry.

### 3.4.2. Turbulent Mixing Time

Another important aspect in fuel/oxidizer mixing is the turbulent mixing time scale. These time scales essentially depends on the eddies length scale [4]. A mixing time based on the life time of large eddies can be calculated based on the correlation given below in equation 3-4.

$$\text{Mixing time} = \tau_{mix} = \frac{l_0}{v'_{rms}} = \frac{D}{U} \quad (\text{Equation 3-4})$$

$D = \text{jet diameter}$

$U = \text{injection velocity}$

$l_0 = \text{integral length scale} = \frac{D}{10}$

$v'_{rms} = \frac{U}{10}$  (assuming turbulence intensity = 10%)

From the correlation it can be noted that the turbulent mixing time varies directly as diameter of the jet and inversely as the injection velocity. Thus, the turbulent mixing time varies as  $D^3$  for the same mass flow rate, where  $D$  is the diameter of jet. Consequently, any reduction in the injection diameter will significantly reduce the mixing time, leading to enhanced mixing between the fuel and the hot diluted oxidizer.

However, smaller jet diameter will result in higher pressure drop across the combustor due to the increased friction losses with the increase in velocity.

### 3.5. **Pressure Loss**

Low pressure loss is desirable to achieve higher efficiency from gas turbines. Previous researches have indicated that the higher the air injection velocity, the bigger the pressure drop will be in the combustor [58]. Computational Fluid Dynamics (CFD)

simulations have been performed to calculate the pressure drop for different injection velocities. It was found that, the higher the injection the velocity, the higher the pressure loss in the combustor. Figure 3-2 gives the pressure loss for different injection velocities as calculated between the combustor inlet and outlet.

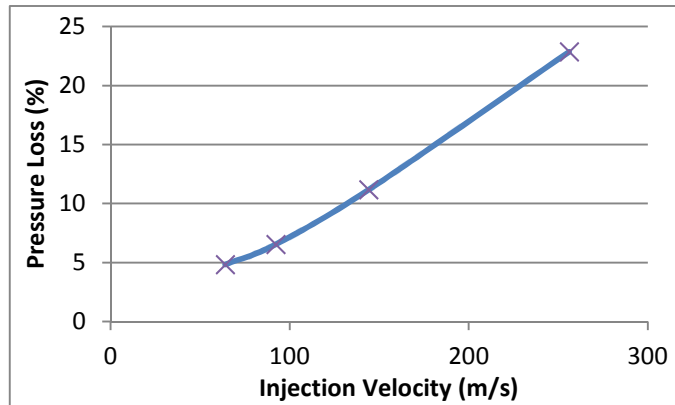


Figure 3-2 Pressure loss for different injection velocities

### 3.6. Thermal Intensity and Flow Configuration

Thermal intensity, heat release intensity, or energy release intensity are all expressions for the amount of heat energy released per unit time in a unit volume of combustor scaled by the operating pressure [6]. The unit of thermal intensity is  $\text{MW}/\text{m}^3\text{-atm}$ . Thermal intensity can be used as a representative of the residence time of gases in the combustor. Furnaces operate at lower thermal intensity, generally  $<1\text{MW}/\text{m}^3\text{-atm}$ , however, gas turbine combustors operate at much higher thermal intensities in the range of  $5\text{-}50\text{MW}/\text{m}^3\text{-atm}$  [6] with much higher intensities for aviation gas turbines. Common stationary gas turbine thermal intensities is  $20\text{MW}/\text{m}^3\text{-atm}$  [7]. Higher thermal intensity is desired to reduce the hardware weight as well as to reduce the capital cost of the system.

The residence time inside the combustor can be approximated by equation 3-5.

$$\text{Residence time} = t_{res} = \frac{\rho V}{\dot{m}} \quad (\text{Equation 3-5})$$

$\rho$  = average gas density in combustor

$V$  = combustor volume

$\dot{m}$  = total mass flow rate through combustor

As the thermal intensity increases, the required reactants mass flow rate increases while the combustor volume is constant. This results in a reduced residence time inside the combustor. This will form many challenges to the combustor designer. The challenges include difficulty to stabilize the flame, higher flow velocities as well as difficulty in achieving complete conversion of fuel as the time required for mixing and complete combustion has to be less than the residence time. Conversion of carbon monoxide is a slow process and lower residence time will result in higher levels of CO at the combustor exit. The effect of residence time on NO and CO emissions has been studied [2] using chemical kinetic simulations assuming perfectly stirred reactor using GRI-3.0 mechanism [85]. It was concluded that CO emissions increases sharply at lower residence time (<10ms), the NO emissions vary mostly linearly with increase in residence time. Hence, lowering residence time can result in lower NO emissions which can be beneficial while designing advanced low NO<sub>x</sub> combustors. Higher residence time will result in more time for conversion from CO to CO<sub>2</sub> and hence result in low CO emissions.

The variance of the average residence time is also important. The higher percentage of gases having low residence time, the higher the CO emissions will be even though

the average residence time is same of all the cases [2]. Hence, favorable residence time distribution where minimal amounts of gases have low residence time can result in conversion of CO and consequently lower CO emissions.

For the same thermal load, higher thermal intensity would result in smaller confinement volume. With reduction in volume, the confinement effects are expected to dominate the flowfield as well as the jet profiles. Such confinement will govern the flowfield and the entrainment of hot gases recirculation. The effect of confinement on the flowfield and combustor behavior have been studied numerically and experimentally [2]. It was observed that for smaller confinement volume the jet decays faster as compared to the free jet, also, for smaller confinement volume, maximum gas recirculation was limited by the confinement size [2].

These considerations are key in guiding the numerical and experimental work reported in the next chapters.

## 4. Chapter Four: Swirling Colorless Distributed Combustor Design

A medium thermal intensity CDC combustor was designed to fulfill the CDC design considerations mentioned in chapter 3. The first step was to use numerical simulation to evaluate the impact of some of the design parameters on the combustor. CFD was used to investigate the flowfield and gas recirculation characteristics inside the combustor to down select appropriate parameters for experimental investigations.

### 4.1. Numerical Modeling

#### 4.1.1. Combustor Exit Configuration

Numerical simulations were performed to investigate the effect of exit port location on the flowfield and recirculation inside the combustor. For these simulations, commercial software FLUENT® was used. The flow was modeled using finite volume method. For solving turbulence, standard k-e model with standard wall function is used. For non-reacting cases, species transport was used to determine mixing between air and fuel prior to combustion. The operating pressure was 1 atmosphere. For any of the numerical models, the volume consisted of around one million tetrahedral mesh cells.

The combustor chamber under investigation is a cylindrical chamber with diameter=16D and height=8D, where D is diameter of air injection port. Fuel injection diameter is D/3 and exit diameter is 2D, where D is 3/16 inch. Air is injected tangentially at half the height of chamber (4D) for all the cases investigated here. Figure 4-1 shows a schematic of the combustor with different exit locations. The numerical model is shown in Figure 4-2.

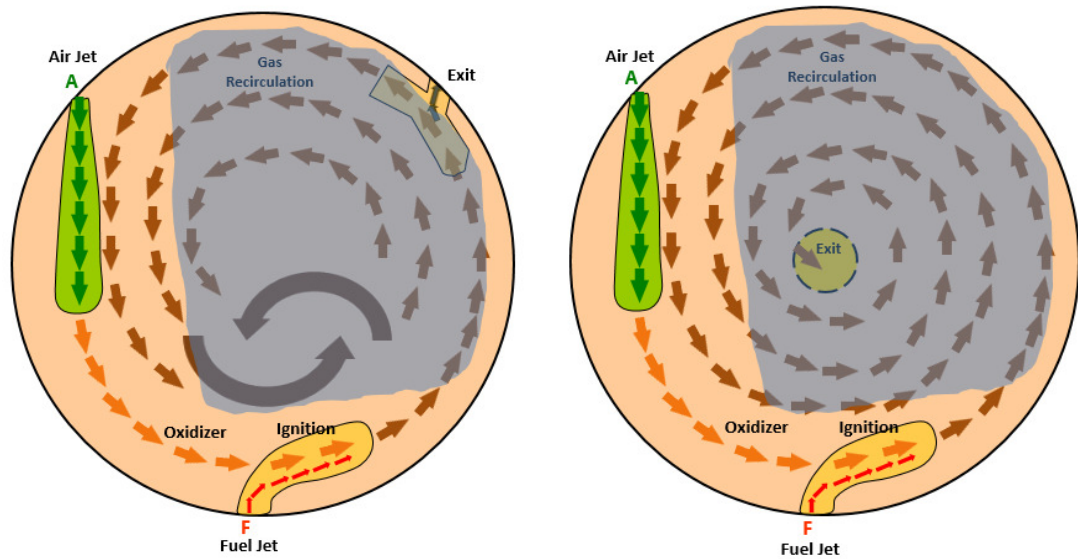


Figure 4-1 Schematic of the combustor for different models

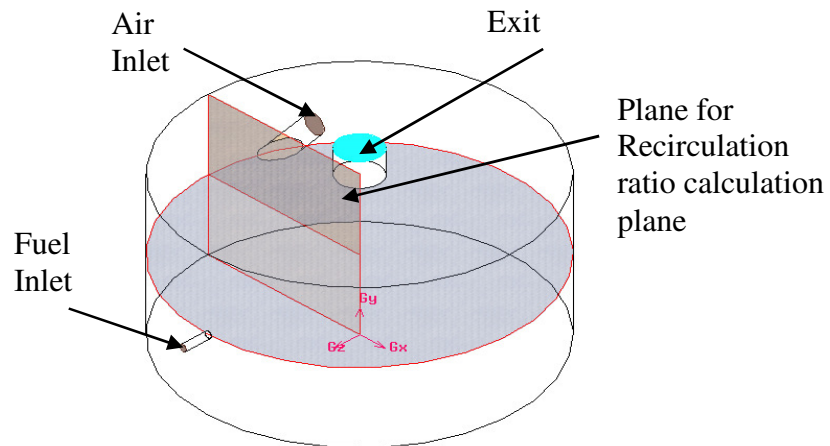


Figure 4-2 Numerical model of the combustor

The model boundary conditions were specified as detailed herein. For air inlet, “mass flow inlet” boundary condition was used with inlet turbulence intensity of 10%, mass fraction of  $O_2$  of 0.233 and inlet temperature of 300K. For fuel inlet, “mass flow

inlet” boundary condition was used with inlet turbulence intensity of 10%, the mass fraction of CH<sub>4</sub> of 1 and inlet temperature of 300K. For hot gases to exit, “pressure outlet” boundary condition was used, with zero gauge back pressure and 10% turbulence intensity for back flow. For all the numerical simulations, the equivalence ratio was 0.8 with methane as the fuel. Air mass flow rate was 0.002682812 kg/s, fuel mass flow rate was 0.000125 kg/s. These boundary conditions were chosen to match the desired heat load of 6.25 kW. The heat release intensity for the modeled combustor is ~36 MW/m<sup>3</sup>-atm. For any numerical simulations, the conversion criterion was that the largest residual is less than 10e<sup>-4</sup>.

Two exit locations were investigated, including an exit normal to the combustor wall (denoted here as “N”) and an exit along the combustor axis (denoted here as “A”), see Figure 4-1. In the present work, the combustor is said to be operating in swirling combustion mode when the product gases exit the combustor axially. The exit normal to the combustor wall is used as a base case where the flowfield is similar to non-swirling CDC flames investigated previously [86] [87] [88]. Change in exit location is expected to have significant effect on the flowfield and gas recirculation inside the combustor as well as on the pollutants emission and flame stability. It is to be noted that for the non-swirling case the product gas exit is on the cylindrical surface. Hence, the flowfield is similar to reverse flow geometry, where both air injection and product gases are located on the same side, and in a sense the flowfield pattern is closer to a “linear” profile. In swirling flow case, the product gases exit from one side of the chamber, hence the flow pattern exhibits a helical pathway where the air is injected tangentially and exits axially. A comparison with these two cases highlights the use of

swirl flow geometry as compared to a linear geometry for CDC. The swirling flow geometry is expected to provide higher residence time for the product gases that will help reduce CO emissions.

The main goal of numerical investigations was to calculate the recirculation ratio of the combustor in each case for non-reacting cases. In these simulations, the recirculation ratio is defined as the total mass flow rate flowing through a certain plane divided by the injected air mass flow rate. Three arbitrary planes normal to flow direction were used to compute the mass flow rate crossing them. Then these mass flow rates were divided by injected air mass flow rate. In each case, the recirculation ratios of all the planes were almost the same with minimal difference. Non-reactive simulation concluded that axial exit (“A”) gives a recirculation ratio of 15 which is higher than the recirculation ratio of 9.6 resulting from normal exit (“N”). Figure 4-3 gives the velocity distribution for both cases. In case “A”, the flow is moving in a uniform circular motion around the center of the combustor (swirling flow), while in the case “N” such behavior was not found.

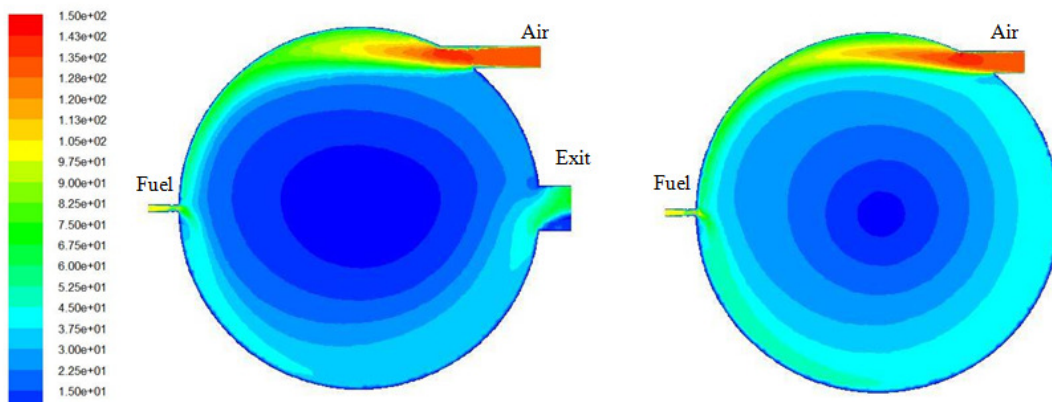


Figure 4-3 Velocity contours for normal exit (left) and axial exit (right).

Fuel injection at different locations did not change the calculated recirculation ratio as the air jet and the hot product gases exit location were the dominant factors under these configurations.

#### 4.1.2. Inlet Air Angle

Numerical investigations were also performed on configuration “A” to evaluate the impact of the inlet air angle on the recirculation inside the combustor. Six air inlet angles were investigated ranging between 0 degrees and 45 degrees. For each of these angles the velocity flow field was obtained and its behavior was analyzed. The obtained velocity fields are shown in Figure 4-4.

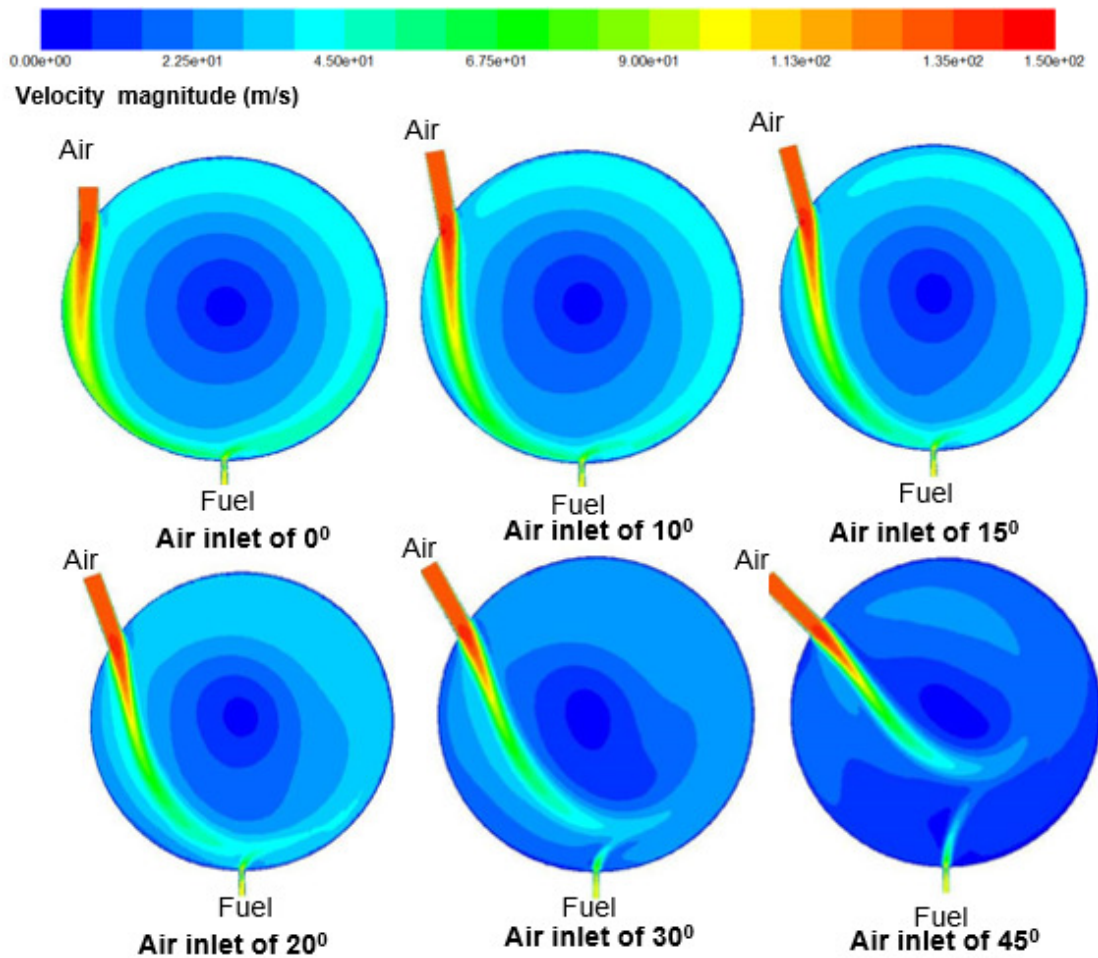


Figure 4-4 Effect of air inlet angle on velocity field

From the velocity contours plot, one can see that as the inlet air angle increases, the recirculation pattern decreases. For instance, at 0 degrees air inlet angle, the high velocity jets remains next to the wall and recirculated inwardly until it exits from the center. On the other hand, for the 45 degree case, the air jet goes directly to the center with minimum recirculation. The calculated recirculation ratio for the configurations outline the impact of the inlet angle and are plotted in Figure 4-5 where it can be seen that the calculated recirculation ratio decreases rapidly with increase in inlet air angle.

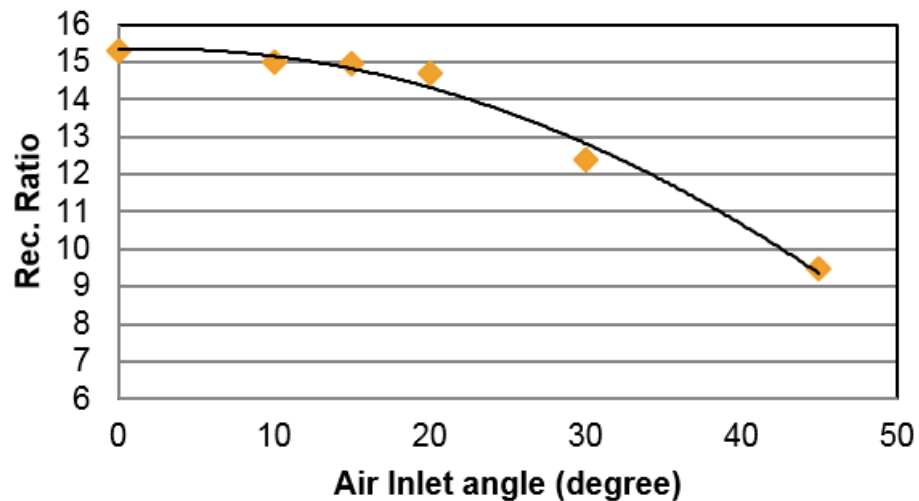


Figure 4-5 Recirculation ratio vs. inlet air angle

#### 4.2. Experimental Investigations (swirling vs. non-swirling)

The effect of product gas exit location and fuel injection location are investigated in this section at a constant heat load of 6.25kW and combustion intensity of 36MW/m<sup>3</sup>-atm. to simulate gas turbine conditions. Two arrangements of product gas exit are examined. One exit is normal to the cylinder axis denoted as ‘N’. The second exit is along the cylinder axis denoted as ‘A’. Fuel injection location relative to the air inlet was examined for different product gas exits denoted as ‘F1’, ‘F2’, ‘F3’ and ‘F4’, see

Figure 4-6. Change in fuel injection location is expected to affect fuel/oxidizer mixing and reaction zone location.

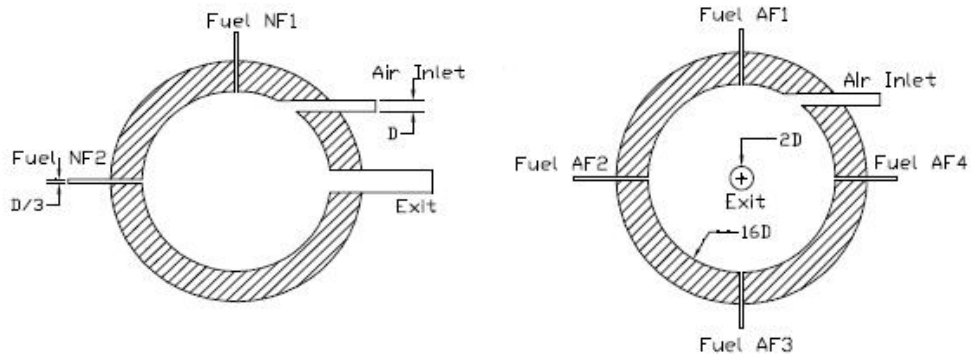


Figure 4-6 Schematic of the combustor for different experimental configurations

Detailed investigation for exhaust emissions and OH\* chemiluminescence emission were performed for the experimental investigations reported here. The experiments related to hot gas exit locations were also performed in premixed combustion mode, denoted as ‘P’ (air + fuel mixture injected tangentially). The air and fuel injection temperature was at normal temperature and pressure (300K, and 1atm.).

#### 4.2.1. Combustor Fabrication

The chamber is formed by a stainless steel cylinder having an inner diameter of 4 inch, outer diameter of 5 inch and height of 2.5 inches. The cylinder is insulated from the inside with a 0.5 inch thick ceramic insulation to reduce heat losses from the combustor. One end of the cylinder is sealed using quartz disc so as to allow full optical access to the combustion chamber. The other end is sealed using stainless steel plate insulated internally with 1 inch thick ceramic insulation. Holes were drilled through the steel assembly to accommodate injection of air and fuel, and to allow hot gases to exit

at desired different locations. Air is injected tangentially to obtain the desired strong swirling flow inside the combustor. Figure 4-7 shows the combustor. Further details about the combustor assembly can be found in appendix B.

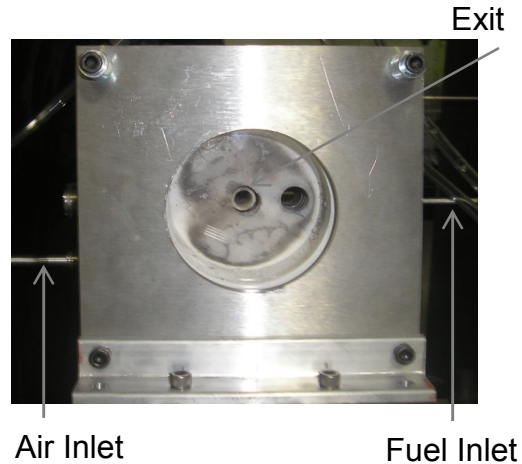


Figure 4-7 Assembled combustor for experimental investigations

Special insulating plugs were made to block different holes that were not in use. A pilot flame was used for initial ignition of the mixture and then transitioned to the CDC mode. Detailed investigation on exhaust emissions and visible emissions were performed for all the experimental investigations.

#### 4.2.2. Emission Measurements

A flue gas analyzer was used to obtain concentrations of NO, CO, CO<sub>2</sub> & O<sub>2</sub> in the hot gasses. Also OH\* chemiluminescence radical species imaging was performed to determine the reaction zone location inside the combustor. The NO concentration was measured using a NO–NO<sub>x</sub> chemiluminescent gas analyzer; CO concentration was measured using the non-dispersive infrared method and O<sub>2</sub> concentration (used to correct the NO and CO emissions at standard 15% oxygen concentration) was

measured using galvanic cell method. The emission readings were observed to stabilize within 3 min for any change in experimental condition (such as the change in equivalence ratio for the same configuration). During a single experiment, measurements were repeated three times for each configuration and the uncertainty was estimated to be about  $\pm 0.5$  PPM for NO and  $\pm 10\%$  for CO emission. Also, all experiments were repeated at least twice to ensure consistency and repeatability of each experiment.

For imaging the OH\* chemiluminescent intensity distribution, an ICCD (Intensified Charge-Coupled Device) camera was used (Princeton Instruments, ICCD camera with 307 nm center wavelength filter for OH\*). The camera was set with f-stop setting of f-8 and the exposure time of 100 msec. The gain for these images was set to 100 with one accumulation per image.

At a given equivalence ratio, fuel mass flow rate was kept constant while air mass flow rate was changed (for example, air flow increased to decrease the equivalence ratio). The reason behind this is to examine the combustor performance for constant heat load at different equivalence ratios to determine the best operating condition that give the intensity of  $36\text{MW/m}^3\text{-atm}$ .

#### 4.2.3. Cases Investigated

Table 4-1 summarizes the investigations performed along with the variables changed for each investigation. The case name is indicative of the location of product gas exit, fuel injection location and combustion mode. As an example, case 'NF1'

means that the product gases exit normally, fuel is injected at location one and that the combustor is operating in non-premixed combustion mode.

Table 4-1 Experimental parameters investigated

<b>Case No.</b>	<b>Product Gas Exit</b>	<b>Fuel Injection</b>	<b>Combustion Type</b>
NF1	Normal	1	Non-Premixed
NF2	Normal	2	Non-Premixed
NP	Normal	With air	Premixed
AF1	Axial	1	Non-Premixed
AF2	Axial	2	Non-Premixed
AF3	Axial	3	Non-Premixed
AF4	Axial	4	Non-Premixed
AP	Axial	With air	Premixed

#### 4.2.4. Results and Discussion

The first set of experimental investigation performed on the combustor was with normal (N) exit. It may be noted that this configuration is similar to the non-swirling cases investigated previously [86] [87] [88]. In these investigations, fuel injection location was changed and the combustor emissions were monitored. Only two fuel injection locations were used (locations one and two). The combustor could not stabilize the flame with fuel injection at location three, as the residence time was not considered sufficient for the reaction to take place due to rapid exit of the fuel and air from the combustor without combustion of the fuel. On the other hand, location four was used as the product gas exit.

Injection at location one (NF1) resulted in low NO and CO emissions. For example, at an equivalence ratio of 0.7, the resultant NO was 6 PPM while CO was 223 PPM. This is lower than injecting fuel at location two (NF2) for which, at the same

equivalence ratio, NO was found to be 10 PPM while CO was found to be 374 PPM. For premixed combustion (NP) mode, the resultant emissions at the same equivalence ratio of 0.7 were 3 PPM of NO and 140 PPM of CO. Figure 4-8 summarizes the measured emission of NO & CO for this product gas exit arrangement. Fuel injection at location one had a lean stability limit at equivalence ratio ( $\Phi$ ) of 0.4, which allowed measurements at  $\Phi=0.5, 0.6, 0.7$  and  $0.8$ . The equivalence ratio  $\Phi$  is defined as overall fuel/air mass to stoichiometric fuel/air mass. For fuel injection at location two and premixed combustion, the lean stability limit was found to be  $\Phi=0.5$ , which allowed measurements at  $\Phi =0.6, 0.7$  and  $0.8$ .

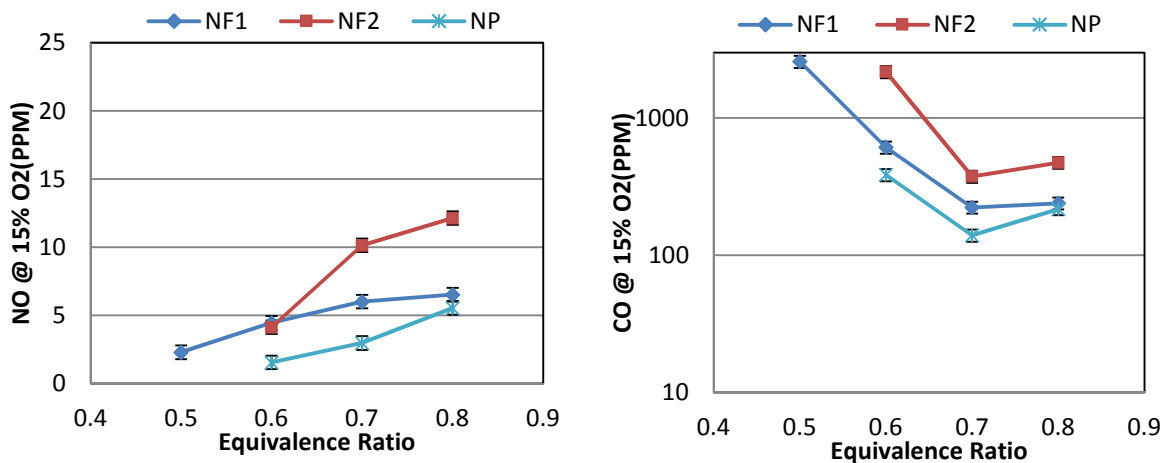


Figure 4-8 NO and CO emissions for "N" exit arrangement

The radical intensity distribution of OH\* chemiluminescence for non-premixed combustion with injection at location one (NF1) shows that the reaction zone is in the shape of a crescent formed opposite to the injection point. This shape is maintained as the equivalence ratio is decreased. For fuel injection from location two (NF2), the reaction zone also takes a crescent shape with an elongation towards the product gas

exit. The presence of reaction zone near the exit suggests lower residence time for CO conversion. Hence, for the case NF2, CO levels are higher than case NF1. For premixed combustion (NP), the reaction zone is also a crescent opposite to air/fuel injection point and it can be seen that as the equivalence ratio decreases, the OH\* intensity decreases. Figure 4-9 gives the OH\* chemiluminescence intensity distribution for the discussed cases.

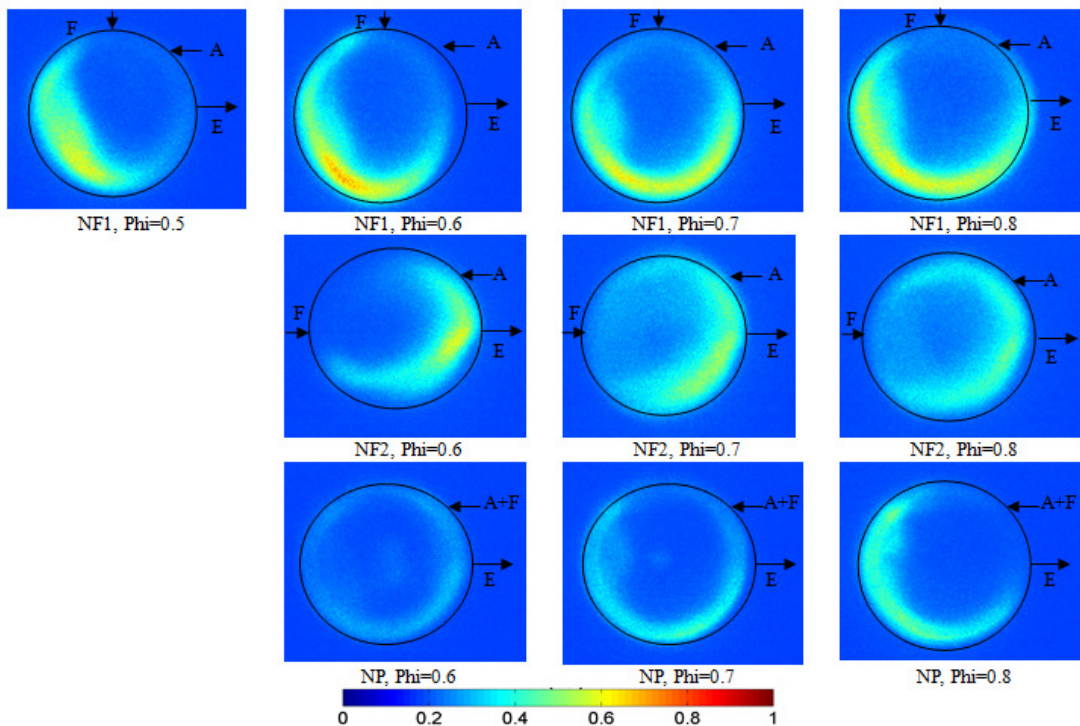


Figure 4-9 OH\* chemiluminescence intensity distribution for “N” exit arrangement.

The results have also been obtained to evaluate the performance of having an axial (A) product gas exit from the combustor under different fuel injection locations. For each case, the lean stability limit and pollutant emissions were recorded. A comparison between NO & CO emissions for different fuel injection configurations is shown in Figure 4-10. It can be observed that pollutants emission are at minimum for case with

fuel injection at location one (AF1), and higher for other cases (AF2, AF3 and AF4). Experimental measurements suggest that injection of fuel close to high velocity air jet (as AF1) gives the lowest NO emission. In this case, NO emissions were measured to be 10, 8 and 2.4 PPM at  $\Phi=0.8, 0.7$  and  $0.6$  respectively. This can be attributed to faster and enhanced mixing between the fuel and hot gases as the fuel is injected in strong cross flow emanating from the air jet.

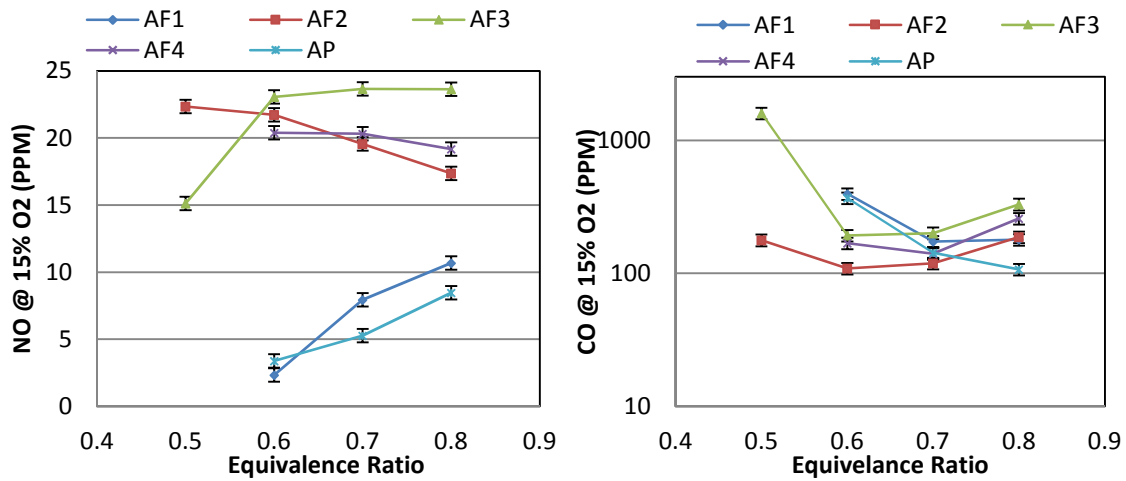


Figure 4-10 NO and CO emissions for "A" exit arrangement

NO and CO emissions for the premixed combustion case (AP) were lower as compared to non-premixed cases. Premixed combustion produced NO emissions of 8.5, 5.3 PPM at  $\Phi=0.8$  and  $0.7$  respectively, which are lower than the emissions resulting from non-premixed combustion with fuel injection at location one (AF1). For  $\Phi=0.6$ , it was noticed that non-premixed combustion (AF1) produced lower NO emission (2.4 PPM) than premixed combustion emission (3.4 PPM). This behavior for non-premixed combustion may be attributed to incomplete combustion occurring near

the lean flammability limit which results in lower temperatures producing lower thermal  $\text{NO}_x$ .

$\text{OH}^*$  chemiluminescence intensity distribution showed that for fuel injection at location one (AF1), the  $\text{OH}^*$  intensity is mostly present near to the lower left portion of the combustor. As equivalence ratio decreases, the  $\text{OH}^*$  distribution maintains the same pattern but the intensity decreases. For fuel injection at location two,  $\text{OH}^*$  intensity is distributed throughout the combustor, with the highest intensity forming an annulus near the combustor wall. However, as the equivalence ratio decreases, the  $\text{OH}^*$  chemiluminescence intensity decreases and the distribution takes the annulus shape with the center mostly having no reaction zone. The  $\text{OH}^*$  chemiluminescence intensity distribution for injection at locations three & four (AF3 & AF4) showed the same trend as that found with injection at point two (AF2). Figure 4-11 gives the  $\text{OH}^*$  chemiluminescence intensity distribution for the cases discussed here.

For premixed combustion, the reaction zone is also in a crescent shape opposite to air/fuel injection location and it can be seen that as the equivalence ratio decreases, the  $\text{OH}^*$  chemiluminescence intensity also decreases.

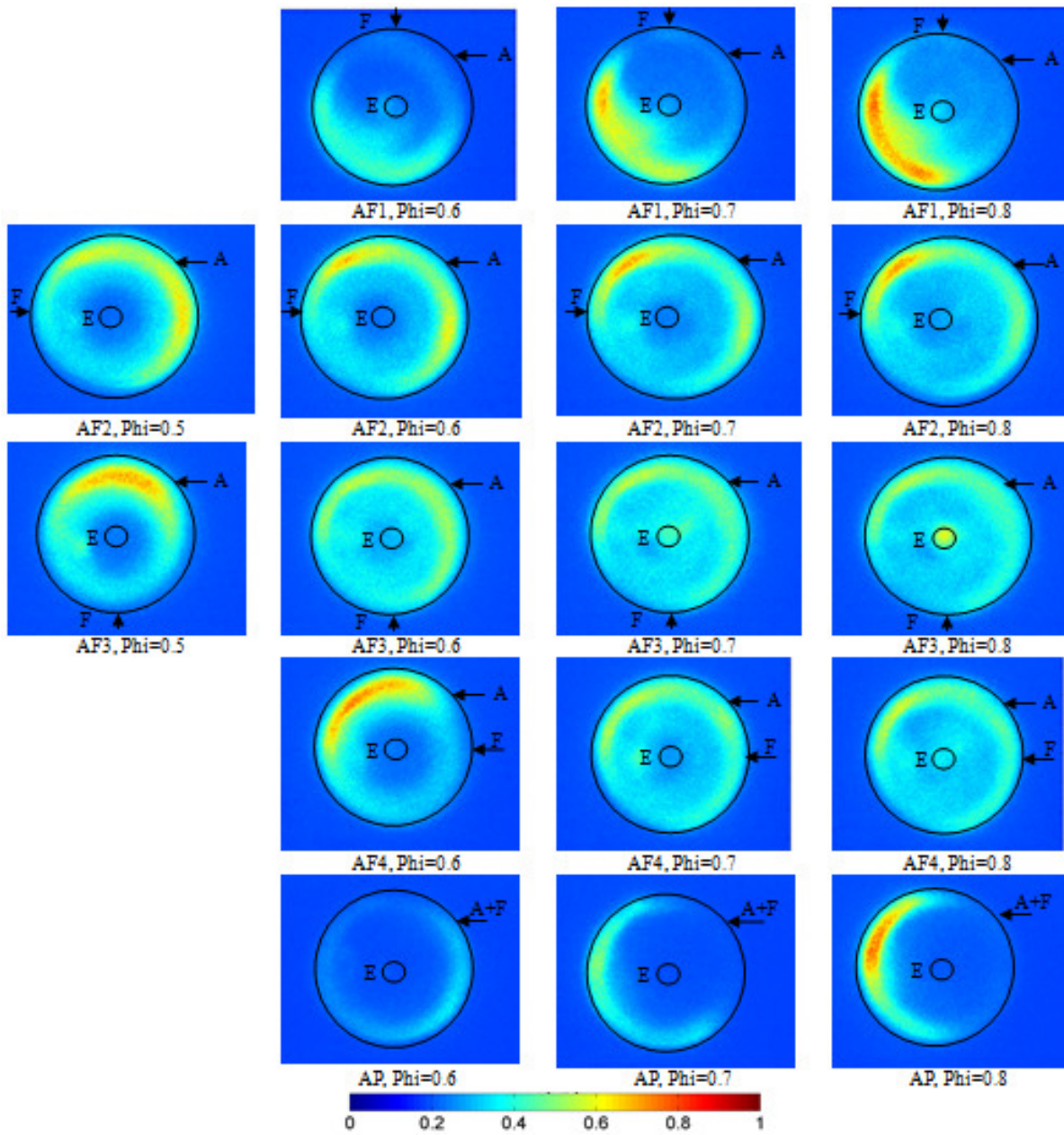


Figure 4-11 OH\* chemiluminescence intensity distribution for "A" exit arrangement

### 4.3. Extended Axial Exit Configuration

To enhance residence time inside the combustor and reduce CO emissions, it was thought to modify the hot product gases exit from the combustor in the swirling case. Instead of having the exit along the axis at the end of the combustor, a tube was extended inside the combustor to the other side with a clearance of  $2D$  to allow the gases to exit. Figure 4-12 shows the difference between the non-swirling, “N”, swirling, “A”, and extended axial exit swirling, “AT”, cases.

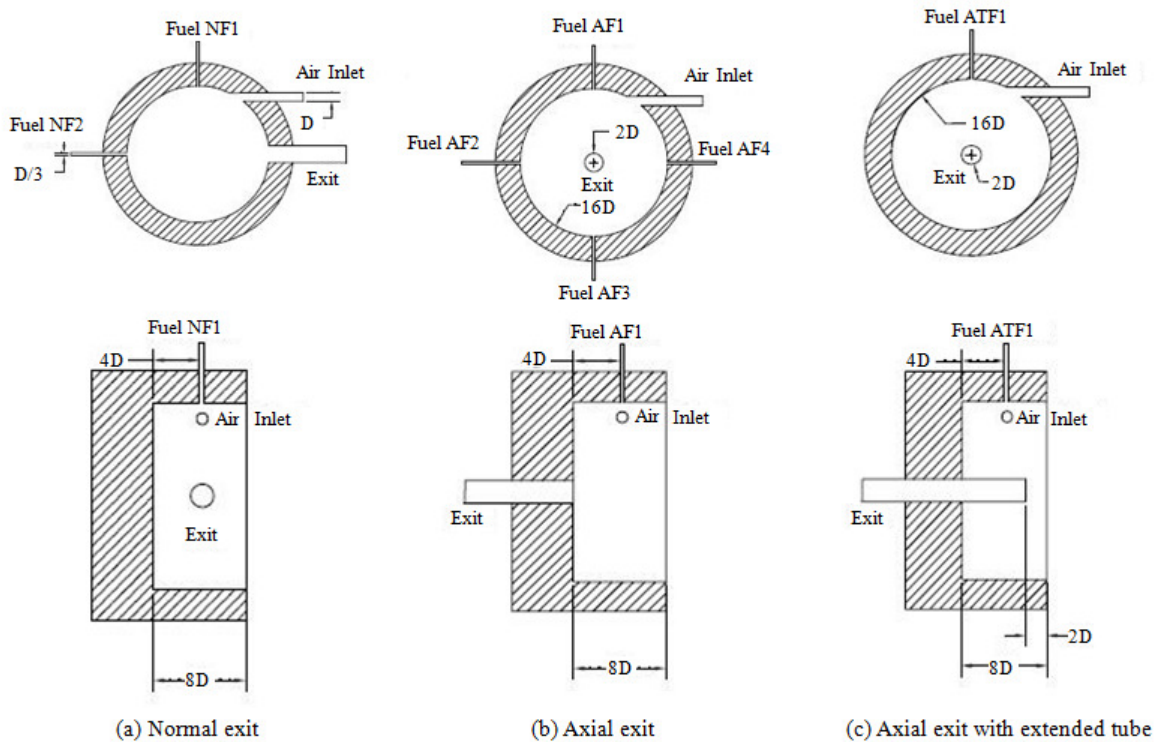


Figure 4-12 Schematic diagram of different exit arrangements and fuel injection locations.

A performance evaluation was carried out for the product gas exit arrangement having an extended tube towards the center of the combustor (in the axial direction) under the most favorable injection location (ATF1, ATP). The goal here was to increase

the residence time of combustion gases so as to decrease CO and increase the combustion efficiency. Consequently, further reduction of CO emission can be achieved.

Figure 4-13 shows the emissions of NO and CO as compared to the more favorable non-premixed combustion (i.e., fuel injected at location one, F1) for different product gas exit arrangements. This exit arrangement (ATF1), resulted in further reduction of NO emissions of 6.4, 3.4, 1.5 PPM of NO for  $\Phi = 0.8, 0.7$  and  $0.6$ , respectively. These values are lower than those measured from the previous configurations of normal and axial exit (NF1 and AF1). Also this arrangement gave remarkably low CO emissions as compared to other exit arrangements. For  $\Phi = 0.7$ , CO emission was found to be 72 PPM, which is significantly lower than the 223 PPM measured for the normal exit (NF1) and the 172 PPM measured for the axial exit (AF1). Such decrease in CO emission can be explained by the higher residence time available for the burned gases leading to higher CO conversion (increased combustion efficiency), as the gases have to travel a longer path before exiting from the combustor. These results provide a direct role of better fuel-air preparation on NO and CO emission and outlines the importance of providing enough time for complete combustion to occur in the combustor. In all cases the focus is on not allowing the mixture to ignite until the mixture is diluted and uniformly distributed in the entire combustion chamber.

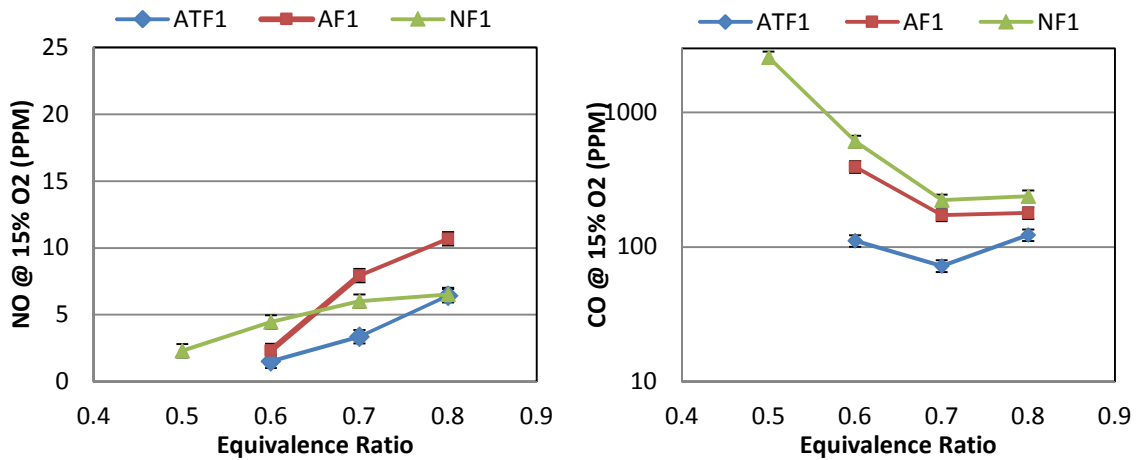


Figure 4-13 NO and CO emissions for different exit configurations (non-premixed)

Figure 4-14 shows the results obtained for NO and CO emissions under premixed combustion condition as compared to the other combustion gases exit arrangements in the premixed combustion mode. The results show that for this combustion gas exit arrangement (ATP), NO and CO emissions are lower than the other combustion gas exit arrangements. For example, at  $\Phi=0.7$ , NO and CO were found to be 2 PPM and 50 PPM, respectively. For normal exit (NP) these values were 3 PPM NO and 140 PPM CO, while they were 5.3 PPM NO and 143 PPM CO for axial exit (AP). These results agree with those of non-premixed combustion, emphasizing that exit tube extension inside the combustor significantly lowers CO levels from increased residence time with negligible impact on NO emission. This also helps in establishing the distributed combustion conditions.

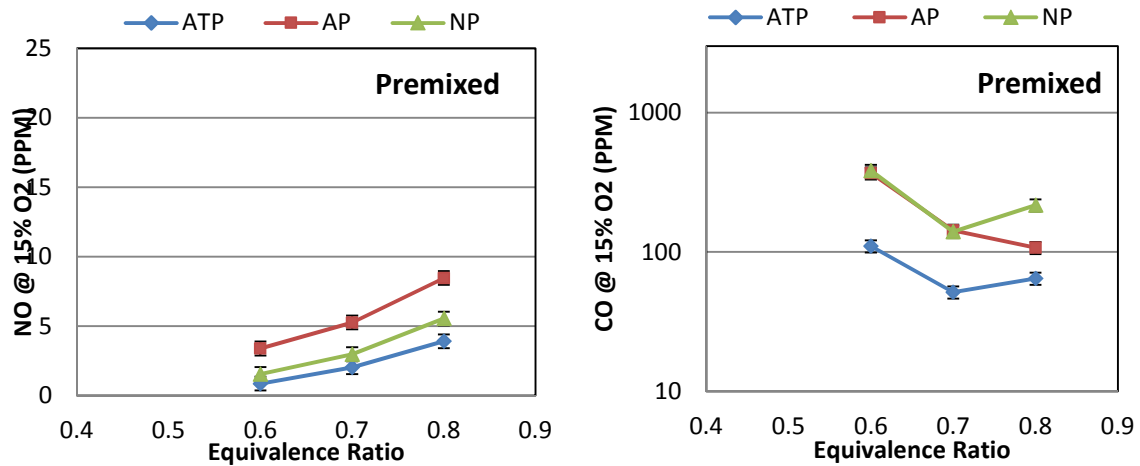


Figure 4-14 NO and CO emissions for different exit configurations (Premixed)

The OH\* chemiluminescence intensity distribution images for cases ATF1 and ATP showed increased reaction zone distribution with the extended combustion gases exit tube inside the combustor (Figure 4-15). The resulting reaction zone formed a crescent opposite to fuel injection location, but the size of the crescent is bigger as compared to the previous cases. This reveals more favorable distributed reaction region for this geometry and operational condition. For premixed combustion, the reaction zone is distributed along the combustor, with the highest intensity being opposite to the injection location of air/fuel. Images of OH\* chemiluminescence intensity show a decrease in intensity with decrease in equivalence ratio for both the premixed and non-premixed cases.

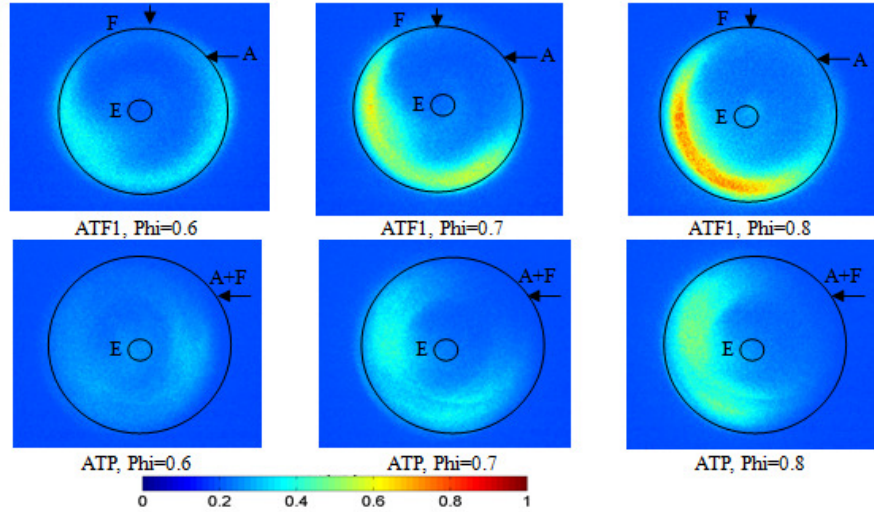


Figure 4-15 OH\* chemiluminescence intensity distribution for "AT" exit arrangement

The results from axial product gas exit with tube extended inside the combustor (AT) suggests that increased product gas recirculation inside the combustor before exiting the combustion chamber results in higher residence time and increased swirl effect. Such higher residence times and stronger swirl allows for higher combustion efficiency (better conversion of CO to CO<sub>2</sub>) to provide low levels of NO and CO as compared to both normal and axial exit arrangements. This behavior is supported in both non-premixed and premixed combustion modes. As an example, at  $\Phi = 0.7$  under non-premixed combustion for axial exit with extended tube (ATF1), emissions were found to be 3.4 PPM NO and 72 PPM CO. These emissions are much lower than those for normal exit (NF1, 6 PPM NO and 223 PPM CO) or axial exit (AF1, 8 PPM NO and 172 PPM CO). Under premixed combustion, the emissions at the same equivalence ratio for axial exit with extended tube were very low (2.2 PPM NO and 49 PPM CO) compared to those from normal exit (NP, 3PPM NO and 140 PPM CO) or axial exit (AP, 5.3 PPM NO and 143 PPM CO) conditions.

#### **4.4. Flowfield Characterization using PIV**

The flowfield under non-reacting conditions (isothermal) is characterized using particle image velocimetry with focus on recirculation generation in order to achieve colorless distributed combustion and enhance thermal and environmental performance of the combustor with ultra-low emissions. Non-reacting flowfield helps in understanding the flow characteristics inside the combustor along with the turbulence generated and the mixing characteristics. These are important aspects to achieve colorless distributed combustion conditions and will explain the difference in pollutants emission that was recorded for the different examined configurations as shown in the previous sections.

##### **4.4.1. PIV Setup Arrangement**

The combustion chamber geometry investigated herein is shown in Figure 4-12. The combustor was modified to allow optical access for particle image velocimetry at the air injection plane (see Figure 4-12). A schematic diagram experimental setup for particle image velocimetry is shown in Figure 4-16. The camera was located at a distance of 0.3 m away from the laser plane. The camera view covered an area of 4.4 cm x 3.36 cm. The camera was mounted on a traverse mechanism to allow capturing the complete flowfield of the combustor. Details of the seeding particles and seeding mechanism can be found elsewhere [35].

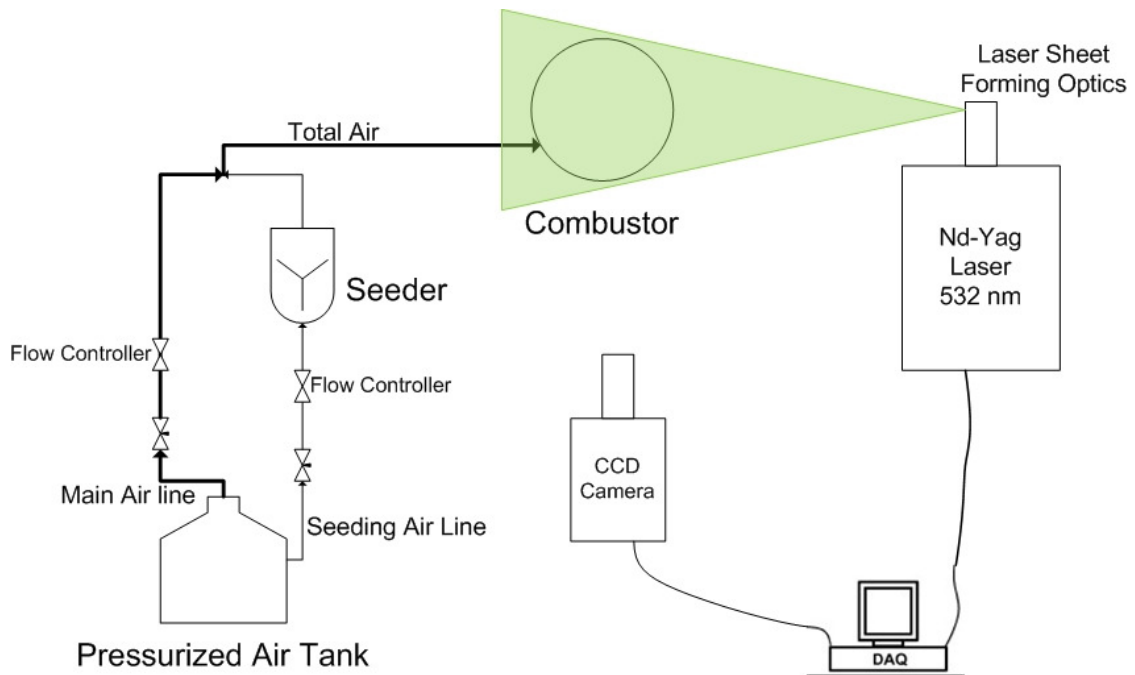


Figure 4-16 Schematic diagram for the PIV setup used

Combustion air was mixed with the seeding air, where with the seeding air flow rate was about 5% of the total supplied air flow rate. The laser sheet beam had a thickness of about 1mm and was used to illuminate the seed particles in the flow. Table 4-2 summarizes the different parameters of the PIV system. For interrogation window size, adaptive mode was used where the correlation is calculated on a subset of the grid points using an interrogation size of at least 24 pixels. The results are validated and used as ‘predicted’ vector values. Then the correlation is calculated and the predicted values are used as a local offset for the delayed image.

Table 4-2 PIV Parameters

Seeding Particle	Alumina
Size	3 $\mu\text{m}$
Rate	5Hz
Response time	0.1 ms
Q-Switch delay	140-160
Laser Sheet thickness	$\sim$ 1mm
Pulse Separation	2 $\mu\text{s}$
Interrogation Window Size	at least 24 x 24pixels
Camera Resolution	1360 x 1036 pixels
Spatial Resolution	0.44 x 0.44 mm
Lens Focal Length	60mm
f-stop setting	2.8

Figure 4-17 shows the actual experimental setup. To enhance the data quality, the inner insulation was painted black (originally white) to minimize background reflection and interference.

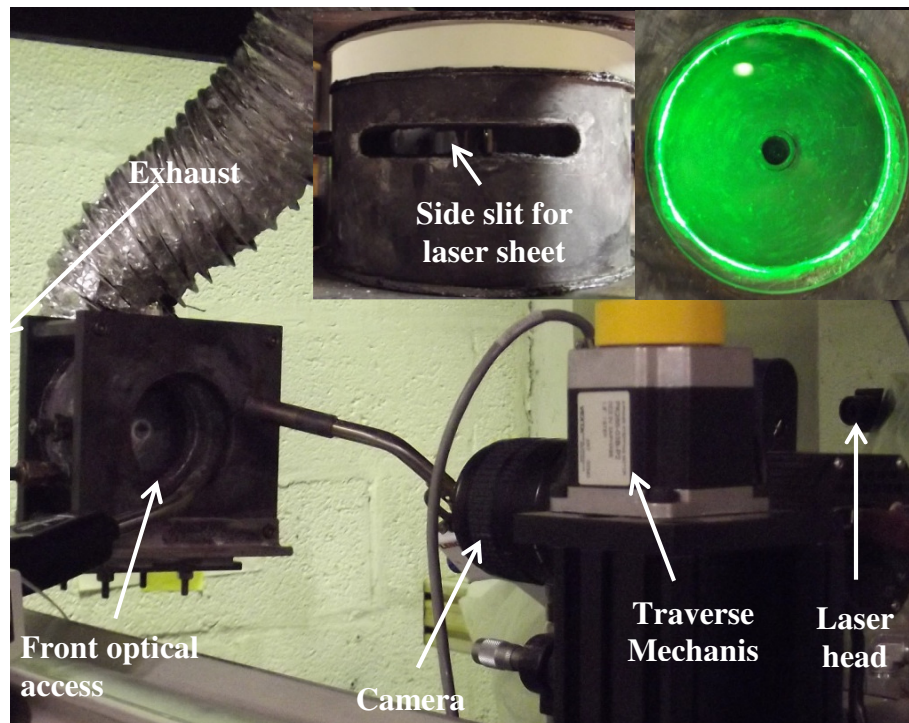


Figure 4-17 Experimental Particle Image Velocimetry setup

#### 4.4.2. Numerical Predictions

Numerical simulations were performed and compared to the experimentally obtained flowfield to help develop an understanding of the flowfield inside the combustor for different flow exit arrangements. For these simulations, commercial software FLUENT® code was used. The flow was modeled using finite volume method. For solving turbulence, both standard k-ε model and Reynolds Stress Model (RSM) were used with standard wall function. Using both models outlines the appropriate use of each of the models and their weakness/strength. For any of the different numerical models, the volume consisted of about 1.5 million tetrahedral mesh cells.

The model boundary conditions used were as follows. For air inlet, “mass flow inlet” boundary condition was used with inlet turbulence intensity of 10%, mass fraction of O<sub>2</sub> of 0.233 and inlet temperature of 300K. For product gases to exit, “pressure outlet” boundary condition was used, with zero-gauge back pressure and 10% turbulence intensity for back flow. For any numerical simulations, the conversion criterion was that the largest normalized residual was less than 10e-5. Different turbulent models were used with their original constants. It is understood that the simulated flowfield and mixing behavior will deviate from the actual case; however, the trends are expected to remain consistent, thus providing an indication for the causes of pollutants emission behavior for the various cases investigated here.

#### 4.4.3. Normal exit arrangement for combustion gases

This set of experimental investigation was performed on the combustor with normal exit “N”. Figure 4-18 shows the obtained flowfield vectors and velocities.

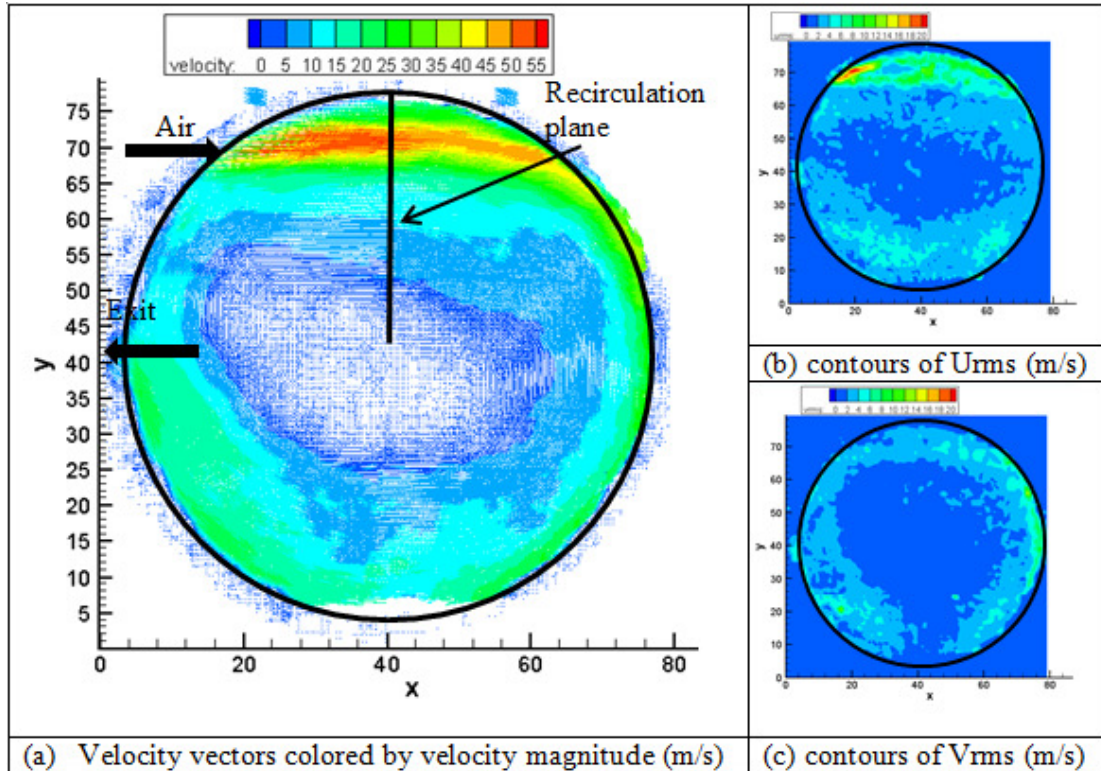


Figure 4-18 Velocity vectors (a), U<sub>rms</sub> (b), and V<sub>rms</sub> (c) for configuration “N”

The flow field of configuration “N” is characterized by stagnant portion in the center of the combustor. The flow velocity for the center part is almost zero as seen by different velocity plots shown in Figure 4-18. The velocity fluctuations were limited to the main air jet as seen in Figure 4-18 (b) and (c), where the velocity fluctuations were found only at the cylindrical wall of the combustor. Such flow behavior indicates minimal use of the combustor volume which leads to lower residence time. Also, limited velocity fluctuations indicate limited mixing possibilities. The recirculation ratio for this configuration was calculated for the investigated plane (shown in Figure 4-18(a)), and is defined for the plane as follows:

$$R_{circulation} = \frac{\dot{m}_{tot} - \dot{m}_{air}}{\dot{m}_{air}} \quad \text{(Equation 4-1)}$$

Where  $\dot{m}_{tot}$  is the total flow rate crossing a plane, and  $\dot{m}_{air}$  is the inlet mass flow rate. Rearranging in terms of velocity and adopting a line for calculation in a 2-D plane, we get

$$R_{circulation} = \frac{V_{Line} * L_{Line} * t_{Line} - V_{air} * d_{air} * t_{Line}}{V_{air} * d_{air} * t_{Line}} \quad (\text{Equation 4-2})$$

Where,  $V_{Line}$  is the average velocity perpendicular on the examined line,  $L_{Line}$  is the length of the examined line,  $V_{air}$  is the air jet inlet velocity,  $d_{jet}$  is the air jet diameter and  $t_{line}$  is thickness of the examined line where the 2-D plane is  $t_{line} * L_{line}$ .

The examined line is shown in Figure 4-18(a), where  $L_{line}$  is the combustor radius. The calculated recirculation ratio for that plane was found to be 0.4 (calculated based on velocity measurements). The value calculated from equation (Equation 3-1) giving the entrainment rate for a free jet of the same dimensions was found to be 0.28, indicating that most of the mass is entrained rather than recirculated.

Numerical simulations were performed for this configuration using k- $\epsilon$  model to simulate turbulence. The results were compared to the experimental results to assess the ability of the model to correctly predict the flowfield. Figure 4-19 shows the velocity vectors of both the numerical prediction and experimental measurement, along with the normalized tangential velocity profiles for four different locations across the combustor. Comparing the obtained normalized tangential profiles numerically and experimentally, one can see the favorable agreement between experimental measurements and numerical prediction. One deviation can be spotted at location L1, where the maximum velocity was found more towards the center (r/R of about 0.75) as compared to numerical predictions (r/R of about 0.85), see Figure 4-19(c), where R is

the combustor radius. The numerically calculated recirculation ratio was also found to be 0.4, consistent with the experimentally calculated one.

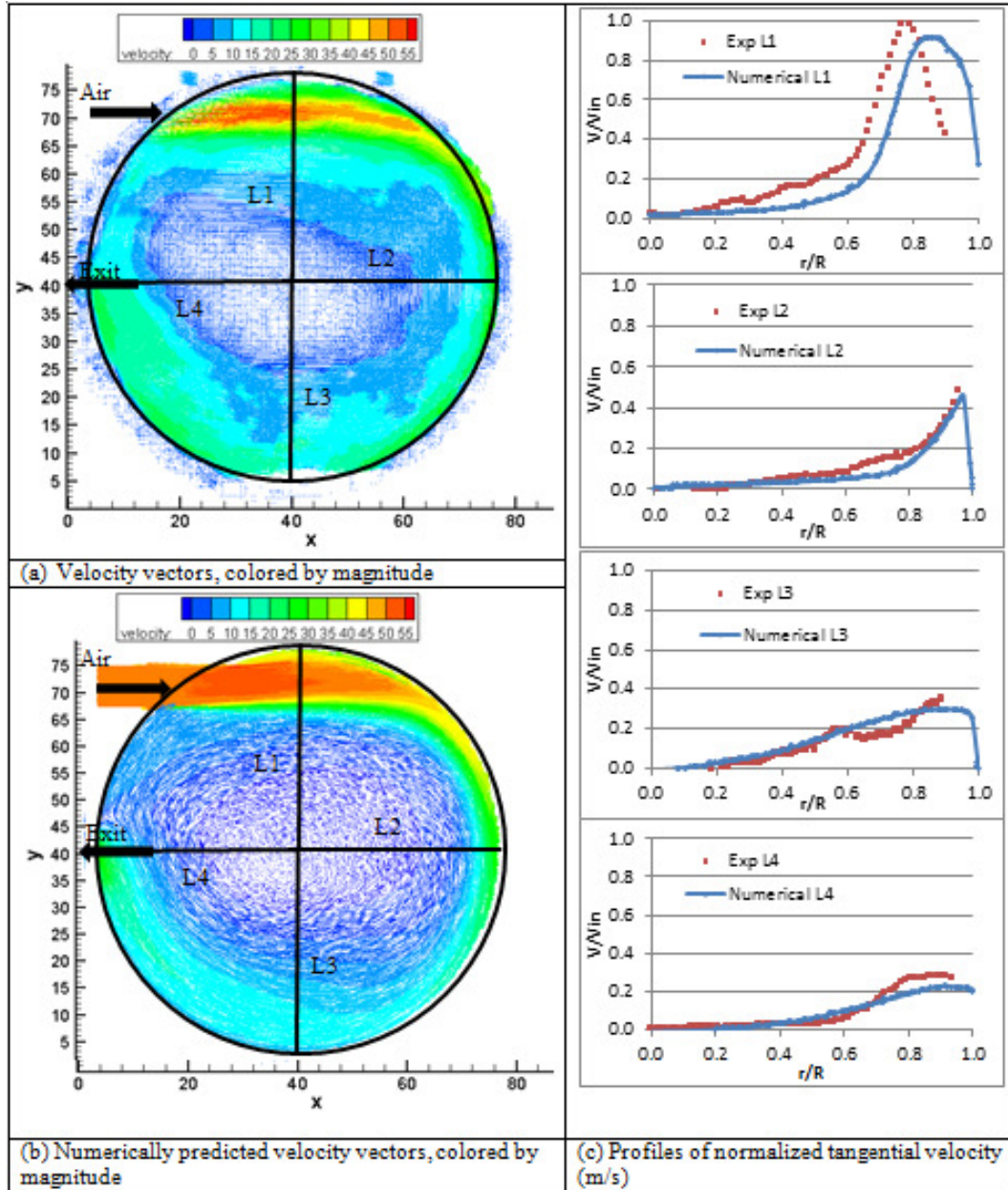


Figure 4-19 Velocity vectors, experimental (a) and numerical (b) along with normalized tangential velocity profiles (c) for configuration "N"

#### 4.4.4. Axial exit arrangement for combustion gases

This set of experimental investigation was performed on the combustor with axial “A” exit. In this configuration, swirl motion is expected to affect the flowfield regarding velocity distribution and fluctuations. Figure 4-20 shows the obtained flowfield vectors and velocities.

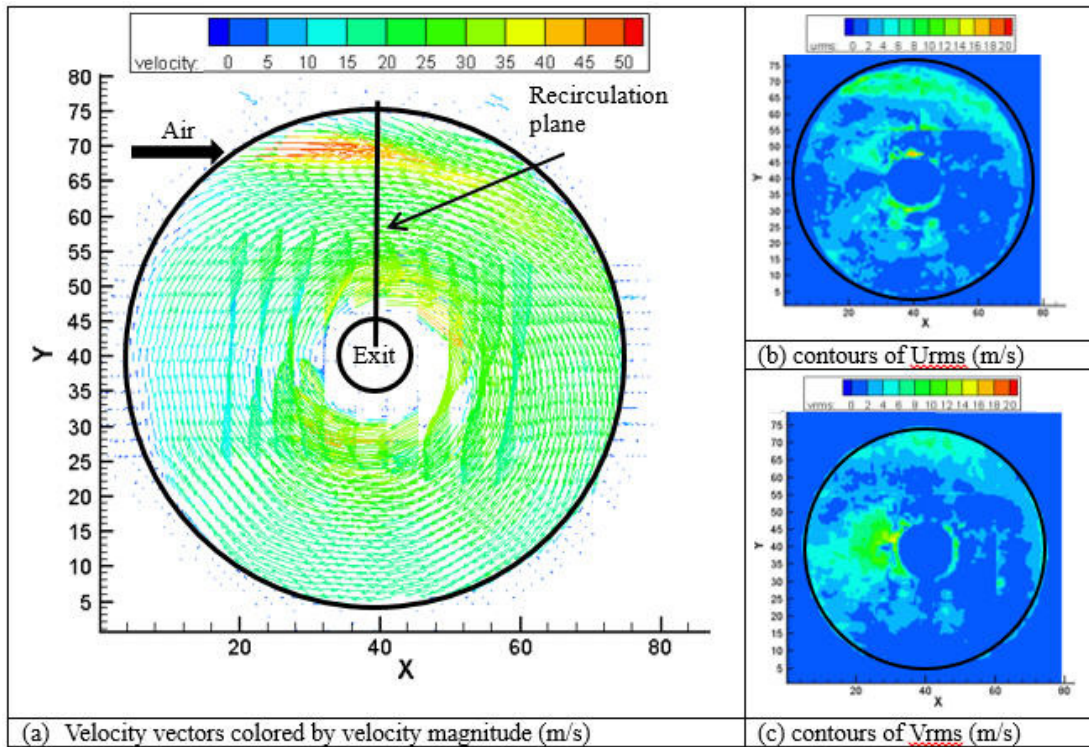


Figure 4-20 Velocity vectors (a),  $U_{rms}$  (b), and  $V_{rms}$  (c) for configuration “A”.

Comparing Figure 4-18 and Figure 4-20, one can outline the difference in flowfield associated with each exit scenario. While configuration “N” showed a stagnant core, with much of the flow staying at the outer part of the combustor. Configuration “A” demonstrated higher recirculation and higher velocities throughout the combustor. There were no seeding particles detected at the exit (combustor center) due to high out of plane motion (axial velocity). Consequently, the velocities were not measured at the

center. Using equation (4-2), the calculated recirculation ratio was found to be 1.25 (calculated based on velocity measurements), which is more than triple the calculated value for arrangement N. The calculated value from equation (3-1), representing jet entrainment in free stream, was found to be 0.28. This difference outlines the enhanced recirculation associated with this flow arrangement “A”, critical to achieve colorless distributed combustion conditions.

The flowfield for configuration “A” is also characterized by the presence of a high velocity region at the outer boundary with another high velocity region near the center. This behavior is consistent with reported velocity behavior in cyclone combustor [89] [90]. A detailed description of the flow pattern in a cyclone is given in the literature [79], where two flows rotating coaxially and carrying the main mass of gas were described. These two flows are the wall flow and the center flow, and they are separated by a zone occupied by the rising turbulent vorticities branching from those two flows.

Another important aspect for colorless distributed combustion is rapid mixing between air, fuel and hot active species gases. As discussed earlier, configuration “A” demonstrated higher recirculation ratio which is highly favorable. Also, configuration “A” exhibited higher velocity fluctuations, when compared to configuration “N”. Configuration “N” only exhibited high velocity fluctuations and turbulence at the entry jet, see Figure 4-18(b) and (c). For configuration “A”, the same velocity fluctuations were seen at the entry jet, but also high velocity fluctuations were seen near the center of the combustor, see Figure 4-20(b) and (c). Higher velocity fluctuations are critical for mixing enhancement, where the increased shear aid in mixing between different streams.

Numerical simulations were also carried out for this configuration and the results are shown in Figure 4-21. For this configuration, numerical simulation using Reynolds Stress Model was performed along with standard k- $\epsilon$  model. Comparing the flowfield obtained experimentally (Figure 4-20(a)) and numerically (Figure 4-21(a) and (b).), one can outline the difference between both numerical models. Standard k-  $\epsilon$  model could not predict the high velocity flow near the center. Simulations showed that the velocity decreased as we move towards the center of the combustor. Reynolds Stress model was more successful in predicting the flow behavior, where the high velocity area near the center was predicted. The predicted normalized tangential velocity profile had the same saddle shape as the experimentally measured one. However, the predicted velocities were not consistent with the measured ones. Figure 4-21(c) shows the experimentally measured and numerically predicted normalized tangential velocities at four different locations.

The difference between the two predicted flowfields outline the important role turbulence play in these flows where the final prediction varied significantly based on the turbulence closure model. Similar behavior has been reported for similar geometries, where Reynolds stress model successfully predicted the flowfield, while k- $\epsilon$  did not yield satisfactory results [91] [92].

Figure 4-21(c) also shows a very important aspect of this configuration, not only high velocity region was found near the center, but also the magnitude of the velocity at the center was higher than that at the wall for the same location. Measured velocities towards the center were found to be 70% more than the outer velocity at plane L2. For

planes L3 and L4, the velocity in the inner zone was almost double that of the outer zone.

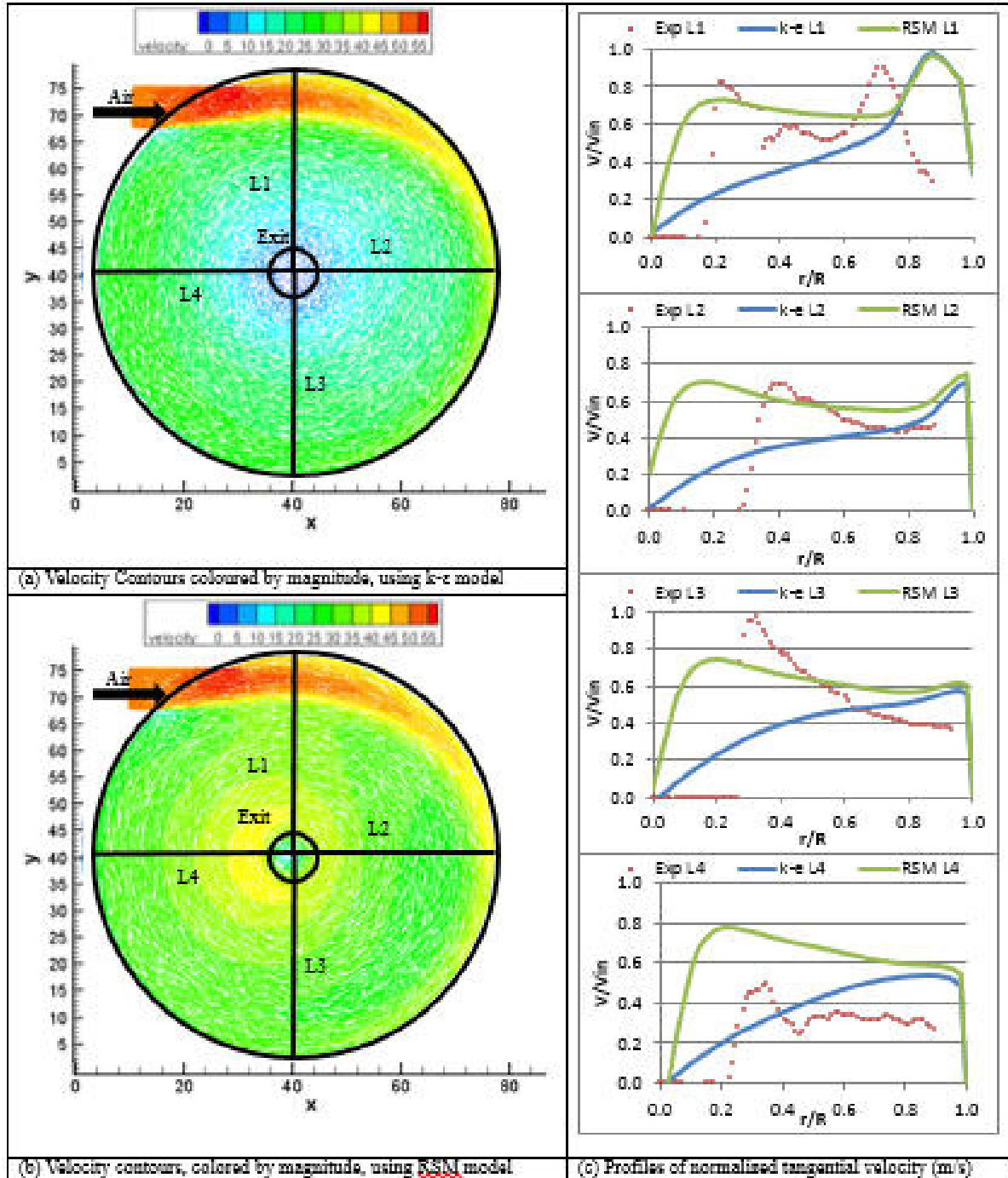


Figure 4-21 Velocity vectors,  $k-\epsilon$  model (a) and RSM model (b) along with normalized tangential velocity profiles (c) for configuration “A”

#### 4.4.5. Axially extended exit arrangement for combustion gases

The flow field was also obtained for configuration “AT”, where the product gases exit extended inside the combustor; see Figure 4-12 (c). Extending the exit inside the combustor is expected to increase the residence time inside the combustor; which is favorable condition for distributed combustion. However, extending the tube inside the combustor resulted in a “blind spot”, where there was no light for the camera to pick up the particles as the laser sheet was obstructed. Figure 4-22 shows the obtained velocity vectors and different velocities contours for this configuration.

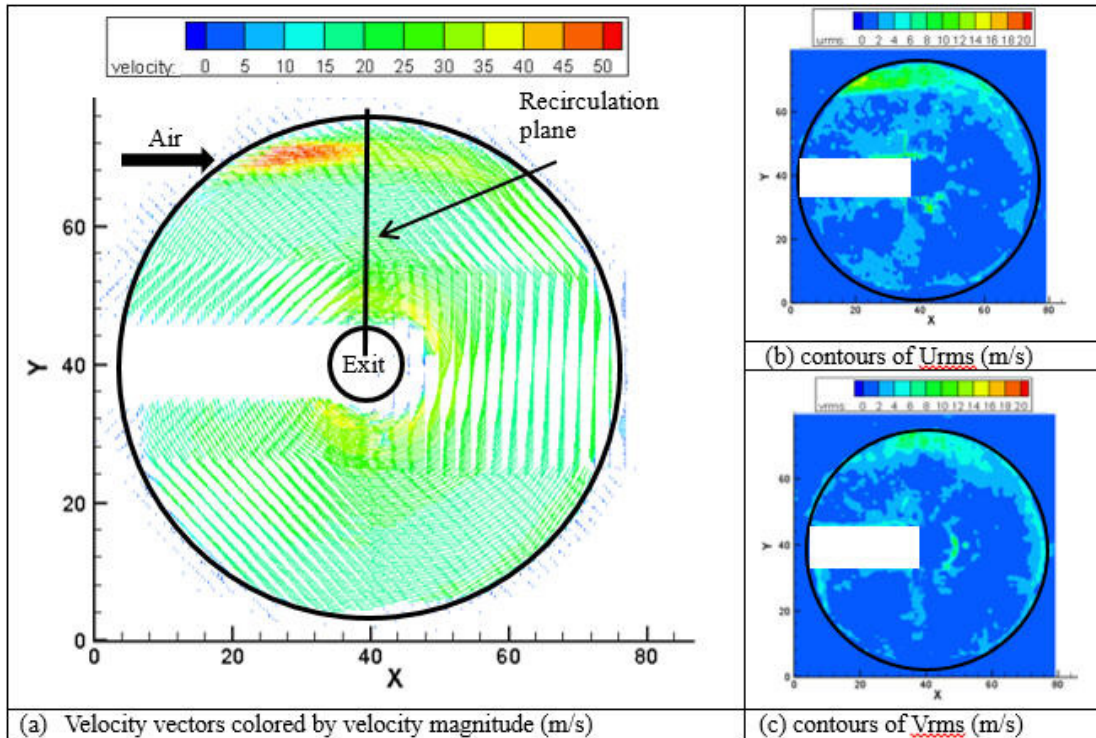


Figure 4-22 Velocity vectors (a),  $U_{rms}$  (b),  $V_{rms}$  (c) for configuration “AT”

Similar to configuration “A”, two high velocity regions were found, one at the combustor cylindrical wall and the other near the combustor center. However, when compared to velocity vectors of configuration “A”, see Figure 4-20(a), the high velocity

regions are well separated from each other with a distinct low velocity flow between them, see Figure 4-22(a). Nevertheless, this low velocity region in the middle did not affect the calculated recirculation ratio (calculated based on velocity measurements), which was found to be the same as the one calculated for configuration “A”.

Numerical simulations for this configuration did not provide any helpful data. The k-ε model failed to predict the increased velocity at the center. On the other hand, Reynolds stress model successfully predicted the velocity pattern but the predicted velocity values were off. It is required to modify existing codes or develop new codes to successfully predict the flowfield in complicated flow conditions.

The experimentally obtained tangential velocity profiles for the three arrangements are compared in Figure 4-23. The velocity profiles for both configuration “A” and “AT” are similar to each other, where the high tangential velocity near the center is present. On the other hand, configuration “N” shows a declining velocity profile as we move towards the center of the combustor. The added recirculated flow for configuration “A” and “AT” plays an important role in achieving colorless distributed reaction conditions which reflects favorably on emission as shown in previous sections.

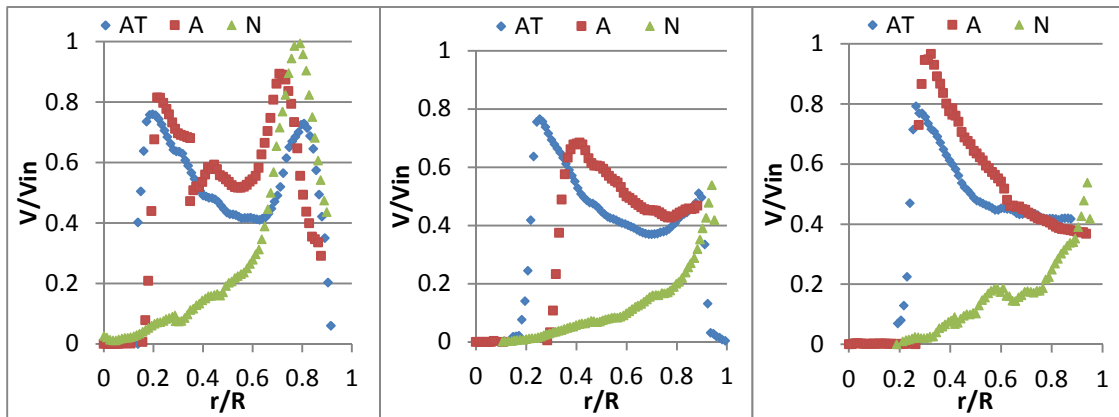


Figure 4-23 Normalized tangential velocity profiles for different arrangements for L1, L2 and L3 lines

#### 4.4.6. Summary

Results obtained with normal product gas exit “N” have shown that the flow only moves in the outer bounds of the combustor with most of the core being stagnant. Such flow indicates the incomplete use of the available volume of the combustor, low residence time for the gases and low velocities promoting flame anchoring. All are factors that have to be avoided to achieve distributed reaction conditions. Also, the flowfield exhibited low recirculation ratio which hampers distributed combustion.

Swirling flow, as in configuration “A”, demonstrated a different flow field, with high velocity region at the core of the combustor. The high velocity region near the center exhibited higher velocities when compared to the outer flow jet, which prevents flame anchoring. The combustor demonstrated higher recirculation ratio, triple that demonstrated with configuration “N”, along with higher velocity fluctuations near the combustor core. High recirculation ratio is critical for colorless distributed combustion as the recirculation of hot product gases is essential to form hot and diluted oxidizer when combined with fresh air stream. Configuration “AT” exhibited similar flow field to that of configuration “A”, yielding the same recirculation ratio.

Numerical simulations using k- $\epsilon$  model showed favorable agreement with measurements for configuration “N”, indicating the possibility of using this model to predict flow under this configuration. For configuration “A”, simulations have outlined the important role turbulence play in this configuration. Standard k- $\epsilon$  model could not predict the high velocity region near the center. Reynolds stress model was more successful in obtaining the flow trend; however the predicted velocities deviated from the measured ones. The same behavior was also encountered in configuration “AT”.

In the previous sections, three flow configurations have been discussed from flowfield point of view. These three flow configurations have been examined under reacting conditions with emphasis on NO and CO emission. Figure 4-24 shows the global flame features for configuration “N” and configuration “AT”. Configuration “N” exhibited a flame only at the outer wall of the combustor, while configuration “AT” exhibited a colorless flame throughout the combustor volume.

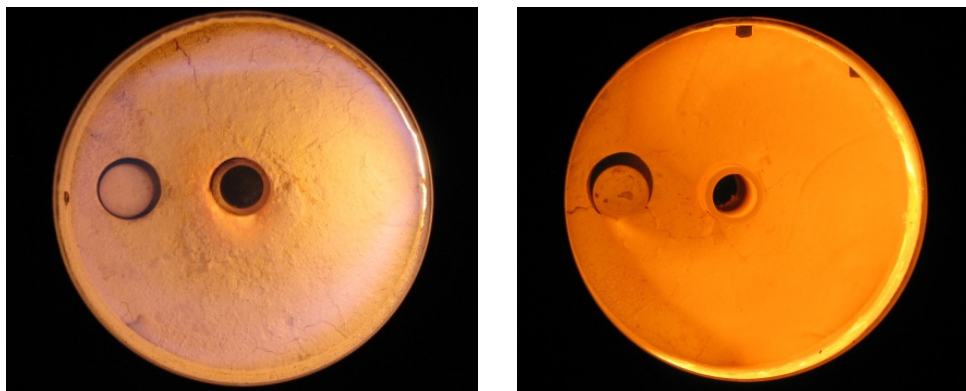


Figure 4-24 Global flame images for normal “N” (left), axial exit with tube “AT” (right).

Comparing obtained emissions for cases “N” and “AT”, one can outline the benefits of incorporating swirling flow into the flowfield. Velocity measurements have shown that configuration “AT” demonstrated higher recirculation ratio and higher turbulence distribution with high velocity regions near the center of the combustor. On the other hand, obtained emission for the two same configurations showed that a reduction of 33% of NO was demonstrated using “AT” configuration over “N” configuration. Also, 66% reduction of CO was achieved. Such reduction resulted in ultra-low emissions of 2 PPM NO and 50 PPM of CO. Near zero NO emission (<1 PPM) was also demonstrated [36]. Such decrease in pollutants emission can be directly related to

enhanced recirculation ratio. Higher recirculation of hot product gases raises the fresh mixture temperature while diluting it to result in a high temperature low oxygen concentration environment, which is an essential condition for colorless distributed conditions. Also, the increased recirculation ratio increases the residence time for complete combustion. Extending the exit tube inside the combustor as in configuration “AT” prevented any gases escaping before incomplete combustion. Enhanced turbulence with swirling motion played an important role in mixing of air/fuel and recirculated hot product gases for ultra-low emissions as demonstrated by the obtained emissions.

#### **4.5. Other Geometrical Parameters**

Different geometrical parameters of the combustor have been examined to evaluate their impact on pollutants emission and reaction distribution. These parameters include the combustor length (depth), the exit clearance of the combustor (distance between extended exit tube and the combustor end wall), the air/fuel injection plane (with respect to the combustor length/depth), and the diameter of the combustor. Detailed investigations of this parameters demonstrated that the current configuration emits the lowest NO and CO for the cases investigated and consequently the combustor length will be set to  $8D$ , exit clearance will be  $2D$ , air/fuel will be injected at the mid height of the combustor and the combustor diameter will remain at  $16D$ . Details of the mentioned investigations are included in appendix C.

#### 4.6. Temperature and Pressure Effects

In order to simulate gas turbine combustion conditions, air is preheated here to evaluate the combustor performance under more relevant gas turbine operating conditions. Increase in the air inlet temperature is expected to drastically affect combustion kinetics and pollutant formation and emissions. Higher air inlet temperature will result in higher flame temperature. Such high flame temperature will aid the formation of thermal  $\text{NO}_x$  which increase dramatically with increase of flame temperature as NO emissions very much depends on the flame temperature. On the other hand, increase in the air inlet temperature will reduce CO as a result of increase in the flame temperature, which accelerates the conversion of CO to  $\text{CO}_2$ . At equivalence ratios of stoichiometric conditions and above, this higher flame temperature promotes the formation of CO by dissociation so that at the high equivalence ratios, the CO concentrations are high for higher inlet air temperature [15]. To further simulate gas turbine combustor operational conditions, the pressure inside the combustor was increased to 2 atm. (~15 psig). Increase in the combustor pressure is anticipated to have a beneficial effect. At low equivalence ratios, increase in pressure diminishes CO by accelerating the rate of conversion of CO to  $\text{CO}_2$ . At high equivalence ratios, increase in combustion pressure reduces CO emissions, albeit to a lesser extent, by suppressing chemical dissociation [15]. For all the experiments performed in this section, the air injection diameter was modified from D to  $5D/3$  to maintain the air injection speed around 100 m/s. If the injection diameter was maintained at D, the injection velocity would have increased to 256 m/s leading to higher pressure drop in the combustor.

#### 4.6.1. High Temperature Experiments

The results have been obtained to evaluate the performance of the combustor with preheated air temperature of 600K. In order to maintain injection velocity associated with the change in air density with temperature, the air injection diameter was increased. It may be noted that higher air inlet temperature will result in higher flame temperature. Such high flame temperature will aid in the formation of thermal  $\text{NO}_x$  which increases dramatically with increase of flame temperature as NO emissions are very dependent on flame temperature. On the other hand, increase in the air inlet temperature will reduce CO as a result of increase in the flame temperature, which accelerates the conversion of CO into  $\text{CO}_2$ . At equivalence ratios of stoichiometric and above, this higher flame temperature promotes the formation of CO by dissociation so that, at the highest equivalence ratios, the CO concentrations are highest for the higher inlet air temperature.

The experimentally measured emissions from the combustor were as expected; NO emission increased due to higher operational temperature and is in agreement with NO dependence on flame temperature. However, CO emission decreased dramatically which is more favorable. CO decrease can be attributed to the fact that as the flame temperature increases; conversion of CO into  $\text{CO}_2$  is accelerated leading to less CO in product gases. This behavior was demonstrated for both non-premixed and premixed combustion conditions.

Figure 4-25 shows a comparison for NO and CO under preheated air combustion condition as compared to normal air inlet temperature condition for non-premixed combustion condition. The results show an increase of NO emission. However, CO

emissions were dramatically reduced. Previously, the lowest demonstrated CO emission was 70 PPM with normal air temperature case. However, with air preheats this value was reduced to 21 PPM.

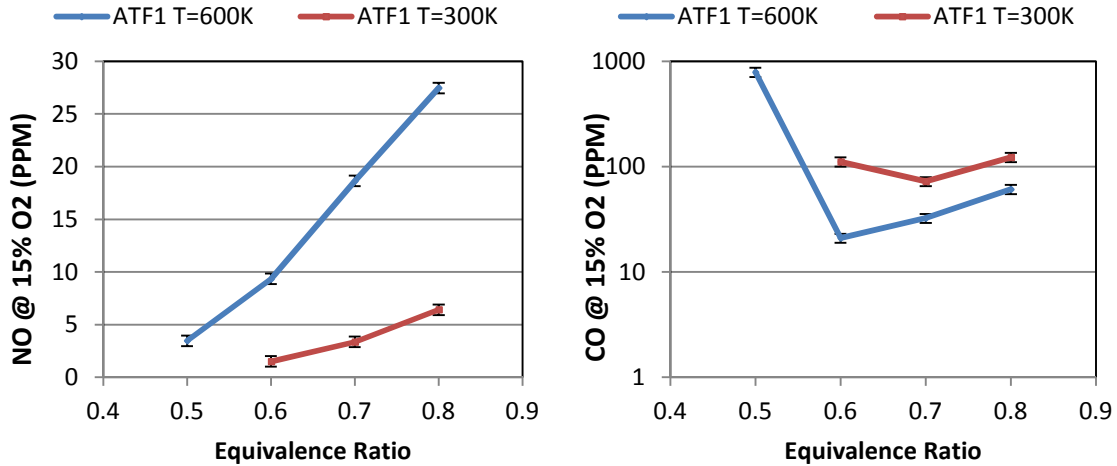


Figure 4-25 Pollutants emission for non-premixed combustion mode with fuel injection at location one for different air inlet temperatures. (Left) NO, (Right) CO

A favorable operating condition for this combustor configuration using preheated air was found to be at an equivalence ratio of 0.6 that resulted in NO and CO emission of 10 and 21 PPM, respectively at a heat release intensity of 27 MW/m<sup>3</sup>-atm.

Figure 4-26 shows emission of NO and CO under preheated air condition and the results are compared to those obtained with normal air inlet temperature condition to the combustor for premixed combustion case. The results showed a trend similar to that exhibited in non-premixed combustion. NO emissions increased slightly. The CO emissions were dramatically reduced with increase in air preheat temperature. Previously, the lowest demonstrated CO emission was 50 PPM. However, with air preheats to the combustion air this value was reduced to 11 PPM. The favorable operating point for this combustor design with preheated air was also found to be at an

equivalence ratio of 0.6, that resulted in NO and CO emission of 4 and 11 PPM respectively at a heat release intensity of 27 MW/m<sup>3</sup>-atm.

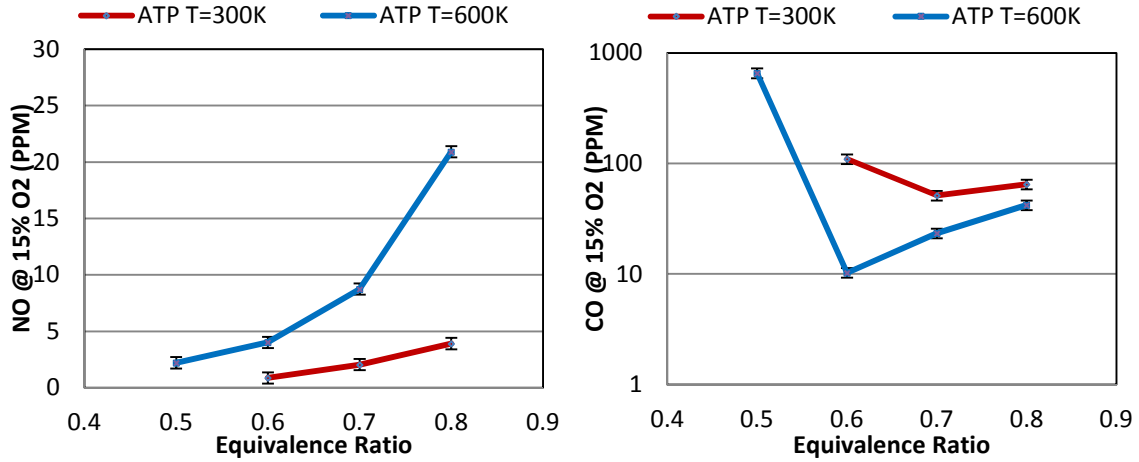


Figure 4-26 Pollutants emission for premixed combustion mode for different air inlet temperatures. (Left) NO, (Right) CO

The radical intensity distribution of OH\* chemiluminescence shows that the reaction zone is in the shape of a crescent formed opposite to fuel injection point for non-premixed combustion and opposite to air/fuel injection point for premixed combustion. The results reveal that the OH\* intensity decreases with a decrease in equivalence ratio. Figure 4-27 shows the OH\* chemiluminescence intensity distribution for the extended axial exit arrangement for the preheated air temperature case. It is to be noted that the intensity scale is different than that used in Figure 4-15 due to the increased OH\* intensity with increase in air preheat temperature that is expected to increase the flame temperature.

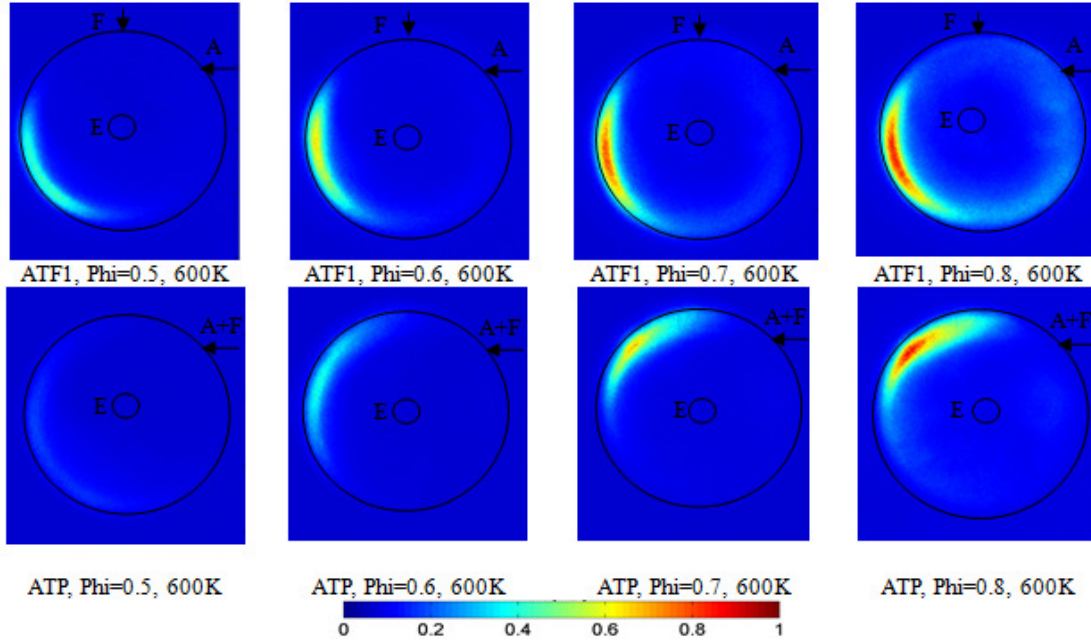


Figure 4-27 OH\* chemiluminescence intensity distribution under preheated air.

#### 4.6.2. Elevated Pressure Experiments

The results have been obtained to evaluate the performance of the combustor at the elevated pressure of 2 atm. (15 Psig). In order to keep constant heat release intensity, air and fuel mass flow rates were increased to double the value. Air injection diameter was increased to increase the air flow rate. Elevated pressure will promote the combustion kinetics to enhance the combustion reactions. At low equivalence ratios, increase in pressure diminishes CO by accelerating the rate of conversion of CO into CO<sub>2</sub>. At high equivalence ratios, increase in combustion pressure reduces CO emissions, albeit to a lesser extent, by suppressing chemical dissociation. So in one aspect high pressures are beneficial, but on the other hand, high pressure also accelerated NO<sub>x</sub> formation leading to higher NO emissions.

The combustor experimental emissions were as expected; NO emission increased due to the accelerated chemical kinetics of the combustion process. However, CO emission decreased dramatically which is a highly beneficial aspect. Figure 4-28 shows a comparison for NO and CO emission under elevated pressure condition and these results are also compared to normal pressure condition for non-premixed combustion. At higher pressure conditions the NO emissions show a slight increase. However, CO emissions were dramatically reduced.

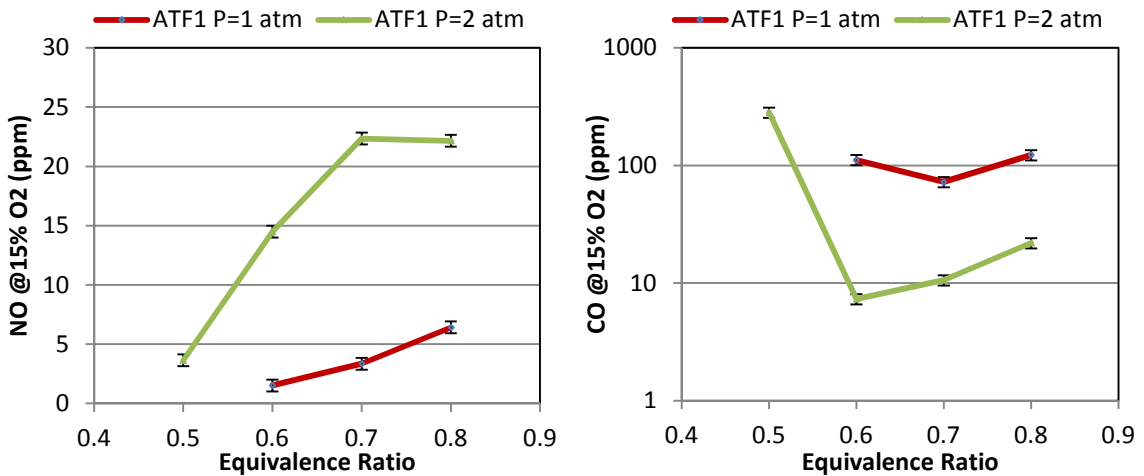


Figure 4-28 Pollutants emission for non-premixed combustion mode for normal and elevated combustor pressure. (Left) NO, (Right) CO.

Previously, the lowest demonstrated CO emission was 70 PPM at normal pressure combustion conditions. However, with combustor pressurized to only 2 atm., this value was reduced to 8 PPM. The favorable operating point for this combustor design with preheated air was found to be at an equivalence ratio of 0.6, resulting in NO and CO of 15 and 8 PPM at a heat release intensity of 27 MW/m<sup>3</sup>-atm.

Figure 4-29 shows a comparison for NO and CO emission under elevated pressure condition and compared to normal pressure condition for premixed combustion condition. The same trend was found under premixed combustion condition. NO emissions were increased slightly while CO emissions were reduced dramatically at elevated pressure. The lowest demonstrated CO emission for the normal pressure case was 50 PPM. However, this value was reduced to 10 PPM at elevated pressure condition. The favorable operating point for this combustor design with normal temperature air pressurized to 2 atm. pressure was found to be at an equivalence ratio of 0.7, resulting in NO and CO emission of 5 and 10 PPM, respectively at a heat release intensity of 31.5 MW/m<sup>3</sup>-atm.

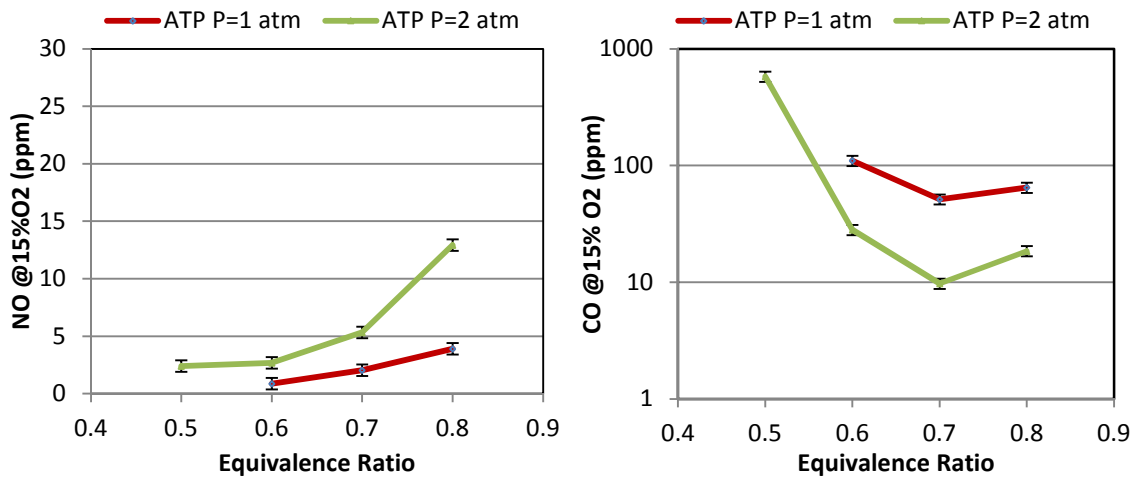


Figure 4-29 Pollutants emission for premixed combustion mode for normal and elevated combustor pressure. (Left) NO, (Right) CO.

The radical intensity distribution of OH\* chemiluminescence shows that the reaction zone is in the shape of a crescent formed opposite to fuel injection point for non-premixed combustion and opposite to air/fuel injection point for premixed combustion. The results reveal a decrease in OH\* intensity with decrease in equivalence

ratio. Figure 4-30 shows the OH\* chemiluminescence intensity distribution for the extended axial exit arrangement under elevated pressure condition. Note that the intensity scale is different in Figure 4-30 than that used in Figure 4-15 due to the increased OH\* intensity with increase in pressure.

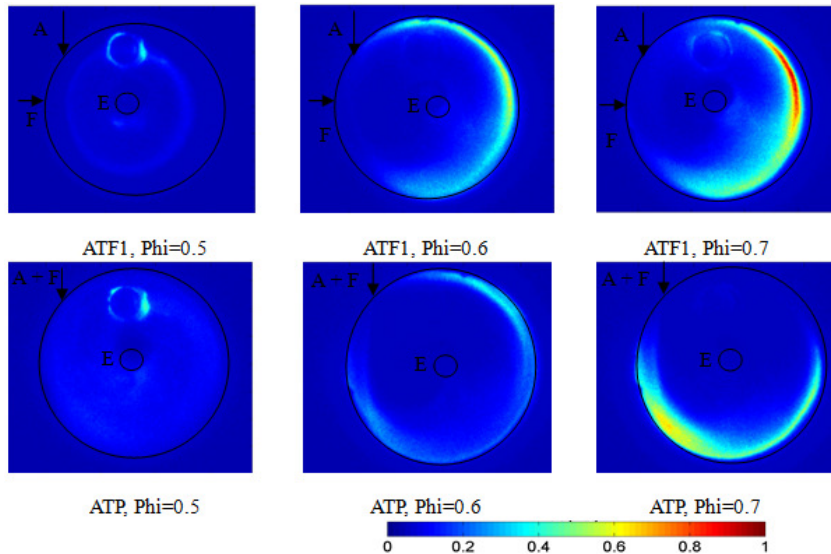


Figure 4-30 OH\* chemiluminescence intensity distribution under elevated pressure condition.

#### 4.6.3. Preheated Air and Elevated Pressure Experiments

The combined effect of both preheated inlet air and elevated combustor pressure is now presented. The focus here was to evaluate the performance of the combustor under both conditions and obtain data from which the performance of the combustor at higher pressures can be extrapolated. It is anticipated that combining both high temperature and elevated pressure will significantly increase NO emissions while simultaneously cause a dramatic decrease of CO emission.

The experimental emissions data obtained from the combustor were as expected; NO emission increased due to the accelerated chemical kinetics and increased temperature. However, CO emission decreased dramatically which is a highly desirable. One very favorable outcome was the ability to sustain the flame at lower equivalence ratio as compared to the previously discussed conditions. Such extension of the lean flammability limit enabled the combustor to run at an equivalence ratio down to 0.5 without having incomplete combustion (presenting with significantly increased emission of CO emission).

Figure 4-31 shows a comparison for NO and CO emission under current conditions as compared to the previous conditions for non-premixed combustion case. A trend similar to that discussed earlier was demonstrated, wherein NO emission increased while CO emission decreased. Under preheated air and elevated temperature conditions, the combustor demonstrated emissions as low as 10 PPM NO and 8 PPM CO for non-premixed combustion at a heat release intensity of 22.5 MW/m<sup>3</sup>-atm.

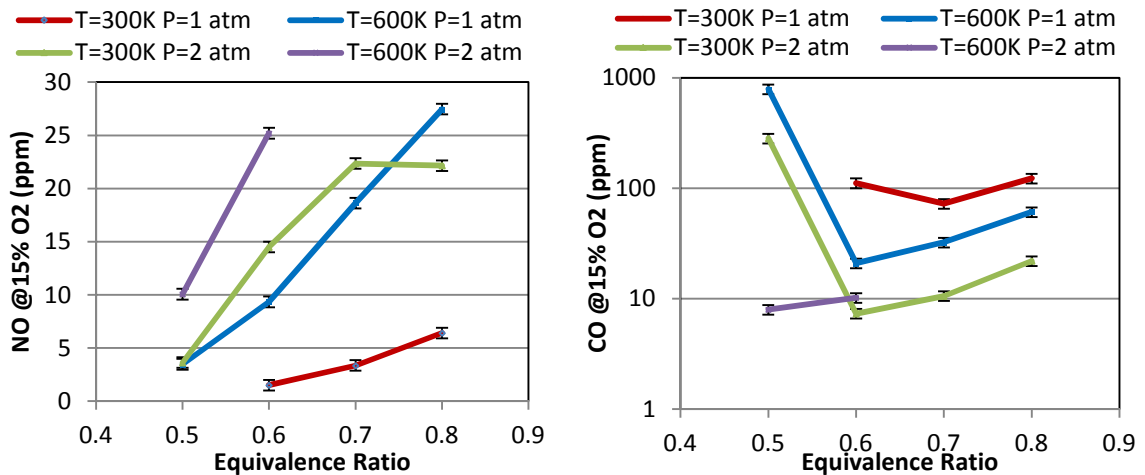


Figure 4-31 Pollutants emission for non-premixed combustion mode for different operational conditions. (Left) NO, (Right) CO.

Figure 4-32 shows a comparison for NO and CO emission under preheated air and elevated pressure conditions and compared to the previously discussed conditions for premixed combustion case. The trend demonstrated for non-premixed combustion case was found for the premixed case. The more favorable operational point was found to be at an equivalence ratio of 0.6 and a heat release intensity of 27 MW/m<sup>3</sup>-atm yielding emissions as low as 5 PPM NO and 8 PPM CO.

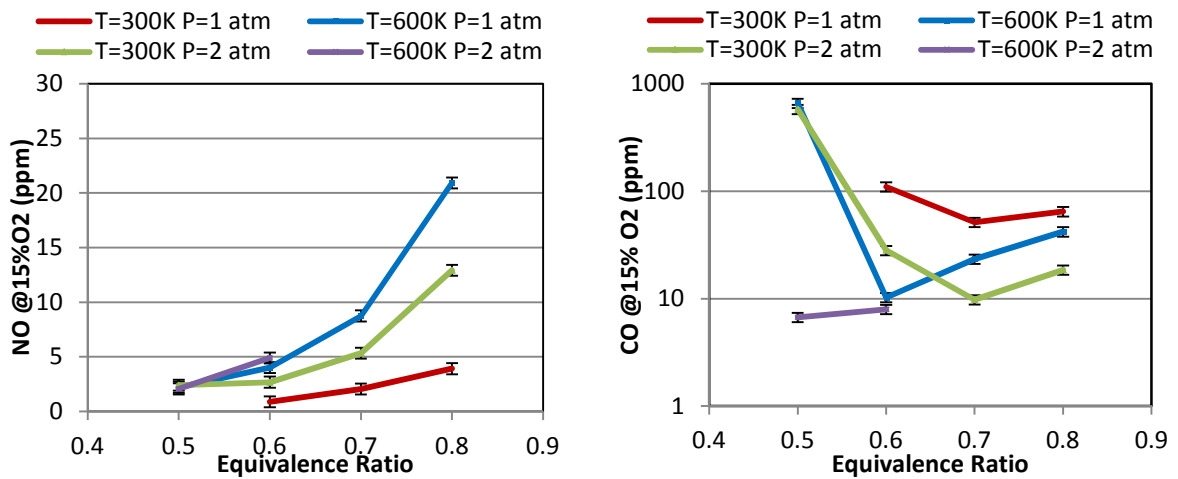


Figure 4-32 Pollutants emission for premixed combustion mode for different operational conditions. (Left) NO, (Right) CO.

The radical intensity distribution of OH\* chemiluminescence showed that the reaction zone is again in the shape of a crescent formed opposite to fuel injection point for the non-premixed combustion case and found to be near to the region opposite to air/fuel injection point for premixed combustion. The results showed a decrease in OH\* intensity with a decrease in equivalence ratio. Figure 4-33 shows the OH\* chemiluminescence intensity distribution for the extended axial exit arrangement under the discussed conditions. Note that the intensity scale is different than that used in Figure 4-15 due to the increased OH\* intensity with preheated combustion air.

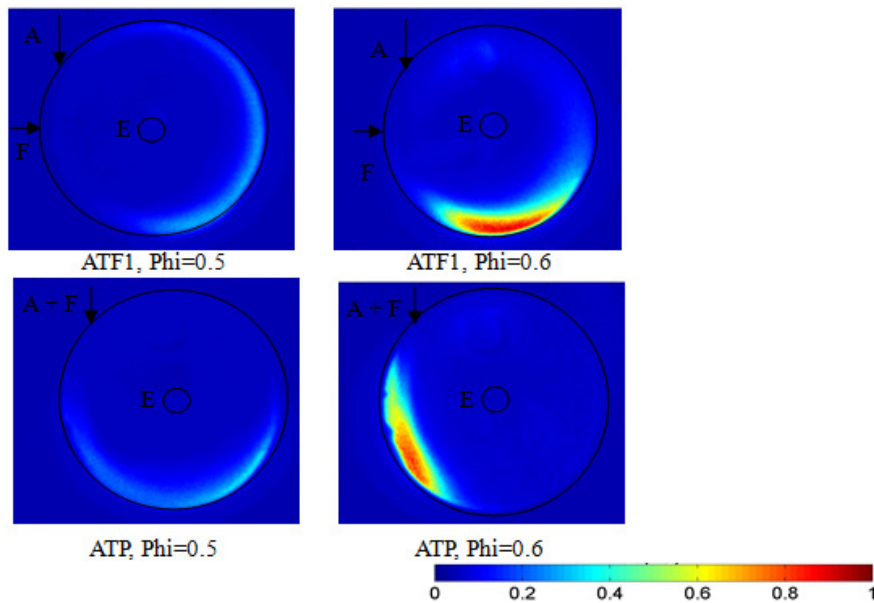


Figure 4-33 OH\* chemiluminescence intensity distribution under elevated temperature and pressure.

The experimental results obtained so far from the combustor shows great promise to achieve near zero pollutant emissions at gas turbine operational conditions where even higher pressures are attributed, which will allow the combustor to sustain flame at even lower equivalence ratios, where much lower NO (near zero) emissions are produced without suffering from incomplete combustion and high CO emissions. Our continued efforts will further reduce the differences in pollutants emission between premixed and non-premixed combustion cases by further efforts on modifying our flowfield with the vision to achieve less (or same) emissions from non-premixed combustion as compared to premixed combustion.

#### 4.7. Summary

In this chapter, numerical and experimental investigations have been performed on three different product gases exit arrangements with different fuel injection scenarios. Numerical simulations showed that axial exit result in a higher recirculation ratio compared to normal exit. This have been confirmed through isothermal flowfield characterization using particle image velocimetry, where it was shown that the measured recirculation ratio for the swirling configuration (axial exit) was three folds that of the non-swirling configuration (normal exit).

Pollutants emission measurements demonstrated that swirling combustor produced lower emissions than its non-swirling counterpart. This is in agreement with the measured recirculation ratio. Recirculated reactive species mix with air to form a hot and oxygen diluted oxidizer which fosters distributed reaction conditions. Extending the hot products gases exit inside the combustor (configuration AT) resulted in an enhanced residence time inside the combustor and lower CO emissions.

The impact of elevated temperature and pressure have been examined with emphasis on better simulating true gas turbine combustor conditions. Increasing the temperature and pressure enhanced the lean operational limit, allowing the combustor to run at lower equivalence ratios and emitting lower pollutants emission. The increase in temperature and pressure has been shown to impact the reaction zone, leading to a smaller reaction area as compared to standard air, atmospheric pressure experiments. Nevertheless, ultra-low emission were demonstrated with configuration “AT”.

In the next chapter, the fuel flexibility of this combustor configuration will be evaluated with view to develop ultra-low emissions fuel flexible combustor.

## **5. Chapter Five: Fuel Flexible CDC**

Depletion of fossil fuels and widespread concern about global warming have motivated engineers to develop novel combustion technologies using conventional and alternative fuels to power the current and future energy systems without any impact on the environment while maintaining high conversion efficiency and performance. Consequently, the necessity for a combustor that is fuel flexible and surpasses the increasingly stringent environmental regulation requirements concerning emissions from different kinds of propulsion and power systems along with quest for environmentally friendly energy systems have challenged combustion engineers to develop novel combustion techniques for achieving ultra-low levels of pollutants emission (such as,  $\text{NO}_x$ , CO, unburned hydrocarbons and soot), along with reduced noise, low flame fluctuations, alleviation of combustion instability and improved pattern factor from gas turbine combustors.

The primary objective of this chapter is to evaluate fuel flexibility of the CDC combustor without changing any of its geometrical parameters. Different fuels are used in the combustor to assess the combustor fuel flexibility while maintaining ultra-low emission. The fuels examined include diluted methane, hydrogen enriched methane, propane, ethanol, and kerosene. Such wide range of fuels examined here, supporting fuel flexibility, are considered important in stationary gas turbines. A brief description of the examined fuels and their applications are given in the following section.

All of the discussed fuels are examined using the final combustor configuration. The combustion chamber is a cylindrical chamber, of diameter  $16D$ , where air is injected

tangentially, into the combustion chamber, at mid height of the combustor. The air injector diameter was  $5D/3$  for inlet air temperature of 600K. Fuel is also injected at the same plane as air injection using a diameter of  $D/3$  for non-premixed cases. The total height of the combustor was  $8D$ . For hot product gas exit, a tube was extended inside the combustor to increase residence of the gases in the combustor with a clearance of  $2D$  between the tip of the tube and end wall of the combustor, see Figure 5-1.

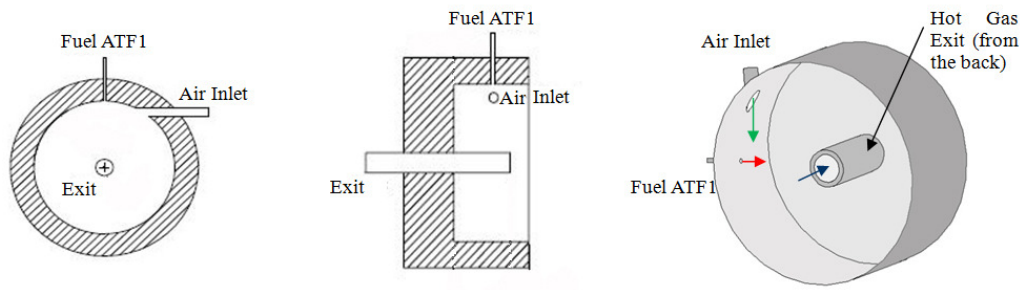


Figure 5-1 Schematic diagrams of the Combustor used

For combustion, air was supplied through an air compressor. Both air and gaseous fuel flow rates were measured using choked flow orifice systems. Precision stainless steel orifices were used to choke the flow of the gases and upstream pressure was controlled to supply the required mass flow rate of gases. The upstream pressure was controlled using pressure regulators to maintain a steady pressure and avoid oscillations in pressure due to compressor turning on and off periodically. The upstream pressure for both air and fuel was maintained between  $\pm 0.2$ psi of the desired pressure. Upstream pressure was measured using a piezoresistive digital pressure gauge with accuracy of

$\pm 0.25$ psi. It was ensured that the downstream pressure was lower than the pressure required for choking the flow based on the upstream pressure.

Detailed investigations on the overall emissions from the combustor as well as visible emissions have been performed for the various experimental conditions. A Horiba PG-250 gas analyzer was used for emissions measurements. The concentration of NO was measured using a NO–NO<sub>x</sub> chemiluminescent method; CO concentration was measured using the non-dispersive infrared method and O<sub>2</sub> concentration (used to correct the NO and CO emissions at standard 15% oxygen concentration) was measured using galvanic cell method. The gas analyzer was continuously calibrated against calibration gases. For NO emissions below 5 PPM, a high accuracy thermo-electron chemiluminescence NO–NO<sub>2</sub>–NO<sub>x</sub> low source analyzer was also used (Model 42C) to verify the measurements. During a single experiment, measurements were repeated at least three times for each configuration and the uncertainty was estimated to be about  $\pm 0.5$  PPM for NO and  $\pm 10\%$  for CO emission. The experiments were repeated at least three times to ensure good repeatability of the experimental data obtained. The recorded data is then corrected to 15% O<sub>2</sub> concentration and averaged.

For imaging the OH\* chemiluminescent intensity distribution, an ICCD camera coupled to a narrow band filter at 307 nm wavelength was used. The gain for these images was set to 70 with one accumulation per image and f-stop setting of 4.5. The exposure time was set to 50 msec.

### 5.1. Low Calorific Value Fuel (Diluted Methane)

Numerous efforts have been reported on the use of various kinds of alternative fuels in existing power plants; however, for gas turbine applications the fuel quality and properties are of pinnacle importance. The combustion of low calorific gases, such as, landfill gas and producer gas can have some impact on the primary energy use while also reducing hazardous emissions. However, the composition and calorific value of these fuels can give problems with flame stability, combustion instability and high levels of pollutants emission. Low calorific value gases are produced from landfills and from some process industries so that their composition can be different not only between sites but also from operations. Upon removal of most of the trace organic compounds, landfill gas can be used as a source of clean fuel in gas turbines for power generation, heat and electricity. Producing energy from landfill gases has the additional benefits of onsite power generation for local use, and prevention of the gases release into the atmosphere and associated greenhouse effects. Municipal waste landfills emit mainly CO<sub>2</sub> and CH<sub>4</sub>. The large amounts of CO<sub>2</sub> in landfill gas (typically 40–50%) presents problems with its utilization for energy production, since it adversely impacts flame stability, combustion efficiency and increased pollutants emission. Low calorific value associated with such fuels results in difficult operation of the combustor over a wide dynamic range of conditions with acceptable level of combustor performance. In contrast, the pyrolysis of organic wastes yields gases with high concentrations of H<sub>2</sub>, CO, N<sub>2</sub> and CO<sub>2</sub>. These mixtures can have very wide range of heating value and flame speed that depends on the fuel gas composition. The main combustion characteristics, such as, laminar flame speed and adiabatic flame temperature of landfill gas have been

examined [93] [94] [95] with a view towards energy extraction. The economic aspects of energy production from landfill gases are discussed elsewhere [96] [97]. Previous research has shown that carbon dioxide acts as an inert energy sink for landfill gas combustion [95]. The combustion characteristics of methane diluted with either nitrogen or carbon dioxide have been examined [94] [98]. Figure 5-2 shows the laminar flame speed and adiabatic flame temperature for diluted methane (percent) with both nitrogen and carbon dioxide [94]. It can be seen that nitrogen and carbon dioxide have similar behavior concerning laminar flame speed and adiabatic flame temperature.

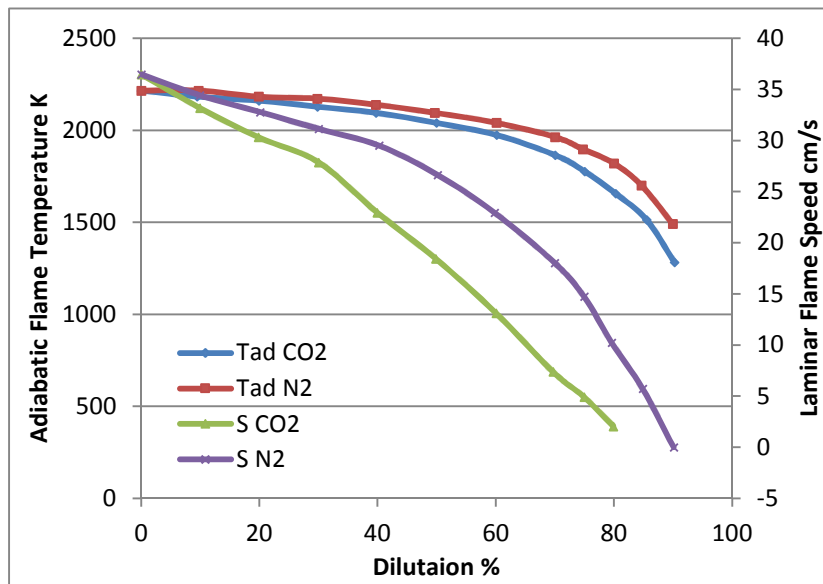


Figure 5-2 Adiabatic flame temperature ( $T_{ad}$ ) and laminar flame speed ( $S$ ) for different dilution percent (by volume) at stoichiometric mixtures

A similar trend can be seen in Figure 5-3, where the laminar flame speed is plotted for various methane/nitrogen and methane/carbon dioxide mixtures at different equivalence ratios [98].

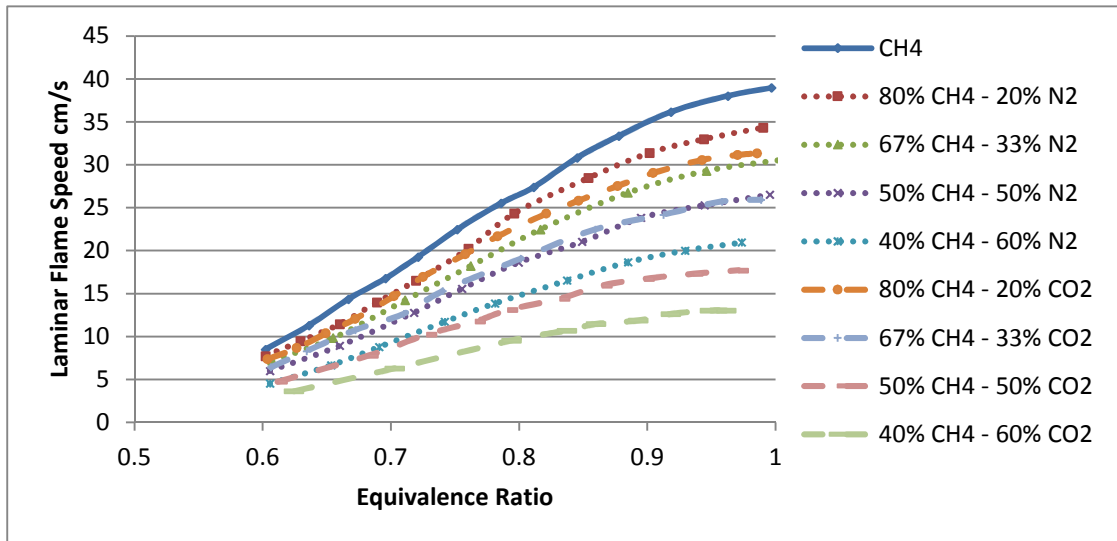


Figure 5-3 Laminar flame speed at different equivalence ratios for different dilution percent (by volume)

The study focuses on simulated landfill gas or similar low to medium calorific value fuel using methane diluted with nitrogen to provide a similarity in the same range of ‘equivalent’ calorific values from the point of view of laminar flame speed and adiabatic flame temperature. This approach helps in understanding the general behavior of burning low calorific value fuels. The results obtained can be used to quantify the key aspects of fuel dilution for syngas or landfill gas use in natural gas fired applications.

### 5.1.1. Experimental Conditions

Detailed investigations on the emissions of NO and CO have been performed using the experimental high intensity combustor. Initial investigations were aimed at comparing the performance of the combustor with fuels of different calorific value. Investigations were also carried out to evaluate the performance of the combustor at different equivalence ratios using defined equivalent calorific value fuel. For this

purpose an equal mixture of methane and nitrogen on volume basis was chosen that resulted in a fuel with an equivalent calorific value of 19.75 MJ/Kg. The injection velocity and nozzle diameter of the fuel and air as well as gas exit were the same throughout all the tests. A comparison between premixed and non-premixed modes of combustion has been performed for each case. Table 5-1 summarizes the selected variables reported here. For the case numbers, the first two letters indicate the hot product gases exit condition, followed by fuel injection mode identification. The last 3 numbers for a case no. represent temperature of air at the inlet. The inlet air to the combustor was preheated to 600K to simulate gas turbine combustion conditions.

Table 5-1 Experimental Parameters for Methane Dilution

Case No.	Combustion Type	Variable
ATF1-300	Non-Premixed	Calorific Value
ATF1-600	Non-Premixed	Calorific Value
ATP-300	Premixed	Equivalence Ratio
ATP-600	Premixed	Equivalence Ratio
ATF1-300	Non-Premixed	Equivalence Ratio
ATF1-600	Non-Premixed	Equivalence Ratio

## 5.1.2. Results and Discussion

### 5.1.2.1. *Calorific Value (N<sub>2</sub> dilution) Variation*

The experimental investigations were performed at a constant thermal load of 6.25KW. The calorific value of the fuel was changed by adding different amounts of nitrogen to the methane flow rate. Pollutant emissions were recorded with the various equivalent calorific values of the fuel. The tests were performed under non-premixed combustion conditions using normal air and preheated air at inlet to the combustor.

Addition of nitrogen to the fuel resulted in decreased emission of NO. As the amounts of nitrogen were increased, the resultant NO emission decreased until a minimum was reached. At the operating point using pure methane as the fuel (baseline case), the resulting NO and CO emissions were 10 PPM and 32PPM, respectively. The addition of nitrogen decreased the NO to about 6 PPM for equivalent fuel calorific value of 25 MJ/Kg or less. On the other hand, CO emissions increased slightly. The behavior of both NO and CO emissions can be explained by the decrease in temperature in the combustion chamber. As nitrogen acts as an energy sink, it decreased temperature in the combustion chamber which consequently decreased the NO emissions due to strong dependence of NO<sub>x</sub> on combustion temperature. The decrease in temperature combined with increase in fuel injection velocity, decreases the residence time so that the CO formed in the combustion zone has less time and temperature to completely convert to CO<sub>2</sub>. Figure 5-4 shows the emissions of NO and CO with several different calorific values of the fuel reported here.

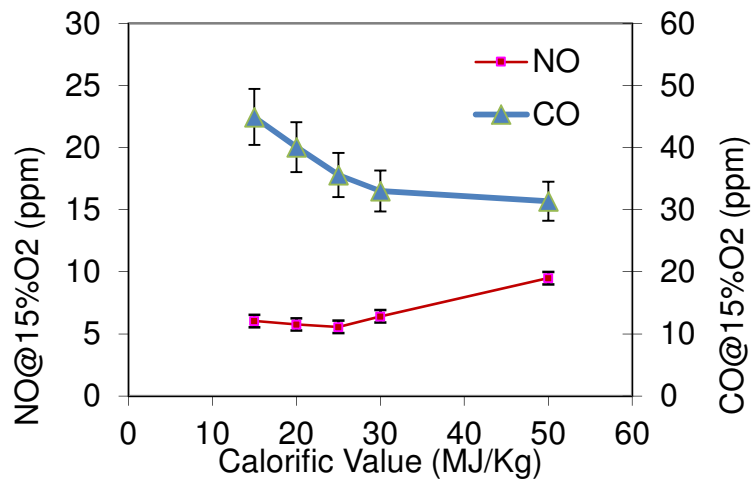


Figure 5-4 NO and CO emissions at different equivalent fuel calorific value under non-premixed conditions

The same experiment was also carried out to determine the role of preheats to the inlet air (at 600K). Figure 5-5 shows the measured NO and CO emissions for the air preheats case. The NO emissions were found to decrease with increase in nitrogen addition to methane fuel while CO emissions were found to remain essentially unchanged. As an example, pure methane resulted in NO emission of 22PPM, this value decreased to 9 PPM at an equivalent calorific value of 20 MJ/Kg, while CO emission remained around 16 PPM. The CO behavior can be attributed to air preheats prior to its introduction to the combustor, resulting in an overall increase in the combustion temperature that helped in converting CO to CO<sub>2</sub>. This effect can also be seen on NO emissions as they are higher compared to those achieved with normal air inlet temperature. It is to be noted that an increase in combustion temperature while operating in a lean combustion regime yields lower CO emissions as the increased temperature helps to convert CO to CO<sub>2</sub>, which have been shown in previous work [36]. On the contrary, if the combustion was considered rich (closer to stoichiometric condition), the increased temperature helps in dissociation of CO<sub>2</sub> to CO [15].

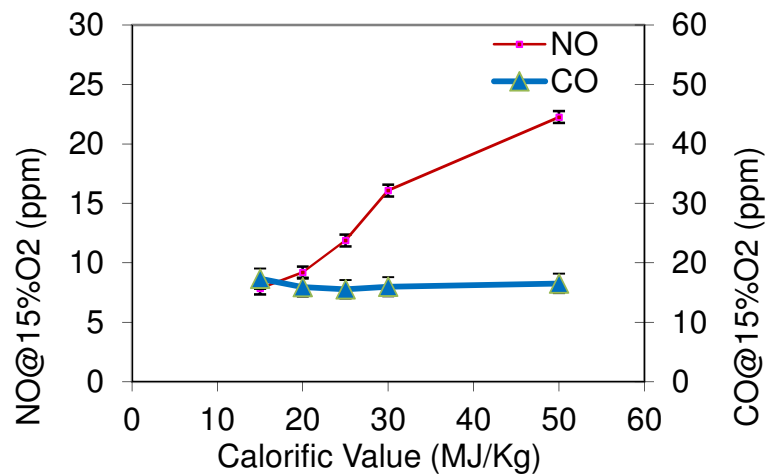


Figure 5-5 NO and CO emissions for non-premixed combustion mode at different equivalent fuel calorific value with inlet air preheated to 600K

#### 5.1.2.2. *Performance Evaluation at Various Equivalence Ratios*

The results have also been obtained under equal methane and nitrogen volume flow rates that resulted in an equivalent calorific value of 19.75 MJ/Kg at different equivalence ratios. For this calorific value of the fuel, experiments were performed under both premixed and non-premixed combustion condition using both normal and elevated temperature air preheats. The experimental results are also compared with those of pure methane case at the same thermal load. Operating the combustor with this fuel mixture while maintaining the same thermal load, dictated doubling the flow velocity through the fuel injector into the combustor. At an equivalence ratio of 0.8, using pure methane, the fuel injection velocity was 97 m/s. However, with nitrogen-methane mixture, the flow velocity was doubled to reach 194 m/s. Such an increase in fuel jet velocity is expected to affect the combustor flowfield, mixing of air, fuel and product gases within the combustor, and chemical kinetics as the fuel jet has more momentum to penetrate the combustor further towards the center.

The results from premixed combustion showed that low calorific fuel produces low emissions of both NO and CO. The NO emissions were reduced by about 30% with minimal impact on CO. Emissions as low as 2.4 PPM NO and less than 30 PPM CO was obtained at an equivalence ratio of 0.7. Note that equivalence ratio of 0.7 is rather high for most gas turbine combustion operation. Combustor operation with pure methane resulted in 4 PPM of NO and 22 PPM of CO. Figure 5-6 shows a direct comparison of the results of running the combustor with pure methane and a mixture of nitrogen and methane gas on the emission of NO and CO.

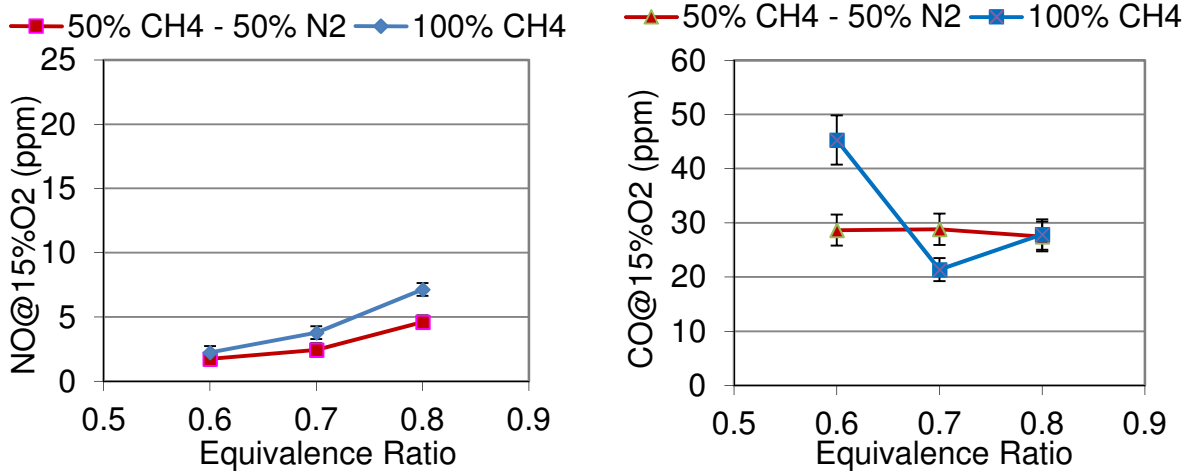


Figure 5-6 NO and CO emissions for premixed combustion mode with pure methane and 50-50 (vol.) mixture of methane and nitrogen.

When the same experiment was repeated using air preheats, NO emission was found to decrease by about 50% while CO emissions remained almost unchanged. Emissions as low as 2.8 PPM for NO and 13 PPM for CO were obtained using 50-50 mixture of CH<sub>4</sub> and N<sub>2</sub> at an equivalence ratio of 0.6. For pure methane, the resultant emissions were 4 PPM for NO and 14 PPM for CO. Figure 5-7 shows the resultant NO and CO emission for pure methane and diluted methane case under air preheats condition.

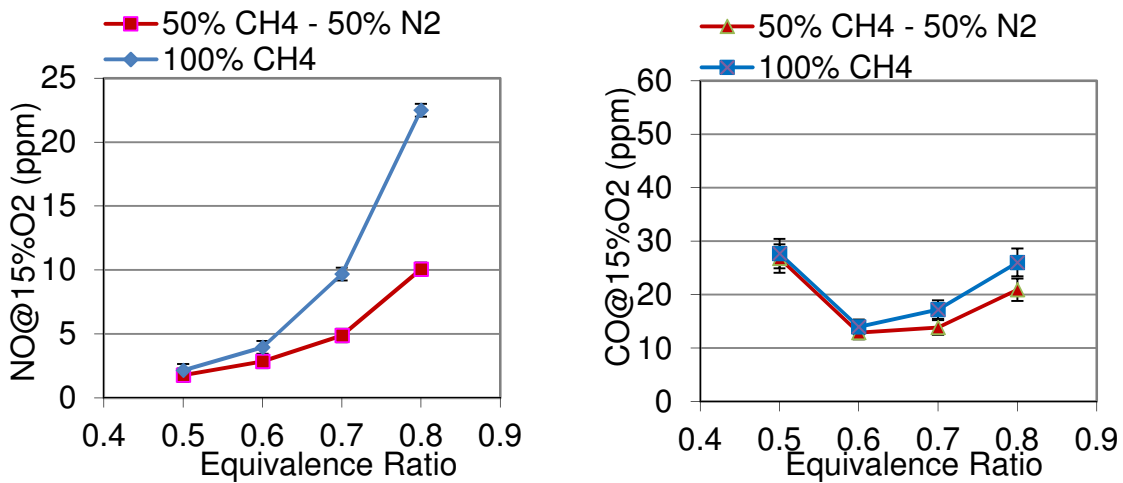


Figure 5-7 NO and CO emissions for premixed combustion mode with pure methane and 50-50 (vol.) mixture of methane and nitrogen with 600K preheated inlet air

The OH\* chemiluminescence intensity distribution showed that for both pure methane and methane-nitrogen mixture, the reaction zone is in a crescent shape opposite to air/fuel injection location. The results reveal that as the equivalence ratio decreases, the OH\* chemiluminescence intensity decreases to provide distributed combustion zone. Figure 5-8 gives the OH\* chemiluminescence intensity distribution for the various cases examined here.

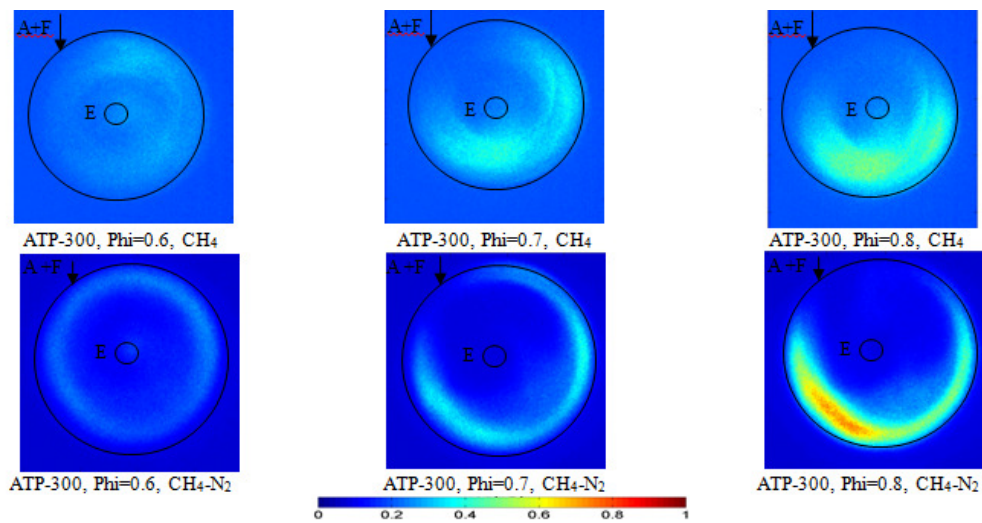


Figure 5-8 OH\* chemiluminescence intensity distribution for premixed cases for pure methane (top) and for 50-50 (vol.) mixture of methane and nitrogen (bottom)

For preheated air case, the OH\* chemiluminescence intensity distribution showed that for both pure methane and methane-nitrogen gas mixture case, the reaction zone is in a crescent shape opposite to air/fuel injection location. However, nitrogen addition resulted in a larger OH\* concentration zone which indicate a more distributed regime inside the combustor. Figure 5-9 shows the OH\* chemiluminescence intensity distribution for the above cases. Note that the scale used in Figure 5-9 is different than that used in Figure 5-8.

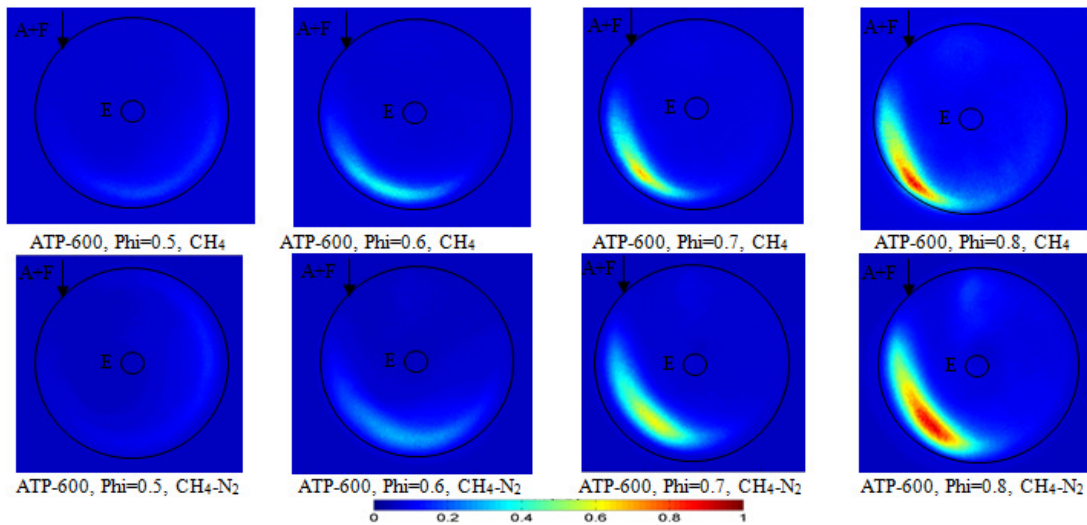


Figure 5-9 OH\* chemiluminescence intensity distribution for premixed cases for pure methane (top) and for 50-50 mixture of methane and nitrogen (bottom) with 600K preheated air temperature

The combustor performance was also evaluated for non-premixed combustion, which is of great interest as this combustion mode alleviates combustion instabilities associated with normal premixed combustion. Fuel was injected from a fuel port that is away from the inlet air flow in the form of a cross flow injection. N<sub>2</sub> addition to the fuel (which decreased the overall calorific value) yielded a 30% reduction in NO emissions with minimal impact on CO. Emissions as low as 6 PPM of NO and less than 40 PPM of CO was demonstrated at an equivalence ratio of 0.7. In contrast, using pure methane as the fuel, the recorded emissions were 8.5 PPM of NO and 22 PPM of CO. Figure 5-10 shows a direct comparison between running the combustor with pure methane or with a mixture of nitrogen and methane on the emission of NO and CO.

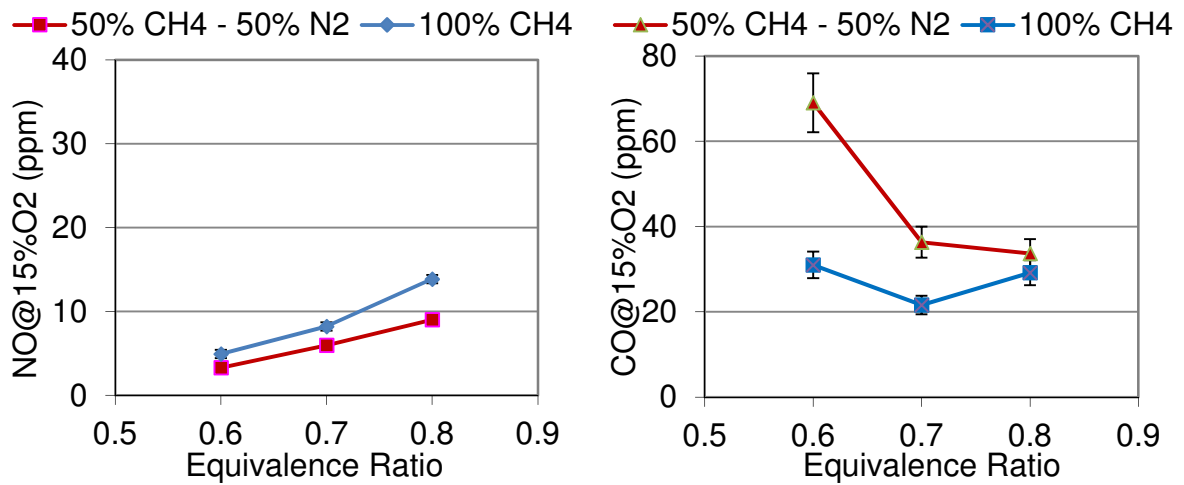


Figure 5-10 NO and CO emissions for non-premixed combustion mode with pure methane and 50-50 (vol.) mixture of methane and nitrogen

The combustor also demonstrated similar behavior at 600K air preheats temperature to the combustor. The NO emissions decreased by more than 50% while the CO emissions remained almost unchanged. Only 7 PPM of NO and 12 PPM of CO were obtained using 50-50 mixture of methane and nitrogen at an equivalence ratio of 0.6. Under the same conditions, using pure methane, the resultant emissions were 15 PPM of NO and 13 PPM of CO. Figure 5-11 shows the resulting NO and CO emissions for pure methane and diluted methane cases under preheated inlet air condition for the non-premixed combustion condition. Note that the CO emission level remained the same as air preheats increased the overall combustion temperature that helped in converting CO to CO<sub>2</sub> regardless of the fuel used.

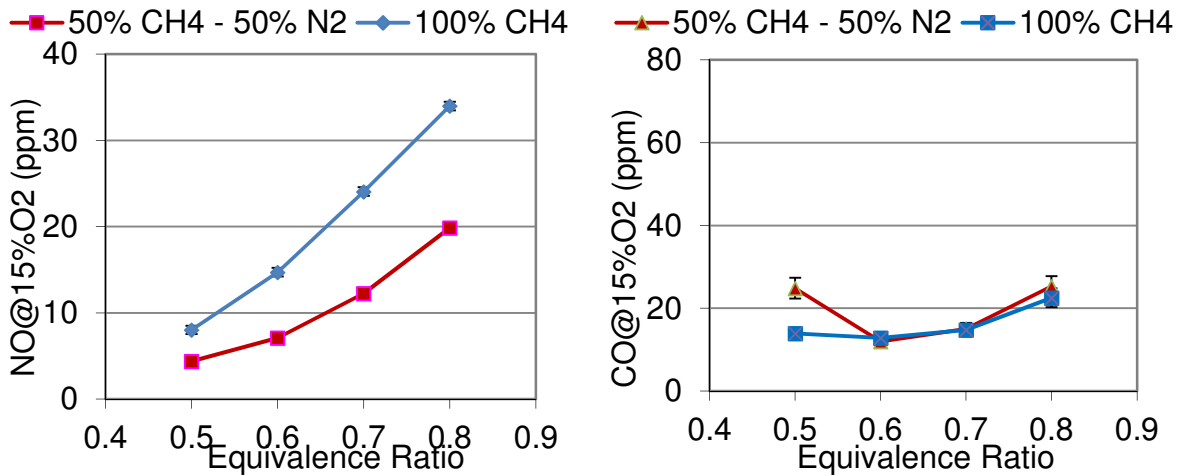


Figure 5-11 NO and CO emissions for non-premixed combustion mode with pure methane and 50-50 (vol.) mixture of methane and nitrogen with 600K preheated inlet air

The OH\* chemiluminescence intensity distribution showed that for both pure methane and methane-nitrogen gas mixture, the reaction zone forms a crescent shape opposite to the fuel injection location. The results revealed that a decrease in equivalence ratio decreased the OH\* chemiluminescence intensity and increased its distribution in entire zone of the combustor. Figure 5-12 gives the OH\* chemiluminescence intensity distribution for the examined cases. It is to be noted that OH\* distribution for the diluted fuel case is distributed over a larger area as compared to the pure methane fuel case.

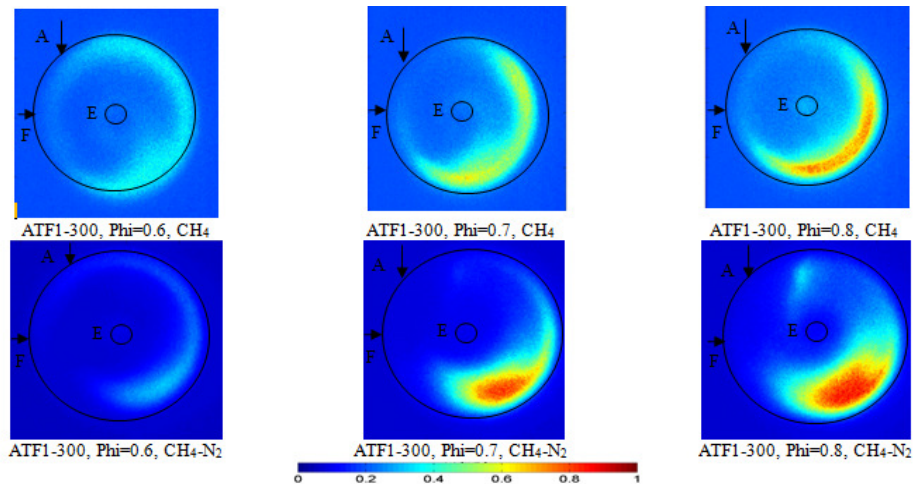


Figure 5-12 OH\* chemiluminescence intensity distribution for non-premixed cases for pure methane (top) and for 50-50 mixture of methane and nitrogen

For preheated air case, the OH\* chemiluminescence intensity distribution showed that for both pure methane and methane-nitrogen gas mixture case, the reaction zone is similar to the cases discussed before, wherein the OH\* intensity is distributed in a crescent shape that is located opposite to the fuel injection location. Figure 5-13 gives the OH\* chemiluminescence intensity distribution for the above cases. Note that the scale used in Figure 5-13 is different than that in Figure 5-12.

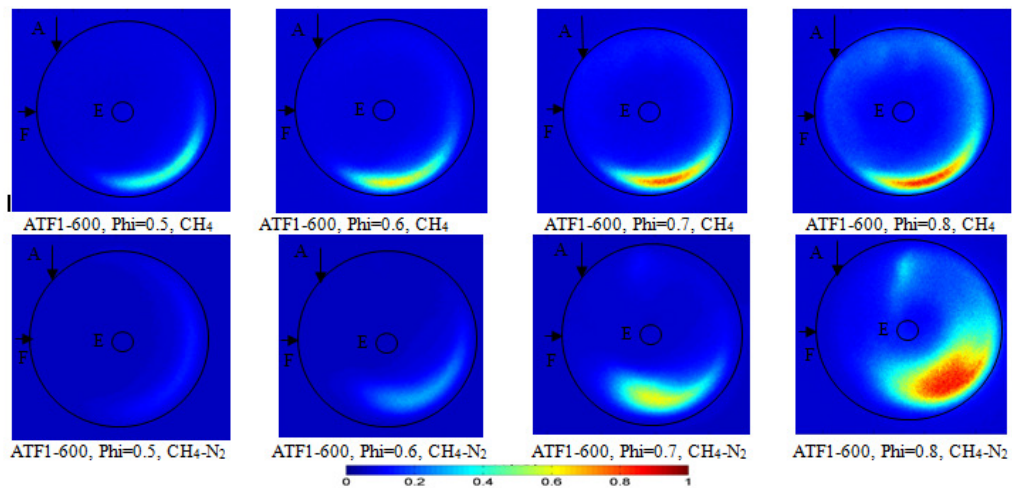


Figure 5-13 OH\* chemiluminescence intensity distribution for non-premixed cases for pure methane (top) and for 50-50% mixture of methane and nitrogen (bottom) with 600K preheated air temperature

A comparison of the OH\* distribution for methane fuel alone and methane-nitrogen fuel mixture cases shows that for the methane-nitrogen mixture cases, the reaction zone was not limited to the crescent shape found in pure methane cases and that it propagated towards the center of the combustor. This behavior is more distinct at higher equivalence ratios. This can be attributed to the fact that nitrogen addition doubled the fuel injection velocity up to 194 m/s (instead of 97 m/s) to maintain the same thermal load present in pure methane combustion case. Such a velocity increase results in a stronger fuel jet momentum allowing it to penetrate further towards the center of the combustor.

For all the previous cases, preheating the air prior to its introduction to the combustor resulted in an increase in the flame stability range. Consequently, the combustor was able to sustain the flame at lower equivalence ratios. However, with nitrogen addition, the stability range was slightly decreased for non-preheated air cases. This is attributed to the temperature drop in the combustor from the direct effect of nitrogen addition to methane fuel.

### 5.1.3. Summary

Results obtained with various methane-nitrogen mixtures simulating different low to medium calorific value fuels have shown that lower calorific value fuels yield lower NO emissions. Experiments using normal temperature air for combustion have demonstrated minimum NO emission at an equivalent calorific value of approximately 25MJ/Kg. Any further decrease in the calorific value had negligible impact on

pollutants emission. Using preheated air, NO emission continued to decrease with decrease in calorific value of the fuel.

The combustor demonstrated ultra-low emissions of NO and CO with a mixture of equal volume flow rates of methane and nitrogen that resulted in an equivalent fuel calorific value of 19.75 MJ/Kg (50%-50% methane nitrogen mixture by volume). For both premixed and non-premixed combustion, a reduction of 30% NO was achieved with negligible effect on CO while operating at normal air temperature. At air preheats of 600K, nitrogen addition to methane showed a significant reduction of both NO and CO. The NO emission was decreased by 50% for both premixed and non-premixed combustion. Such favorable performance with low equivalent calorific value fuel indicates the suitability of this combustor to handle multi-fuels including low calorific values, such as, diluted natural gas, landfill gas and syngas for gas turbine combustors.

The OH\* chemiluminescent distribution indicated that for all the cases shown here, highest intensity was found at regions opposite to fuel injection location. The effect of nitrogen addition to methane fuel resulted in a spreading out of the OH\* intensity distribution, occupying larger zone in the combustor. The stronger jet momentum allowed further fuel jet penetration towards the center of the combustor. Such jet penetration and OH\* distribution is favorable to alleviate hot spot zones in the combustor and produce a uniform thermal field for mitigating thermal NO<sub>x</sub> formation.

The results presented here demonstrate the ability of the combustor to handle medium to low grade fuel which require higher fuel velocities and volume flow rates without change of fuel injection nozzle. Such property is critical for low calorific value fuels as higher flow rates are required to furnish the combustor with the required

amount of fuel to maintain the same thermal load and high performance. These results also demonstrate the environmental benefits of diluting methane with nitrogen to increase the fuel jet momentum for better jet penetration and faster mixing with air and recirculated gases. This helps to yield ultra-low NO emission with negligible impact on CO emission, and enhanced distributed reaction zone with more favorable pattern factor. The lean flame stability increased with increase in inlet air temperature to the combustor. Global imaging showed no observable unsteadiness in the flame for all the conditions investigated here.

## **5.2. Hydrogen Enriched Methane**

Lean premixed combustion have been inherently used in gas turbine combustors to lower flame temperatures and to avoid stoichiometry non-uniformities that arise due to incomplete mixing of fuel and air. However, such method of lean premixed combustion often causes combustion instabilities, resulting in damage to the combustor and engine. Ultra-lean flames are susceptible to local flame extinction and quenching, leading to undesirable characteristics, such as, flame quenching, poor combustion efficiency, and acoustic combustion instabilities. In addition these flames produce elevated levels of carbon monoxide (CO) and unburned hydrocarbon (UHC) [99]. These premixed instabilities can lead to undesired phenomenon of flame flashback.

Higher combustibility of hydrogen has received increased attention as an additive to fuels for extending the lean combustion limits of gaseous fuels, reduce flame temperatures and reduce NO<sub>x</sub> emissions. Ultra-lean combustion is possible by mixing hydrogen and gaseous hydrocarbon fuels for combustion in traditional gas turbines with

low emission of  $\text{NO}_x$ , owing largely to lower overall equivalence ratio which results in lower flame temperatures in the combustion zone. Lower flame temperatures in the combustion-zone result in lower  $\text{NO}_x$  levels emanating from the Zeldovich thermal  $\text{NO}_x$  mechanism [9]. Note that the reduction of flame temperature results in weaker flames that are closer to the lean flammability limit.

Hydrogen enriched methane has shown considerable promise for ultra-lean premixed combustion for low emissions of  $\text{NO}_x$ , owing largely to the lower overall equivalence ratio which results in lower temperatures in the combustion zone. However, ultra-lean flames are susceptible to local flame extinction and quenching, leading to undesirable characteristics, such as, flame quenching, poor combustion efficiency, and acoustic combustion instabilities. Under distributed combustion conditions for gas turbine combustion, the addition of hydrogen to traditional hydrocarbon fuels show considerable potential of increasing lean flame stability and reduce  $\text{NO}_x$  emission. The enhanced lean flame stability allows stable ultra-lean combustion without any adverse effect on increased emissions of CO and UHC. Even though the addition of hydrogen may increase  $\text{NO}_x$  emission due to higher flame temperature, this can be offset by the ability to burn an overall leaner mixture so that lower thermal  $\text{NO}_x$  is produced [100] [101] [102]. Studies have been reported that describe the influence of hydrogen addition on flame stability and flame speed under fuel-lean condition in a swirl-stabilized flame [103]. The lean stability limit was extended significantly with the addition of hydrogen to hydrocarbon fuel in a combustor. The improved stability with hydrogen enrichment of the fuel was postulated to be from the direct result of higher OH, H and O radical concentrations in the resulting

flames [104] [105]. Higher  $\text{NO}_x$  levels have been reported in upstream region of the reaction zone with the addition of hydrogen, while nearly the same levels have been observed at further downstream positions in a premixed flame combustor for the same adiabatic equilibrium flame temperature condition [105].

Even though the role of hydrogen is well understood in theory, its practical application to combustors is still limited because hydrogen addition changes the fate of reaction zone significantly. In one of the studies, it was concluded that the effects of hydrogen addition on  $\text{NO}_x$  emissions vary according to the application [106]. Hydrogen addition to methane in shock tube lowered  $\text{NO}_x$  emissions; however, higher  $\text{NO}_x$  emissions were recorded for engine tests. Hydrogen addition to traditional hydrocarbon fuel in swirl-stabilized flames provides favorable effects, such as, lower emission of carbon monoxide and soot in a diffusion flame combustor. Then again, it sometimes has a negative effect on  $\text{NO}_x$  emission in premixed combustion system because the reaction zone is heated up by reduction in relatively cooler recirculation flow, especially with higher hydrogen addition and under lean burn condition [107]. The behavior of turbulent flame speed or ignition delay time may be highly non-linear with the change in fuel mixture composition. It is also anticipated that hydrogen provides many unique impacts on this behavior. This is due to its significantly different transport properties and flame speed as compared to methane fuel. To fully understand and predict different fuel mixtures of hydrogen and methane, it is important to gain more understanding of the relationship between fuel mixture composition and properties, such as, flame speed, ignition and chemical delay times [108]. Detailed evaluation of

different mixture behaviors have been carried out with special focus on combinations of hydrogen, carbon monoxide, and methane [109] [110].

Hydrogen enrichment has been examined on CDC in a reverse flow configuration for hydrogen enrichment of 4% and 8% by mass with air inlet temperature of 300K. The investigation showed that addition of hydrogen to methane increased NO emission in the non-premixed case, while CO emission decreased with the addition of hydrogen for both premixed and non-premixed modes [111]. Minimal effect of hydrogen addition was observed on NO emissions in premixed combustion case [111].

The objective of this section is to examine the role of amounts of hydrogen addition to methane fuel in a swirling colorless distributed combustor under premixed and non-premixed combustion modes with emphasis on reaction distribution, reaction location, and stability issues arising from different flame velocities of methane and hydrogen (hydrogen in air flame speed is  $\sim 2.8$  m/s while methane in air flame speed is  $\sim 0.4$  m/s [112]). Hydrogen enrichment effect is examined here with different amounts of hydrogen enrichment; up to 15% by mass with air preheated to 600K, as this degree of air preheats is more relevant to air intake temperature in gas turbine combustors. The results are reported on pollutants emission and global features of the reaction zone (identified by flame marker from OH\* chemiluminescence) with view to evaluate the key features associated with hydrogen enrichment on the combustor performance under various operational conditions. Numerical simulation for hydrogen enrichment of methane has been performed using perfectly stirred reactor approach and compared to experimental data in an effort to better predict NO emissions.

### 5.2.1. Experimental Conditions

The investigations performed on experimental combustor were aimed at comparing the performance of combustor under different hydrogen enrichment conditions to the methane fuel. The combustor performance can then be evaluated for defined hydrogen enrichment to methane fuel at different equivalent ratios. Table 5-2 summarizes the investigations reported here along with the variables manipulated for each investigation. The case name indicates fuel injection method, so that ATP and ATF indicate premixed and non-premixed combustion mode, respectively. The effect of thermal loading and equivalence ratio from the hydrogen addition is reported here.

Table 5-2 Experimental Parameters for Hydrogen Enrichment

<b>Case No.</b>	<b>Hydrogen addition (% mass)</b>	<b>Heat Load (kW)</b>	<b>Equivalence Ratio</b>	<b>Variable</b>
ATP	0% - 15%	4.72	0.6	Hydrogen Enrichment
ATF1	0% - 15%	4.72	0.6	Hydrogen Enrichment
ATP	0%	6.25-3.9	0.8-0.5	Equivalence ratio
ATPH8	8%	6.25-3.9	0.8-0.5	Equivalence ratio

### 5.2.2. Results and Discussion

#### 5.2.2.1. *Role of Hydrogen Enrichment*

The experimental investigations were focused on examining the combustor performance behavior with different amounts of hydrogen addition to the methane fuel in order to develop an understanding of the characteristics of flames with hydrogen enrichment. It is to be noted that hydrogen has a higher flame speed as compared to methane which can lead to stability issues. Also, the higher adiabatic flame temperature

with hydrogen addition may lead to higher NO<sub>x</sub> emission. Air preheating was employed to simulate air temperature at inlet to the gas turbine combustor. The heat load and equivalence ratio matched the optimum operational conditions reported for the combustor using pure methane fuel with air preheats [36] and as shown in section 4.6. Adiabatic flame temperature with different amounts of hydrogen enrichment was calculated using NASA Chemical Equilibrium with Applications software. Table 5-3 summarizes the enrichment amounts examined (both by mass and by volume basis) along with the respective calculated adiabatic flame temperatures.

Table 5-3 Hydrogen enrichment amount and adiabatic flame temperature

<b>Hydrogen addition (% mass)</b>	<b>Hydrogen addition (% volume)</b>	<b>Adiabatic flame temperature (K)</b>
0%	0%	1876
4%	25%	1886
8%	41%	1899
10%	47.1%	1903
15%	58.5%	1915

Increase in hydrogen enrichment increased the calculated adiabatic flame temperature significantly. This is attributed to higher temperatures encountered with hydrogen combustion. Also, for hydrogen enrichment of 8%, 10% and 15%, the flame is governed by hydrogen behavior as it volumetrically equal to about half the fuel supplied to the combustor, which contributes to the higher adiabatic flame temperatures.

Emissions of NO and CO were recorded for each percentage of hydrogen addition to the methane fuel at different condition to result in a total thermal load of 4.72 kW and an energy release intensity of 27 MW/m<sup>3</sup>-atm. Figure 5-14 shows the emission

levels with different amounts of hydrogen addition to the fuel for premixed and non-premixed combustion cases. The NO emission data obtained from premixed combustion case indicates that addition of hydrogen slightly increases the NO emission from 4.4 PPM (for pure methane case) to 5.2 PPM (with 15% hydrogen addition by mass to the methane fuel). On the other hand, CO emission decreased dramatically by almost 50% with 15% hydrogen addition to the methane fuel as compared to the baseline case of methane fuel. Non-premixed combustion showed similar behavior, wherein the NO emission increased while the CO emission decreased. The difference in emission shown in Figure 5-14 left and right is related to less than adequate mixture preparation obtained through mixing between air, hot active species and fuel in the non-premixed case (right figure) as compared to premixed case (premixed fuel and air mixture that is then mixed with the hot reactive gases, left figure).

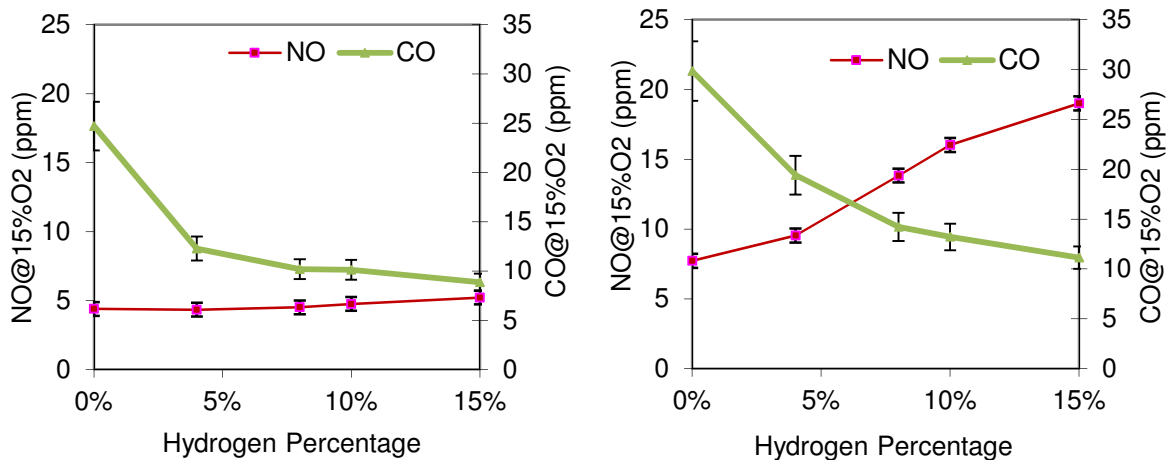


Figure 5-14 NO and CO emissions with different amounts of hydrogen addition (by mass) to methane fuel (left: premixed, right: non-premixed).

The position of the reaction zone (captured via OH\* chemiluminescence) moved gradually with increase in hydrogen addition to the methane fuel. Figure 5-15 shows the

OH\* chemiluminescence intensity distribution for hydrogen addition under both premixed and non-premixed conditions. For premixed cases (ATP), the flame moved upstream closer to the air/fuel injection location. However, with the addition of about 8% H<sub>2</sub> to the methane fuel the reaction zone location was not altered any further into the air/fuel injection port and that no flame flashback occurred with this mode. This can be attributed to high injection velocities of about 96 m/s, which is much higher than the flame speed of hydrogen fuel so that the flame could not be stabilized at that location. Also no change in the reaction zone with time (flame fluctuations) was observed as the reaction was extremely stable for each case reported here. The flame also moved upstream for the non-premixed combustion case (ATF1) closer to the fuel injection port with the increase in hydrogen percentage to the fuel. Similar to that found for the premixed case for hydrogen addition of 8% (by mass) to the methane fuel, the flame location did not move further upstream with further increase in hydrogen addition. This could be explained by the lack of adequate mixing between the fuel and air for the non-premixed case to prevent the flame moving further upstream.

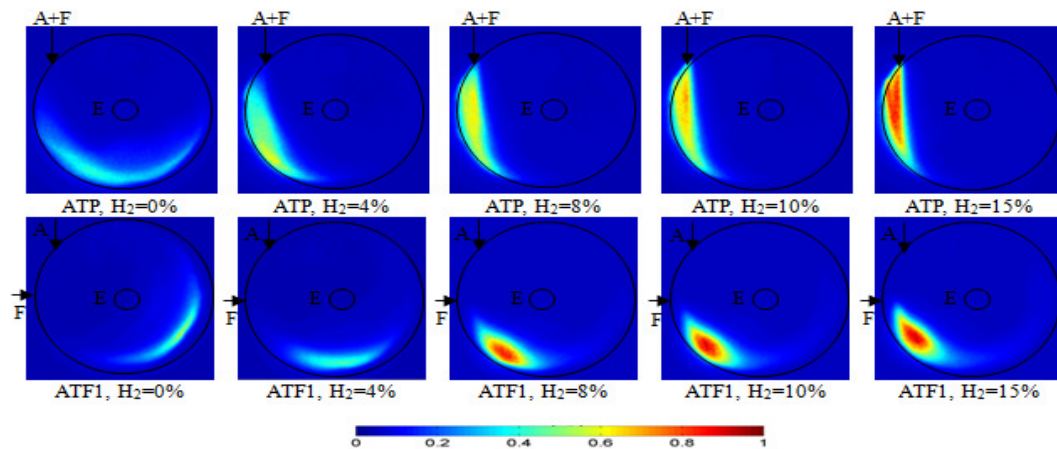


Figure 5-15 OH\* chemiluminescence intensity distribution for different H<sub>2</sub> enrichment

The same trend for OH\* chemiluminescence was observed when the exposure time was reduced to 50 $\mu$ s instead of 50ms, and the gain was increased to 850 instead of 70. Smaller exposure time allow instantaneous OH\* value rather than integrated value over a longer time period. The OH\* formation is seen to start at the bottom left in the methane case. Increase in hydrogen enrichment revealed that the OH\* formation started earlier as seen from the detected OH\* formation, moving upstream and taking the shape of the inlet air/fuel mixture jet, see Figure 5-16. OH\* chemiluminescence did not show any fluctuations or shift for this exposure time.

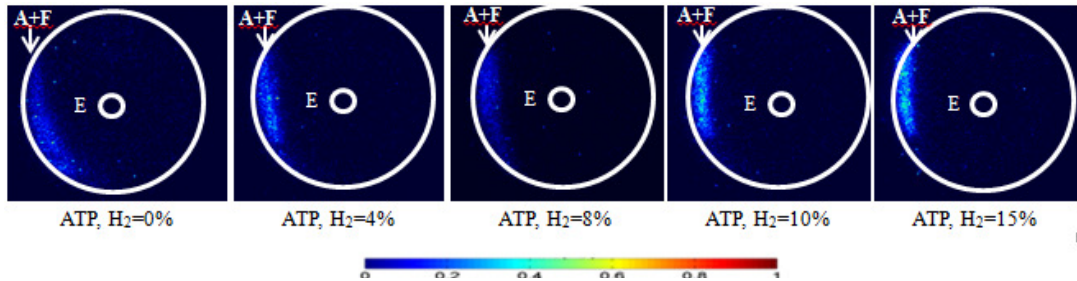


Figure 5-16 Instantaneous OH\* chemiluminescence intensity distribution for different H<sub>2</sub> enrichment

Global imaging of the flames obtained at short exposure times with different amounts of hydrogen enrichment (percentage) did not show any flame fluctuations. In all of the cases, the exhibited flames were colorless with no visible flame observed. The glow resulting from the background insulation did not change much with the change in hydrogen addition percentage to the fuel as seen from Figure 5-17. These images were obtained with camera f-stop setting f-10. The exposure time was automatically determined and is indicated beneath every image.

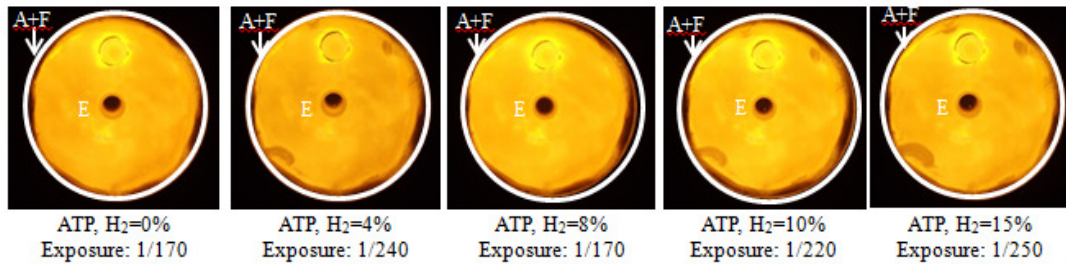


Figure 5-17 Global images for different H<sub>2</sub> enrichment

#### 5.2.2.2. Variation of Equivalence Ratio

To further evaluate the effect of hydrogen addition to methane fuel on combustion, methane enriched with 8% hydrogen (by mass) was used and the combustor operated at different equivalence ratios at a nominal thermal load of 6.25 kW and nominal energy release intensity of 36 MW/m<sup>3</sup>-atm. The resulting pollutants emission levels were compared directly with the pure methane case in order to examine the performance over the operational range. Figure 5-18 shows the emission of NO and CO for the premixed combustion case. It can be seen that hydrogen addition to methane fuel resulted in a slightly higher NO emission at all the operational conditions examined here. In contrast, remarkably low CO emissions resulted from the addition of hydrogen to the fuel. At equivalence ratio of 0.5 the CO emission from pure methane is extremely high (650 PPM) indicating incomplete combustion. However, with hydrogen addition, keeping the total thermal load constant, the CO emission was only 9 PPM. Such a large decrease in CO emission indicates improved or complete combustion of fuel at lean combustion conditions. This provides the direct benefit of hydrogen addition to the fuel to reduce emissions in addition to alleviating combustion instabilities that are often encountered under lean premixed combustion conditions. For pure methane case, at

equivalence ratio of 0.5, NO emission was 2.2 PPM while CO emission was 650 PPM. When the fuel was modified to 92% methane, 8% hydrogen (by mass), the resultant emissions were 3.2 PPM NO and 9 PPM CO. Note that the addition of hydrogen to methane fuel also allowed the combustor to operate at lower equivalence ratio with the result of even lower emissions. The lower flammability limit for hydrogen enriched methane was found to be at an equivalence ratio of 0.33. Without hydrogen enrichment, the lean flammability limit was found to be at an equivalence ratio of 0.4.

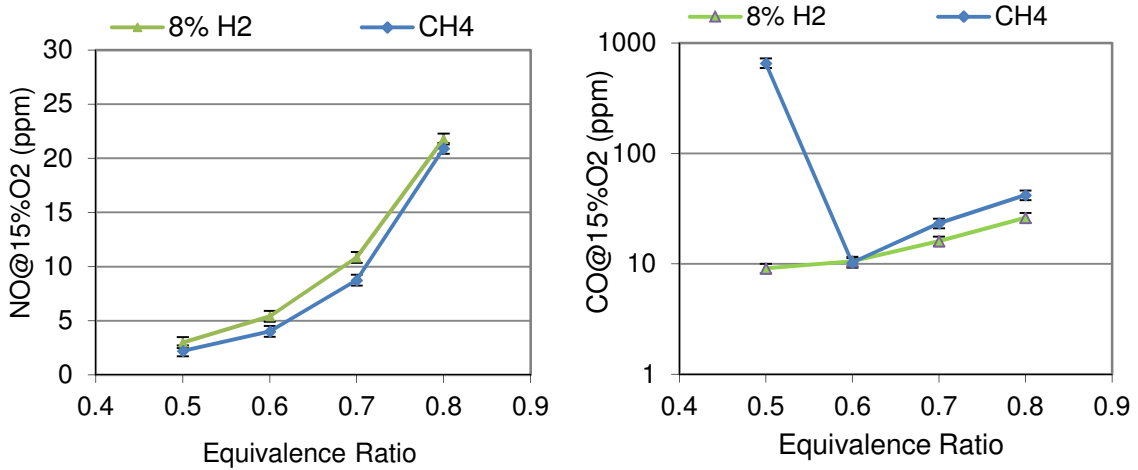


Figure 5-18 NO and CO emissions at different equivalence ratios

The OH\* radical chemiluminescence intensity distribution is shown in Figure 5-19. The reaction zone is spread out in the form of the inlet jet. Note that the reaction zone location did not vary much with change in equivalence ratio. However, the chemiluminescence intensity decreased with decrease in equivalence ratio. It is worth noting that OH\* chemiluminescence showed no fluctuation, indicating improved stability of the flame even at lower equivalence ratios. The reaction zone shape is different than that obtained with pure methane fuel case, wherein more distributed flame was observed (occupying a larger volume of the combustor) having a crescent

shape opposite to the fuel injection location as shown in section 4.6. The difference in the reaction zone shape and size can be attributed to the different reaction kinetics, ignition delay and flame speed of hydrogen as compared to methane. Nevertheless, pollutants emission from the combustor and stability were not hampered much while the combustion stability increased marginally with low emissions for operation at lower equivalence ratios.

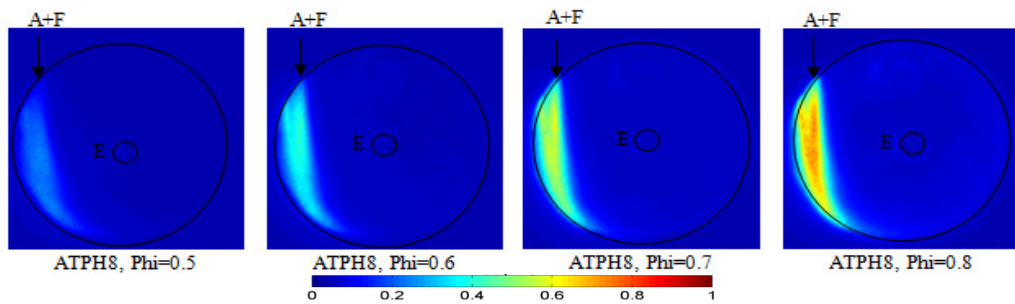


Figure 5-19 OH\* chemiluminescence intensity distribution under premixed combustion

The same trend for OH\* Chemiluminescence was observed when the exposure time was reduced to 50 $\mu$ s instead of 50ms, and the gain was increased to 850 instead of 70. The OH\* production took the shape of the inlet air/fuel jet. As the equivalence ratio increased, the OH\* production maintained its location, however the recorded intensity increased as shown in Figure 5-20. OH\* Chemiluminescence did not show any fluctuations or shift for this exposure time.

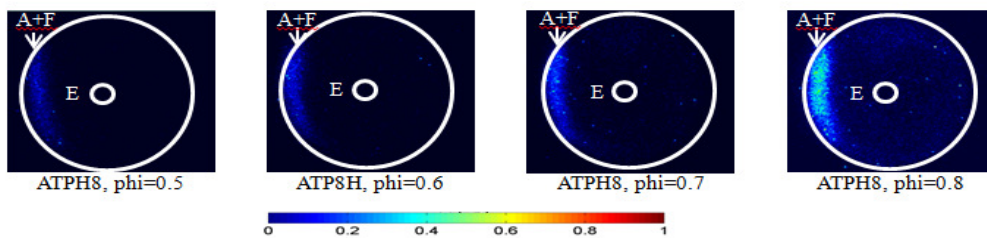


Figure 5-20 Instantaneous OH\* chemiluminescence intensity distribution under premixed combustion

### 5.2.2.3. Numerical Simulations

Emission of pollutants was also calculated using CHEMKIN-PRO software assuming perfectly stirred reactor and GRI 3.0 mechanism [85] for reactor dimensions that matches the current combustor. Two cases of pure methane as fuel and 8% hydrogen enriched methane are reported here. Figure 5-21 shows NO emissions at equivalence ratios of 0.5 to 0.8.

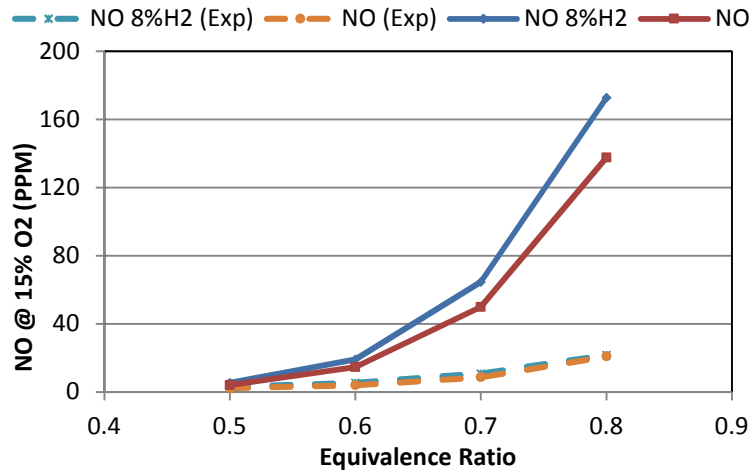


Figure 5-21 Calculated NO emissions using GRI 3.0 (CHEMKIN-PRO)

From Figure 5-21, it can be seen that the predicted emissions are much higher than the experimentally measured values. However, from the numerical simulations results, a simple correlation was developed relating NO emissions for 8% hydrogen enrichment case to that of pure methane. This correlation is given below:

$$NO_{8\%H_2} = 1.2516 \times NO_{CH_4} + 0.9322 \quad \text{(Equation 5-1)}$$

with a coefficient of determination,  $R^2=0.9999$

The above equation was used to predict NO emissions for the 8% hydrogen enrichment case using the measured NO emissions for the pure methane case. The result is plotted in Figure 5-22 against the measured emissions for 8% hydrogen enrichment case. It can be seen that the measured emissions and predicted ones agree quite favorably.

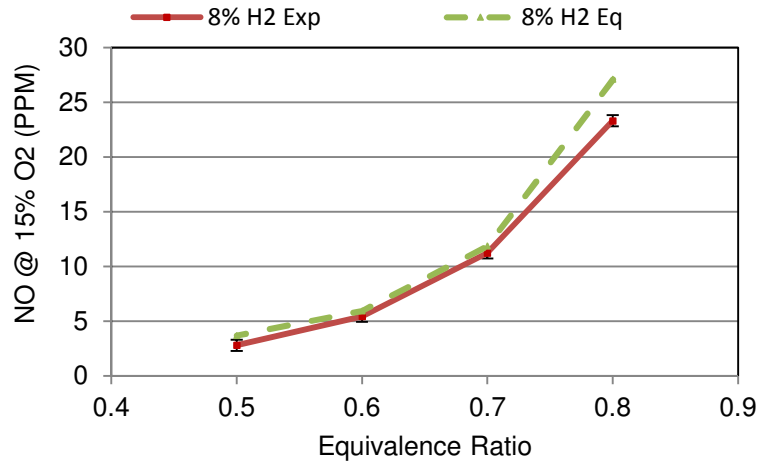


Figure 5-22 NO emissions from experimental and numerical work

This agreement indicates the possibility of using chemical kinetics software to obtain a relation between NO emission of the hydrogen enriched methane and NO emission of methane. Then this relation can be used to predict the actual NO emission of the desired fuel using the actual NO emission of methane, thus help reduce experimental time and cost.

### 5.2.3. Summary

Results obtained with hydrogen enrichment to methane fuel showed the direct benefits of low pollutants emission with the combustor design incorporating swirling flow. The results showed that enriching methane with hydrogen results in increased

fuel lean stability limits and reduced pollutants emission. Novel premixed combustion design using swirling flow has yielded low pollutants emission with extremely stable combustion with hydrogen addition. Though NO increased slightly with the increase in hydrogen addition to the fuel, the combustor was able to produce substantially lower CO emissions, thus allowing the combustor to operate at lower equivalence ratios with improved combustion efficiency. The OH\* chemiluminescence intensity distribution revealed the reaction zone move upstream with increase in hydrogen addition to the fuel until about 8% hydrogen enrichment. Further increase in hydrogen enrichment did not alter the flame location. The flame flashback phenomenon was mitigated with high injection velocities to inhibit the flame from traveling upstream. No flame fluctuations within the flame zone were recorded with increase in hydrogen enrichment to the methane fuel. The large difference between the flame speeds of methane and hydrogen did not cause any flame instabilities. The role of hydrogen is more evident in non-premixed combustion case as observed from the increase in NO emission and decrease in CO emission as compared to the premixed combustion case.

Results obtained with 8% hydrogen enriched methane fuel under different equivalence ratios showed great promise for applications. Novel premixed combustor design demonstrated low emission of both NO and CO with hydrogen enrichment of methane fuel. The combustor demonstrated 3.2 PPM of NO and 9 PPM of CO at an equivalence ratio of 0.5. This is a significant reduction as compared to the methane fuel only (2.2 PPM NO and 650 PPM CO). This behavior indicates that the combustor is able to operate at leaner conditions without suffering from lean combustion instabilities or incomplete combustion. The OH\* chemiluminescence intensity distribution with 8%

hydrogen enrichment for the premixed combustion mode revealed that the reaction zone location is not impacted with the change in equivalence ratio. However, the flame was observed to be less volume distributed as compared to pure methane case. The addition of hydrogen improved the lean stability limit. Global imaging showed no observable unsteadiness in the flame with hydrogen addition.

A correlation for NO emission with the 8% hydrogen enrichment case was developed using CHEMKIN-PRO and the results provided good agreement with the experimental data indicating the possibility of good prediction on emissions from different hydrogen enrichments amount using measurements from pure methane.

### 5.3. Heavier Fuels

In the previous sections, the combustor demonstrated stable operation with low emissions for both diluted methane and hydrogen enriched methane. To further evaluate the fuel flexibility of the combustor, operation with three different fuels is examined in this section and the results are combined with those of methane, diluted methane, and hydrogen enriched methane fuels with view to develop fuel flexible colorless distributed combustion. The three fuels are discussed in the next subsections.

#### 5.3.1. Fuels Examined

##### 5.3.1.1. *Propane*

Propane is considered to be the simplest hydrocarbon whose combustion characteristics are close to the heavier and more complex (liquid) hydrocarbon fuels [4] while avoiding the issues on atomization and vaporization of the liquid fuel.

Consequently, propane can be used as an indicator for heavier hydrocarbon fuels behavior in the combustor. Also, propane is used in various applications as liquid petroleum gas (LPG) in domestic, industrial and transportation sectors.

#### 5.3.1.2. *Ethanol*

Bio-fuels offer significant interest as an alternative for fossil fuels. The use of bio-fuels in gas turbine engines offers a good viable solution for continually decreasing fossil-fuel reserves and the associated environmental concerns from their combustion. Bio-fuels are alternative fuels, made from renewable energy sources. The desire for energy independence, foreseen depletion of nonrenewable fuel resources and fluctuating petroleum fuel costs has created a strong desire for the development and implementation of bio-fuels. The term bio-fuel is referred to alternative fuel which is produced from bio-materials, such as, biomass and wastes. Such fuels include bio-diesel, bio-ethanol, bio-methanol, pyrolysis oil, biogas, synthetic gas and hydrogen.

Ethanol has already been examined in gas turbines and found to be favorable as a sustainable and renewable fuel. Ethanol produced from sugarcane is already being used in the transportation sector. The results show this fuel to be a more sustainable source of renewable liquid fuel compared to other bio-fuel crops. Ethanol lower lubricity and low heating value dictate that modifications have to be performed to most currently used gas turbine and combustion systems in order to use it as a fuel [113]. The environmental benefits of using biofuels compared to traditional fossil fuels are carbon neutral operation and reduction in the net amount of carbon dioxide emitted into the atmosphere. Carbon dioxide emitted from the burning of a fuel made from plants, will

be re-absorbed by plants during the photosynthesis process, resulting in no net carbon dioxide emissions excluding the process footprint since the carbon dioxide will also be emitted through the planting, growing, and harvesting of the crop used to make the bio-fuel. Fossil fuels, on the other hand, are produced from beneath the surface of the earth, and when burned they emit carbon dioxide without practical means of removing that carbon dioxide from the atmosphere. This does not mean that the CO<sub>2</sub> cannot be removed from the atmosphere via natural and industrial means, but the burden of removing large amounts of CO<sub>2</sub> continues to grow as more and more fossil fuels are used in ever increasing power demands from power generation systems. Experimental and numerical studies of the combustion and oxidation of ethanol has been performed and provided numerous new data which are an appropriate starting material for modeling studies on the oxidation and combustion of ethanol [114]. Ethanol has been also investigated as an alternate fuel for diesel engines [115].

#### 5.3.1.3. *Kerosene*

Other viable biofuels can also be used in gas turbine applications. Bio-diesel, which is a surrogate fuel for aviation and land based applications have been used as an environmentally friendly fuel. Kerosene based fuels with different additives are widely used, such as, JP-8, JP-10 and Jet-A. All of these fuels are used for propulsion applications in various types of gas turbine engines. Note that some additives are added to the fuels to inhibit icing, corrosion and improve combustion characteristics. The combustion of kerosene and the various surrogates used to simulate kerosene have been examined with emphasis on ignition and oxidation [116]. Kerosene combustion has

been investigated numerically and experimentally in swirl flames [117]. However, for all of the liquid fuel research discussed, atomizers have been used to prepare the liquid fuel into large number of smaller size droplets for improved combustion.

In this section, fuel flexibility of the CDC combustor is investigated using different fuels, including, diluted methane, hydrogen enriched methane, propane, ethanol and kerosene with emphasis on pollutants emission and combustor performance. For the fuels investigated, the air and fuel injection into the combustor were not modified. The results are reported on pollutants emission and global features of reaction zone (identified by OH\* chemiluminescence) with view to evaluate the key features associated with each fuel under various operational conditions. A comparison with methane combustion has been conducted to outline the fuel flexibility and flame stability of the combustor.

### 5.3.2. Liquid Fuel Introduction

Liquid fuels were supplied to the combustor using a syringe pump with accuracy of 0.35%. The fuel was directly introduced into the preheated air stream at an upstream location of the combustor in a premixed combustion mode. No atomization or fuel spray method was used to outline the combustor ability to operate on different fuels without any change of its components. Other researchers have used thin liquid fuel film combustion demonstrating the ability of liquid fuel combustion without the need for atomizers using a mixture of methane and methanol, and heptane [118]. This approach was not adopted here as the injection velocity was much higher (96 m/s) compared to the injection velocities for film formation (1-10 m/s [118]).

The inlet air temperature to the combustor was preheated to 600K to simulate elevated air temperatures at inlet to the combustor (simulating outlet temperature from a characteristic gas turbine compressor). The preheating of the inlet air affects the combustion kinetics and pollutants emission as discussed earlier.

### 5.3.3. Experimental Conditions

Table 5-4 summarizes the fuels reported here along with their calorific value along with the Reynolds number at the injection point. For each case the fuel flow rate was changed to allow combustor operation at different equivalence ratios. The respective case name indicates the combustor geometry (e.g., ATP) and the fuel used. The inlet air to the combustor was preheated to 600K to simulate gas turbine combustion conditions.

Table 5-4. Experimental parameters for Different Fuels

<b>Case No.</b>	<b>Fuel</b>	<b>CV [kJ/Kg]</b>	<b>Composition</b>	<b>Re</b>
ATP	Methane	50,000	CH <sub>4</sub>	~15500
ATP-DM	Diluted Methane	19,750	36% CH <sub>4</sub> – 64% N <sub>2</sub>	~16500
ATP-H	Hydrogen Enriched Methane	55,600	92% CH <sub>4</sub> – 8% H <sub>2</sub>	~15600
ATP-P	Propane	46,350	C <sub>3</sub> H <sub>8</sub>	~14500
ATP-E	Ethanol	28,000	C <sub>2</sub> H <sub>5</sub> OH	~14700
ATP-K	Kerosene	43,000	~C <sub>12</sub> H <sub>26</sub>	~14300

### 5.3.4. Results and Discussion

The experimental investigations were focused on evaluating the combustor performance operating with different fuels. Each fuel has its characteristic flame speed and adiabatic flame temperature which will affect the combustion characteristics, including flame stability and pollutants emission. Adiabatic flame temperature for

different fuels used has been calculated using NASA Chemical Equilibrium with Applications software. Figure 5-23 summarizes the calculated adiabatic flame temperatures for the fuels examined. Diluted methane exhibited a lower adiabatic flame temperature due to the diluent nitrogen acting as a heat sink. Such lower flame temperature is expected to result in lower thermal  $\text{NO}_x$  emission.

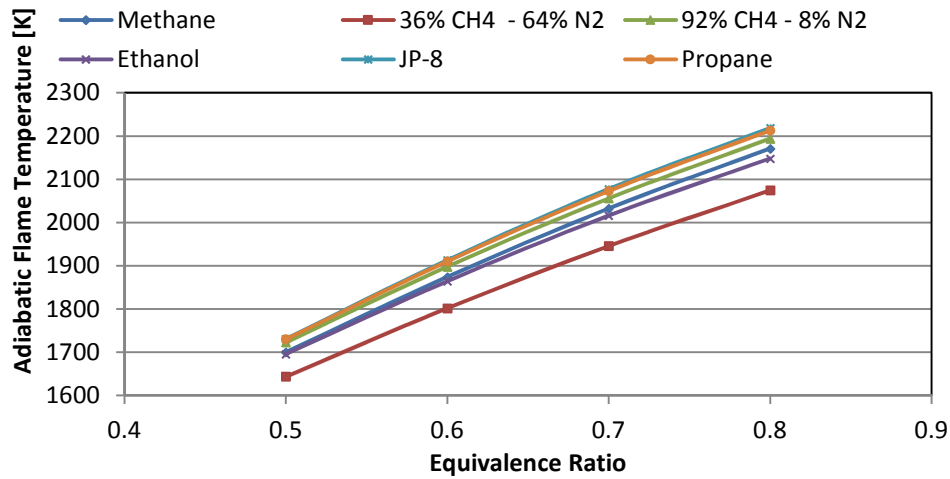


Figure 5-23 Calculated adiabatic flame temperature for the different fuels used

Different researchers have measured the laminar flame speed of the discussed fuels. Details on the techniques used and their equivalence can be found in the respective references [93], [98], [119], [120], [121], and [122]. Figure 5-24 shows the laminar flame speed for these fuels. Data for N-Dodecane was used for kerosene. For diluted methane, 40% methane–60% nitrogen was chosen as an approximation for the actual mixture used. Hydrogen enriched methane (8% hydrogen by mass) is translated to 40%  $\text{H}_2$  - 60%  $\text{CH}_4$  by volume. The laminar flame speed varies widely, with the flame speed of kerosene and ethanol almost three folds higher than that of diluted methane. Though the combustion is essentially turbulent under CDC conditions, however, the flame speeds are expected to scale similarly. The high flame speed encountered with

kerosene, ethanol and hydrogen enriched methane might result in problems with flame flashback and combustion instabilities.

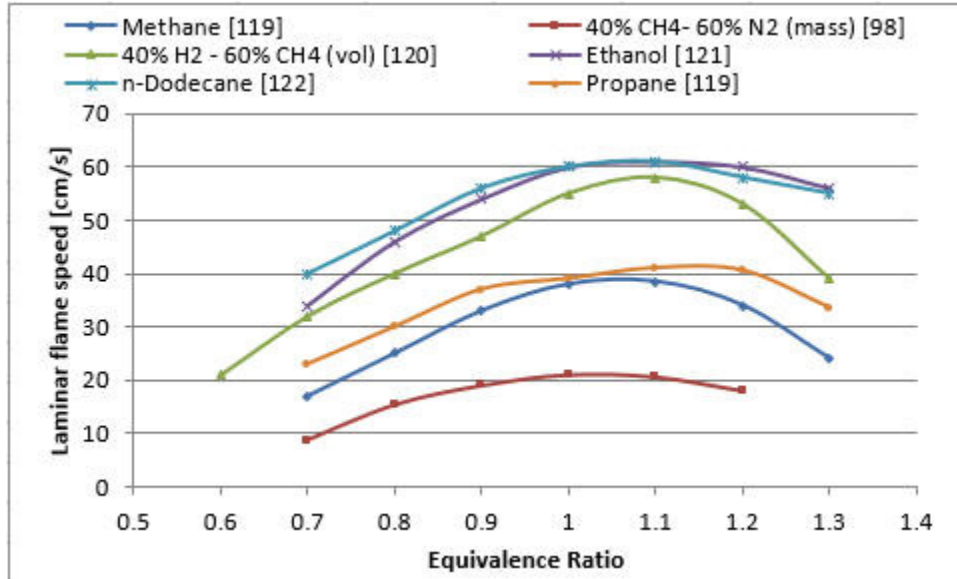


Figure 5-24 Laminar flame speed for the different fuels used

Emissions of NO and CO were recorded for the different fuels used. For all of the fuels examined, the heat load was kept constant at 6.25 kW (having heat (energy) release intensity (HRI) of 36 MW/m<sup>3</sup>-atm) at an equivalence ratio of 0.8. Air flow rate was adjusted to furnish the combustor with the adequate air requirement for each fuel used. Fuel flow rate was varied to allow changes of equivalence ratios ranging from 0.8 to 0.5 and the subsequent overall emissions were then measured. Figure 5-25 shows the NO emission levels resulting from operating the combustor with different fuels for novel premixed combustion configuration. The NO emission data obtained for the premixed combustion case shows that ultra-low emissions were demonstrated regardless of the fuel used. Figure 5-25 shows that there is a dependency of NO emission on the type of fuel used. Diluted methane provided low NO emissions across the range

as compared to the other fuels examined. On the other hand, kerosene, and propane offer somewhat higher NO levels than the other fuels examined. This behavior can be attributed to higher adiabatic flame temperature of these fuels as compared to diluted methane case (see Figure 5-23). It is also conjectured that kerosene (as well as ethanol) will require some time to atomize and vaporize the liquid fuel for the combustion which incur a role in increased emissions.

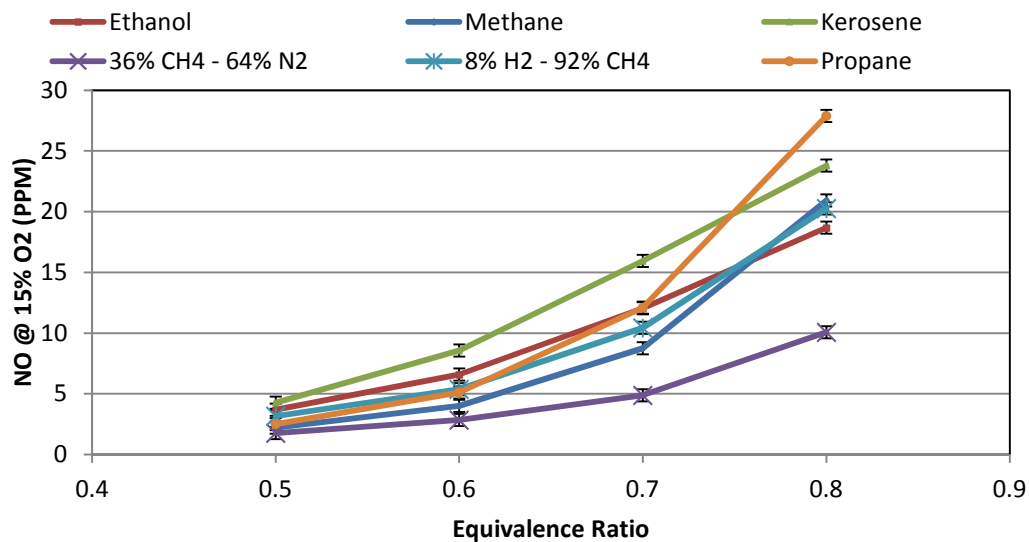


Figure 5-25 NO emission for the different fuels used

At equivalence ratio of 0.6, recorded NO emissions varied from 3 PPM (for diluted methane) up to 7.5 PPM (for kerosene). Thus, less than 7.5 PPM of NO emission is demonstrated regardless of the fuel used. This is a substantial benefit as it reduces the complexity of the fuel introduction system and still operate the combustor with different fuels without any change in the combustor geometry and flow configuration. Also, less than 4.5 PPM of NO was demonstrated at an equivalence ratio of 0.5 regardless of the fuel used and without the use of any atomizers or fuel spray for the

liquid fuels. These emissions are substantially lower than the current EPA regulations of 42 PPM for units larger than 250 MW operating on fuels other than natural gas [5].

The CO emissions were also obtained for the above fuels and the results are shown in Figure 5-26. For different fuels, CO emission decreased with decrease in equivalence ratio until a minimum was reached, and then it started to increase again. The decrease in CO emission is attributed to excess oxygen that helps in complete conversion of CO to CO<sub>2</sub>, while the increase near the extinction limit is attributed to lower temperatures and weaker flames found near the extinction limit. Comparing CO emissions of methane and hydrogen enriched methane, one can see the important role of hydrogen in stabilizing the flame and reducing CO emissions as enriching the methane with 8% hydrogen by weight decreased CO emissions from ~100 PPM to only 9 PPM at an equivalence ratio of 0.5. Also it is observed that liquid fuels produce somewhat higher CO emission as compared to methane fuel and its variants. This can be attributed to the more time required for mixture preparation since the time required for liquid fuels to atomize and vaporize, which might exceed the residence time in the combustor.

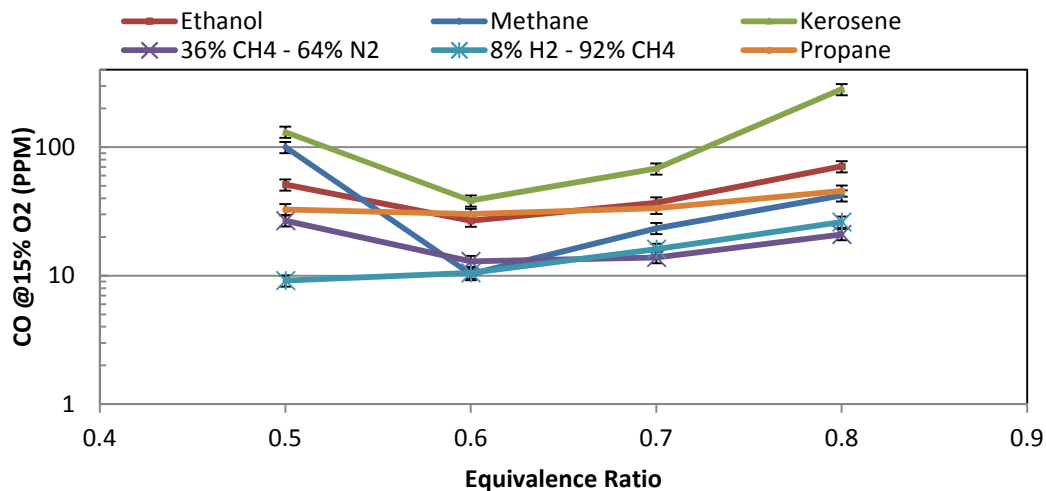


Figure 5-26 CO emission for the different fuels used

However, at an equivalence ratio of 0.6, CO emission of about 10 PPM was demonstrated for methane based fuels, while emission less than 40 PPM was demonstrated for liquid fuels and propane. CO emissions are expected to further decrease upon operation of the combustor at elevated pressures.

The radical intensity distribution of OH\* chemiluminescence was acquired and the results are shown in Figure 5-27, Figure 5-28, Figure 5-29, and Figure 5-30 for the different fuels used. OH\* chemiluminescence distribution for both methane and diluted methane show that the reaction zone was found around the entry jet, particularly at high equivalence ratios. This suggests the use of multiport fuel injection into the combustor. In the case of diluted methane, the reaction started downstream as compared to methane since diluted methane is characterized by a lower flame velocity as compared to methane, see Figure 5-24. Also, the reaction intensity decreased and moved further downstream with decrease in equivalence ratio, see Figure 5-27. This behavior is attributed to more favorable mixture preparation with small amounts of fuel injection but lacked proper mixture preparation using large amounts of fuel with the same injection speed of air. It appears there is a lack of distributed mixture in the combustor at higher equivalence ratios as a result of lack of entrained reactive species to the fuel (and also air) prior to decayed velocity of the jet to form a flame. It is for this reason one can see the presence of a flame crescent at farther downstream of the fuel injection point. At low equivalence ratios, the reaction zone moves farther downstream due to the lower flame speeds. The shift downstream allows for longer mixture preparation time prior to mixture ignition leading to a better mixture distribution for enhanced reaction distribution to result in a more dispersed OH\* chemiluminescence.

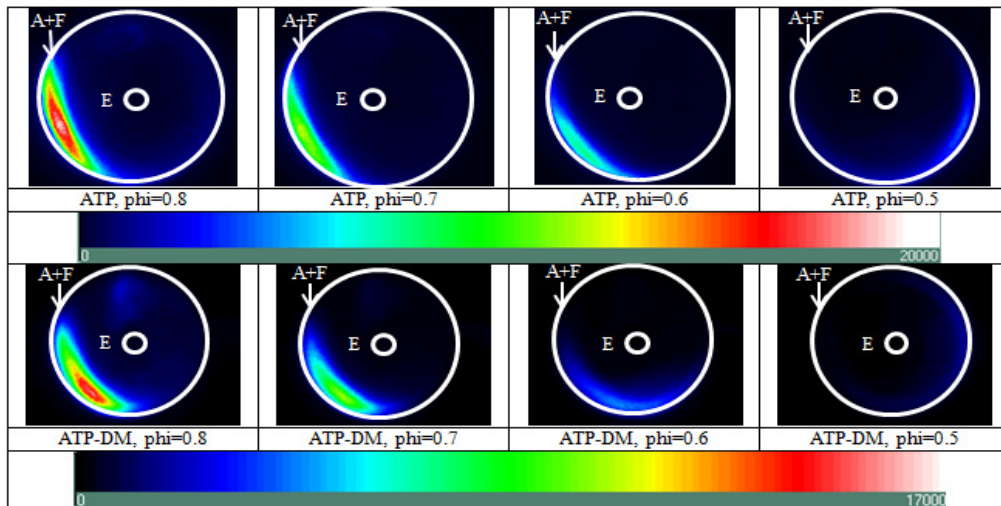


Figure 5-27 OH\* chemiluminescence for methane and diluted methane flames

On the other hand, for hydrogen enriched methane, the reaction zone (marked by OH\* chemiluminescence) takes the shape of the air jet itself with the reaction starting as soon as the fresh mixture is introduced into the combustor. This can be attributed to the higher flame velocity associated with hydrogen, as compared to methane, leading to the flame moving upstream towards the mixture injection location. The chemiluminescence intensity (reaction intensity) decreased with decrease in the equivalence ratio. However, the reaction zone did not move downstream with decrease in the equivalence ratio and this is in contrast to results from methane and diluted methane flames, see Figure 5-28.

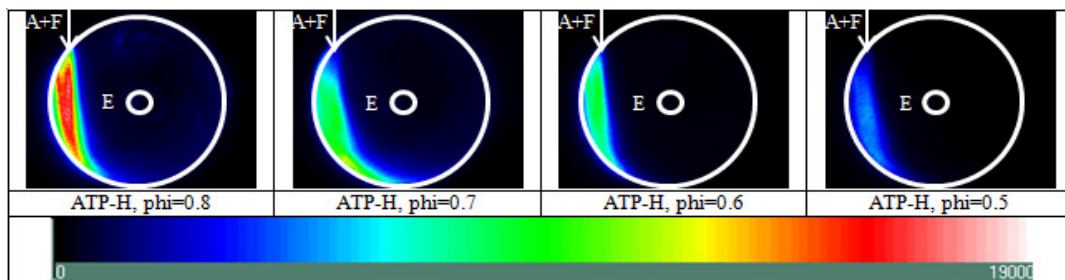


Figure 5-28 OH\* chemiluminescence for the hydrogen enriched methane flame

For propane, the reaction zone, similar to hydrogen enriched methane, takes the shape of the air jet itself with the reaction starting as soon as the fresh mixture is introduced into the combustor, see Figure 5-29, indicating that the reaction starts earlier as compared to methane case. The chemiluminescence intensity (reaction intensity) decreased with decrease in the equivalence ratio. Contrary to hydrogen enriched flame, the reaction zone moved downstream with decrease in the equivalence ratio but not to the same extent as exhibited from methane and diluted methane flames, see Figure 5-27, Figure 5-28, and Figure 5-29.

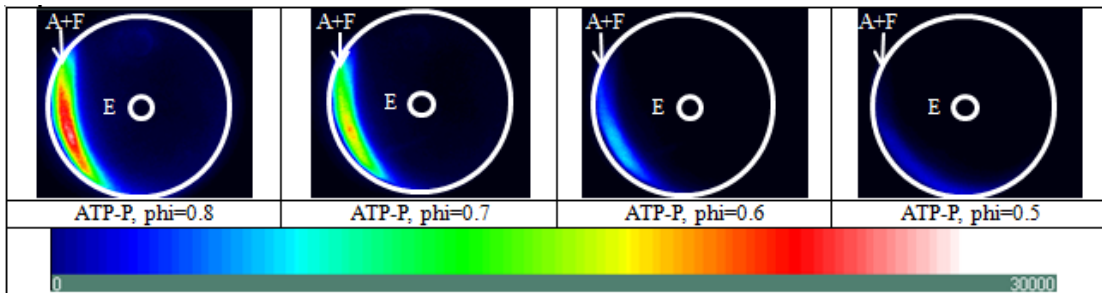


Figure 5-29 OH\* chemiluminescence for the propane flame

A similar trend was found with ethanol fuel wherein the reaction zone took the shape of the air jet entering the combustor. Early ignition of ethanol can be related to the oxygen content in the fuel that will decrease the mixing time required before ignition along with the high flame speed of ethanol. However, the reaction zone was found to extend further downstream as compared to hydrogen and propane. Also, for ethanol, the maximum intensity was found to be located downstream of the air jet as compared to that of hydrogen. The reaction zone did not move downstream with the decrease in equivalence ratio. For kerosene combustion, the reaction zone took the shape of the air jet with the maximum intensity near the inlet as compared to ethanol. Also, the reaction

zone moved downstream with the decrease in equivalence ratio. The OH\* chemiluminescence revealed that the fuels examined here demonstrated similar behavior globally in terms of reaction zone location with minor differences wherein the difference in flame speed as described in Figure 5-24 did not cause any flame flashback or combustion instability. This behavior outlines the ability of the swirl distributed combustor to handle different fuels with improved performance. It is noteworthy that the injection velocity and Reynolds number at injection point varied by about 8% from the base case of methane as the fuel, leading to minimum impact on the fluid mechanics behavior of the combustor with change in fuel prior to ignition.

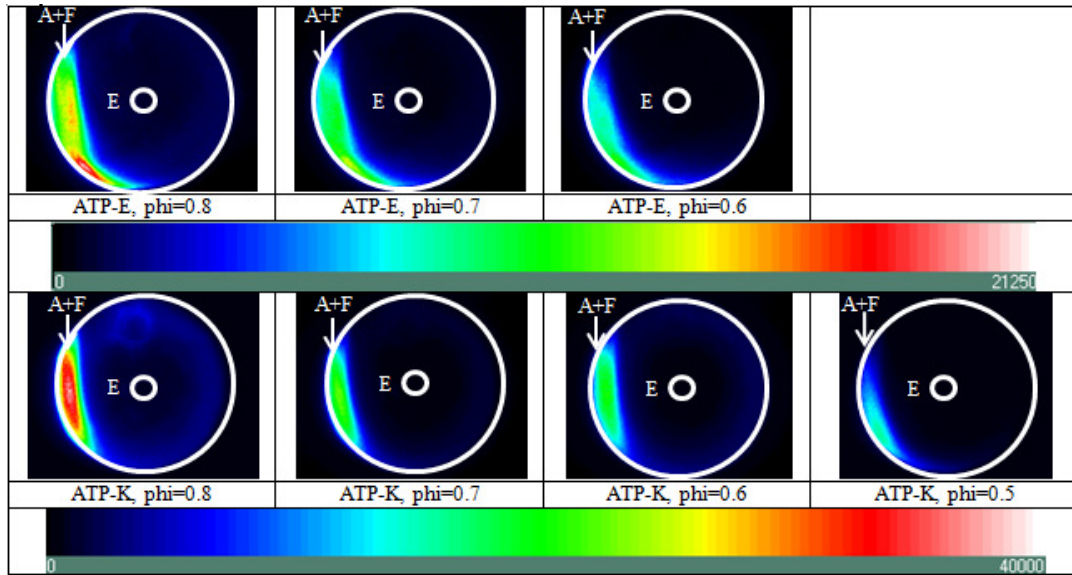


Figure 5-30 OH\* chemiluminescence for ethanol and kerosene flames

### 5.3.5. Summary

Results obtained with different fuels used here have demonstrated stable combustion and low pollutants emission from the combustor design that incorporated near distributed combustion using swirl flow in the combustor. The results showed direct

beneficial aspects of this design in terms of fuel flexibility and ultra-low pollutants emission using a range of fuels of different physical and chemical composition. Emissions less than 7.5 PPM of NO were demonstrated for all of the fuels used at an equivalence ratio of 0.6 regardless of their phase (gaseous or liquid) and calorific value. Note that the examined equivalence ratio of 0.6 is higher than that used in most gas turbine engines at full power. This is of significant importance for demonstrating fuel flexible operation as all of the experiments shown here were performed on the same combustor with no change in its geometrical parameters and without the use of any fuel atomizers for liquid fuel operation. The CO emission of about 10 PPM were demonstrated at the same equivalence ratio (0.6) for methane based fuels while liquid fuels exhibited somewhat higher CO emission (less than 40 PPM) as a result of the limited residence time available as compared to the time required for vaporization, mixing, and combustion of fuel, including complete CO to CO<sub>2</sub> conversion, with the liquid fuel. Less than 4.5 PPM of NO was demonstrated at an equivalence ratio of 0.5 regardless of the fuel used. Further enhancement in flowfield and reaction distribution to reach more favorable distributed reaction is expected to bring NO and CO emissions to near zero levels (~ 1 PPM).

OH\* chemiluminescence intensity distribution showed that the fuels examined herein demonstrated similar behavior globally in terms of reaction zone location with minor differences in the OH\* chemiluminescence contour distribution thus outlining the ability of swirl distributed combustor to handle different fuels with improved performance. The reaction zone was not concentrated but rather distributed over a portion of the combustor volume at lower equivalence ratios, which is more relevant to

gas turbine applications. Further enhancement in the flowfield design will help improve distributed combustion conditions. Difference in flame speed between the different fuels did not cause any instabilities or flame flashback phenomenon. Global imaging showed no observable unsteadiness in the flame for all of the fuels examined here.

#### **5.4. Biofuels for Energy**

In the previous sections, the fuel flexibility of the combustor was evaluated using different fuels (fossil and renewable). In this section, the performance of a new fuel (Butyl Nonanoate) is examined and compared to traditional aviation fuel (JP-8) and hydrogenated renewable jet (HRJ) fuel. Several papers exist in the literature that discuss the viability of different biofuels [123] [124] [125] [126]. The current interest from the commercial and military aviation sectors in alternative jet fuel stems from multiple factors including high conventional fuel prices, price volatility, lack of energy diversity, global climate impacts, and potential air quality benefits. Civil and military jet aircraft require a near-term fuel replacement to conventional petroleum based jet fuel that is a “drop-in” hydrocarbon substitute that functions with the existing aircraft infrastructure while meeting rigorous safety and quality standards. Such drop-in alternative jet fuel pathways can be broken into five broad categories: jet fuel from unconventional sources of petroleum such as oil sands, very heavy oils, and oil shale; synthetic jet fuel from thermochemical processes involving natural gas, coal, and/or lignocellulosic biomass such as Fischer-Tropsch (F-T) synthesis and pyrolysis; advanced fermentation, catalytic, and other means of converting sugars to jet fuel; hydro-processing of conventional oils to synthetic jet fuel; and conversion of calorific

liquids from micro-organisms to synthetic jet fuel [127]. Through both ground and flight tests, the USAF has already approved a 50% blend of F-T fuels with conventional jet fuels and the certification of a 50% blend of hydro-processed renewable oils with conventional jet fuel should be complete in the near future [128]. Commercial and military aviation have set ambitious alternative fuel and environmental targets for the next half century. The International Air Transport Association has set a goal of 10% alternative fuel use by 2017, carbon neutral growth in 2020, and a 50% decrease in aviation CO<sub>2</sub> emissions by 2050, relative to 2005 levels. In a detailed research on the viability of different alternative jet fuels, it was concluded that switchgrass F-T fuel and camelina HRJ have the potential to reduce life cycle greenhouse gas emissions by 60-80% [127]. Synthetic isoparaffin-rich fuels produced by hydro-processing camelina oil show great promise as “drop-in” alternatives to petroleum jet and diesel fuel. Recent evaluations of HRJ fuel derived from camelina oil indicate that the fuel performed just as well as petroleum based fuel but with lower exhaust and GHG emissions. Using updated estimates of camelina cultivation and commercial scale estimates of oil recovery and refining requirements, a life cycle GHG savings of 75 and 80% was estimated for camelina-derived HRJ and Green Diesel (GD) relative to their petroleum counterparts. Using data from recent field trials, GHG savings of >67% are achieved [129]. Also reduction in NO<sub>x</sub> emissions can be achieved via biofuels. On the other hand, CO emissions depended on the engine type [126]. The use of biofuels have also been extended to furnaces with emission reduction of both NO and CO [130]. A study on biofuel using T63 test engine revealed that there was minimal changes in CO emissions with slight increases in total hydrocarbon (THC) emissions (10%) at idle

with biodiesel concentrations of 20%. This increase was attributed to incomplete combustion of biodiesel at the low power setting. At the higher power conditions, there was little or no change in CO and THC. The addition of biodiesel had negligible effects on oxides of nitrogen ( $\text{NO}_x$ ) emissions for all of the test cases. This was expected, because the primary route for  $\text{NO}_x$  formation is via thermal  $\text{NO}_x$ , and the relative combustion temperature was not changed during the blends tests. Only slight reductions in oxides of sulfur ( $\text{SO}_x$ ) emissions were observed as the biodiesel concentration was increased, which was likely a dilution effect, because the biodiesel does not contain sulfur [131].

On the other hand, Butyl Nonanoate has not been used as a biofuel. It is characterized by a lower calorific value, higher viscosity and density. This fuel have been processed by Michigan State University. The characteristics of this novel fuel will be evaluated with view to use in gas turbines. The most important parameters are the ability of the fuel to be atomized (which depend on surface tension, viscosity, and density), along with the pollutants emission resulting from the combustion. These characteristics will be compared to JP-8 to determine the viability of using Butyl Nonanoate in gas turbine applications. The properties of Butyl Nonanoate, HRJ and JP-8 are listed below.

Table 5-5 Properties of Bio-Fuels

<b>Property</b>	<b>Butyl Nonanoate (BN)</b>	<b>JP-8</b>	<b>HRJ</b>
Calorific Value [kJ/Kg]	35,677	43,000	44,300
Density [Kg/m <sup>3</sup> ]	849-855	795	751
Kinematic Viscosity [mm <sup>2</sup> /s]	1.989 @ 23.6 °C	1.692 @ 20 °C	1.1 @ 40 °C
Surface Tension [N/m]	0.029 @ 25 °C	0.026 @ 25 °C	0.0264 @ 25 °C
Cetane Number	51.5	44.1	58

#### 5.4.1. Droplet Size and Atomization

Liquid fuel atomization is of critical importance for combustion, as larger droplet size will require more time to evaporate and mix before ignition, which leads to improper mixing and concentrated flames which shall be avoided to achieve distributed reactions and near zero emissions. Comparing the properties of Butyl Nonanoate to standard JP-8 properties, it was found that Butyl Nonanoate has higher surface tension, viscosity and density, leading to bigger droplet diameter compared to JP-8 for a given set of conditions.

To evaluate the size average and size distribution difference between both fuels, a standard spray nozzle was installed in the measuring volume of a Phase Doppler Droplet Particle Analyzer (PDPA). The liquid fuel tank was pressurized to an upstream pressure of 40 Psi to ensure same operational conditions for all of the experiments. Both fuels were tested multiple times successively and separately. For each experiment, 10,000 droplets are measured and the size distribution is obtained. Average diameters based on number, area, volume and volume to area were calculated from the obtained

histogram and are used to evaluate the average droplet size diameter for both fuels. Figure 5-31 shows the nozzle used with measurement volume.

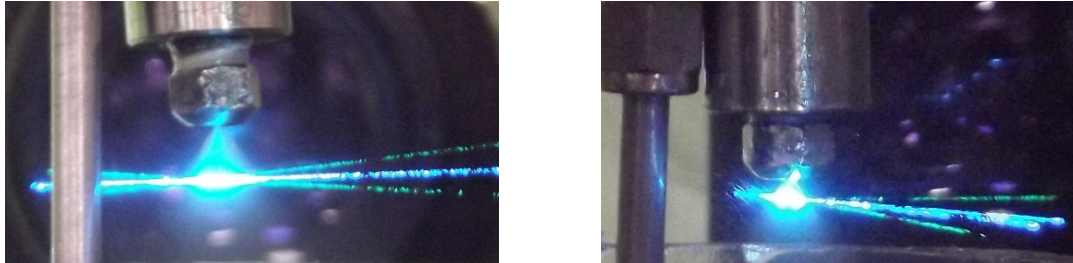


Figure 5-31 PDPA arrangement with spray nozzle

The obtained data on size distribution for both fuels showed that Butyl Nonanoate had a 10-15% bigger droplet size compared to JP-8. For instance, the average number droplet diameter ( $D_{10}$ ) for Butyl Nonanoate was about  $42.2 \mu\text{m}$  compared to  $37.07 \mu\text{m}$  for JP-8. Table 5-6 gives a sample of the averaged diameters for both JP-8 and Butyl Nonanoate. Figure 5-32 gives a sample size distribution for both fuels. It is noteworthy that the reported values are the probe volume corrected values to accommodate the laser beam power Gaussian distribution.

Table 5-6 Average diameters for Butyl Nonanoate and JP-8

	Symbol	JP-8 ( $\mu\text{m}$ )	Butyl Nonanoate ( $\mu\text{m}$ )	Difference %
<b>Number Average</b>	$D_{10}$	37.07	42.2	13%
<b>Area Average</b>	$D_{20}$	40.42	46.95	15%
<b>Volume Average</b>	$D_{30}$	43.51	50.42	15%
<b>Volume/Area Average</b>	$D_{32}$	50.44	59.04	17%

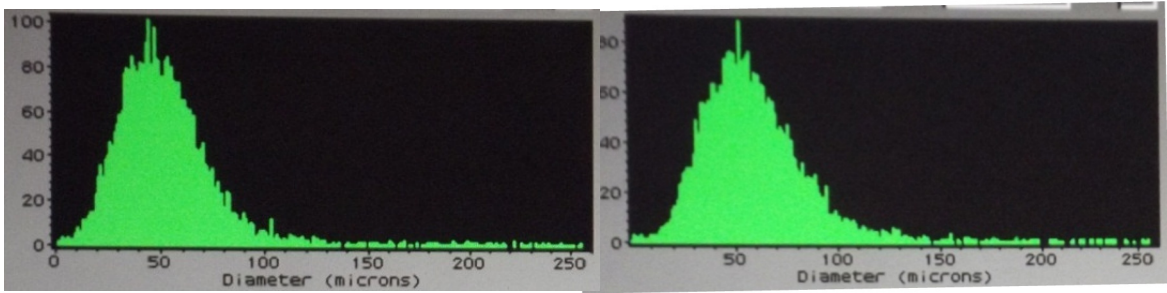


Figure 5-32 Number diameter distribution for JP-8 (left) and Butyl Nonanoate (right)

The results obtained outline the difference between the average droplet sizes produced, where Butyl Nonanoate demonstrated 13-17% bigger droplet size compared to JP-8. A mixture of both fuels should result in a smaller difference compared to JP-8. Such smaller size difference can be tolerated in actual combustion systems.

The obtained data on size distribution for 50% Butyl Nonanoate 50% JP-8 mixture as compared to JP-8 showed that fuel mixture had a 3-4% bigger droplet size compared to JP-8. For instance, the average number droplet diameter ( $D_{10}$ ) for the mixture was about 36.19  $\mu\text{m}$  compared to 34.67  $\mu\text{m}$  for JP-8. Table 5-7 gives a sample of the averaged diameters for both JP-8 and Butyl Nonanoate – JP-8 mixture. Figure 5-33 gives a sample size distribution for both fuels. It is noteworthy that the reported values are the probe volume corrected values to accommodate the laser beam power Gaussian distribution.

Table 5-7 Average diameters for fuel mixture and JP-8

	Symbol	JP-8 ( $\mu\text{m}$ )	50% Butyl Nonanoate – 50% JP-8 ( $\mu\text{m}$ )	Difference %
<b>Number Average</b>	$D_{10}$	34.67	36.19	4.3%
<b>Area Average</b>	$D_{20}$	39.43	40.89	3.6%
<b>Volume Average</b>	$D_{30}$	43.47	44.95	3.4%
<b>Volume/Area Average</b>	$D_{32}$	52.83	54.32	2.8%

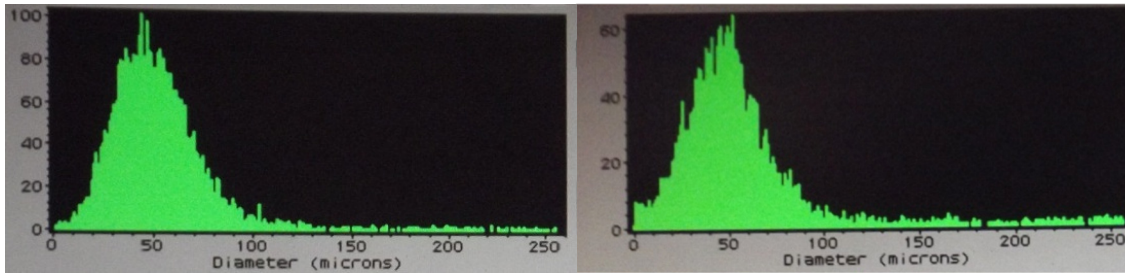


Figure 5-33 Number diameter distribution for JP-8 (left) and fuel mixture (right)

The results obtained outline the difference between the average droplet sizes produced. A mixture of both fuels (50% - 50% by volume) showed only about 3-4% difference in size compared to JP-8 (pure Butyl Nonanoate resulted in 13-17% larger droplets). Such smaller size difference can be tolerated in actual combustion systems.

#### 5.4.2. Experimental Conditions

The pollutants emission from the biofuel was also measured where the fuel was fed to a swirling distributed combustor operating at a nominal heat load of 6.25 kW and energy release intensity of 36 MW/m<sup>3</sup>-atm. Different liquid fuels were injected in a preheated air stream (for simulating gas turbine combustor intake with elevated temperature after air exiting the compressor) upstream the combustor.

For combustion, air was supplied through an air compressor. Air flow rates were measured using choked flow orifice systems. Liquid fuels were supplied to the combustor using a compressed fuel tank that delivers liquid fuel at a certain pressure to a thin tube (inner diameter of 0.01 inch). This thin tube causes pressure drop and controls the flow rate of the fuel, where the flow rate varies with the change in the tank pressure. This fuel delivery system was calibrated for every fuel more than once to

ensure that the delivered flow rates are adequate to the examined condition. The experimental setup is shown in Figure 5-34.

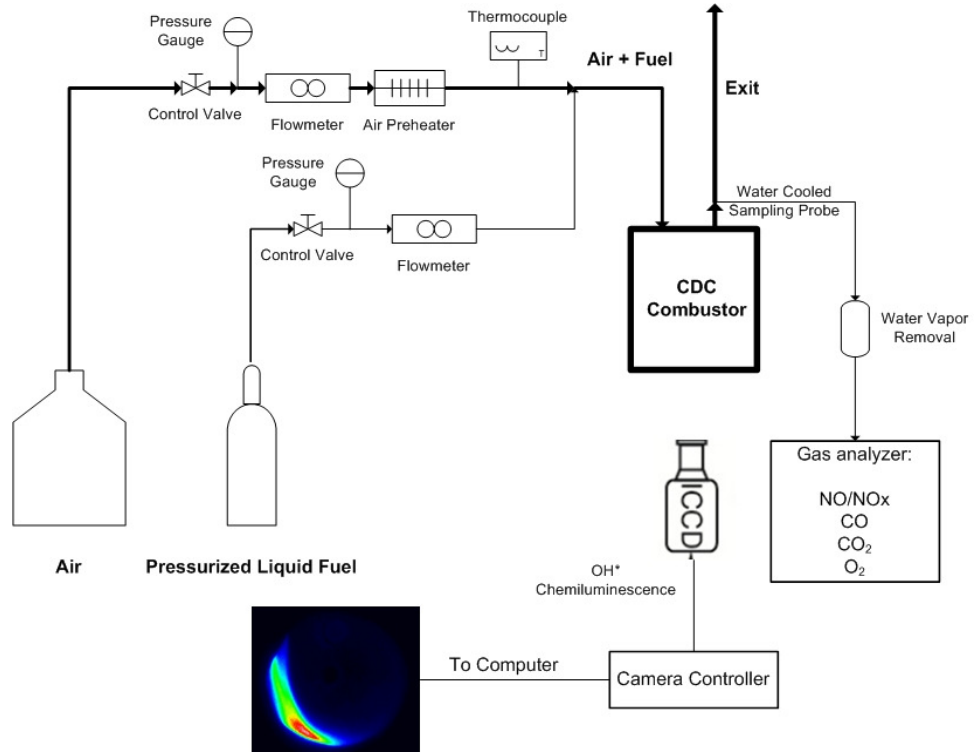


Figure 5-34 Schematic of the experimental combustion facility for biofuel

Table 5-8 shows the experimental investigations performed using JP-8, Hydrogenated Renewable Jet fuel and Butyl Nonanoate biofuel as described earlier.

Table 5-8 Bio-Fuels Examined

Case No.	Fuel	CV [kJ/Kg]
ATP-JP-8	JP-8	43,000
ATP-BN	Butyl Nonanoate	35,677
ATP-HRJ	Hydrogenated Renewable Jet Fuel	44,300

### 5.4.3. Results and Discussion

Emissions of NO and CO were recorded for the different fuels used. For all of the fuels examined, the heat load was kept constant at 6.25 kW (having heat (energy) release intensity (HRI) of 36 MW/m<sup>3</sup>-atm) at an equivalence ratio of 0.8. Air flow rate was adjusted to furnish the combustor with the adequate air requirement for each fuel used. Fuel flow rate was varied to allow changes of equivalence ratios ranging from 0.8 to 0.5 and the subsequent overall emissions were then measured. Figure 5-35 shows the NO emission levels resulting from operating the combustor with different fuels for novel premixed combustion configuration. Obtained data outlined the performance of Butyl Nonanoate as compared to JP-8. Butyl Nonanoate produces less NO emission at higher equivalence ratio. At lower equivalence ratios, the emissions from Butyl Nonanoate and JP-8 were identical. Emissions less than 8 PPM of NO were demonstrated for equivalence ratio of 0.6, with lower NO emission at lower equivalence ratios. These emissions are substantially lower than the current EPA regulations of 42 PPM for units larger than 250 MW operating on fuels other than natural gas [5].

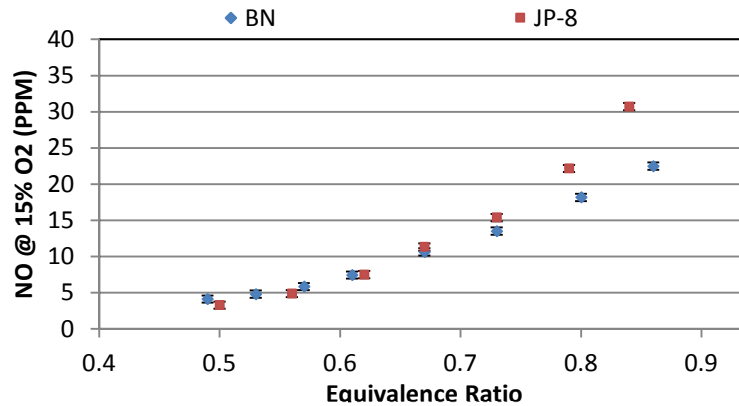


Figure 5-35 NO emissions for Butyl Nonanoate and JP-8

The CO emissions were also obtained for the above fuels and the results are shown in Figure 5-36. For different fuels, CO emission decreased with decrease in equivalence ratio until a minimum was reached, and then it started to increase again. The decrease in CO emission is attributed to excess oxygen that helps in complete conversion of CO to CO<sub>2</sub>, while the increase near the extinction limit is attributed to lower temperatures and weaker flames found near the extinction limit. Comparing CO emissions of Butyl Nonanoate and JP-8, one can see the beneficial aspects of using Butyl Nonanoate as a fuel. CO emissions were identical for high equivalence ratio, however, near the lean flammability limit, Butyl Nonanoate produced less CO emissions. Butyl Nonanoate combustion emitted 32 PPM of CO at an equivalence ratio of 0.6. JP-8 combustion emitted about 40 PPM at the same equivalence ratio.

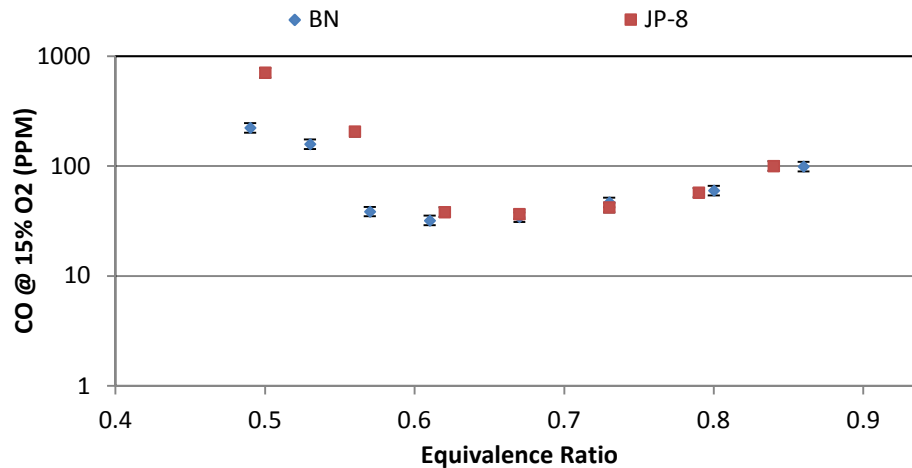


Figure 5-36 CO emissions for Butyl Nonanoate and JP-8

To further evaluate the performance of Butyl Nonanoate as a biofuel. Emissions from Butyl Nonanoate are compared against a Hydrogenated Renewable Jet (HRJ) biofuel representing a certified biofuel that is currently in use in both military and civilian applications. NO and CO emissions for the three fuels are shown in

Figure 5-37. One can see that HRJ produces less NO emissions as one would expect from biofuels. However the reduction in NO emissions through the use of Butyl Nonanoate was higher especially at higher equivalence ratio. HRJ also produced higher CO emissions as compared to both JP-8 and Butyl Nonanoate.

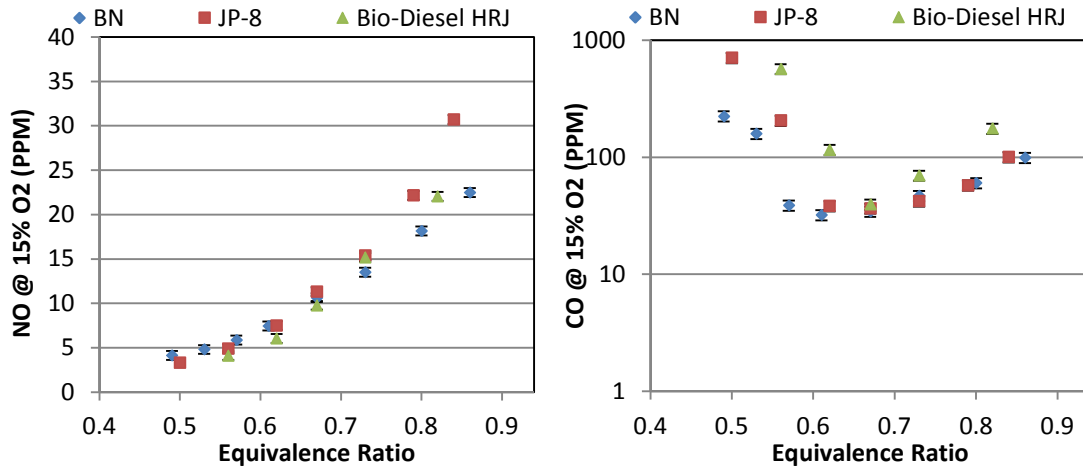


Figure 5-37 NO and CO emissions for Butyl Nonanoate, JP-8, and HRJ

The radical intensity distribution of OH\* chemiluminescence was acquired and the results are shown in Figure 5-38. OH\* chemiluminescence distribution for both JP-8 and Butyl Nonanoate show that the reaction zone was found around the entry jet, particularly at high equivalence ratios. This suggests the use of multiport fuel injection into the combustor. In the case of Butyl Nonanoate, the maximum reaction intensity was located downstream as compared to JP-8 indicating a slower reaction process. Also, the overall reaction intensity was decreased compared to JP-8 (22500 a.u. as compared to 30000 a.u.). Such less intense reaction can be related to the lower NO emissions emitted by Butyl Nonanoate. Also, the delayed reaction gives more time for favorable mixture preparation (mixing with hot recirculated reactive species) prior to combustion.

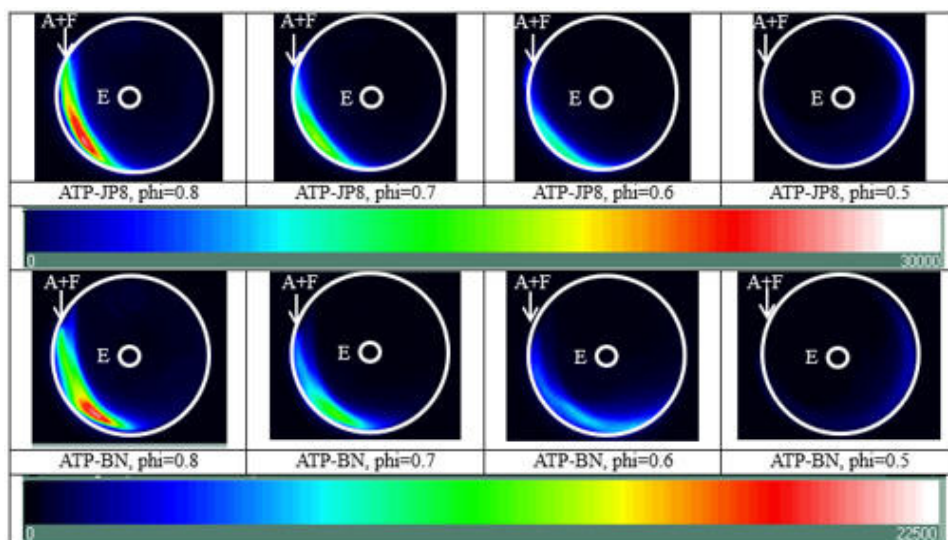


Figure 5-38 OH\* chemiluminescence for JP-8 and Butyl Nonanoate

#### 5.4.4. Summary

Results obtained with Butyl Nonanoate demonstrated the potential of this fuel for power generation and other application. Butyl Nonanoate was harder to atomize as compared to JP-8 as shown earlier, resulting in a larger droplet size. However, lower NO and CO emissions were shown especially at higher equivalence ratios. Even when compared to certified biofuel (Hydrogenated Renewable Jet Fuel), Butyl Nonanoate demonstrated lower NO and CO emissions. OH\* chemiluminescence showed that the resultant reaction from both fuels (JP-8 and Butyl Nonanoate) share the same general characteristic with minor differences concerning the maximum intensity value and maximum intensity location. The combustor did not show any instabilities or fluctuation while running on any of those fuels outlining the potential of Butyl Nonanoate as a future biofuel and outlining the fuel flexibility of the CDC combustor previously shown using other fuels.

## **6. Chapter Six: Injection Design**

In this chapter, to further reduce pollutants emission and enhance reaction distribution, the injection of reactants into the combustor is studied with view to enhance mixture preparation and reaction distribution. The first examined parameter is the fuel injection location. Four injection locations have been examined in the previous chapter. Two more locations are investigated with view to enhance mixing.

Another parameter examined was the shape of the injector. Previously, all the experiments were performed using circular injectors. The performance of elliptical injectors is evaluated with different aspect ratios and orientation in the combustor. The third examined variable was reactants injection velocity, with view to study the role of injection velocity and turbulence on mixing and reaction distribution. Air dilution was investigated as means to achieve lower emissions as indicated by nitrogen diluted methane experiments in section 5.1. Dual injection is also investigated in a view to develop multi-injection combustor for scale-up

### **6.1. Fuel Injection Location**

The effect of fuel injection on the combustor performance under various operational conditions is first investigated. High velocity coaxial air in jet diffusion flames has been successfully demonstrated to reduce  $\text{NO}_x$  emission levels in hydrocarbon flames [132]. Enhanced shear produced by high velocity coaxial air results in enhanced mixing between fuel and air before combustion and also lowers the residence times resulting in lower emission levels. Mixing in coaxial jets has been studied in details, where the

main characteristics of these jets were described [133]. Coaxial jet has been also used in gas turbine model combustors demonstrating low pollutants emission over their range of operation [33]. However, it is anticipated that mixing between air, fuel, and hot reactive product gases to achieve CDC conditions does not depend solely on the air and fuel injection method, but rather on the interaction between fresh streams introduction method combined with flowfield developed inside the combustor.

#### 6.1.1. Geometries Examined

Four fresh streams (air and fuel) injection scenarios are reported here to show the direct role of mixture preparation in achieving distributed combustion conditions and ultra-low pollutants emission. Figure 6-1 shows a schematic diagram of the arrangements on the fuel injection scenarios presented here with their relative dimensions in terms of  $D$ , where  $5D/3$  is the air injector diameter. In the first configuration, named “PR” fuel is injected in the air jet upstream of the combustor, and the jet entering the combustor can be considered as perfectly mixed air/fuel jet (see Figure 6-1(a)) which is the same geometry reported earlier as “ATP”. The second configuration involves a coaxial nozzle, where fuel is introduced as a center jet, while air is introduced through the annulus, named “CA” (see Figure 6-1(b)). The third and fourth configuration had separate fuel jet introduced in a “cross flow” behavior. Two different separation distance between the air and fuel jets were investigated, namely “NP0” and “NP1” (see Figure 6-1(c), (d)). Configuration “NP1” is the same geometry reported earlier as “ATF1”. Changes in the fuel injection method are expected to have

a significant effect on mixture preparation between air, fuel, and product gas. Adequate mixture preparation is critical to achieve distributed reactions as discussed earlier.

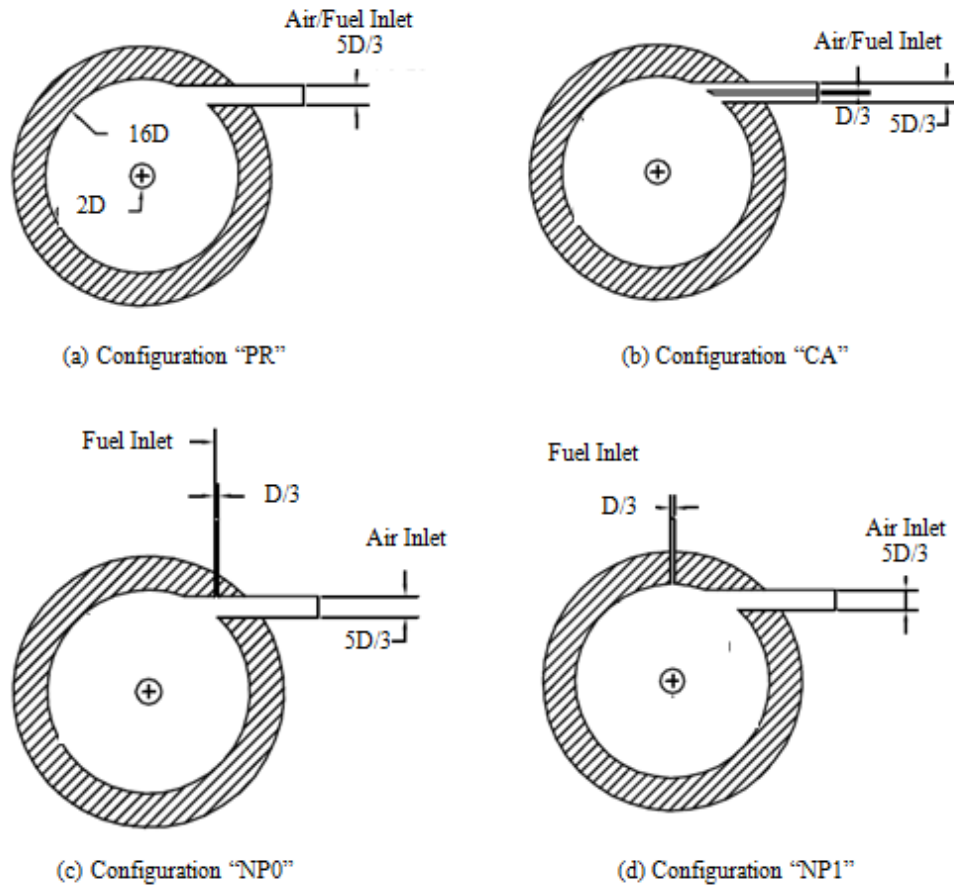


Figure 6-1 Schematic diagram of different fuel introduction scenarios, end cross-sectional view at middle location of the combustor

The investigations compared the performance of the combustor under different fuel injection scenarios. Table 6-1 summarizes the investigations performed along with the variables manipulated for each investigation. The case name represents the location of fuel injection.

Table 6-1 Fuel Injection Scenarios

<b>Case No.</b>	<b>Mixing</b>	<b>Fuel Introduction</b>	<b>Air Temperature</b>
PR	Premixed	With air	600K
CA	Partially Premixed	Center of air jet	600K
NP0	Non-Premixed	Separate	600K
NP1	Non-Premixed	Separate	600K

### 6.1.2. Numerical Investigations

Numerical simulations were performed to help develop an understanding of the flow field and the mixing process inside the combustor for different air and fuel streams conditions entering the combustor. For these simulations, commercial software FLUENT® code was used. The flow was modeled using finite volume method. For solving turbulence, standard k-ε model with standard wall function was used. For reacting cases, a two-step methane combustion model was adopted to determine mixing between air, fuel and burned gases prior to combustion. The operating pressure was one atmosphere. For any of the numerical models, the volume consisted of more than one million tetrahedral mesh cells.

The model boundary conditions are described in this section. For air inlet, “mass flow inlet” boundary condition was used with inlet turbulence intensity of 10%, mass fraction of O<sub>2</sub> of 0.233 and inlet temperature of 600K. For fuel inlet, “mass flow inlet” boundary condition was used with inlet turbulence intensity of 10%, the mass fraction of CH<sub>4</sub> was set to 1, and the inlet temperature was set to 300K. For hot product gases to exit, “pressure outlet” boundary condition was used, with zero-gauge back pressure and 10% turbulence intensity for back flow. For all the numerical simulations, the resultant equivalence ratio was 0.8 with methane as the fuel. For any numerical simulations, the conversion criterion was that the largest residual was less than 10e-4.

It is understood that the simulated flowfield and mixing behavior will deviate from the actual case as shown earlier in isothermal PIV experiments (section 4.4). However, the trends are expected to remain consistent, specially prior to ignition near the entry jet, thus providing an indication for the causes of pollutants emission behavior for the various cases investigated here.

### 6.1.3. Results and Discussion

The experimental investigation was focused on examining different methods of fuel introduction into the combustor to help develop an understanding of the mixing process so as to enhance and accelerate the mixing and achieve adequate mixing prior to ignition. The distributed combustion process requires that air and/or fuel be mixed with the hot and chemically active gases from the combustion zone prior to the mixture ignition for seeking distributed reactions. In this study air preheats was employed to simulate gas turbine combustion conditions with elevated inlet combustion air temperatures. The experimental results are reported at equivalence ratios of 0.8, 0.7, 0.6 and 0.5. These upper ends of equivalence ratios are higher than that used in current engines and are used due to higher efficiency that can be achieved at higher equivalence ratios. Emissions of NO and CO were recorded for each arrangement at different equivalence ratios. Figure 6-2 shows the emission levels at different equivalence ratios with each arrangement.

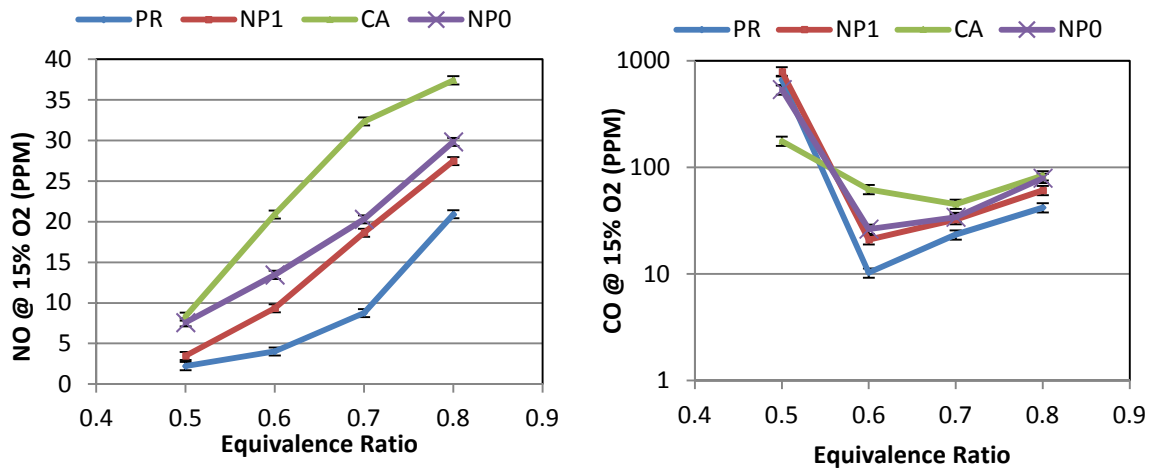


Figure 6-2 NO and CO emissions for different injection arrangements

The results obtained on NO emission indicate that coaxial injection provides highest NO emission levels as compared to other fuel introduction methods. Separate air and fuel introduction exhibited lower emission levels. The premixed combustion mode “PR” revealed the lowest emissions. For instance, at an equivalence ratio of 0.6, coaxial injection provided emission levels of 21 PPM NO and 62 PPM CO. Separate injection mode “NPO” yielded emission levels of 14 PPM NO and 26 PPM CO. Case “NP1” yielded lower emissions at 10 PPM NO and 21 PPM CO. However, premixing air and fuel prior to their introduction to the combustion chamber demonstrated ultra-low emission levels of 4 PPM NO and 11 PPM CO. The lower emissions demonstrated from premixed combustion agrees with the trend obtained previously for various combustor configurations. This can be attributed to the fact that the mixing problem in this mode is less complicated. To achieve distributed combustion mode, air and hot products gases mix together to form hot diluted oxidizer. Then, the fuel is mixed with that hot diluted mixture to achieve uniform mixture and spontaneous ignition.

However, in premixed mode, air and fuel are well mixed upstream, which helps in mixture preparation for distribution condition.

The NO emissions decreased with the decrease of equivalence ratio as a direct result of lower combustion temperature for all the cases presented here. Emission of CO diminishes with decrease in equivalence ratio, reaching a minimum value. Beyond this point, any further decrease in the equivalence ratio causes CO emissions to increase. The observed high levels of CO at low equivalence ratios are due to the slow rates of oxidation associated with low combustion temperatures. However, for configuration CA, the observed CO emission at equivalence ratio of 0.5 is lower than the observed emissions for the other configurations examined. Such behavior indicates that the reaction rate is higher at higher temperatures. This suggests that the combustion occurs in a less diluted oxidizer (higher oxygen concentration) so that colorless distributed conditions are not satisfied. NO emission for this configuration, compared to other configurations, was found to be higher to reveal the effect of higher reaction rate and temperature encountered in this configuration.

The radical intensity distribution of OH\* chemiluminescence showed that the reaction zone is in the shape of a crescent. It can be seen that as the fuel introduction method is changed, the reaction zone move gradually downstream. Premixed combustion case “PR” resulted in the earliest reaction zone, whereas separate air and fuel introduction as in case “NP1” resulted in a longer ignition delay. OH\* zone movement, which can be seen as a flame marker, outlines the difference between mixing and ignition delay in each case discussed here. Figure 6-3 shows the OH\*

chemiluminescence intensity distribution at an equivalence ratio of 0.8 for the different cases presented here. A similar trend was also observed at other equivalence ratios.

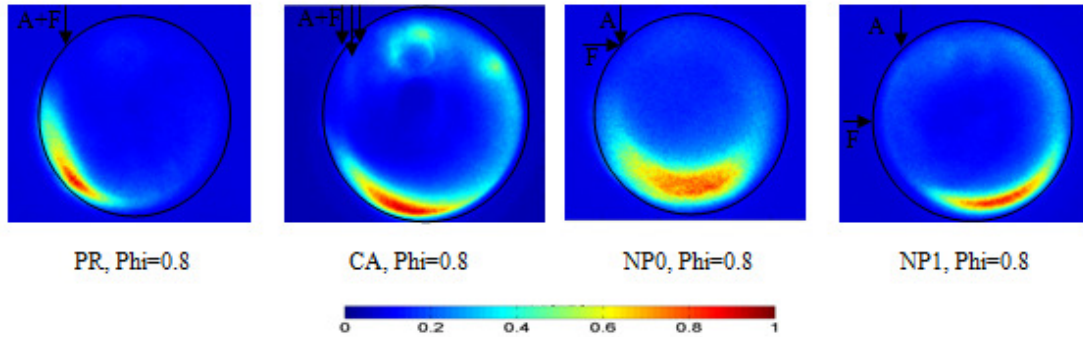


Figure 6-3 OH\* chemiluminescence intensity distribution for different injection arrangements

Numerical simulations were carried out to help develop an understanding of the difference in behavior between each of the fuel injection scenarios discussed herein. It is understood that the simulations will somewhat deviate from the actual experiments, however, they are helpful in providing insights of the reaction progression in the combustor. The calculated results showed that, for each fuel injection scenario, the ignition of the mixture is essentially different. Temperature distribution for the air/fuel injection plane is shown in Figure 6-4. It can be seen that in case CA (see Figure 6-4(b)) there is a rapid temperature increase at the center of the air/fuel jet. The temperature at the center of the jet approaches 1700K which is relatively high as compared to the surrounding jet flow with a temperature of about 1300K. This rapid temperature increase indicates that ignition occurs at this point, where the igniting mixture consists of air and fuel with minimal amounts of hot and reactive gases. One should note that, according to temperature plots, burned gases having a temperature of about 2000K are separated from the ignition zone with cooler air jet (of about 1300K). Such oxygen-

rich combustion fosters thermal NO production and indicates lack of adequate mixing under this scenario. Consequently distributed reaction requirements are not satisfied leading to a “diffusion flame” behavior that should be avoided in combustors for near zero emissions. A similar behavior can be seen in case “NP0” case but to a smaller extent (see Figure 6-4(c)), where combustion occur only between air and fuel without recirculated hot products. On the other hand, temperature distribution for cases PR and NP1 (see Figure 6-4(a and d)) indicate that such early ignition of only air and fuel does not exist.

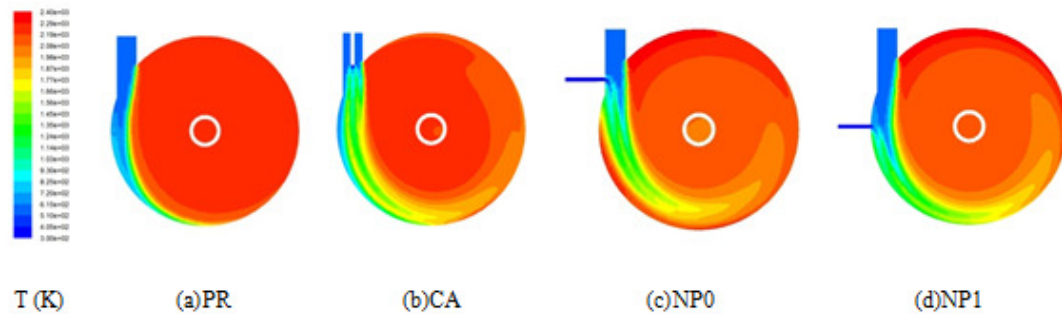


Figure 6-4 Temperature distribution obtained numerically at the air/fuel injection plane for the different cases

Figure 6-5 shows the fuel jet decay for each of the cases discussed here. By comparing methane decay plots with temperature plots, one can interpret the mixing and ignition process. For case CA, the area at the jet center with high temperature rise as shown in Figure 6-4(b) corresponds with methane depletion shown in Figure 6-5(b). It is to be noted that for premixed combustion, the plotted results are for fuel mixture fraction relative to the inlet fuel mixture fraction.

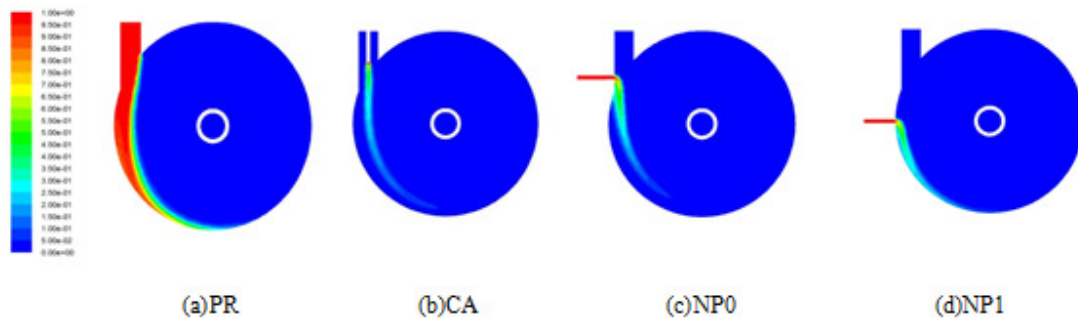


Figure 6-5 Methane mass fraction distribution at the air/fuel injection plane for the different cases

The above analysis can be verified comparing the temperature plots (Figure 6-4) and OH\* chemiluminescence images (Figure 6-3). One can see that the onset of high temperature rise seen in numerical simulation temperature plots corresponds with the presence of OH\* as indicated by chemiluminescence for the different geometries discussed herein. OH\* chemiluminescence technique detects the thermally excited OH radicals (OH\*) in high temperature zones and is used as flame marker, indicating zones of high temperature and validating this analysis.

#### 6.1.4. Summary

Experimental investigations have outlined the importance of flow field design and the relationship between the fuel jet location and resulting pollutants emission. Novel premixed combustion design along with swirling flow has yielded low pollutants emission. At a rather high equivalence ratio of 0.6, the resulting pollutant emissions were 4 PPM of NO and 11 PPM of CO with inlet air preheats temperature of 600K to the combustor. Novel non-premixed combustion design, which is of great interest to eliminate premixed combustion instabilities, flame flash back and other risks

associated with premixed combustion has shown the ability to achieve low pollutants emission. The results have shown that flow field design and mixture preparation in non-premixed combustion is critical. The results showed that a change in fuel injection location greatly affects pollutants emission. For instance, NO emission decreased dramatically from 21 PPM (for coaxial air/fuel injection, case “CA”) to 10 PPM (for non-premixed, case “NP1”). CO emission variation was minimal between the different cases due to the fact that inlet air preheats dramatically decreased CO emission due to faster reaction kinetics and complete conversion to CO<sub>2</sub>.

The experimental data on emissions and numerical predications revealed that high NO emissions recorded for cases “CA” and “NP0” can be attributed to poor mixing of air, fuel and burned gases. Numerical simulations showed that high temperature rise (indicating ignition) was found in areas where only air and fuel existed with minimal amounts of burned gases. Such ignition occurring in oxygen-rich mixture fosters thermal NO formation which should be avoided. In order to achieve distributed reaction the air, fuel and burned gases should be thoroughly mixed prior to ignition and that mixing time to be less than ignition delay. Such good mixing can be found in premixed case “PR” and non-premixed case “NP1”.

The data obtained can be combined with previously performed experiments to outline the role of fuel injection for ultra low emissions. Data shows that NP1 offers good mixing prior to ignition as compared to later injection locations. Also this injection location is delayed enough to prevent early ignition between air and fuel with mixing with hot recirculated gases as seen in cases CA and NP0. Figure 6-6 and Figure 6-7 show different injection locations and measured emissions.

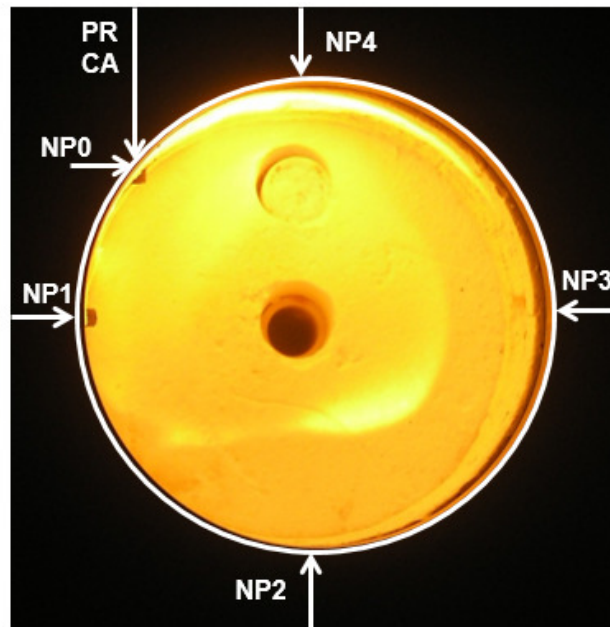


Figure 6-6 combustor with different injection locations

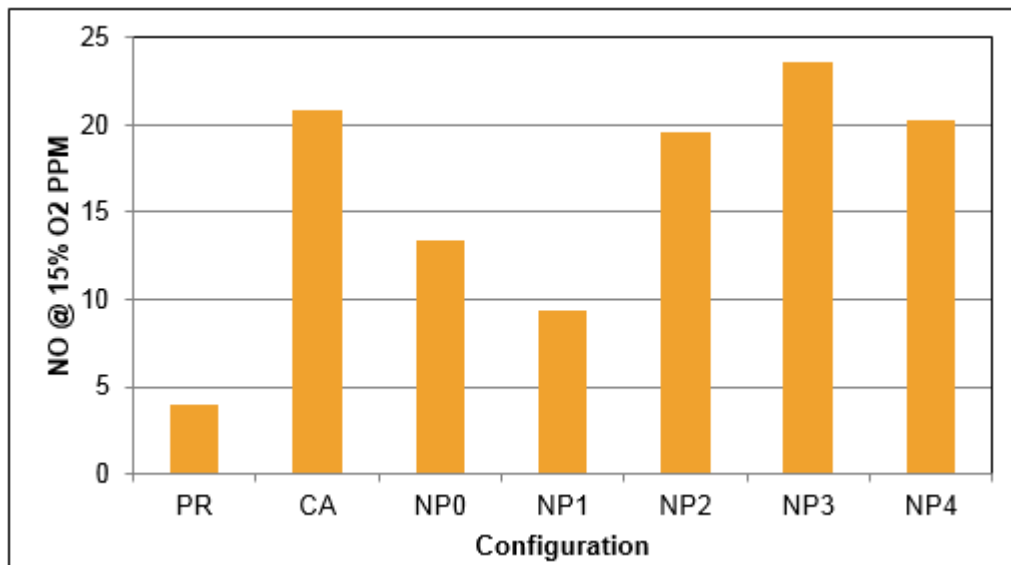


Figure 6-7 NO emissions for different configurations at  $\phi=0.6$

## 6.2. Injector Shape

The influence of the injector geometry (entry jet shape) has been the focus of mixing and entrainment studies. The experimental study shows that noncircular jets provide greater entrainment and mixing with ambient fluid than circular jets, in general. However, the entrainment ratio depends on the mixing tube diameter [134]. In another study, it was concluded that circular jets have the lowest velocity decay and entrainment rate as compared to rectangular, elliptical and triangular nozzles at subsonic speeds [135]. Results compiled by Gutmark and Grinstein agreed with these findings as listed in their review paper [136]. On the other hand, earlier studies of jets emerging from noncircular nozzles with corners, e.g., triangular or square nozzles, showed that the introduction of sharp corners in the outlet nozzle can increase significantly the small-scale turbulence intensity at the corners relative to the flat segments of the nozzle [137] [138]. In another paper, the effect of the coflow geometry of a coaxial jet was studied. It was shown that the elliptical coflow flames are shorter, yield less soot, have lower peak temperature, and produce more NO and less CO to the flames in a circular coflow. This behavior was related to the higher entrainment of air and more oxygen availability for combustion between the center and coflow [139].

In the previous section, coaxial injection in circular jets produced higher emissions compared to other fuel injection scenarios. This behavior was related with early ignition that occurs between air and fuel without proper mixing with recirculated hot reactive gases. Consequently, in this section, the role of the injector shape with no coaxial flow will be examined.

### 6.2.1. Experimental Conditions

Elliptical injectors were machined from alumina silicate to the required aspect ratio of the ellipse. Afterwards, the injectors were heat treated to enhance their physical properties to withstand operational temperatures. The nozzles were machined from copper at first but the nozzles oxidized and eroded. Consequently Alumina Silicate was used instead. The first experiments compared the orientation of the elliptical nozzle (major diameter vertical or horizontal). Vertical orientation indicates that the major axis of the ellipse is parallel to the combustor depth. Horizontal orientation indicates that the major axis is parallel to the combustor diameter. Afterwards, different aspect ratios were examined with view to evaluate the impact of the elliptical nozzle on the pollutants emission of the combustor. Table 6-2 summarizes the different orientations and aspect ratios examined. The air injection temperature was 600K for all the experiments performed here.

Table 6-2 Elliptical Nozzles Experimental Parameters

<b>Case No.</b>	<b>Aspect Ratio</b>	<b>Orientation</b>	<b>Mode</b>
ATP	1		Premixed
ATP-AR:1.5 V	1.5	Vertical	Premixed
ATP-AR:1.5 H	1.5	Horizontal	Premixed
ATP-AR:2 H	2	Horizontal	Premixed
ATP-AR:2.25 H	2.25	Horizontal	Premixed
ATF1	1		Non-Premixed
ATF1-AR:1.5 V	1.5	Vertical	Non-Premixed
ATF1-AR:1.5 H	1.5	Horizontal	Non-Premixed
ATF1-AR:2 H	2	Horizontal	Non-Premixed
ATF1-AR:2.25 H	2.5	Horizontal	Non-Premixed

## 6.2.2. Results and Discussion

### 6.2.2.1. Ellipse Orientation Effect

The first set of experiments is aimed at evaluating the effect of the orientation of the elliptical nozzle with respect to the combustor geometry. An elliptical nozzle with an aspect ratio of 1.5 was positioned vertically and horizontally. The experiments were performed in both premixed and non-premixed configuration (ATP and ATF1). The obtained results were compared to circular nozzle previously used for air injection. The obtained emissions for the premixed case are shown in Figure 6-8. The recorded NO emissions for circular injector case was found to be lower compared to the two orientations of the elliptical nozzle. On the other hand, CO emissions were somewhat higher.

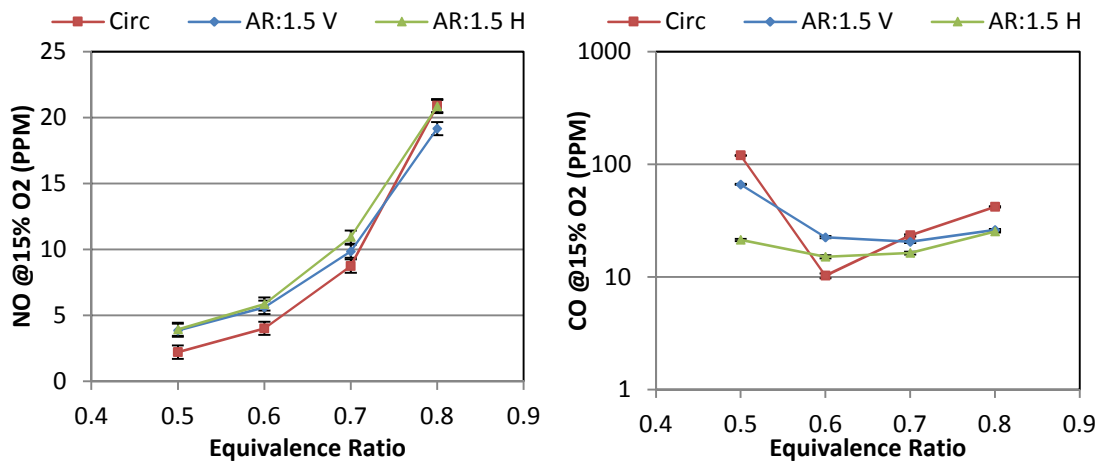


Figure 6-8 NO and CO emissions for elliptical injectors under premixed conditions

The difference in NO emissions under premixed condition was not significant. Consequently, the experiments were repeated under non-premixed conditions (ATF1). The recorded emissions are shown in Figure 6-9. Under non-premixed condition, the

variation in emission was clear. The circular injector resulted in lower NO emissions compared to both elliptical data sets. It can also be seen that the horizontal orientation resulted in less NO emissions compared to the vertical orientation. This can be related to the flowfield inside the combustor. In the vertical arrangement (major axis parallel to the combustor depth), mixing with fuel is not that adequate (fuel is injected at the center plane passing through the nozzle parallel to its minor axis). Also most of the entrained reactive gases are away from the fuel injection plane. On the other hand, for the horizontal orientation (where the major axis is parallel to the combustor diameter), most of the entrainment is within the plane of fuel injection leading to a somewhat better mixture preparation as compared to the vertical orientation. CO emissions were slightly lower for the elliptical nozzles as compared to the circular nozzles.

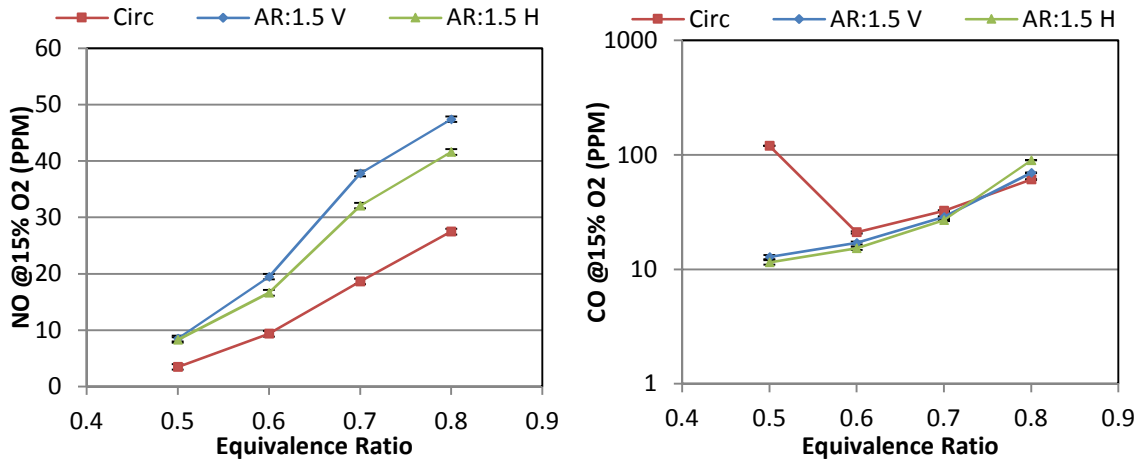


Figure 6-9 NO and CO emissions for elliptical injectors under non-premixed conditions

#### 6.2.2.2. Aspect Ratio Effect

The second set of experiments is aimed at evaluating the effect of the aspect ratio of the elliptical nozzle (ratio of major to minor axes). Three aspect ratios of 1.5, 2, and

2.25 were examined. The experiments were performed in both premixed and non-premixed configuration (ATP and ATF1). The obtained results were compared to circular nozzle previously used for air injection. The obtained emissions for the premixed case are shown in Figure 6-10. The recorded NO emissions showed that the circular injector demonstrated the lowest NO emissions. On the other hand, for higher equivalence ratios, elliptical nozzle of aspect ratio 2.25 demonstrated the lower NO emissions. However, the performance of this nozzle (elliptical of AR=2.25) was not favorable for CO emissions as demonstrated high CO emissions across the range of combustor operation.

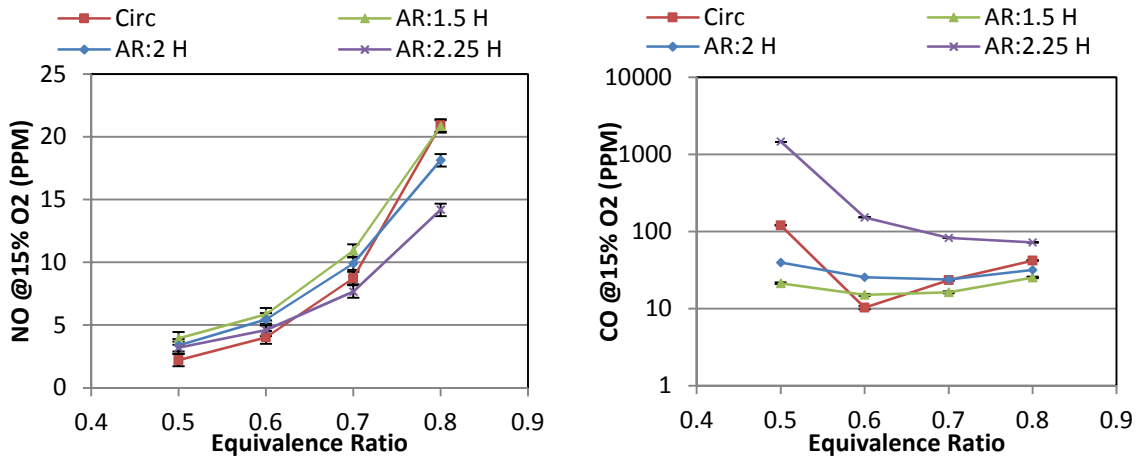


Figure 6-10 NO and CO emissions for different aspect ratios under premixed combustion

The experiments were repeated under non-premixed conditions (ATF1). The recorded emissions are shown in Figure 6-11. The circular injector resulted in the lower NO emissions compared to the elliptical nozzles except at equivalence ratio of 0.8. At this high equivalence ratio, the same behavior demonstrated in premixed combustion was found, where the NO emissions from elliptical nozzle with an aspect ratio of 2.25 were lower. Unfortunately, this configuration demonstrated the highest CO emissions

similar to the behavior exhibited under premixed combustion mode. The aspect ratio of 2 demonstrated a diffusion liked behavior, where NO emissions were high regardless of the global equivalence ratio.

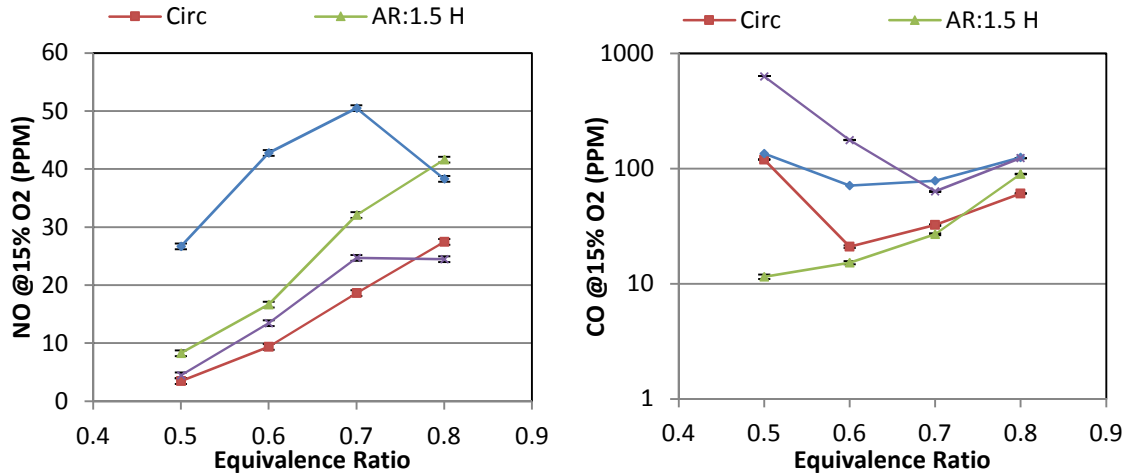


Figure 6-11 NO and CO emissions for different aspect ratios under non-premixed combustion

### 6.2.3. Summary

Results obtained on NO and CO emissions for elliptical injectors showed that the elliptical injector orientation plays an important role on the emission of NO and CO. Orientation with major axis parallel to the combustor diameter demonstrated lower emissions as compared to vertical orientation. Also, the aspect ratio substantially impacted the pollutants emission. High aspect ratio of 2.25 demonstrated lower emissions compared to other configurations. However, this performance was coupled to the highest CO emissions reducing the potential deployment of this nozzle shape. Circular injection produced lower NO emissions when compared to the entire elliptical configurations examined with the exception of the elliptical nozzle with aspect ratio of

2.25 operating at high equivalence ratio. OH\* chemiluminescence for the discussed configurations did not demonstrate major differences between these configurations (orientation and aspect ratio) and consequently they were not included herein. Examination of other aspect ratios was not possible due to physical constraints on the combustor nozzle size and installation.

### **6.3. Air Injection Velocity**

Different researchers have investigated the effect of reactants injection velocity on pollutants emission. Kim *et al.* investigated the effect of fuel air mixing on NO<sub>x</sub> emission in non-premixed flames with coaxial air using hydrogen and diluted hydrogen as fuels [132]. The major parameters used to modify mixing were the fuel jet velocity and coaxial air velocity. Chen and Driscoll investigated the effect of coaxial air amount on the behavior of jet diffusion flame [140]. They concluded that for hydrogen flames, six folds reduction was achieved with increased coaxial air velocity to fuel velocity. However, such reduction was not demonstrated with methane flame as the emission index of NO<sub>x</sub> (EINO<sub>x</sub>) slightly increased with increasing the co-axial air to fuel velocity [140]. Other researchers investigated the effect of jet momentum and injection velocities on the formation of flameless combustion and associated NO<sub>x</sub> emission [141]. It was concluded that increasing injection velocity decreases NO<sub>x</sub> emission at a constant equivalence ratio of 0.77. However, flameless oxidation could not be established for equivalence ratios lower than 0.59 which is more relevant to gas turbine applications [28].

### 6.3.1. Experimental Parameters

In this section, the effect of air injection velocity on pollutants emission and combustor flowfield is investigated. The isothermal flowfield for different air inlet velocities are characterized, with emphasis on recirculation and turbulence generation. Pollutants emission from reacting flow experiments will be recorded for the different air injection velocities with view to develop relation between injection velocity and combustor performance under both premixed and non-premixed combustion modes.

The investigations performed on experimental combustor were aimed at comparing the performance of combustor with different air injection velocities. The facility allowed variation of the injection velocity and nozzle diameter of the fuel and air as well as hot gasses exit. Table 6-3 summarizes the cases reported here. For each case the fuel flow rate was changed to seek operation at different equivalence ratios. The respective case name indicates the combustor geometry (ATP) and the air injection diameter.

Table 6-3 Experimental Parameters for Different Injection Velocities

<b>Case No.</b>	<b>Injection Velocity [m/s]</b>	<b>Air Injection Temperature [K]</b>	<b>Mode</b>
ATP-31	46	300	Premixed
ATP-24	78	300	Premixed
ATP-20	103	300	Premixed
ATP-T-31	92	600	Premixed
ATP-T-24	156	600	Premixed
ATP-T-20	206	600	Premixed
ATF1-T-31	92	600	Non-premixed
ATF1-T-24	156	600	Non-premixed
ATF1-T-20	206	600	Non-premixed

### 6.3.2. Isothermal Flowfield

The first set of experiments is aimed at evaluating the isothermal flowfield. The extended hot product gases exit tube inside the combustor resulted in a “blind spot”, where there was laser sheet was blocked by the extended exit tube. Consequently there was no light for the camera to pick up the particles as the laser sheet was obstructed. The first air injection diameter chosen ( $5D/3$ ) resulted in an air injection velocity of 46 m/s (configuration ATP-31). The obtained velocity vectors and contours of mean velocity in X & Y directions are shown in Figure 6-12.

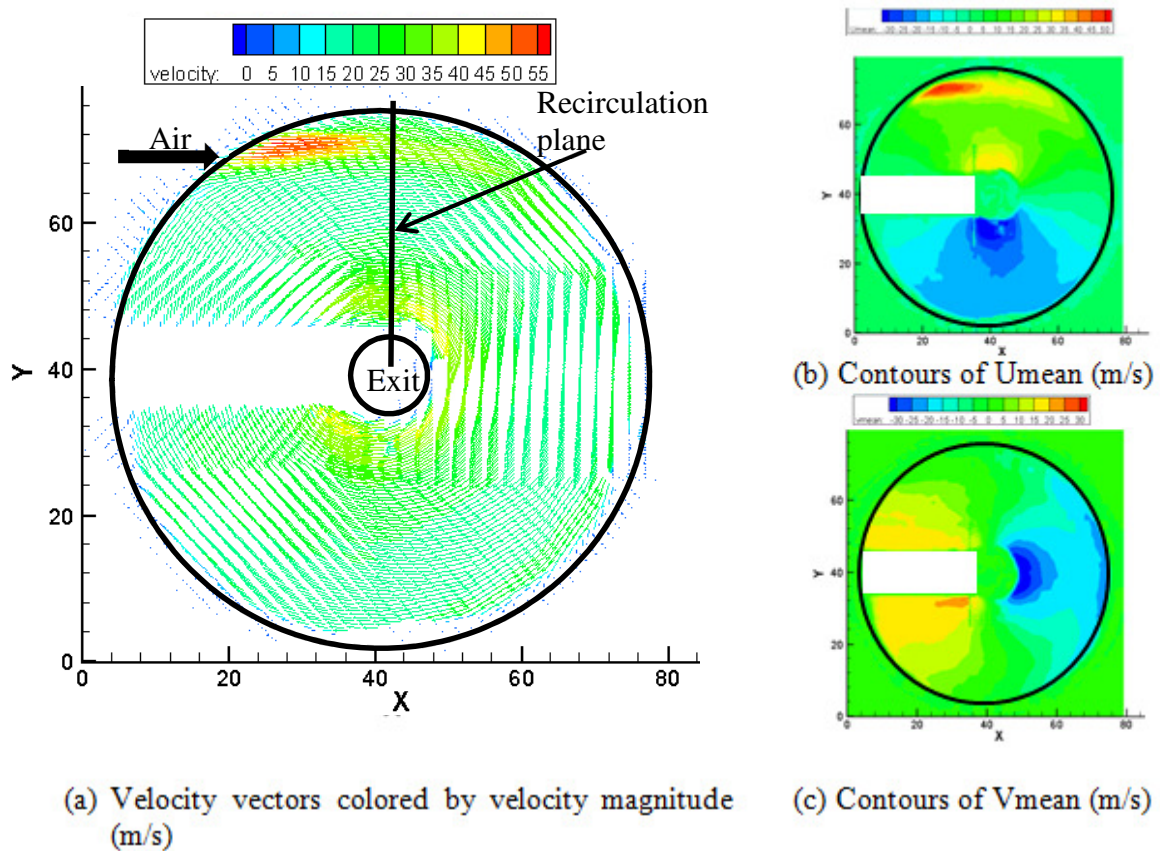


Figure 6-12 Velocity vectors (a),  $U_{mean}$  (b), and  $V_{mean}$  (c) for configuration ATP-31

The second examined flowfield had an air injection diameter of  $4D/3$  that resulted in an injection velocity of 78 m/s (configuration ATP-24). The obtained velocity vectors and contours of mean velocity in X & Y directions are shown in Figure 6-13.

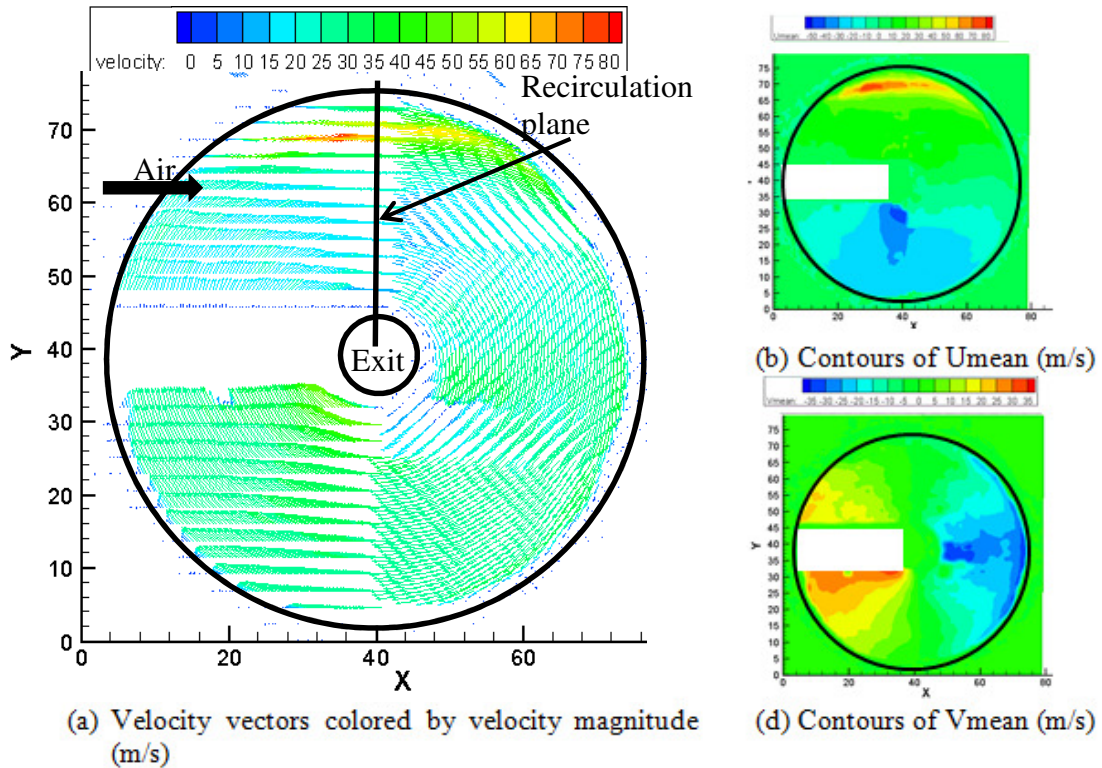


Figure 6-13 Velocity vectors (a),  $U_{mean}$  (b), and  $V_{mean}$  (c) for configuration ATP-24

The Particle image velocimetry showed that the flowfields in both configurations are similar in behavior; however, the velocity magnitudes were higher in the configuration ATP-24 due to the higher air injection velocity at the inlet. The higher injection velocity resulted in a higher recirculated mass. The recirculation ratio for this configuration was calculated for the investigated plane. Following equation 4-2, it was found that the recirculation ratio increased by 15% with higher air injection velocity (case ATP-24 as compared to case ATP-31).

Also, the velocity fluctuation at the inlet region was found to increase with the increase in the air injection velocity. Figure 6-14 shows the velocity fluctuations (Urms) for the region covering the entry jet. It can be seen that for configuration ATP-31, the velocity fluctuation had a maximum intensity of 17m/s at the entry jet. On the other hand, for configuration ATP-24, the velocity fluctuation had a maximum of 40m/s, double that of configuration ATP-31, though the inlet velocity was only increased by 70%.

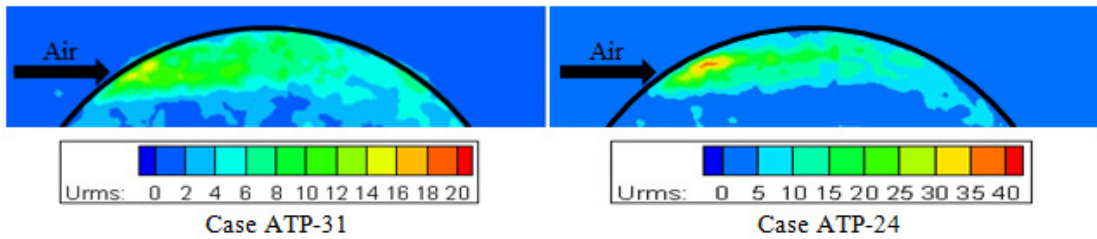


Figure 6-14 Velocity fluctuations (Urms) at the jet entry region

The increased inlet turbulence is expected to play an important role in the mixture preparation process between fresh mixtures and hot active gases from within the combustor to achieve colorless distributed conditions. For non-premixed cases, increased turbulence will play a critical role as the mixing of the fuel jet in cross flow is mainly dominated by turbulence in both near and far field for the low velocity ratios [83]. The overall high flow velocity is expected to prevent flame anchoring, eliminating local hot spots, which is important to achieve ultra-low emissions.

### 6.3.3. Pollutants Emission Results and Discussion

#### 6.3.3.1. *Standard Temperature Premixed Experiments*

Experimental investigations were performed for the discussed cases and the associated pollutants emissions were recorded for cases ATP-31, ATP-24 and ATP-20. These cases were investigated with air injection at room temperature as shown in Table 6-3. Figure 6-15 shows NO emission for the different cases, where the effect of injection velocity on NO emissions can be seen. Increasing the injection velocity from 46 m/s (ATP-31) to 78 m/s (ATP-24) decreased NO emissions by about 13% for different equivalence ratios examined. Further increase in air injection velocity up to 103 m/s (ATP-20) resulted in further decrease of NO emissions by 20% compared to the injection velocity of case ATP-31.

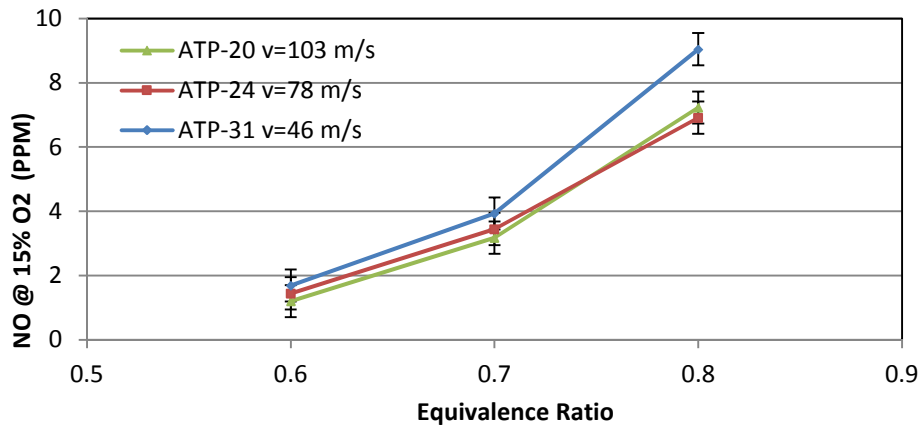


Figure 6-15 NO emissions for different injection velocities. Inlet air temperature =300K

Figure 6-16 shows the experimentally measured CO emissions for different air injection velocities discussed earlier. It can be seen that the velocity affected CO emissions to some extent as emission increased with increase in air injection velocity.

This can be related to the decrease in residence time inside the combustor as the injection velocity is increased.

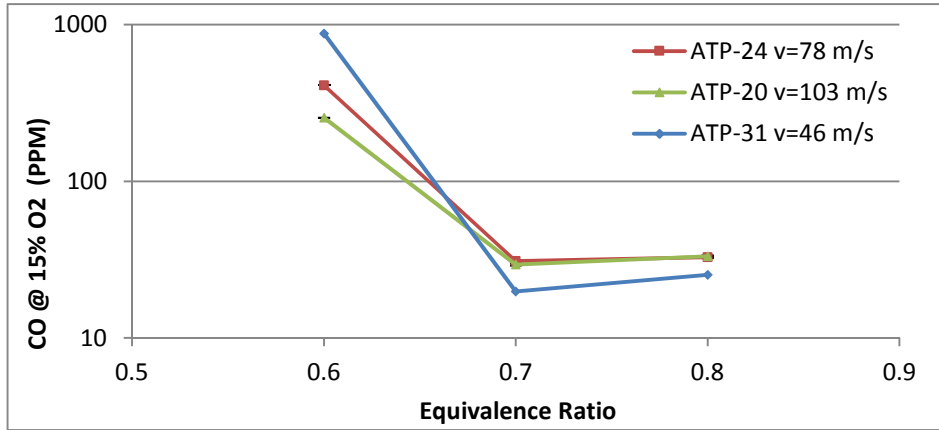


Figure 6-16 CO emissions for different injection velocities. Inlet air temperature =300K

#### 6.3.3.2. Preheated Air Premixed Experiments

The same experiment was repeated with inlet air preheated to a temperature of 600K, simulating the combustor intake temperature after the compressor. With the preheated air, NO emissions have been found to increase while CO emissions decreased. Also, increasing the air inlet temperature from 300K to 600K doubled the air injection velocities as shown in Table 6-3. The effect of air injection velocity was accentuated by the increase in inlet air temperature. Figure 6-17 shows the recorded NO emissions for the three cases; ATP-T-31, ATP-T-24 and ATP-T-20. Increasing the injection air velocity has decreased NO emissions by 25% (between cases ATP-T-31 and ATP-T-24) and by 45% (between cases ATP-T-31 and ATP-T-20). At an equivalence ratio of 0.6, NO emissions were decreased from 5.6 PPM (case ATP-T-31) to 4.15 PPM (case ATP-T-24) and then to 3.19 PPM (case ATP-T-20). Such reduction emphasizes the important role of the air injection velocity and its effect on emissions through flame

anchoring prevention and enhanced mixing. Lower emissions were also demonstrated at lower equivalence ratios with 2PPM demonstrated at an equivalence ratio of 0.5 for case ATP-T-20.

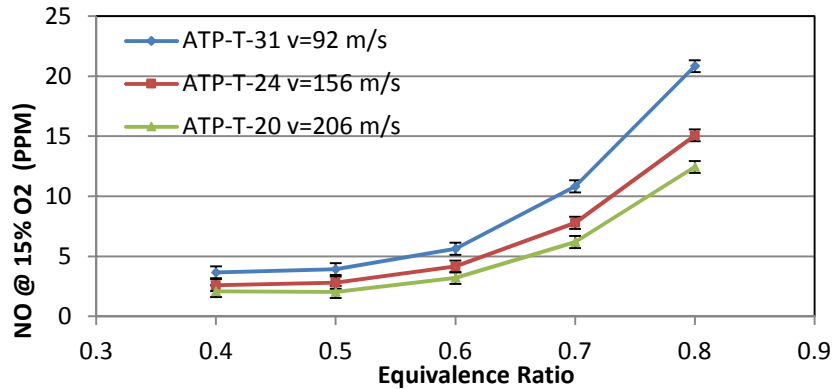


Figure 6-17 NO emissions for different injection velocities. Inlet air temperature =600K

Figure 6-18 shows experimentally measured CO emissions for different air injection velocities discussed with preheated air temperature of 600K. The trend obtained with these measurements agrees with the previously measured data for the 300K case where the velocity affected CO emissions as emission increases with increase in air injection velocity. This can be related to the decrease in residence time inside the combustor as the injection velocity is increased. However, the increase in CO emissions with increase in air injection velocity was less compared to the room temperature air injection. This can be related to the effect of air preheating on CO emissions. CO emissions were found to decrease with increasing inlet air temperature under lean combustion conditions. The increases temperature aids in complete CO to CO<sub>2</sub> conversion

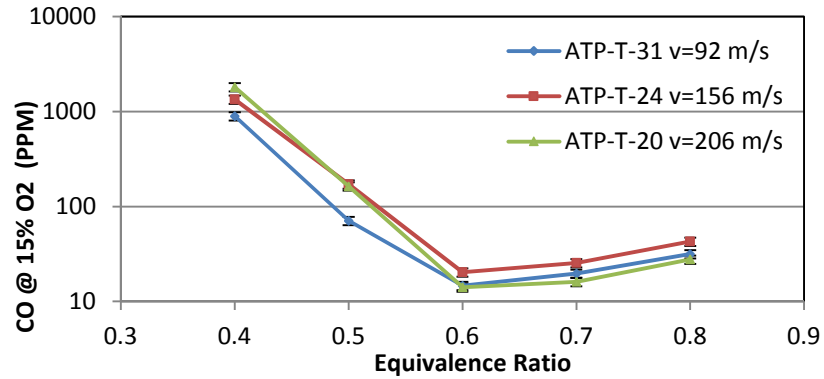


Figure 6-18 CO emission for different injection velocities. Inlet air temperature =600K

The radical intensity distribution of OH\* chemiluminescence was acquired for cases ATP-T-31 and ATP-T-20. The acquired images are shown in Figure 6-19. For the different equivalence ratios examined, it can be seen that in case ATP-T-20, the reaction starts more downstream as compared to case ATP-T-31. This can be attributed to the higher air injection velocity that leads to the flame stabilizing further downstream. As the flame reaction zone moves downstream, more time is given prior to spontaneous ignition. This allows for better mixing between the injected mixture of air and fuel and the recirculated hot active species. Also it can be seen that the reaction is more distributed in case ATP-T-20 compared to that of ATP-T-31, especially at higher equivalence ratios of 0.8 and 0.7, where higher OH\* signal was recorded away from the main reaction zone. Relating reaction behavior (obtained through OH\* chemiluminescence) to pollutants emission, one can see the desirable impact of higher injection velocities on NO emissions. NO emission decreased from 21 PPM to 12.5 PPM at an equivalence ratio of 0.8 (where reaction distribution is more evident). This reduction in emissions is directly related to the better mixture preparation prior to

ignition and the resulting enhanced reaction distribution. For all the cases, the reaction intensity decreased and moved further downstream with decrease in equivalence ratio, see Figure 6-19.

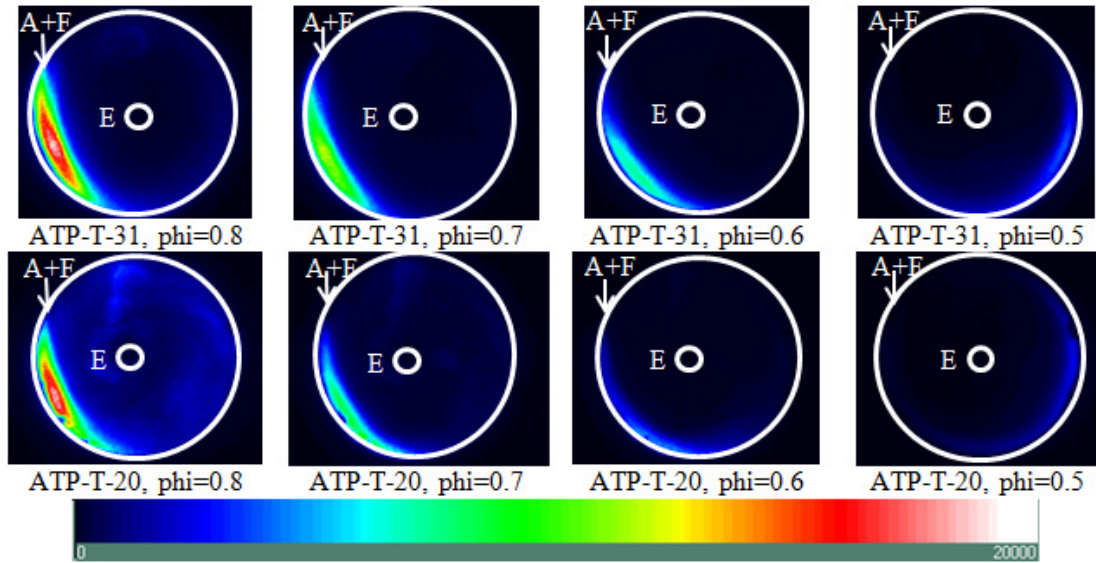


Figure 6-19 OH\* chemiluminescence for cases ATP-T-31 and ATP-T-20

### 6.3.3.3. Preheated Air Non-Premixed Experiments

Non-premixed experiments with inlet air preheated to a temperature of 600K, simulating the combustor intake temperature after the compressor, yielded similar results. Figure 6-20 shows the recorded NO emissions for the three cases; ATF1-T-31, ATF1-T-24 and ATF1-T-20. Increasing the injection air velocity has decreased NO emissions by 24% (between cases ATF1-T-31 and ATF1-T-24) and by 46% (between cases ATF1-T-31 and ATF1-T-20). At an equivalence ratio of 0.6, NO emissions were decreased from 9.6 PPM (case ATF1-T-31) to 7.33 PPM (case ATF1-T-24) and then to 5.82 PPM (case ATF1-T-20). Such reduction emphasizes the important role of the air injection velocity and its effect on emissions through flame anchoring prevention

and enhanced mixing in both premixed and non-premixed combustion mode. Under non-premixed combustion, ultra-low emission of NO was demonstrated at an equivalence ratio of 0.5 (2.28 PPM of NO) for case ATF1-T-20.

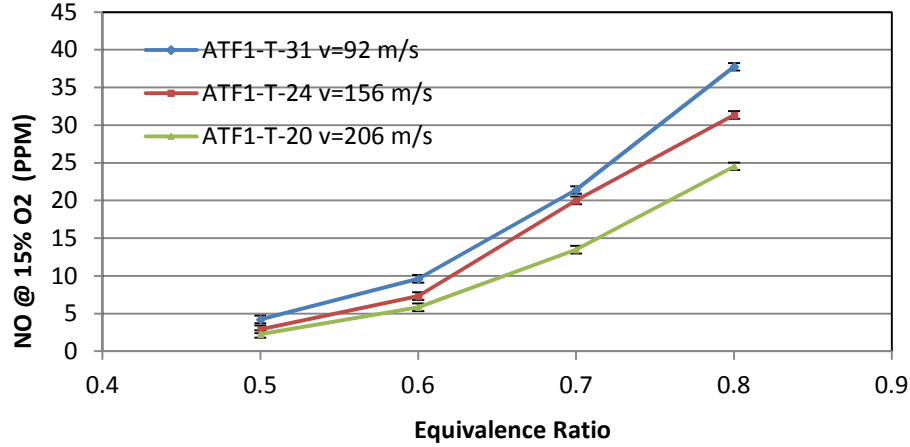


Figure 6-20 NO emissions for different injection velocities, non-premixed. Inlet air temperature=600K

This reduction might be somewhat surprising. As the air injection velocity increases, the velocity ratio between the cross flow and the fuel jet dramatically decreases from 1.108 (case ATF1-T-31) to 0.495 (case ATF1-T-20). The Velocity ratio can be defined as follows [83]:

$$VR = \left[ \frac{\rho_j v_j^2}{\rho_{cf} v_{cf}^2} \right]^{1/2} \quad (\text{Equation 6-1})$$

where  $\rho$  is the density,  $v$  is the velocity, and the subscripts  $j$  stands for the fuel jet,  $cf$  stands for crossflow [83]. As the velocity ratio decreases, the fuel jet penetration decreases [84]. This affects mixing dramatically; however, this effect is reversed by the dominance of turbulence at such low velocity ratios. The turbulence is enhanced

through increasing the air injection velocity (increasing the cross flow velocity) as shown in Figure 6-14 leading to an overall enhanced mixing and lower NO emissions.

Figure 6-21 shows the experimentally measured CO emissions for different air injection velocities discussed with preheated air temperature of 600K under non-premixed combustion mode. The trend obtained with these measurements agrees with the previously measured data where the velocity affected CO emissions as emission increases with increase in air injection velocity. This is specifically true comparing the cases ATF1-T-31 and ATF1-T-24. For case ATF1-20, CO emissions were actually lower compared to the other cases (ATF1-T-31 and ATF1-T-24).

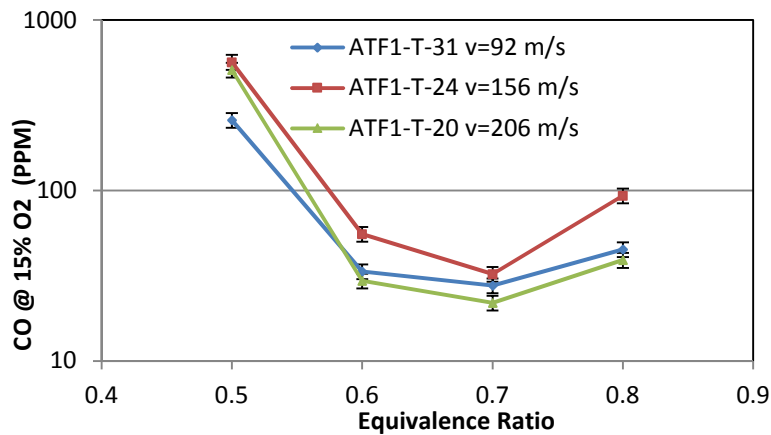


Figure 6-21 CO emission for different injection velocities, non-premixed. Inlet air temperature =600K

#### 6.3.3.4. Pressure Loss

Lower pressure loss is desirable to achieve higher efficiency from the gas turbines. Previous researches have indicated that the higher the air injection velocity, the bigger the pressure drop will be in the combustor [58]. Pressure loss across the CDC combustor with air preheat temperature of 600K was measured and is presented in Figure 6-22. From the figure it can be noted that pressure loss of less than 8% can be

achieved at the most desirable operating condition (at an equivalence ratio of 0.6). Pressure loss is observed to increase with equivalence ratio, possibly due to higher heat addition at higher equivalence ratios. Pressure loss was also measured in cold flow condition at air inlet temperature of 600K and 300K and is shown in Figure 6-22. These values are lower than the recommended values of gas turbine combustors in cold flow (4-8%) [3].

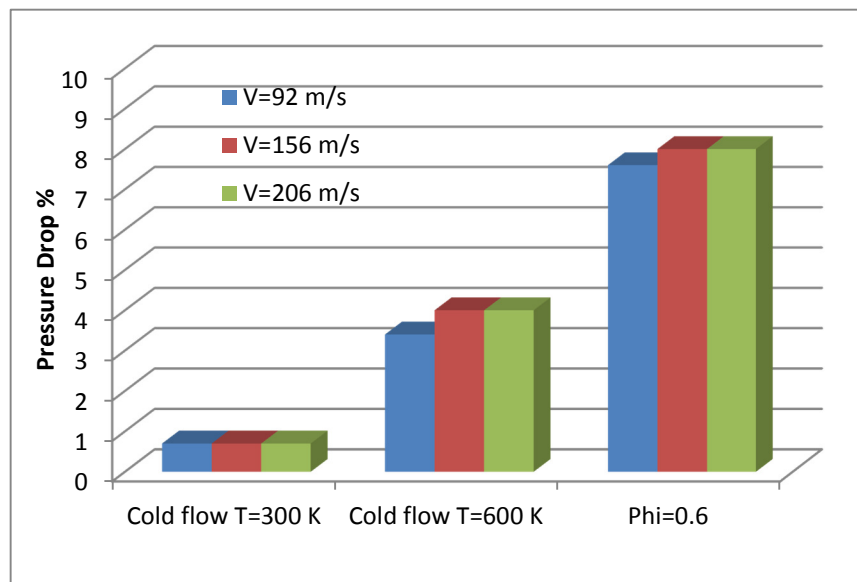


Figure 6-22 Pressure loss percentage for different air injection velocities

#### 6.3.4. Summary

Experimental investigations outlined the important role air injection velocity and recirculation play in pollutants emission reduction. Isothermal particle image velocimetry measurements have shown that increasing air injection velocity increased the recirculation ratio and the velocity fluctuations (turbulence) in the combustor. Increased recirculation ratio is critical for mixing hot active species with fresh air and

fuel stream. Increased turbulence aids in mixing between these streams to result in a more distributed combustion as compared to lower air injection velocity.

Pollutants emission measured for different air injection velocities demonstrated that the higher the air injection velocity, the lower the recorded NO emissions. Increasing the injection velocity from 46m/s to 103 m/s reduced NO emissions by about 20%. When preheated air is employed, the reduction in NO emissions was found to increase. NO emission for injection velocity of 92m/s at an equivalence ratio of 0.6 was found to be 5.6 PPM. Increasing the air injection velocity to 206m/s reduced NO emissions to 3.2 PPM resulting in 44% reduction. NO Emission as low as 2 PPM has been demonstrated under increased air injection velocity. The increase in air injection velocity did not impart large pressure drop in the combustor as the pressure drop for reacting cases remained almost constant for the different velocities examined. The obtained data outlines the important role air injection velocity plays for near zero emissions of NO.

#### **6.4. Air Dilution**

Air and fuel dilution with flue gasses have been studied with emphasis on the effect of air dilution versus fuel dilution on nitric oxides emissions [142]. It was concluded that fuel dilution has the greater effectiveness as compared to air dilution in practical applications due to the enhanced turbulent mixing and heat transfer. Dilution of fuel with inert gases and lower heating value fuel has been investigated for combustor operation with ultra-low emission. Nitrogen addition has been shown to decrease NO emissions by 50% to achieve emissions of 2 ppm of NO 12 ppm of CO as shown in

section 5.1 [143]. The same trend was observed with air and carbon dioxide dilution [144]. The decrease in pollutants emission is attributed to the fuel jet having higher jet momentum (due to the added diluents). Also, the added mass acts as a thermal sink that lowers the overall combustor temperature which significantly lowers thermal  $\text{NO}_x$  through Zeldovich mechanism [9].

In this section, fuel dilution effects with different amounts of air (and also air dilution effects with different amounts of fuel) are investigated with emphasis on achieving ultra-low emissions comparable to or less than those from novel premixed combustion in distributed combustion without encountering any flashback or combustion instabilities. Different dilution scenarios were examined on a different combustor, one was of special interest, where NO emissions were as low as premixed combustion case [145]. It is worth noting that in these dilution cases, the mixture formed (Fuel added to Air, or Air added to Fuel) had an equivalence ratio that is well outside the fuel flammability limits. Consequently no flashback is possible. The relevant data for this experiment can be found in appendix D. The relevant case (case 2) is further investigated in the swirling CDC combustor with view to evaluate the beneficial aspects of dilution and how that depends on the flowfield of the combustor.

#### 6.4.1. Experimental Investigations

The combustor was operated at a heat load range of 3.9-6.25 kW for equivalence ratio variation from 0.5-0.8, using methane as the fuel. Three cases were compared in this investigation, a fully premixed case (ATP), a non-premixed case (ATF1), and the dilution case. Table 6-4 summarizes the cases investigated

Table 6-4 Experimental parameters for air dilution

Case	Air (Top) Stream			Fuel (Cross) Stream			Overall Equivalence Ratio
	Air flow (SLPM)	CH <sub>4</sub> flow (SLPM)	$\Phi$	Air flow (SLPM)	CH <sub>4</sub> flow (SLPM)	$\Phi$	
Premixed	137	11.5-7.2	0.8-0.5	-	-	-	0.8-0.5
Non-Premixed	137	-	-	-	11.5-7.2	-	0.8-0.5
Dilution	119.9-126.3	2.5-1.6	0.2-0.12	17.1-10.7	9-5.6	5	0.8-0.5

The main air stream was preheated to 600K for all the configurations investigated here. The fuel temperature was 300K upon injection. Air was injected at elevated temperature of 600K to simulate the heating due to the compressor in a gas turbine engine. A schematic for the experimental facility is shown in Figure 6-23.

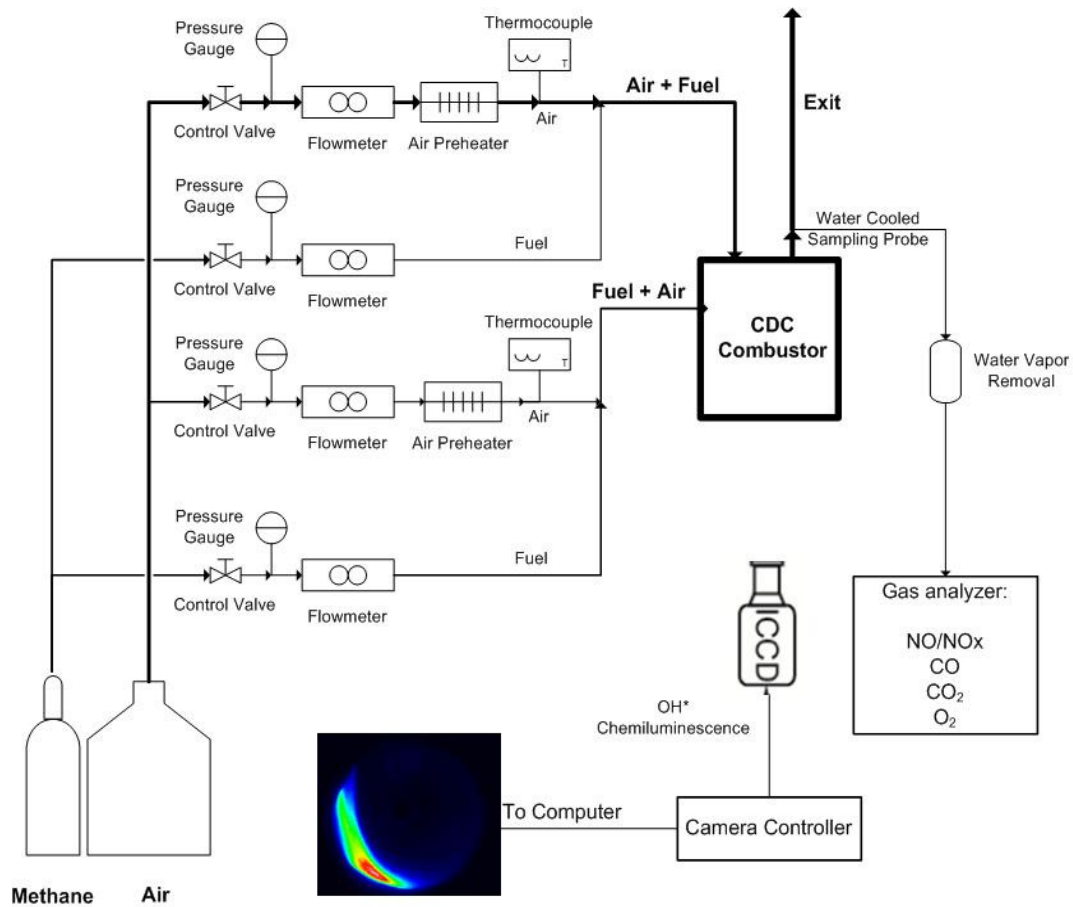


Figure 6-23 Schematic of the air dilution experimental facility

In the dilution case, air and fuel flow rates are split into two streams. The main “top stream” injects most of the air flow rate, while the other “cross stream” injects most of the fuel. Fuel is added to the “top stream” and air is added to the “cross stream” such that the equivalence ratio for each streams is well outside of the flammability limits for methane-air combustion. Such mixing method is expected to yield favorable results as the mixing required inside the combustor is less compared to the non-premixed combustion case. Also, the higher cross stream momentum is expected to affect the turbulence inside the combustor, significantly enhancing the mixing process. The cross flow equivalence ratio was kept at 5. The top flow equivalence ratio varied from 0.2 to 0.12. Both air and fuel flow rates were varied to furnish the combustor with the required air and fuel to operate in the desired range of equivalence ratios. The experiments were done successively to ensure that the comparison between these three cases is at the same conditions. The experiments were repeated multiple times for ensure consistency and repeatability.

#### 6.4.2. Results and Discussion

Figure 6-24 shows the measured NO emissions for the premixed, non-premixed and dilution cases. Air dilution demonstrated favorable performance as NO emissions were substantially lower than that resulting from non-premixed combustion. Compared to premixed case, NO emission were almost as low as the premixed case especially at lower equivalence ratio. Previously, this air dilution case has demonstrated emissions equal to those of premixed case [145]. However, due to the difference in the flow field, the behavior is different. This difference in the flowfield arises from the center exit

tube which prevents the fuel (cross jet) from further penetration into the combustor, see Figure 4-12.

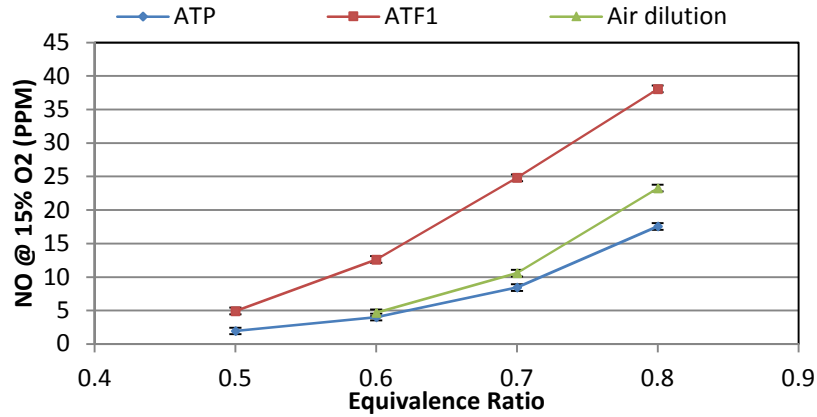


Figure 6-24 NO emission for premixed, non-premixed, and air dilution case

The CO emissions were also recorded for these cases, and shown in Figure 6-25.

Air dilution case demonstrated higher CO emissions compared to the premixed case, however, this emissions were lower compared to the non-premixed case. This is in contrast with previously reported CO data on air dilution under similar condition, where similar cases produced higher CO emissions compared to non-premixed and premixed combustion cases [145]. This can be related to the difference in the combustor geometry and heat release intensity where the combustor examined herein has lower heat release intensity.

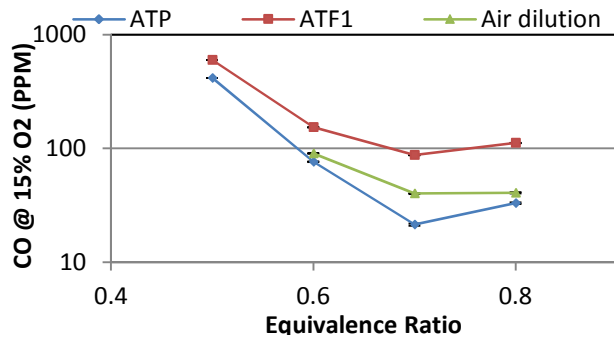


Figure 6-25 CO emission for premixed, non-premixed, and air dilution case

To further examine the effect of air dilution, OH\* chemiluminescence was used to identify the reaction zone and outline any differences between traditional non-premixed combustion and the air dilution cases. The obtained OH\* intensity is shown in Figure 6-26 for both cases, where it can be seen that the air dilution changed the reaction zone location into a larger area compared to a crescent like zone near the wall of the combustor. This is related to the higher jet momentum of the fuel diluted with air compared to the non-premixed. The increased momentum of the fuel jet leads to a better mixing process and bends the main air jet to change the reaction zone as shown. Such better mixing process and enlargement in the reaction zone location led to the demonstrated decrease in NO emissions.

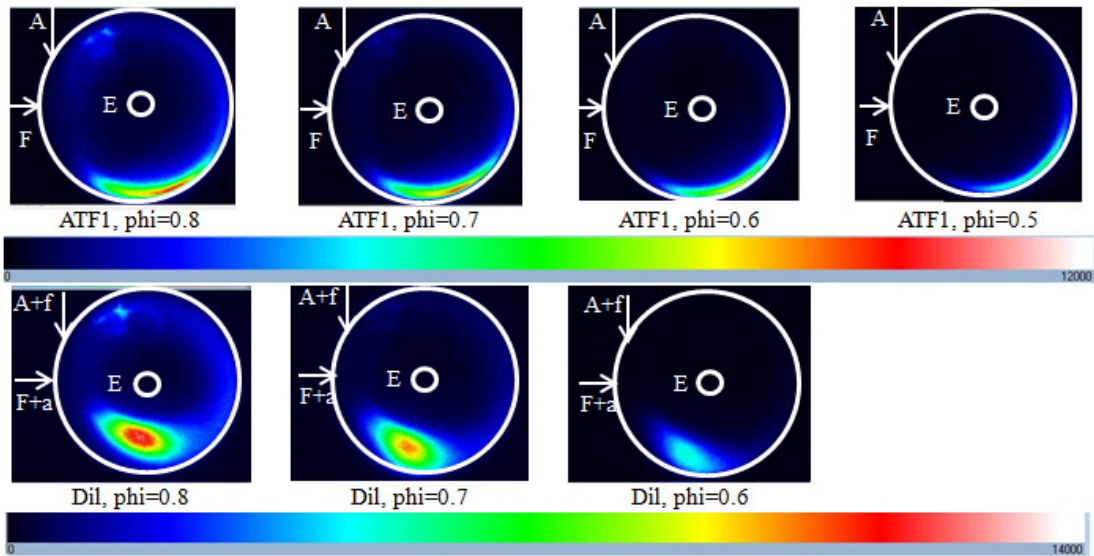


Figure 6-26 OH\* chemiluminescence intensity distribution for both non-premixed and dilution cases

### 6.4.3. Summary

Novel air and fuel mixing, where fuel is diluted with air while portion of the fuel is introduced in the main air jet, has demonstrated NO emission comparable to those encountered in premixed combustion mode. Fuel dilution, characterized by high cross jet momentum, not only demonstrated NO emission comparable to premixed mode of combustion operation but also lower CO emissions compared to non-premixed combustion. Such novel mixing technique eliminates the possibility of flame flashback as the equivalence ratio in the jets is outside the methane air flammability limit. OH\* intensity distribution showed that the combustion zone is affected by the cross jet momentum and equivalence ratio. The ability of this mixing technique to demonstrate near zero emission suggests very good performance with NO emissions equivalent to that of premixed combustion without any of the premixed combustion drawbacks, such as, flame flashback and combustion instability.

### 6.5. **Dual Injection**

For all the investigations performed, single injection was used, either as one air/fuel premixed injector or one air injector and one fuel injector for non-premixed combustion. Also the combustor used was a lab scale test combustor operated at a heat load of 6.25 kW. A conventional combustor for electricity generation can release up to 48,000 kW of energy through combustion which indicates a scaling factor in the order of thousands. Different approaches exist for scaling up have been discussed in the literature [2]. The scaling up techniques includes keeping the injection velocity constant (CV), keeping the residence time constant (CRT), increasing both the injection

velocity and diameters (Cole’s approach [146]), and keeping the thermal intensity constant [54]. Table 6-5 summarizes these approaches stating the scaling in terms of thermal load,  $Q$ , defined as the amount of energy released within the combustor

Table 6-5 Different scaling approaches

Scaling approach	Geometric scaling	Velocity scaling	$\tau_{\text{mixing}}$ (D/U)	Heat release intensity
CV	$\sim Q^{1/2}$	$\sim \text{Const.}$	$\sim Q^{1/2}$	$\sim Q^{-1/2}$
CRT	$\sim Q^{1/3}$	$\sim Q^{1/3}$	$\sim \text{Const.}$	$\sim \text{Const.}$
Cole [146]	$\sim Q^{1/4}$	$\sim Q^{1/2}$	$\sim Q^{-1/4}$	$\sim Q^{1/4}$
Kumar [54]	$\sim Q^{1/3}$	$\sim \text{Const.}$	$\sim \text{Const.}$	$\sim \text{Const.}$

Following Table 6-5, CV approach leads to increase in mixing time and significant decrease in thermal intensity, whereas CRT approach resulted in very high velocity which will result in unacceptable levels of pressure drop across the combustor. However, thermal intensity and mixing time is constant for CRT approach. In Cole’s [146] approach the velocity is increased significantly and this does not seem to be a feasible solution for scaling a CDC combustor in terms of pressure drop inside the combustor. Increasing the air injection velocity increases the pressure drop inside the combustor, limiting the amount of energy to be extracted in the turbine [58]. Such pressure loss was also demonstrated in chapter five regarding air injection velocities. In Kumar’s [54] approach the geometry was scaled based on the CRT approach and the number of air and fuel injection ports were increased to maintain constant mixing time.

The multiple air and fuel injection into a combustor requires further examination. Fuel and air staging has been used in burners and furnaces to control pollutants

emission. However, those stages are generally located close/far enough from each other to produce/eliminate flame to flame interaction (a reaction zone affected by the following or preceding reaction zone) in any desirable way. Thus an interaction between different injection ports needs to be studied. Evaluating the behavior of multiple air and fuel injectors and whether they form one large reaction zone or form multiple small reaction zones is critical. In this section, multiple injector behavior is investigated with the lab scale combustor modified to allow for two injectors rather than single injection. The two injector configuration (dual injection) is expected to reveal the benefits and drawbacks of using such injection scheme over single air and fuel injection. The air/fuel injection velocity was kept constant in all the experiments. NO and CO emissions are recorded to outline the combustor behavior under dual injection configuration. Furthermore OH\* chemiluminescence intensity was captured to outline the reaction zone behavior under different operational conditions.

#### 6.5.1. Experimental Facility

The combustor performance was evaluated under single and dual injection configurations using methane fuel. The combustion chamber utilized was a cylindrical chamber; air was injected tangentially at half the height of chamber. For Dual injection configurations, both injectors were located at half the height of the chamber also. To enhance the residence time of reactants in the combustor, a tube was extended inside the combustor for product gas exit. Figure 6-27 shows a schematic diagram of the combustor used along with the combustor itself.

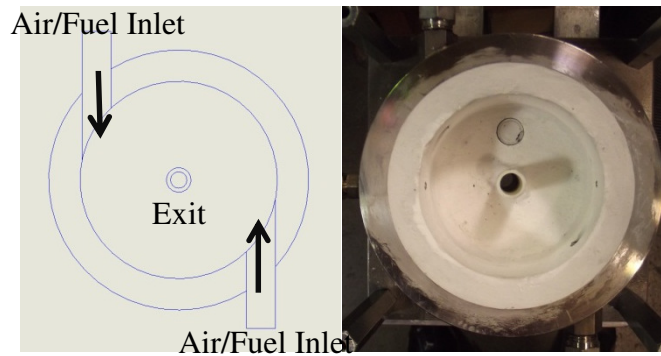


Figure 6-27 Schematic diagram of the combustor with extended axial exit “at” (left: top section at mid location, and right: combustor interior).

To maintain constant air/fuel injection velocity, the diameter of the injectors in the two injector configuration (dual injection) is reduced. The total injection area has to be constant, dictating that the diameter of the injectors used in dual injection is to be 0.707 that of the diameter used in single injection. The inlet air temperature to the combustor was preheated to 600K to simulate elevated air temperatures at inlet to the combustor (outlet temperature from the gas turbine compressor). Figure 6-28 shows the combustor operating under dual injection mode, where colorless (no visible emission) combustion is obtained.

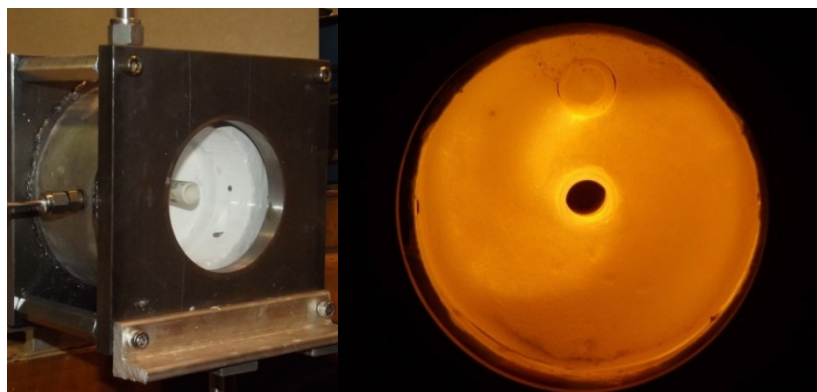


Figure 6-28 Colorless combustion with dual injection combustor

### 6.5.2. Experimental Investigations

The investigations performed on the experimental combustor were aimed at comparing the performance of combustor under single and dual injection scenarios. Also the fuel distribution was varied between the injectors in the dual injection case. Table 6-6 summarizes the investigations reported here along with the variables manipulated for each investigation. The case name indicates fuel injection method, where ATP indicates single injection, while ATP-D indicates dual injection.

Table 6-6 Experimental parameters for dual injection

<b>Case No.</b>	<b>Heat Load (kW)</b>	<b>Variable</b>
ATP	6.25-3.9	Equivalence ratio
ATP-D	6.25-3.9	Equivalence ratio
ATP-D-F%	4.72	Fuel Distribution

### 6.5.3. Results and Discussion

Experiments were conducted using two air/fuel injectors at opposite sides of the combustors. The injectors were sized to result in the same injection velocity as that of the single injector experiment. Dual injection is expected to result in lower NO emissions as the reaction zone is now split into two, leading into more distribution of the reaction across the combustor. Figure 6-29 shows the NO emissions obtained under dual injection compared to the single injection case. Results showed that dual injection resulted in higher NO emissions, which might be counter intuitive. However, flame to flame interaction might be causing this. If the air/fuel mixture from the first injection does not completely burn before the second injection location, the colder fresh reactants may interrupt the reaction and may result in higher local equivalence ratio and/or local hot spots. It is of extreme importance to distribute the reaction (distributed reaction

zone) rather than create a localized area with higher reaction rate that contributes to higher thermal NO emissions.

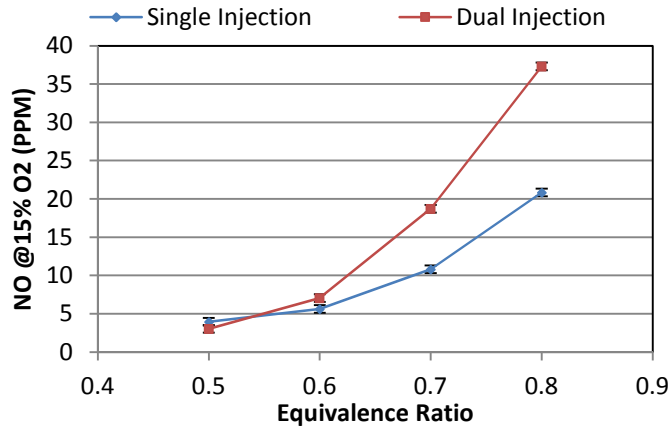


Figure 6-29 NO emissions for single and dual injection cases

To investigate the cause of such high NO emissions, OH\* chemiluminescence was used to identify the reaction zone and outline any high reaction rate spots. The obtained OH\* intensity is shown in Figure 6-30 for both single and dual injection cases, where it can be seen that the OH\* intensity scale for the dual injection case is lower than single injection (maximum of 11000 instead of 17000 a.u.). However, it can be seen that the reaction zone created for each injector is not equal. The second reaction zone (on the right of the combustor) always has a higher intensity compared to the first reaction. This indicates that air and fuel injected from the first jet reacts (on the left), then the reaction rate is dramatically decreased due to the introduction of the fresh reactants from the second jet (to the right). Now as the mixture starts to react again, the equivalence ratio is not uniform leading to a somewhat concentrated reaction and higher reaction rate as seen through the higher OH\* chemiluminescence detected at the second reaction zone.

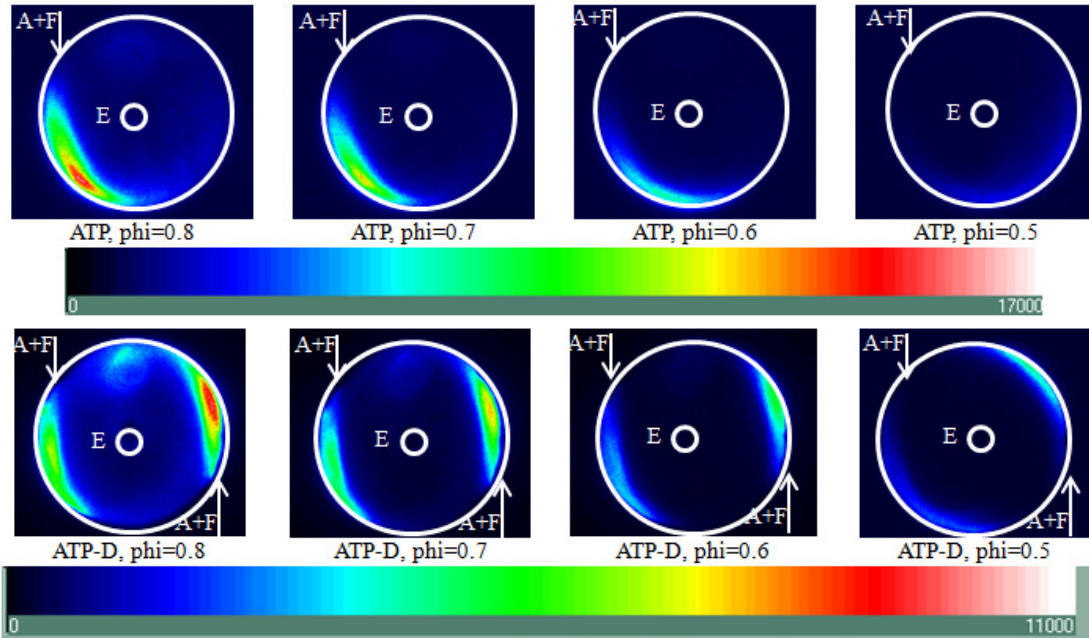


Figure 6-30 OH\* chemiluminescence intensity distribution for premixed single and dual injection

As a means to better control the reactions, the fuel distribution between both injectors is manipulated. Up to this point, for dual injection, the amount of air and fuel was split evenly between both injectors. Here the air was evenly split; however, the fuel flow rate was distributed differently. For each case the amount of the fuel in the first injector is described as a percentage of the total required fuel flow rate for the combustor to operate at the required condition. The change in fuel distribution will change the local equivalence ratio of each jet (the global equivalence ratio is kept constant), leading to a change in the local flame characteristics such as flame speed and temperature. Figure 6-31 shows the NO emissions recorded for equivalence ratio of 0.6 varying the fuel distribution.

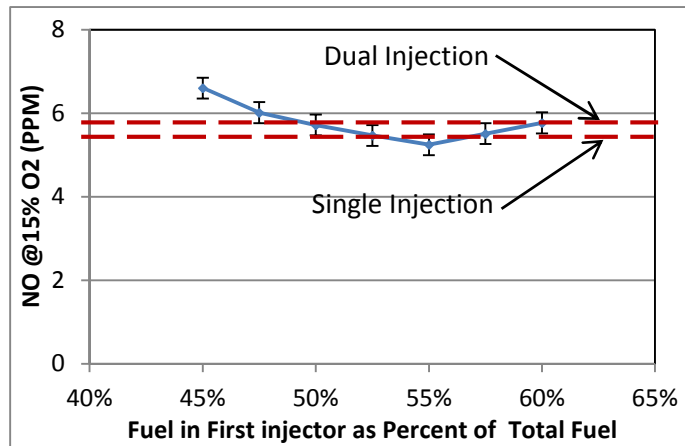


Figure 6-31 NO emissions for fuel distribution variation dual injection cases

From Figure 6-31 it can be seen that careful distribution of the fuel between both injectors can decrease emissions to levels lower than those achieved with single injection. This result is important for scaling up the combustor as single injection can pose difficulties in large size combustors due to extremely high flow velocities dictated to deliver the required flow rates to the combustor.

OH\* chemiluminescence intensity distribution was also captured with different fuel distributions in order to evaluate the reaction zones behavior. The captured distribution is shown in Figure 6-32. Starting from 45% of the overall fuel introduced at the first injector, it can be seen that the second reaction zone (at the right of the combustor) exhibits higher intensity compared to the first reaction zone (on the left of the combustor). As the amount of the injected fuel at the first injector is increased, the first reaction zone intensity increases and the second reaction zone intensity decreases. At about 55% of the fuel dispensed through the first injector, one can see that the reaction zones are almost identical in terms of intensity. Further increase in the fuel dispensed in injector one resulted in an increase in the first reaction zone intensity and a decrease

in the second reaction zone intensity. Relating this behavior to Figure 6-31, one can see that, NO emission behavior agrees favorably well with reaction zone intensity. Minimum emission of NO corresponds to the case where both reaction zones were identical in intensity. Whenever one of the zones becomes more intense than the other, NO emissions are set to increase. Experiments conducted at a higher heat lead of 5.91 and an equivalence ratio of 0.7 showed similar results, with fuel distribution of 55% at the first injection and 45% for the second injector demonstrated the lowest NO emission compared to the other fuel distributions examined.

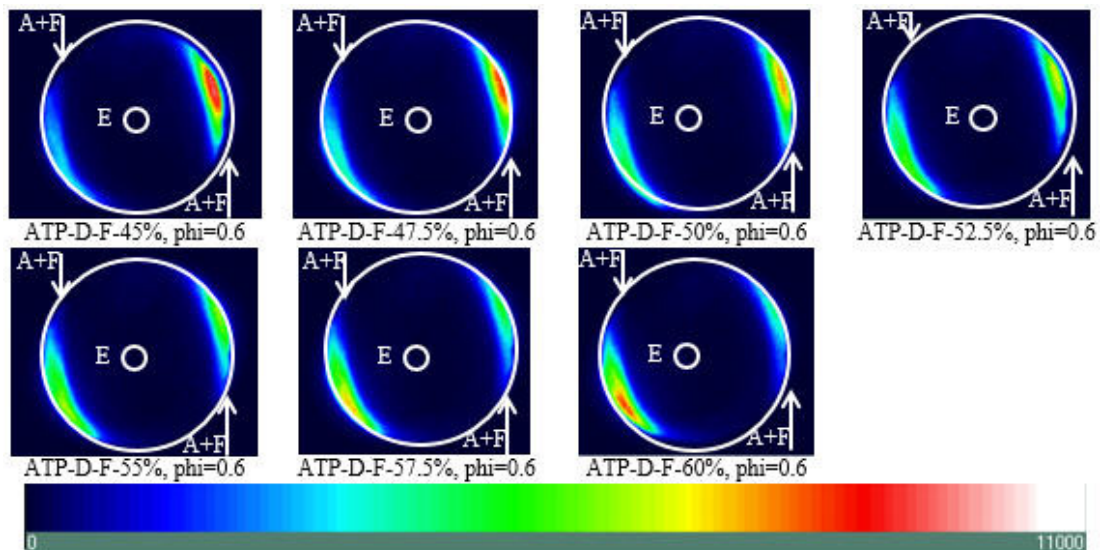


Figure 6-32 OH\* chemiluminescence intensity for dual injection fuel distribution variation cases

#### 6.5.4. Dual injection under non-premixed combustion

Dual injection experiments have been also performed under non-premixed combustion conditions. Pollutants emission results showed that under non-premixed combustion, the reaction proceeded in a diffusion like manner, where NO emissions were almost constant regardless of the overall equivalence ratios. OH\*

chemiluminescence images showed that, similar to premixed combustion cases Figure 6-30, the two formed reaction zones were not equal in size or intensity, with the second reaction zone being much stronger. Even when fuel was not furnished equally between both injectors, the emissions remained high. This can be related to the fact that, in non-premixed combustion, more time is required for mixture preparation prior to ignition. In all the investigation that we have performed, non-premixed reaction zone was found to be further downstream as compared to the premixed reaction zone. In the dual injection experiments, where air and fuel are injected separately to mix and ignite prior to the second injection, the time given for such mixing and ignition is not enough even under non-equal fuel distribution. This behavior resulted in no change in the pollutants emissions with fuel division variation. This lack of adequate time for mixing and ignition can be mitigated in larger combustors where better control on the mixing and ignition can be exerted, furnishing the flow with the required time.

#### 6.5.5. Summary

Results obtained with single injection of air and fuel demonstrated ultra low emissions, emissions as low as 5 PPM NO were demonstrated at an equivalence ratio of 0.6 with 10 PPM of CO. Lower NO emissions were also demonstrated at lower equivalence ratios. Experiments with dual injection demonstrated higher emissions than those demonstrated with single injection. For the same equivalence ratio, NO emission increased by about 20%, with minimal change in CO emissions. Increase in NO emissions outlined that there is an interaction between both injections jets leading to an un-equal distribution in the flame region. OH\* chemiluminescence verified the

presence of un-equal reaction intensity distribution as one of the flame regions was stronger than the other. Such higher reaction intensity gives rise to local temperature (hot spots) contributing to the formation of thermal  $\text{NO}_x$ .

Fuel flow rate distribution was modified to circumvent unequal fuel distribution. Instead of air and fuel being split evenly between both injections, the amount of fuel for each injector is manipulated to control the strength of each reaction zone. Such fuel variation changed the local equivalence ratio of the jet affecting different flame characteristics such as flame speed. Slightly increasing the fuel amount in the first jet (about 55% of total fuel) led to a decrease in NO emission compared to even fuel distribution. Also these emissions were lower than NO emission obtained with single injection arrangement at the same equivalence ratio. Consequently, fuel variation can be used as means to control flame characteristics and emissions to produce favorable performance and lower emissions than those demonstrated through single injection. This is of extreme importance for combustor scaling up as multiple injectors will be required to maintain adequate residence time and injection velocities within the combustor.

$\text{OH}^*$  Chemiluminescence intensity distribution showed that for the 55% fuel being injected in the first injector, the two reaction zones were of equal intensity as compared to other distribution scenarios examined. This emphasizes the importance of reaction distribution and the need to eliminate any concentrated reaction zone forming local hot spots. Further emission reduction can be achieved through enhancement in reaction distribution to achieve truly distributed combustion conditions.

## **7. Chapter Seven: Planar Laser Induced Fluorescence**

In the previous chapters, different geometries have been investigated in a quest to achieve ultra low emissions through distributed combustion. Investigations included changing the combustor geometry, air and fuel injection locations, injection velocity, and injector shape. In this chapter, further investigations are performed on our best performing geometry to try to quantify the reaction progression inside the combustor and characterize the reactive species recirculation in the combustor. For this purpose, planar laser induced fluorescence (PLIF) is used to detect the OH concentration in the combustor under different equivalence ratios. This technique is discussed next.

### **7.1. Planar Laser Induced Fluorescence Technique**

Planar Laser Induced Fluorescence is a 2-D diagnostic technique widely used in combustion diagnostics introducing a plane of light created by a laser passing through a region of interest (ROI). This technique is an extension of Laser Induced Fluorescence (LIF) which makes use of the molecular absorption and emission of energy in the form of light at high energy levels. In a general sense, a molecule absorbs a photon, which excites the electrons of that molecule to a higher energy state. Following this excitation, the molecule naturally tends to relax back to a balanced electron configuration, releasing energy, again in the form of photons, in the process. This photon release is called fluorescence [147] [148]. Fluorescent absorption refers to wavelengths of light which, when introduced upon a molecule, result in fluorescence at a different wavelength.

### 7.1.1. Mechanics of LIF

The concept of fluorescence is relatively simple and follows the law of conservation of energy. Fluorescence is an energy absorption followed by a light emission. In the case of LIF, a photon generated by a laser excites a molecule to a higher energy state, but the molecule is unstable at that excited state. In order for the molecule to return to a lower, more stable, energy state, it emits energy in the form of a photon (light). The light emitted by the molecule makes up the fluorescent signal and can be generally detected by a camera to produce an image. The fluorescence signal or intensity directly correlates with the concentration of the emitting species [147] [148]. The fluorescence phenomenon is depicted in Figure 7-1 by an arrow going up representing the photon being absorbed and moving to a higher energy state, and then an arrow going back down representing a photon release and return to a lower energy level.

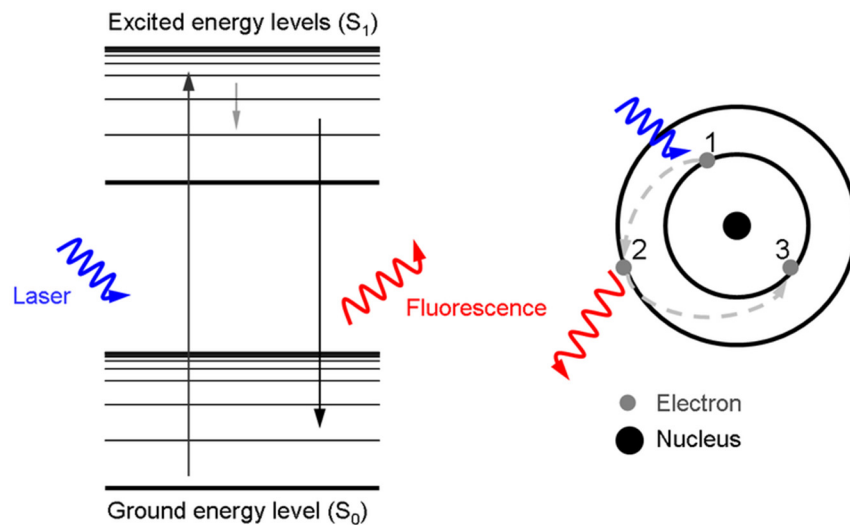


Figure 7-1 Laser induced excitation followed by spontaneous emission

For LIF, the absorption occurs at a precise wavelength and the emission occurs over a span of different wavelengths as depending on the excited state. LIF can be used to detect the concentration of several different molecules in a combustion environment. Most electronic transition occurs within the visible light spectrum and almost all important molecules in a combustion environment containing H, O, C, N, and S have been detected by LIF.

The unique spectral absorption bands for each molecule means each molecule will only absorb a photon at very specific wavelength. Table 7-1 shows a list of common species detected using LIF methods and the known range of electronic transitions for that molecule. In general, the fluorescence wavelength is different from that of the incident excitation and primarily occurs at longer wavelengths.

Table 7-1 Wavelength spectra for laser absorption fluorescence

<b>Molecule</b>	<b>Electronic Transition (nm)</b>
C <sub>2</sub>	230-330, 400-600
CH Radical	360-450, 430-500
CO	150-240 , 200-250
NO	195-340, 200-500
O <sub>2</sub>	170-220, 500-900
OH Radical	240-400

Electronic transition does not occur over the entire range listed in Table 7-1, but rather at a few discrete wavelengths within that range. Therefore, a prerequisite of any LIF experiment is a database of known absorption spectra for the molecule of interest. This research relied on work of Dieke *et al* [149] and augmented by LIFBASE [150], a freely available database system used for the simulation of electronic transition behavior for diatomic molecules. It has the capability to simulate both absorption and

emission, including the calculation of the collisional and Doppler broadening correction factors. The collisional correction factor is necessary to account for deviations from the theoretically expected fluorescence due to pressure effects. The Doppler broadening is due to a shift in the expected wavelength due to temperature effects [150].

### 7.1.2. Detection of the OH Radical

The most common molecule detected by LIF methods in combustion research is the hydroxyl (OH) radical. The OH molecule is good for combustion diagnostics because it is a radical produced in the intermediate reactions of combustion and then destroyed by the end of the combustion process. The OH radical is very abundant in most flames and its spectroscopy is well known [149]. The OH molecule is a great indicator of the behavior of the flame and can provide information on flame mixing, propagation, ignition, structure, and local extinction. OH-PLIF has a range of uses, including acting as a flame marker for flame location studies, temperature measurement, and determining OH species concentration [147] [148] [151] [152] [153].

## 7.2. **PLIF System Setup**

The excitation of OH radicals requires activation through a specific laser wavelength. Two systems are widely used in PLIF studies, the first being a pump laser that is coupled with optical parametric oscillator. The second system is a pump laser coupled with a dye laser and a UVT unit. A comparison between both systems have been performed where it was concluded that the dye laser system offers a narrower laser bandwidth coupled with a higher laser intensity [154]. The dye laser will be the

system of choice due to the before mentioned advantages. A brief description of the system will be given next.

#### 7.2.1. Dye Laser system

The dye laser system consists of main three components. The first being the pump laser, which is a powerful laser (Continuum PL9000) that is required to excite “pump” the dye. The second component is the dye laser unit (ND6000), where a dye of a certain composition is circulated and exposed to the pump laser. The dye is excited and produces a laser of a different wavelength that is dependent on the dye being circulated. This system can produce a laser of wavelength within the range of 420nm to 900nm. The dye laser produced is then introduced to the third and last component which is Ultraviolet Tracking (UVT) unit. The UVT unit contains a number of interchangeable crystals that doubles the laser frequency or mixes two different lasers, increasing the tuning range capabilities. For OH, a Rhodamine 590 dye is used, producing a laser that can be tuned between 552 – 584nm. With a doubling crystal, the produced laser can be tuned in the range 276-292nm. Most common OH excitation lies in the 281-285nm wavelength, making this arrangement adequate for our application. Figure 7-2 shows the laser system arrangement.

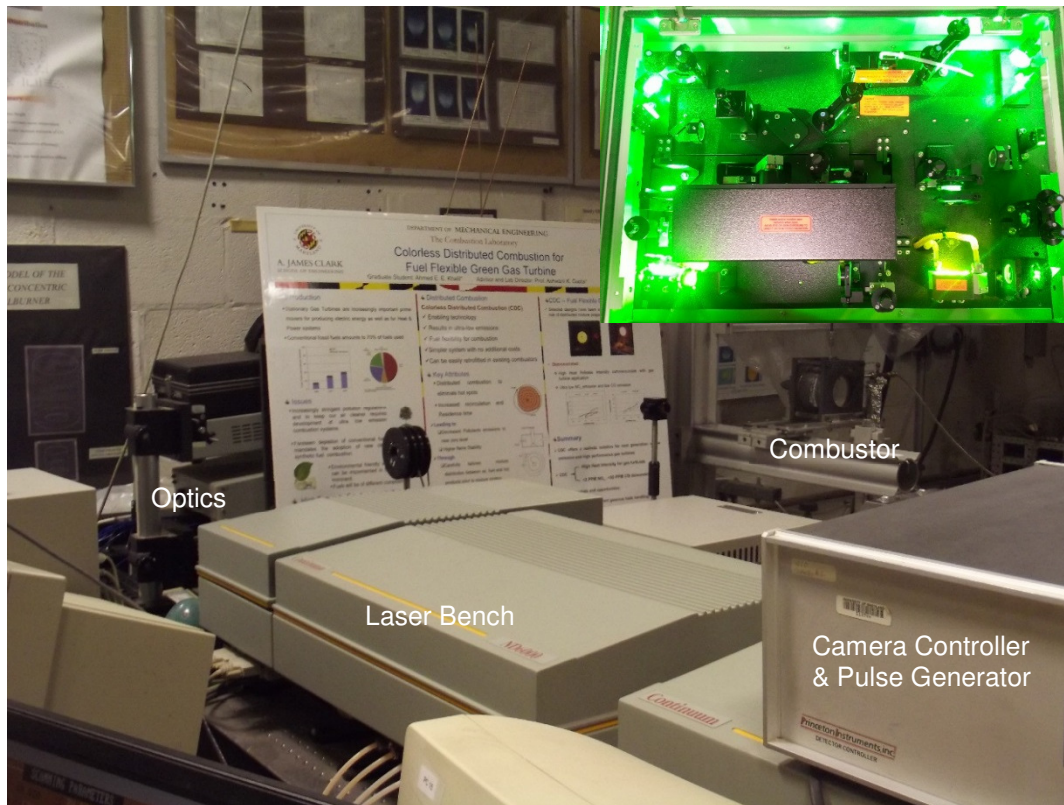


Figure 7-2 PLIF System at UMD Combustion Lab

### 7.2.2. System Optics

The laser produced through the dye laser system is a beam of about 4mm diameter. Optical arrangement is required to transfer that beam to the test section and transform it into a sheet for 2D imaging. For that purpose two 90 degrees prisms are used to adjust the beam height and direction to point towards the combustor test section. A plano-cylindrical lens was used to transform the beam into a sheet prior to the laser being introduced to the combustor. Figure 7-3 shows the optical arrangement for the experiment.

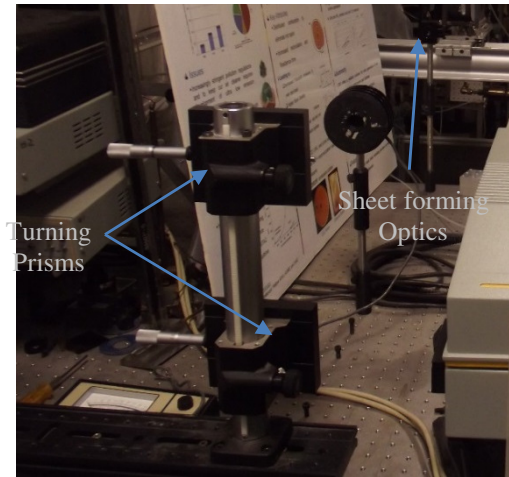


Figure 7-3 Optical arrangement for laser beam

The obtained laser sheet had a thickness of about 4mm and was directed to the test section. The laser sheet could be examined by using a white material/business card where the laser can be seen as a blue light. Figure 7-4 shows the formed laser sheet. To enhance the laser sheet power per unit area, a plano-convex lens was installed to reduce the laser sheet thickness to about 1mm.

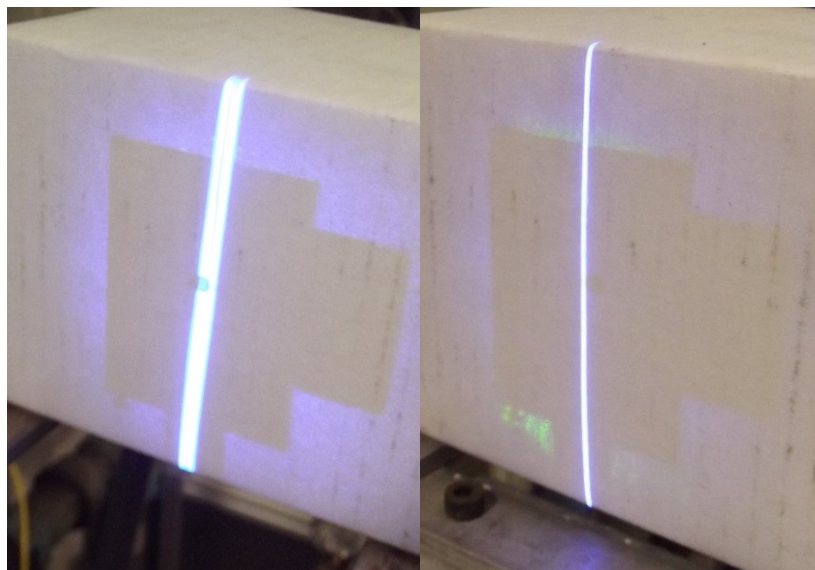


Figure 7-4 Formed UV laser sheet

### 7.2.3. Data Acquisition System

To capture the OH-PLIF signal, an Intensified Charge Coupled Device (ICCD) camera was used. To allow for short exposure time (60 ns), a high voltage pulse generator is required to power the camera's intensifier. The camera needs to operate in adequate timing with respect to the laser to capture the excited OH signal. The acquisition system was set up as follows. The high voltage pulse generator sends a signal to operate the flashlamp and signal the camera to prepare for acquisition. After a certain delay (that controls the laser power), a signal is sent from the pulse generator to the Q-switch to fire the pump laser. Afterwards, a high voltage signal is sent to operate the ICCD camera. This high voltage signal can be adjusted to control timing between the laser and the camera. The width of the high voltage pulse controls the exposure time of the camera. A feedback signal from the camera controller inhibits the pulse generator from emitting a new round of signals until the camera is ready to acquire new data. That arrangement dictated that the camera readout must occur in certain time that is less than the time between the laser shots (which is set at 10Hz, 100ms). Such limitation forced the camera to operate at a lower resolution to have such quick read out time using hardware binning. A 4x4 binning was used to enable the camera to acquire and read out the signal in a timely manner leading to a resolution of 144x96 pixels. A schematic of the timing scheme is shown in Figure 7-5.

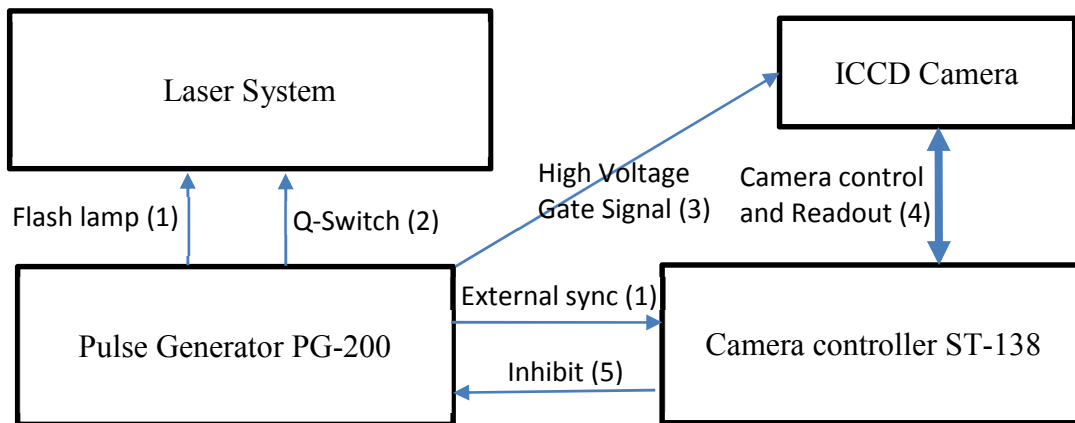


Figure 7-5 PLIF system timing sequence

#### 7.2.4. System Tuning

The OH excitation have been performed with different excitation laser wavelength, targeting various excited stated of the OH radical. The OH excitation possibilities for different energy levels can be found in the literature [147]. Valuable information about the nomenclature of different states with relevance to OH activation system [147]. The work of Dieke *et al.* is considered to be the most comprehensive measurements of different energy levels for the OH system [149]. Previous PLIF experiments performed at the combustion laboratory were aimed at characterizing the performance of swirl flames. For that purpose, the R<sub>2</sub>(14) transition was used to excite OH using a laser with a wavelength of 282.954 nm [155]. Choudhuri *et al.* studied hybrid gas fuel flames using the P<sub>1</sub>(8) line at 285.265nm [151]. The work of Meier *et al.* extended beyond measuring concentration of OH to include temperature measurements using two line PLIF technique. They used the Q<sub>1</sub>(1) and Q<sub>1</sub>(11) lines to obtain the OH images and temperature contours [152]. On the other hand, Hanson *et al.* activated the Q<sub>1</sub>(3) line in their work [156]. Cattolica *et al.* used the Q<sub>2</sub>(9) line to measure OH concentration in

a constant volume combustion chamber [157]. Sadanandan *et al.* investigated a gas turbine model using simultaneous PIV and OH-PLIF. In their investigations they used the Q<sub>1</sub>(8) line for OH imaging [158]. Swirl stabilized spray flames were also studied using OH-PLIF techniques using the Q<sub>1</sub>(9) transition [159]. Katoh *et al.* used the Q<sub>1</sub>(7) line to visualize OH radical distribution in methane hydrogen mixture flame [160]. Q<sub>1</sub>(6) line was also used for OH measurements in stagnation point reverse flow combustor [33].

This was a sample of the used lines to investigate OH concentrations. Most of the activation lines were in the Q<sub>1</sub> transition. These transitions are characterized by their high signal output compared to others as indicated by Dieke *et al.* [149]. To obtain the signal intensity using the existing system, an activation scan was performed across the range 281.5 nm to 285.278 nm. The laser was transformed into a sheet and directed to a standard propane torch to qualitatively identify the recorded OH signal. The following transitions were activated with various intensities. It is noteworthy that the maximum laser strength is at 281.5nm and it drops as we move away from that wavelength.

Table 7-2 gives the activated transitions

Table 7-2 Excited OH states

<b>Transition</b>	<b>States</b>
Q <sub>1</sub>	1-12
Q <sub>2</sub>	6, 8-11
R <sub>1</sub>	10, 12
R <sub>2</sub>	3-8,10
P <sub>1</sub>	4, 5
P <sub>2</sub>	5

A sample of the obtained images are shown in Figure 7-6. In general, all the  $Q_1$  transitions resulted in powerful signals. The experiments were also used to adjust the timing of the laser with the ICCD camera and adjusting the camera's gain.

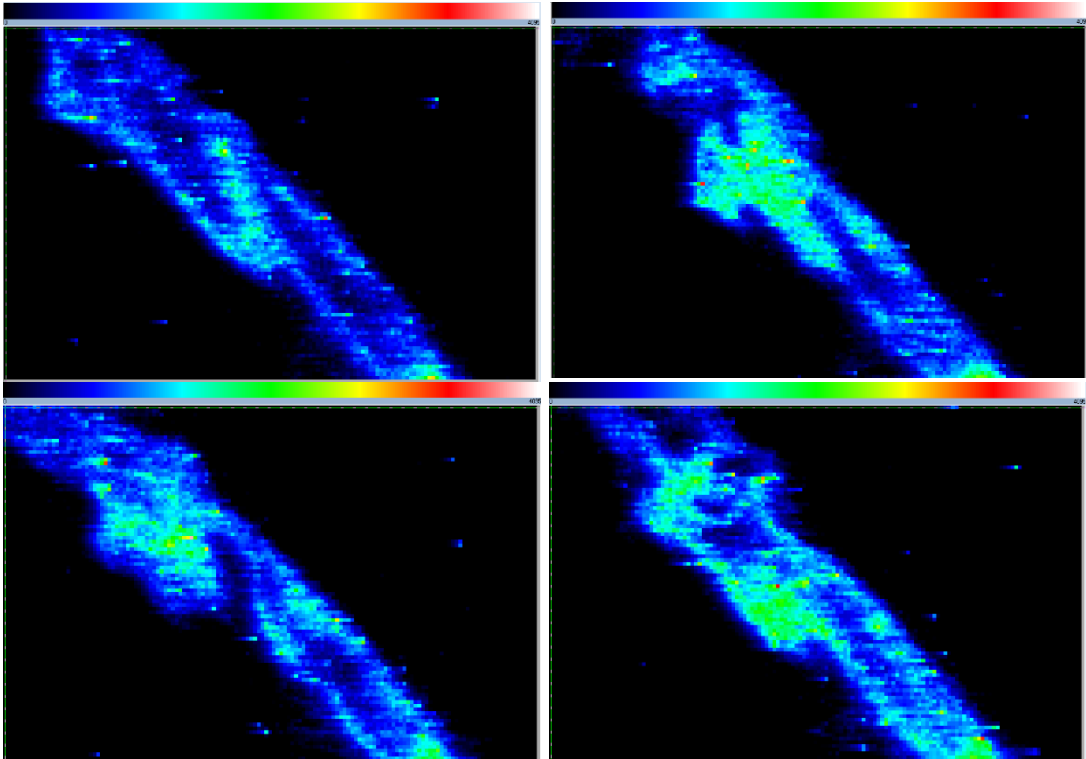


Figure 7-6 OH-PLIF signal for  $Q_1(6)$  excitation

#### 7.2.5. Combustor Setup

The combustor to be examined using OH-PLIF is shown in Figure 5-1. The combustor side was modified to allow the laser sheet propagation into the combustor. A side slit was added to the combustor side which was sealed using a quartz segment with same internal diameter as that of the combustor. The quartz segment was held in place using ceramic bonding to prevent leakage. This arrangement has been previously used for the PIV setup discussed earlier. However, the PIV experiments were

performed at low temperature as the experiments were conducted to examine the isothermal flowfield. Special attention was directed towards the finishing of the combustor so as to prevent any leakage or perturbation that may affect the characteristics of the reacting flow. The side slit was sealed and adjusted to allow for the full width of the laser sheet be introduced into the combustor. Figure 7-7 shows the laser sheet illuminating the combustor.



Figure 7-7 Combustor with PLIF laser

### 7.3. OH-PLIF Concentration Experiments

#### 7.3.1. Initial Experiments

After the system was examined and the experimental setup constructed, initial tests began. As discussed earlier, the full spectrum of wavelengths between 281.5 and 285.287nm was scanned with the fluorescence image collected. This scan was important to identify various peak. While conducting the experiments, it was found that there is a shift of 0.3 A (0.03 nm) in the dye wavelength due to grating error. The

grating was consistent for a single experiment, however, whenever the system was turned off than back on, that shift was encountered. This shift led to the activation of different lines being shifted by 0.15 Å (0.015 nm) than what was found in the literature. This shift was consistent for all the lines. Also that shift was too small to cause confusion between different peaks.

For every experiment, the grating of the dye laser was self calibrated. Then, a scan was performed on a propane torch to identify the grating shift as discussed earlier. Afterwards, the combustor is installed in place and the experiments were done at activation lines and different equivalence ratio. The experimental settings can be found in Table 7-3.

Table 7-3 PLIF system parameters

UV Laser Power	25-35 mJ
Repetition Rate	10 Hz
Pulse Duration	4-6 ns
Gate Delay (from Q-switch signal)	80 ns
Gate Width	60 ns
Camera Gain Setting	950
Hardware Binning	4x4
Final Camera Resolution	144x96

As the initial experiments were performed on the actual combustor, two things were noticed. First, there is a high noise signal from the laser reflections in the combustor. Second, the produced signal from weak activation lines was lower than the noise signal leading to faulty OH images. However, for the more powerful activation lines, the OH signal was clear as shown in Figure 7-8.



Figure 7-8 OH signal, unactivated (left) and activated using Q<sub>16</sub> line (right), with the combustor in the background

The reflection of the laser can be seen on the right of the combustor as seen in Figure 7-8 (the laser sheet enters the combustor from the left). As one would expect, the intensity of that noise from reflection decreased when OH was activated. This is attributed to the fact that OH absorbs some of the laser energy to get to the excited state, and less laser power reflects from the inner insulation. It is noteworthy that for the combustor experiments, the PLIF laser was fired at its maximum power to achieve a considerable signal over reflection noise, contrary to the propane torch tests, where good OH signal was obtained with much lower laser power.

### 7.3.2. OH-PLIF Concentration

The first set of experiments were aimed to qualitatively find the OH concentration. The first step was to obtain the experimental signal of OH. Such signal will give us a qualitative measurement of the OH distribution in the combustor. Quantitative measurements require further calibration for the data acquisition system and measurements of the laser power. Also, the residual laser (after excitation) power shall

be measured. These measurements are complicated, especially with the combustor geometry, rendering it hard to evaluate the residual laser power. Consequently, OH qualitative measurements are performed with further extension possibility to include quantitative measurements.

For OH concentration, the  $Q_1(5)$  and  $Q_1(6)$  activation lines were chosen as both demonstrated the highest OH signal. These lines were activated at 282.729nm and 282.9565nm wavelength with a laser power of about 35mJ. The experiments were performed for both premixed and non-premixed experiments with the equivalence ratio varying from 0.6 to 0.8. Figure 7-9 shows a sample of the obtained signal.

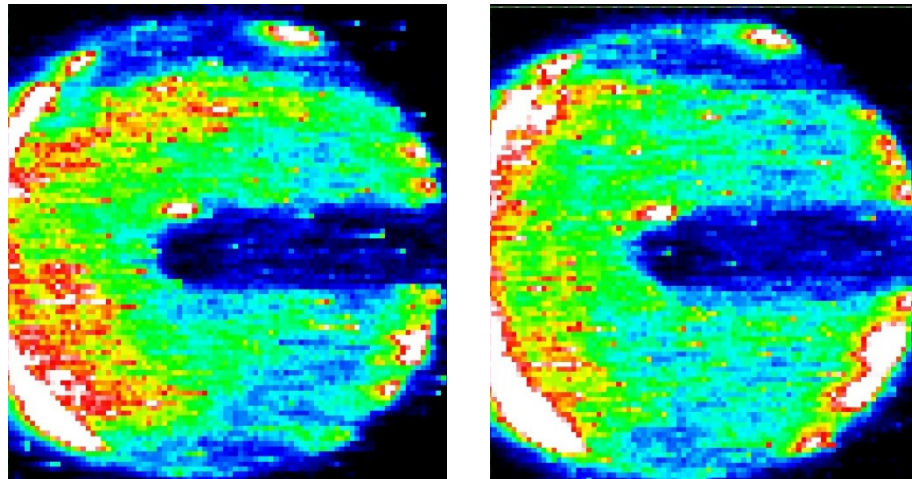


Figure 7-9 OH-PLIF Signal for non-premixed (left) and premixed (right) for an equivalence ratio of 0.7

For each condition, 100 image was acquired and averaged. Noise signal was recorded just outside the activation range ( $\pm 0.07$  A) to maintain the laser power at the same level as the activation line. 100 shot of the noise was also obtained and averaged. A sample of the obtained signal and noise signal is shown in Figure 7-10. The final image was obtained by subtracting the averaged noise signal from the

averaged raw signal. For that purpose, a Matlab code was written to handle all the calculations.

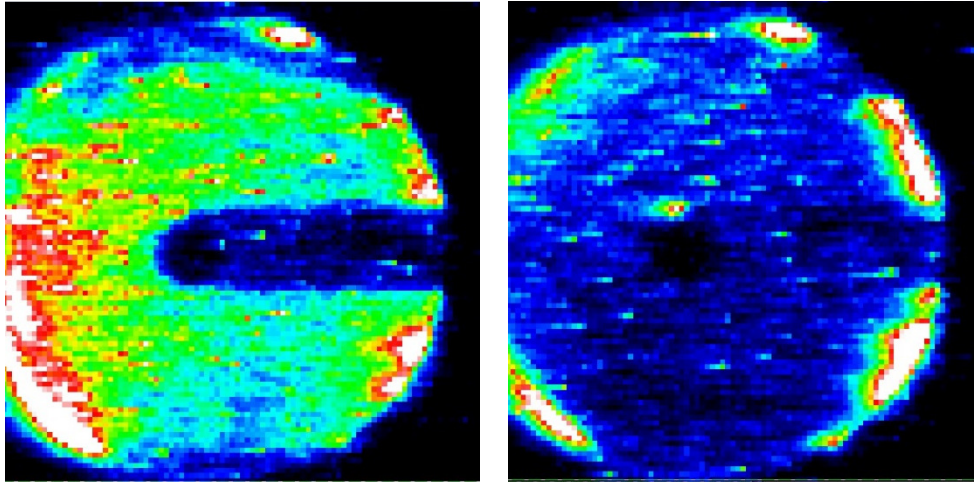


Figure 7-10 OH-PLIF Signal for non-premixed (left) and noise signal recorded with a shift of 0.07 A

The data was processed in the following steps. First, the instantaneous shots were averaged together to obtain an average of the 100 images. The same was done with the noise signal (also 100 image). Then the average noise image was subtracted from the average signal image. To minimize error, the averaging process was performed first as the instantaneous shots and the noise shots were not performed at the same exact moment. The images were processed twice, once with the noise recorded by shifting the laser 0.07 A below the activation line and the second time is done with the laser being 0.07 A above the activation line. However, there was no difference between both noise files and the final image was identical.

#### 7.3.2.1. $Q_1(5)$ Signal

After the system was examined and the experimental setup constructed, initial tests began. The first set of experiments were performed on the  $Q_1(5)$  line. The laser was

tuned to a wavelength of 282.729 nm to achieve excitation. The noise was recorded at a laser wavelength of 282.7225nm. The recorded images were averaged over a 100 shots (10 seconds period) to remove any fluctuations. The obtained images were then processed by subtracting the averaged noise signal, and any negative signal was ignored. This treatment led to a reduction in the maximum signal from 4095 counts to 2500 counts. Figure 7-11 shows both an instantaneous shot and an averaged shot, both processed to account for background noise.

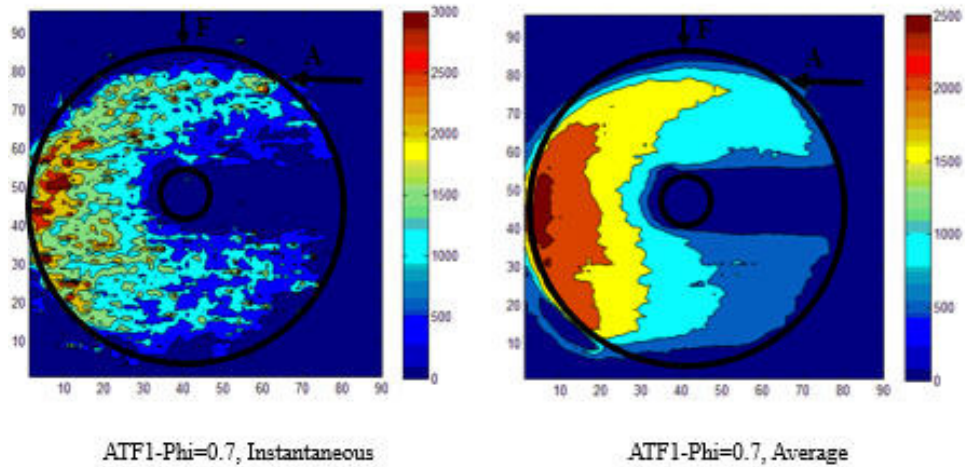


Figure 7-11 OH-PLIF instantaneous and average shots

This reduction is attributed not only to the noise but also to the averaging process. The hot products exit led to an obstruction of the laser sheet, creating a blind spot similar to the PIV experiments in Chapter four. The processed signal is shown in Figure 7-12 for the non-premixed combustion mode.

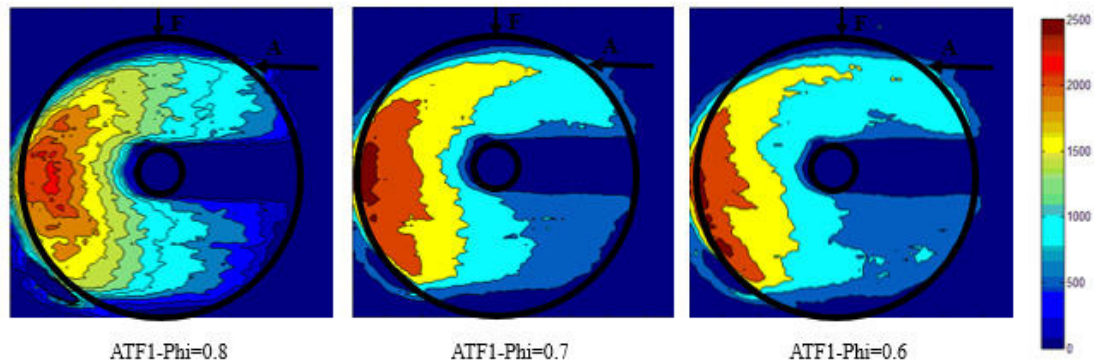


Figure 7-12 OH-PLIF intensity distribution for  $Q_1(5)$  line under non-premixed combustion mode

Figure 7-13 shows the same plot for premixed combustion mode. The difference in combustion behavior is clearly demonstrated in these plots. The signal intensity and distribution is completely different between the premixed and non-premixed combustion modes. Also a variation was observed with the change in equivalence ratio.

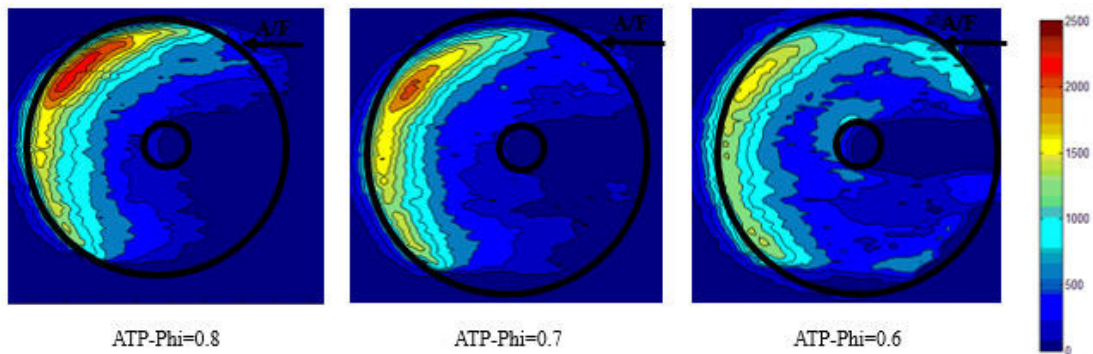


Figure 7-13 OH-PLIF intensity distribution for  $Q_1(5)$  line under premixed combustion mode

The previous data was analyzed to determine the amount of signal distribution over the combustor. For that purpose, the mean value of each averaged shot was calculated and normalized by the maximum average signal intensity. The results are shown in Figure 7-14.

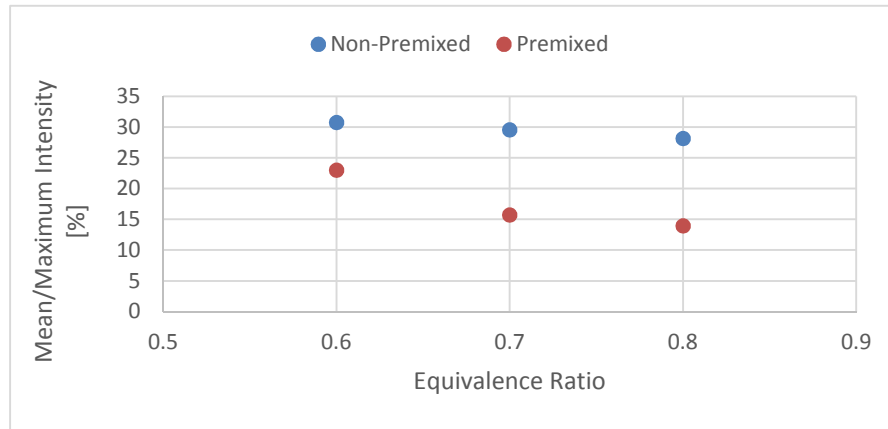


Figure 7-14 Signal distribution for  $Q_1(5)$  vs. equivalence ratio

The intensity signal is affected by the blind spot and the zero intensity outside the combustor as the calculations were performed on the full image shown in Figure 7-12 and Figure 7-13, leading to a lower calculated mean. Nevertheless, it is evident that as the equivalence ratio decreases, the ratio of the mean of the signal to the maximum signal increases, indicating that larger portion of the combustor is at a higher OH concentration which is an indication for better reaction distribution. Ideally the difference between the mean and the maximum should be minimal to result in a true distributed combustion.

#### 7.3.2.2. $Q_1(6)$ Signal

The second set of experiments were performed on the  $Q_1(6)$  line. The laser was tuned to a wavelength of 282.9565 nm to achieve excitation. The noise was recorded at a laser wavelength of 282.9585 nm. The recorded images were averaged over a 100 shots (10 seconds period) to remove any fluctuations. The obtained images were then processed by subtracting the averaged noise signal, and any negative signal was ignored. This treatment led to a reduction in the maximum signal from 4095 counts to

2000 counts. This reduction is attributed not only to the noise but also to the averaging process. The processed signal is shown for the non-premixed combustion mode in Figure 7-15.

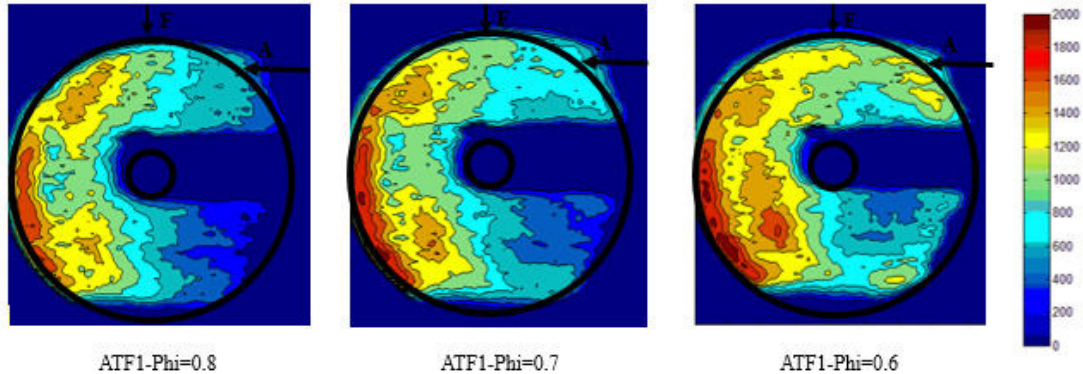


Figure 7-15 OH-PLIF intensity distribution for  $Q_1(6)$  line under non-premixed combustion mode

The premixed combustion OH-PLIF images are shown in Figure 7-16. The OH-PLIF for  $Q_1(6)$  demonstrated similar distribution to that of  $Q_1(5)$  in terms of signal location and its variation with both the combustion mode (premixed and non-premixed) and equivalence ratio.

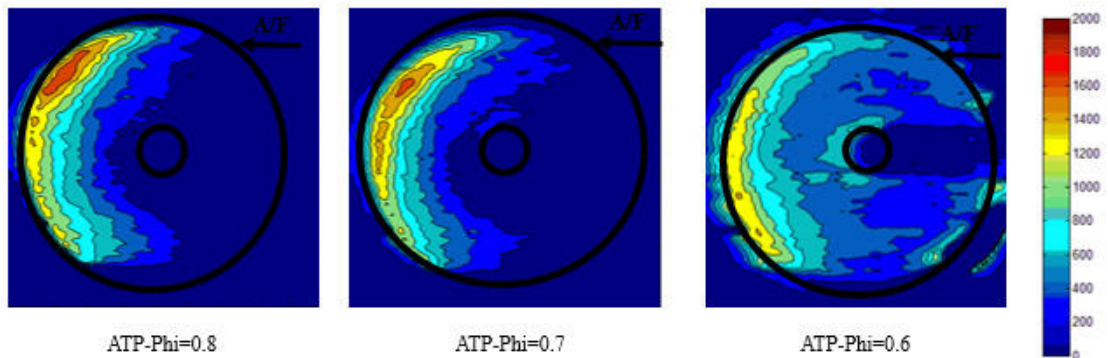


Figure 7-16 OH-PLIF intensity distribution for  $Q_1(6)$  line under premixed combustion mode

The signal was stronger in the  $Q_1(5)$  line as demonstrated in Figure 7-12 and Figure 7-13. Both  $Q_1(5)$  and  $Q_1(6)$  lines have equal transition probabilities and absorption and excitation coefficients [150]. Also, the observed signal from those two excitation lines were found to be of similar intensity as demonstrated by Dieke *et al.* [149]. Also the dye laser power was almost constant for those two excitation results. It is noteworthy that, for low equivalence ratio ( $\phi=0.6$ ), some of the signal is not absorbed through OH, resulting in a higher reflection from the combustor right wall, see Figure 7-15. The mean of the averaged shots was calculated and normalized by the maximum intensity of the averaged shots. The results are plotted in Figure 7-17. The results show similar trend to that of  $Q_1(5)$  activation line, where the ratio of mean to maximum increases with a decrease in equivalence ratio fostering distributed reaction conditions.

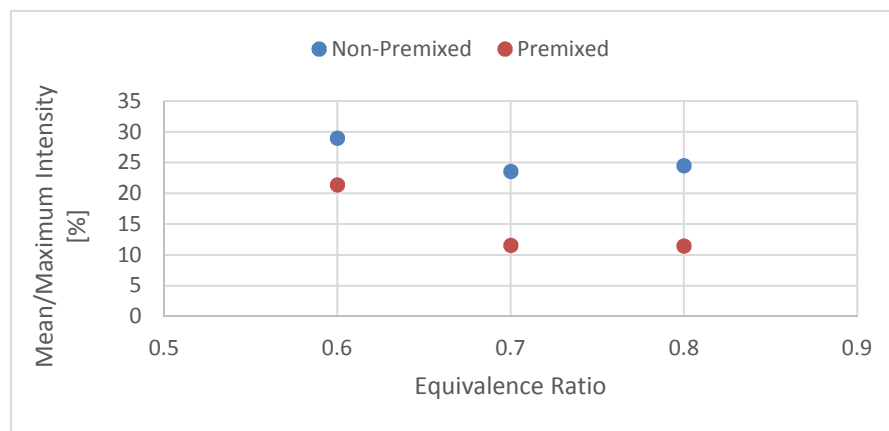


Figure 7-17 Signal distribution for  $Q_1(6)$  vs. equivalence ratio

Before further analysis is performed, OH\* chemiluminescence will be performed to verify maximum OH radical location and outline the differences between both techniques for OH detection.

### 7.3.3. OH\* Chemiluminescence

OH\* chemiluminescence intensity distribution was captured directly after the OH-PLIF experiments so that the combustor is running under the same exact condition. The camera settings were modified to be able to capture the signal of OH\* chemiluminescence. The exposure time was set to 100 ms (instead of 60 ns for PLIF) and a gain of 100 (significantly reduced from the gain of 950 for PLIF). Since no timing was required, the camera resolution was restored to its maximum of 576x384 pixels. The maximum intensity of the obtained signal was 22000 a.u.. The raw signal was not modified as there was no background noise due to the absence of laser reflections. Also for this range of detection (307nm), the combustor insulation did not produce any background noise (contrary to higher wavelengths). The obtained images are shown in Figure 7-18. Comparing the chemiluminescence signal and fluorescence signal, one can see that both of them outline the maximum OH\* signal consistently. Also the same behavior of the OH\* signal with the respect to combustion mode was demonstrated. OH\* signal for premixed combustion mode is shown to be upstream compared to non-premixed combustion mode signal. This is attributed to the nature of injection where the premixed mixture is ready to ignite while in non-premixed mode, air and fuel need to mix first prior to ignition. Also the combustion at low equivalence ratio ( $\phi=0.6$ ) demonstrated a more distributed combustion as compared to higher equivalence ratios. The same images were acquired with the same resolution set for PLIF experiments (144x96 pixel) with much shorter exposure time of 10 ms to prevent saturation of the camera (as now the readout location handles the charge from 16 pixels (4x4) binning compared to 1 pixel in full resolution mode). These images were found to be identical

to that shown in Figure 7-18 with the exception of having lower spatial resolution and quality.

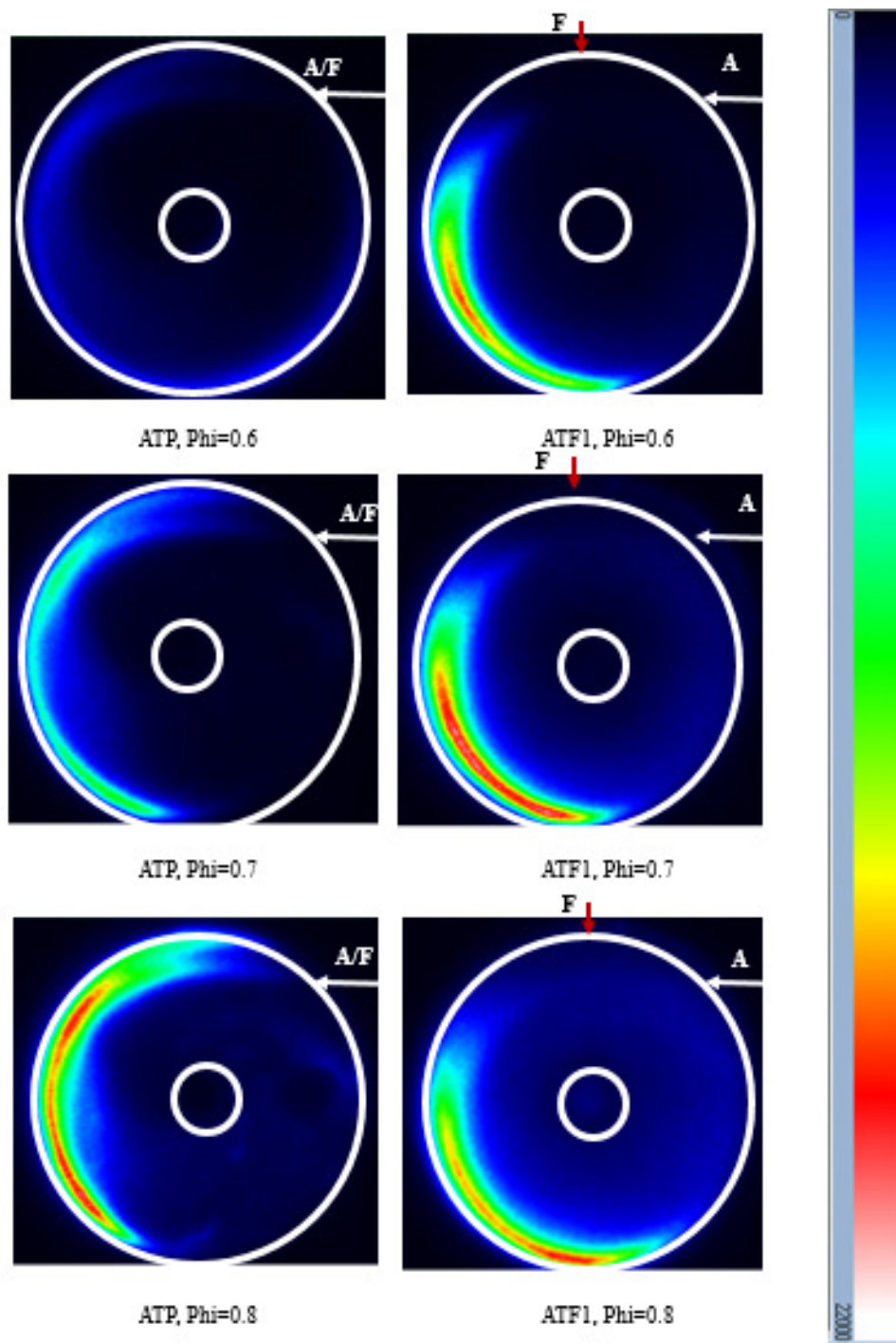


Figure 7-18 OH Chemiluminescence signal

Using OH\* chemiluminescence to outline the reaction zone is a less complicated technique (compared to OH-PLIF) with good detection of maximum intensity location. However, OH-PLIF technique is able to detect the presence of OH\* outside of the high temperature zones which is beneficial in determining the extent of reaction distribution in the combustor.

#### 7.3.4. Fluorescence vs. Chemiluminescence

OH\* chemiluminescence have been widely used as flame marker to identify the reaction zone. Throughout this dissertation, conclusions were drawn based on the OH\* intensity distribution. However, chemiluminescence only identifies the activated OH\* radicals due to higher temperature, not the full OH radical existence. Consequently, if the reaction is progressing at a very low rate or at a lower temperature, OH\* chemiluminescence might not produce meaningful information. On the other hand, laser induced fluorescence activates all of the existing OH with some losses due to collision and quenching. However, it still covers a wider spectrum of OH as compared to chemiluminescence. A comparison of the obtained signal in both cases is shown below in Figure 7-19.

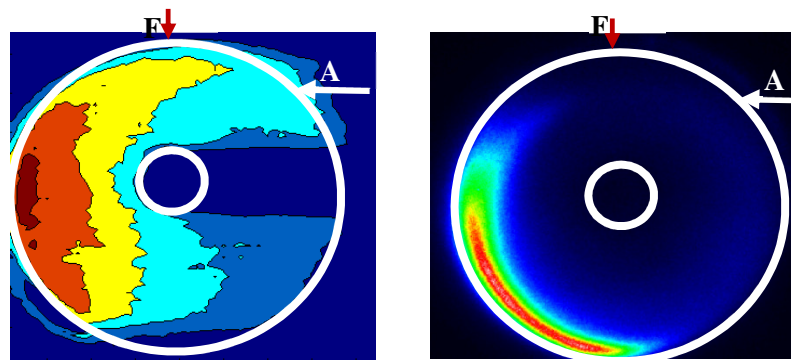


Figure 7-19 OH-PLIF Signal and chemiluminescence signal for non-premixed combustion at equivalence ratio of 0.7.

Comparing both signals, one can see that the PLIF signal suggests the presence of OH radicals all over the combustor as compared to the somewhat area limited signal in chemiluminescence. Also, PLIF detected some OH at the inlet region, indicating the presence of hot recirculated reactive gases and species which is required to promote reaction distribution. A feature that was not observed using chemiluminescence.

The same analysis can be performed on premixed combustion mode as shown in Figure 7-20. The same trend can be seen where the PLIF signal indicated that OH is present in a larger area compared to the chemiluminescence signal. Also PLIF indicated the presence of OH at the combustor inlet, upstream to where OH\* was detected via chemiluminescence. It is noteworthy that the chemiluminescence signal showed a high signal near the bottom of the combustor (image), however, that area was out of sight for the PLIF laser limiting the signal obtained in this region.

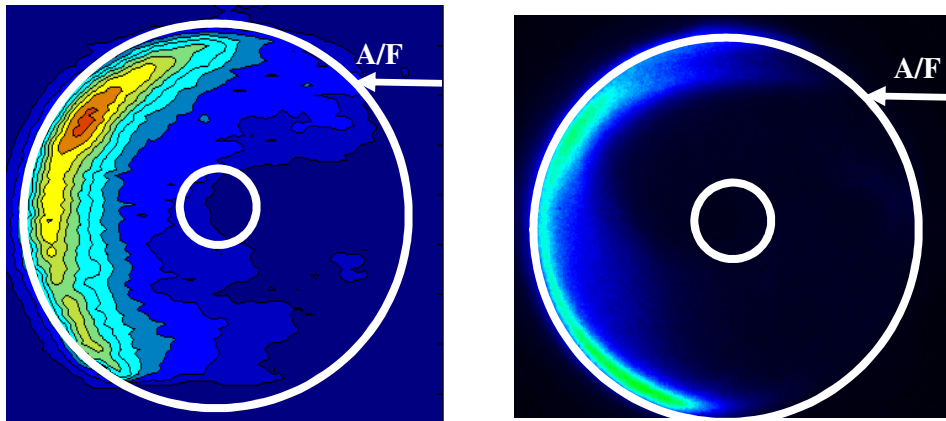


Figure 7-20 OH-PLIF Signal and chemiluminescence signal for premixed combustion at equivalence ratio of 0.7

To further compliment this analysis, the average of the obtained signals in Figure 7-18 are calculated and normalized by the maximum signal. These values are

shown in Figure 7-21 along with those obtained from OH-PLIF  $Q_1(5)$  line. The first thing to notice is that the percentages for the premixed experiments under chemiluminescence (crosses) are lower than those obtained with PLIF (round). However, the same trend was preserved. The low value at equivalence ratio of 0.8 can be related to the concentrated nature of the flame temperature (hot spots) at this high equivalence ratio. On the other hand, for non-premixed data, the chemiluminescence signal (crosses) slightly decreased with decrease in equivalence ratio, which contradicts with what obtained from PLIF analysis. This can be related to imperfect mixing in the non-premixed case as compared to the premixed case. Though the OH is present in a large portion of the combustor, as indicated by OH-PLIF, the reaction is concentrated to a smaller area as indicated by OH\* chemiluminescence which is a direct representative of high temperature spots. The difference in behavior between both premixed and non-premixed cases are evident with the decrease in the maximum signal in premixed combustion with decrease in equivalence ratio, however, that did not happen with non-premixed combustion, see Figure 7-18

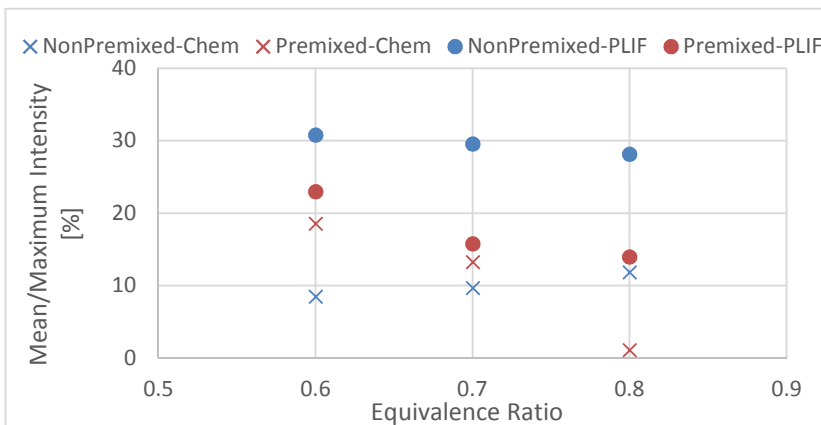


Figure 7-21 Signal distribution for  $Q_1(5)$  and chemiluminescence

This difference in behavior between chemiluminescence and PLIF signals can explain the difference in emissions discussed earlier. Though OH-PLIF indicated that OH is more distributed in non-premixed combustion cases as compared to premixed combustion cases (round markers in Figure 7-21). Chemiluminescence revealed that thermally excited OH\* (as a result of high temperature location, i.e. reaction zones) is actually less distributed in the non-premixed cases as compared to the premixed cases (crosses in Figure 7-21), leading to a higher NO<sub>x</sub> emission for the non-premixed cases (almost 65% more than that of premixed combustion case as shown in section 4.3). This outlines the difference in mixing and between both modes. However, ultra low emissions were obtained under both conditions (1.5 PPM for non-premixed, 0.87 PPM for premixed case at equivalence ratio of 0.6).

#### **7.4. Temperature Measurement with PLIF**

Two line OH excitation as a temperature measurement technique has been widely used in combustion. In this technique, a signal from two different OH excitation lines (states) is obtained and then the ratio between those two signals is analytically or empirically related to the temperature. This can be achieved through relating the signal at the different energy levels to the distribution of energy (Boltzmann's distribution) and the temperature can be obtained, or by simple calibration. *Lucht et al.* examined different activation lines suitable for temperature measurements [161]. A variation of P<sub>1</sub> and Q<sub>1</sub> lines were used to activate OH with the output signal compared to the actual temperature with an error of 3-5% for some of the ranges. Other researchers used different lines such as R<sub>2</sub>(5) and Q<sub>2</sub>(11) [162] or Q<sub>1</sub>(1) and Q<sub>1</sub>(11) [152]. Other lines

were found in literature, however these lines were outside the optimum tuning range of the current Dye laser system. The first step was to identify which of these lines are possible to activate using the system at hand. Initial trials were performed on a propane torch to narrow down the suitable activation lines. Only the lines reported by Seitzman *et al.* [162] and Meier *et al.* [152] produced considerable signal. The signal was recorded using Lucht *et al.* [161] produced a completely different signal as compared to the signals obtained using Seitzman *et al.* [162] and Meier *et al.* [152] lines, see Figure 7-22. Also  $R_2(13)$  and  $P_1(2)$  lines reported in Lakusta's work [163] did not yield any significant signal. Consequently, experiments on the combustor will concentrate on lines used by Seitzman *et al.* [162] and Meier *et al.* [152].

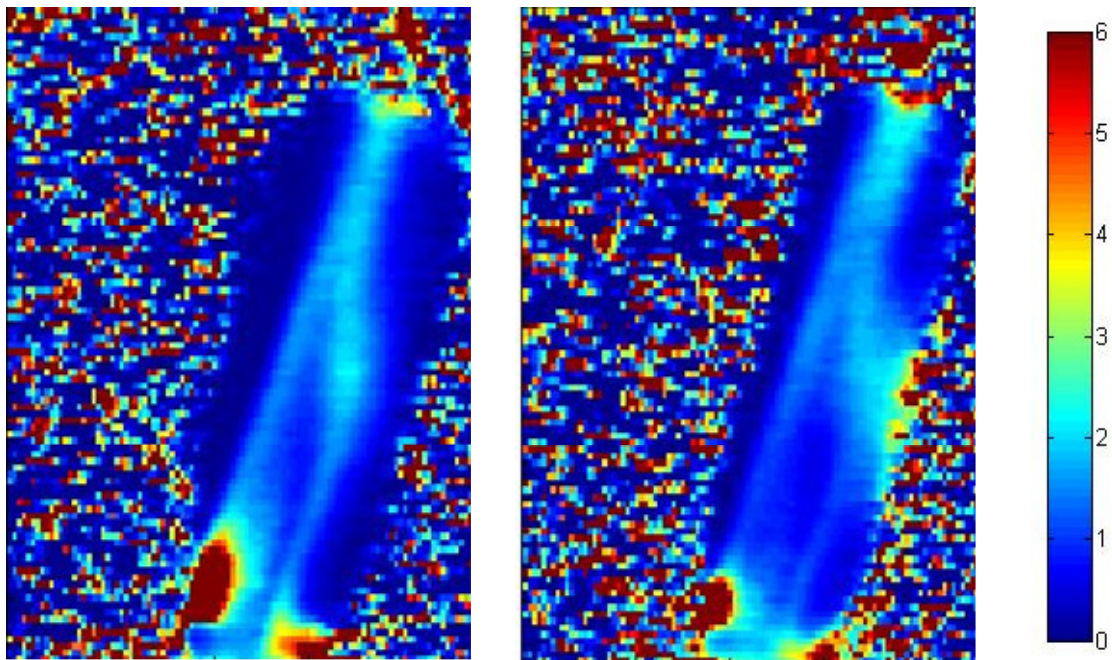


Figure 7-22 Signal ratio,  $Q_1(11)/Q_1(1)$  (left) and  $Q_2(11)/R_2(5)$  (right)

#### 7.4.1. Q<sub>2</sub>(11), R<sub>2</sub>(5) Signal

Experiments were performed on the combustor to obtain the fluorescence signal from the lines used by Seitzman *et al.* [162]. However, Q<sub>2</sub>(11) line was only activated for the combustor as no signal was obtained from the R<sub>2</sub>(5) peak. This can be explained by the fact that the R<sub>2</sub>(5) result in weaker signal as compared to Q<sub>2</sub>(11) as described in the literature [149]. This weaker signal was easier to detect using the propane torch, however, when the combustor was used, it was harder to distinguish that weak signal from the noise resulting from reflections within the combustor as no significant change was detected in the obtained signal scanning through the R<sub>2</sub>(5) range.

#### 7.4.2. Q<sub>1</sub>(11), Q<sub>1</sub>(1) Signal

The same experiment was repeated for the activation lines Q<sub>1</sub>(1) at 281.9505nm and Q<sub>1</sub>(11) at 284.7375nm reported in the work of Meier *et al.* [152]. The data for Q<sub>1</sub>(1) activation line has been processed as discussed earlier, where an average of 100 shots is obtained with the noise signal obtained directly before the activation line subtracted from the obtained average. This treatment led to a reduction in the maximum signal from 4095 counts to 1400 counts. Figure 7-23 Shows the obtained signal at phi=0.6.

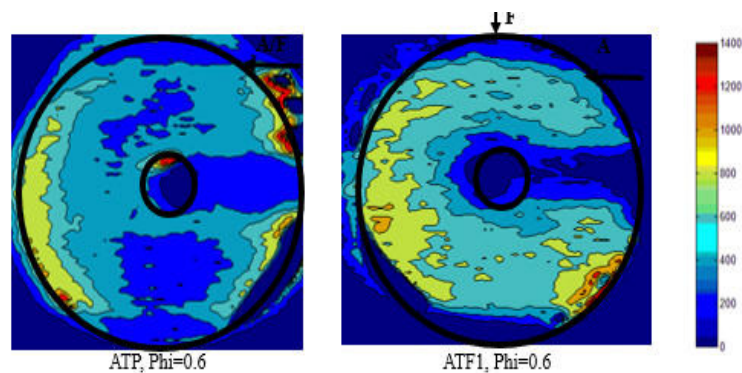


Figure 7-23 OH-PLIF signal for Q<sub>1</sub>(1) activation line

The signal was also obtained at other equivalence ratios, however, the signal was much weaker and confined to a limited area of the combustor especially in premixed combustion mode. The laser/camera settings were the same as reported in the previous experiments. The lower values for  $Q_1(1)$  band compared to  $Q_1(5)$  and  $Q_1(6)$  agrees with the literature [149].

The data for  $Q_1(11)$  activation line has been processed in the same way. Figure 7-24 Shows the obtained signal for both premixed and non-premixed combustion at  $\phi=0.6$ . The signal was also obtained at other equivalence ratios, however, the signal was much weaker and confined to a limited area of the combustor especially in premixed combustion mode.

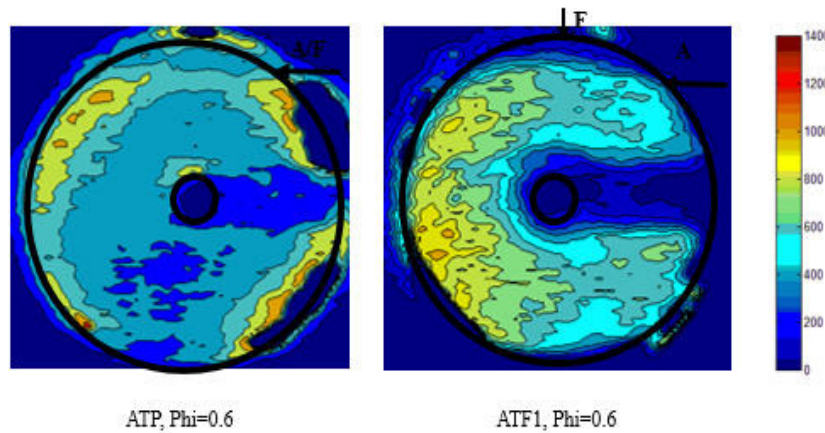


Figure 7-24 OH-PLIF signal for  $Q_1(11)$  activation line

The laser/camera settings were the same as reported in the previous experiments. Though  $Q_1(11)$  band has comparable intensity to that of  $Q_1(5)$  and  $Q_1(6)$  as in the literature [149], however,  $Q_1(11)$  is at the end of the laser power regime leading to a lower activation energy (25 mJ) as opposed to  $Q_1(5)$  and  $Q_1(6)$  (30 mJ) in the non-premixed case.

### 7.4.3. Analysis for Temperature plots

As discussed earlier, the ratio between the activation lines  $Q_1(1)$  and  $Q_1(11)$  have been used to obtain the temperature field [152]. It is noteworthy that in their work, the authors reported that the ratio almost varies linearly with the temperature. For a temperature of about 1500 K, the ratio is about 0.44. At a temperature of 2000, the ratio is about 0.74. The ratio reaches unity for a temperature of 2500 K, with a ratio of about 1.2 at a temperature of 2950K.

The first step in this analysis was to obtain the ratio of  $Q_1(11)$  to  $Q_1(1)$  signals. Figure 7-25 shows the obtained ratios for these experiments at an equivalence ratio of 0.6. The experiments for  $Q_1(1)$  and  $Q_1(11)$  were repeated with the laser power at 25mj for both experiments to eliminate any discrepancies. In here it can be seen that the ratio in premixed case is higher than that of the non-premixed case. However, in the non-premixed case, the laser power was not matched leading to some variation in the output signal.

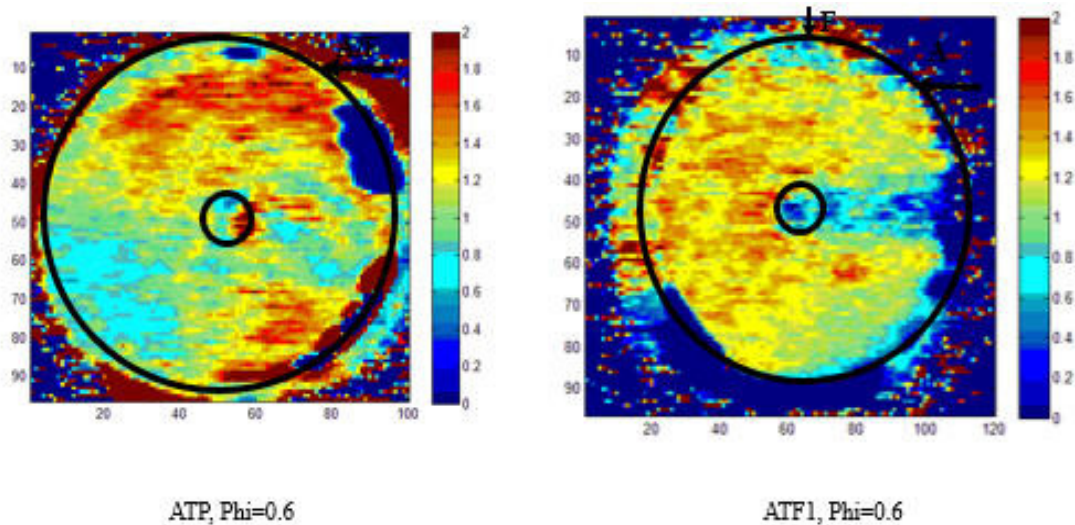


Figure 7-25  $Q_1(11)/Q_1(1)$  ratio at  $\phi=0.6$

A major variation between our experiments and the work of Meier *et al.* [152] is the operational pressure. Meier *et al.* performed the experiments at elevated pressure of 6 bar, while these experiments were performed at atmospheric pressure. Various researches have tried to quantify the impact of pressure on fluorescence signal. Battles *et al.* [164] [165] investigated the PLIF of radical species in high pressure flames. Their proposed model indicated that the signal is significantly reduced with increase in pressure, with about 40% reduction at 5 atm. compared to 1 atm. and 50% reduction at 10 atm. [164] [165]. Allen *et al.* also demonstrated the same impact of pressure on fluorescence signal with the same amount of reduction in signal intensity with increase in pressure [166].

This difference in fluorescence signal due to difference in pressure is expected to affect both bands equally or with very small variation. Consequently, the ratio of the bands  $Q_1(11)$  and  $Q_1(1)$  shall remain the same. This ratio was converted to temperatures by using a linear fit for the data produced by Meier *et al.* [152]. The obtained temperature plot is shown in Figure 7-26

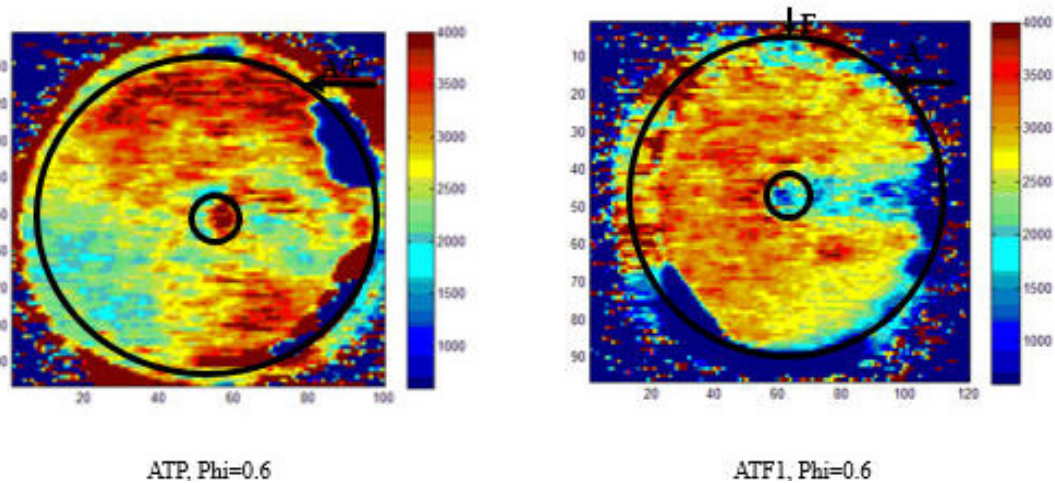


Figure 7-26 Temperature plot based on  $Q_1(11)$  and  $Q_1(1)$  ratio

A close look on the obtained temperature plot shows that this technique overestimates the temperature. The maximum temperature obtained was about 4000K which is unrealistically high. This error temperature can be a direct result to the differences between the conditions Meier *et al.* performed their experiments and this experiments. On the other hand, the location of maximum temperature corresponds with location of highest OH\* intensity, where the temperature is expected to be the highest. Nevertheless, the increase in temperature requires a detailed calibration for this system for actual temperature measurements.

If we consider the  $Q_1(11)/Q_1(1)$  ratio alone, Figure 7-25 shows that, for non-premixed combustion, the variation of the ratio inside the combustor is minimal except near the exit tube at the center. For the majority of the combustor, the ratio varied between 1.3 and 1.5. Also, a singular area where the ratio was high (indicating a thin reaction sheet or thin flame) was not encountered. The same cannot be said about premixed combustion. The maximum ratio was found to be near the air entry region with lower signal across the rest of the combustor. The high ratio at the lower right portion results from the difference in noise signal as the laser is reflected from the side of the combustor. In precious cases that was mitigated through subtraction of average noise shots. However the noise is not the same for all the wavelengths (line), leading to this error at the bottom right as shown in Figure 7-27.

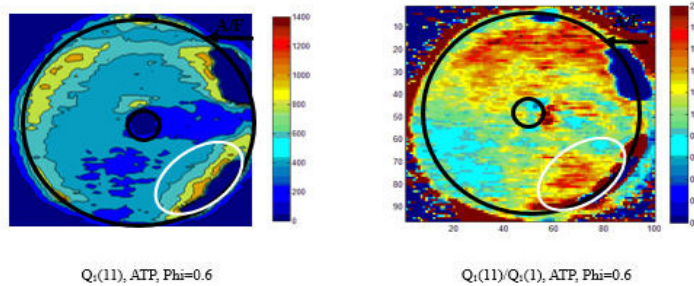


Figure 7-27 Error in ratio due to reflected laser

### 7.5. Other Configurations

Other configurations were examined using PLIF. Configuration NP/NF1 (see Figure 4-6) was examined to outline the difference between swirling and non-swirling flow. Configuration NP/NF1 have been shown to have lower entrainment rate leading to lower reaction distribution. However, the resultant PLIF signal was extremely weak for all of the lines examined. The noise was also much higher as the camera gain had to be reduced to 750 (compared to 950 for most of the previous experiments). The higher noise can be related to the lower temperature as portion of the reaction was completed in the exit manifold. This is supported by the fact that during the previous experiments, starting from cold start, the signal without OH excitation is enough to saturate the camera even at a low gain of 400. This signal decreases as the combustor is started and warms up until the combustor reaches its operational point where the OH excitation can be easily distinguished from the noise as discussed earlier. Such distinction was not possible under configuration NP/NF1. Different Injection velocity was also examined, with air inlet velocity of 103 m/s instead of 46 m/s. However, the data did not show any difference in behavior as compared to the lower velocity results reported here.

## 7.6. Summary

In this chapter PLIF technique was discussed and employed to characterize the OH distribution in the swirling CDC combustor. The system was first discussed with its operational procedure and limits. Then the system was examined and the timing sequence was set. Experiments were performed on the combustor in both premixed and non-premixed configurations with activation lines  $Q_1(5)$  and  $Q_1(6)$ . Results showed the superiority of OH-PLIF compared to OH\* chemiluminescence, where OH was identified at locations at which no OH\* chemiluminescence signal was detected before. Also OH-PLIF suggested that the reaction is more distributed than what is shown through chemiluminescence. Difference in distribution between OH-PLIF signal and OH\* chemiluminescence explains the high NO emission under non-premixed combustion though OH seems to be more distributed compared to premixed mode.

$Q_1(1)$  and  $Q_1(11)$  were activated in an effort to obtain temperature plots. Other activation lines failed to produce enough signal for analysis. The ratio obtained between  $Q_1(1)$  and  $Q_1(11)$  showed minimal variation across the combustor where there was no sharp increase in the ratio specifically for the non-premixed case. This ratio can be related to the temperature, however, the relation used resulted in unrealistically high temperatures inside the combustor. Further calibration using temperature measurements to correlate the ratio value to temperature is required. Other configurations were examined using PLIF. However, these configuration did not yield useful data for further analysis.

## 8. Chapter Eight: Towards Distributed Combustion

### 8.1. Summary

Design and development of colorless distributed combustion (CDC) for gas turbine applications requires careful examination on the role of various input and operational parameters to achieve ultra-low  $\text{NO}_x$  emission and stable combustion operating at ultra-high thermal intensity. In this dissertation various flowfield configurations, such as swirling and non-swirling flow, were investigated for a nominal thermal intensity of about  $36 \text{ MW/m}^3\text{-atm}$ .

The impact of swirling and non-swirling flow have been investigated with focus on isothermal flowfield and pollutants emissions. Emissions as low as 1 PPM of NO have been demonstrated for premixed combustion. Different fuel injection locations have been also examined with view to develop ultra-low emission non-premixed mode combustor. Low emissions in non-premixed mode were demonstrated though slightly higher than those obtained in premixed mode. The impact on temperature and pressure has also been investigated as the examined geometries were down selected to a swirling flow geometry having an extended tube for product gases exit (with emissions of 5 PPM NO and 8 PPM CO).

The combustor's performance was next studied with view to develop fuel-flexible ultra-low emissions combustor. First, diluted methane was examined to simulate low quality natural gas, which led to a decrease of about 40% in NO emissions. Next, hydrogen enriched methane was examined with view to enhance combustion stability at ultra lean conditions which was demonstrated with 8% addition of methane by mass (leading to emissions as low as 3 PPM NO and 9 PPM CO). Other fuels were also

examined such as propane, ethanol, and kerosene. With aviation applications in mind, JP-8, hydrogenated renewable jet fuel, and novel biofuels were also used in the combustor. Emissions below 7.5 PPM of NO were demonstrated regardless of the fuel used with no modifications to the combustor design or injectors under premixed mode. 10 PPM of CO were shown for methane based fuels with somewhat higher CO emissions for heavier fuels.

Different injector shapes were also examined with focus on emissions. Air injection velocity was also examined where NO was reduced by about 40% with increased air injection velocity. Isothermal flowfield characterization showed that increasing the air injection velocity led to enhanced recirculation inside the combustor fostering CDC conditions. Dilution of fuel using air shown great promise to lower NO emissions from non-premixed combustion mode to match those of premixed mode with minimal impact on CO emissions. Dual injection was also examined to outline the possibilities and challenges for multi-injection that is required for combustor scale-up.

## **8.2. Colorless Distributed Combustion**

To achieve CDC conditions, high amounts of hot reactive gases are to be recirculated internally to form a high temperature and low oxygen concentration oxidizer prior and its mixing with the fuel to ignition. The fuel auto ignites in this environment to result in a flame with volume distributed combustion. This large volume flame will result in the same fuel consumption but with the elimination of concentrated thin flame fronts, locally formed hot spots and avoidance of incomplete combustion. Such flame is made possible through the use of low oxygen concentration

in the oxidizer with the reaction zone maintained at higher initial temperatures to support the chemical reaction. Consequently, the formation of the hot and diluted oxidizer is of crucial importance to achieve CDC conditions. The amount of recirculated hot reactive species is essentially governed by the combustor geometry and the injection velocity. Flame stabilization and location is governed by operating conditions, such as, air injection velocity and flame speed. Flame speed varies with operational temperature and pressure as well as with the local equivalence ratio.

In the previous chapters, different operational conditions have been examined. These conditions include the equivalence ratio and inlet air temperature. Different combustor geometries have been examined under different flowfield conditions for their impact on combustion intensity and pollutants emission. Injection velocities and injection locations (air and fuel) have also been examined. Each of these operational conditions and parameters affect the combustor performance including the pollutants emission.

In this section, numerical and experimental approaches are analyzed with focus on CDC considerations discussed in chapter 3. These results will be used to obtain a relationship that describes the behavior of swirling CDC combustor on NO emission with special focus on the development of distributed index based on the input and operational conditions to the combustor as discussed in section 8.3.

#### 8.2.1. Reactive Gas Recirculation

Different combustor geometries have been examined to achieve ultra low emissions with CDC combustors. This include change in the combustor flowfield using either

swirling or non-swirling flowfields. These flowfields adversely affect the mixing process within the combustor and the amount of hot reactive gases recirculated within the combustor to subsequently impact pollutants formation and emission. Non-swirling configuration resulted in a recirculated gas portion of about 28.6% of the total flow. That translates to an O<sub>2</sub> concentration of about 18% and T<sub>in</sub> of 600K using equilibrium calculations. Now for swirling configuration, these numbers are substantially changed to 55.6% recirculated gas of the total flow with O<sub>2</sub> concentration of 13% and T<sub>in</sub> of 1000K. Difference between both configurations outline the role of the flowfield design on achieving distributed reaction conditions. These conditions (low O<sub>2</sub> and high T<sub>in</sub>) are more favorable for fostering distributed reactions. Though ignition delay increases linearly with reduction in O<sub>2</sub>, this is counterbalanced by the exponential decrease of the ignition delay with respect to temperature (equation 3-2) [81]. Under these conditions, the ignition delay is less than the residence time inside the combustor fostering distributed reactions condition. Further reduction in O<sub>2</sub> and increase in T<sub>in</sub> will result in more favorable performance.

The presence of hot recirculated gases at ignition has been confirmed through OH-PLIF experiments, where OH was detected at the entry region indicated the presence of recirculated reactive species at this location (see section 7.3.2)

### 8.2.2. Air Injection Velocity

Air injection velocity affects the mixture preparation prior to ignition of the mixture that subsequently impacts combustor performance. Higher air injection velocity enhances recirculation inside the combustor that promotes turbulent mixing. Also high

air injection velocity prevents flame anchoring until further downstream to support better mixing between fresh stream and hot reactive species already present in the combustor. High injection velocity results in pressure drop inside the combustor and large entrainment of gases that must be controlled.

Experiments in section 6.3 showed that increasing the velocity enhanced the recirculation ratio to about 1.5 with a 60% of the total mass flow being recirculated reactive gases. That in return further reduce the  $O_2$  concentration and increase  $T_{in}$ , fostering distributed conditions. Not only that, but also increasing the velocity by 70% led to doubling the turbulence in the entry jet which enhances the mixing between air, recirculated gases and fuel as indicated by numerical simulations [2] as the mixing under non-premixed mode is dictated by turbulence for this velocity ratio between jets [83]. This results in the mixture being ready for ignition in shorter time (shorter than ignition delay) to result in spontaneous ignition of the uniform mixture rather than ignition of imperfect mixtures.

Higher injection velocity is favorable in terms of entrainment and shortening ignition delay, however, higher injection velocity will reduce residence time inside the combustor. Such reduction is favorable in  $NO_x$  emission, however CO emission will increase significantly.

### 8.2.3. Fuel Injection Location

Mixture preparation is of critical importance to achieve distributed conditions. Variation of fuel injection location adversely affect mixture preparation to either result in ultra-low emissions or premature ignition with hot spots and high emissions. Various

injection scenarios have been examined including premixed injection, coaxial injection, and discrete injection of air and fuel. Early injection of fuel led to early ignition of air/fuel mixture without proper entrainment of hot recirculated gases from within the combustor. On the other hand, delayed fuel injection cause the fuel to burn instantaneously without enough time for it to mix with the hot diluted oxidizer (air with hot recirculated reactive gases) leading to local hot spots and high NO<sub>x</sub> emission. To that sense, the separation distance between air and fuel plays an important role in dictating the combustor behavior. If the distance is too large, the temperature is too hot and the ignition delay is shortened leading to ignition prior to proper fuel mixing. If the separation distance is too short, the ignition delay is shorter than the mixing time required to prepare the low oxygen concentration high temperature oxidizer leading to combustion outside the distributed regime as shown in section 6.1.

#### 8.2.4. Ignition Delay

The key attributes of distributed combustion can only be realized if one can achieve desirable mixture preparation prior to the ignition of the mixture under gas turbine combustion conditions, with the mixing, ignition and combustion completed prior to the gases exiting the combustor. This can be summarized by the following equations.

To ensure complete combustion, the following shall be satisfied:

$$t_{residence} \geq t_{ignition\ delay} + t_{combustion} \quad (\text{Equation 8.1})$$

For distributed reactions to occur, the following has to be satisfied as well for premixed combustion

$$t_{ignition\ delay} \geq t_{mixing\ air\ fuel\ mixture\ and\ gases} \quad (\text{Equation 8.2})$$

For non-premixed combustion the timing requirements is different as air and hot recirculated gases needs to be mixed before the fuel injection point

$$t_{flow\ to\ reach\ fuel\ injection\ point} \geq t_{mixing\ of\ air\ and\ gases} \quad (\text{Equation 8.3})$$

And upon fuel injection, fuel should not ignite until it's well mixed with air and reactive gases mixture.

$$t_{ignition\ delay} \geq t_{mixing\ fuel\ with\ air\ and\ gases\ mixture} \quad (\text{Equation 8.4})$$

If the separation distance is too small, equation 8.3 is not satisfied. If the separation distance is too long, the mixture temperature is too high to result in short ignition delay leading to violation of equation 8.4. In all cases, equation 8.1 has to be followed to prevent incomplete combustion and high CO and UHC emissions. On the other hand, if the residence time is too long, more time will be available for the slow NO<sub>x</sub> reaction to progress resulting in higher NO<sub>x</sub> emissions.

In order to give an idea about the timing scales, the residence time for configuration ATP is about 10 ms based on numerical simulations performed in section 4.4. The ignition delay based on the isothermally measured recirculation ratio for this configuration is 3 ms based on CHEMKIN-PRO simulations [2]. This dictates that air and recirculated gases have to mix in time shorter than 3 ms to form that hot and diluted oxidizer that foster distributed reactions. Also, that means that about 7 ms are available for the combustion to be completed prior to exiting the combustor. This timings are obtained from simulations and may differ from the actual case, however, they are useful in providing insight to understand the reaction progression inside the combustor.

Adhering to these timing constraints result in achieving true distributed combustion conditions that can provide such low temperature rise with uniform thermal field by creating distributed reaction in the entire combustion chamber.

### 8.3. Distribution Index

One can envision a distribution index (DI) which relates the actual combustion parameters with the condition optimized for distributed combustion conditions. Such index will be affected by recirculation ratio (entrainment rate), injection velocity, injection configuration (premixed and non-premixed) with distance between different injectors, and the fresh reactants conditions (equivalence ratio, temperature and pressure)

$$DI = f(\textit{entrainment}) \times f(\textit{injection velocity}) \times f(\textit{configuration}) \times f(\textit{operating conditions}) \quad (\text{Equation 8-5})$$

An expression will be developed for each of these functions based on the analysis of the previously reported data in this dissertation as follows.

#### 8.3.1. Combustion Geometry

The combustor geometry is expected to affect the flowfield within the combustor, leading to a variation in both combustion behavior and pollutants emission. The resultant pollutants emission for different combustor geometries have been reported, along with the isothermal flowfield. With the significant impact of flowfield on reaction zone and pollutants emission shown in previous sections, it is possible to define a distribution index that describes the extent of uniform reaction distribution within the combustor. Combining pollutants emissions, OH\* chemiluminescence, and

velocity measurements data, one can deduce that the recirculation ratio plays an important role for distributed reaction zone that can form an essential part of the distribution index. The increased recirculation of hot reactive species using swirling motion raises the fresh mixture temperature while diluting it to form high temperature low oxygen concentration reactive environment to support distributed combustion.

As a first step, equilibrium calculations were performed for different recirculation amounts (entrainment of product gases back into the reactants). The impact of the recirculation on the inlet reactants temperature and product gas temperatures, along with variation of oxygen concentration in the mixture, is shown in Figure 8-1. As the product gases percentage in the ignition mixture increases, the oxygen concentration decreases and the inlet temperature increases. Also the product gas temperature is decreased.

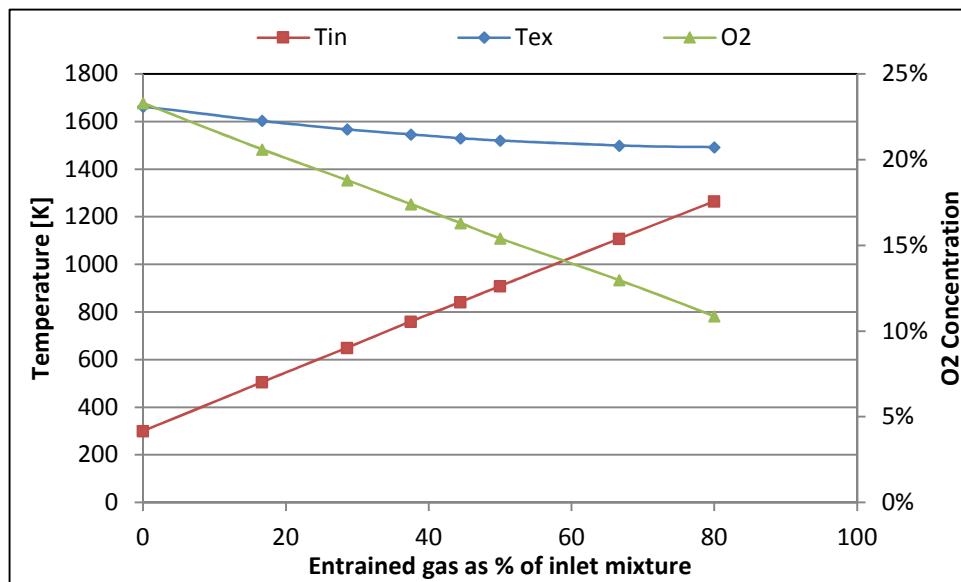


Figure 8-1 Effect of entrainment on temperature and oxygen concentration

Figure 8-1 shows that entrained gas percentage of 50% or higher (reduced oxygen concentration of the reactants and increased fresh mixture temperature) is favorable for promoting distributed combustion conditions. When translated into an actual combustor this means that an entrained mass flow rate (entrainment rate) of 1 or higher will be required. It can be noted that the entrainment rate in a reacting jet is lower than a non-reacting jet [77]. For free reacting jet the constant,  $C_e=0.13$  as compared to 0.32 for non-reacting jet as given in the equation proposed by Ricou and Spalding [76] that governs entrainment in a free jet. Yang et al. [78] have suggested that for lower oxygen concentration oxidizer the value of constant  $C_e$  increases and lies closer to non-reacting value of 0.32, where the oxygen concentration is less than 5%. Following this approximation, one can use the measured recirculated mass flow rate under isothermal flow condition as an approximation for the actual reacting case under low oxygen concentration conditions. Case “N” has shown a recirculated mass flow ratio of 0.4 (equivalent to 28.5% product gases in ignition mixture). On the other hand, configuration “AT” has shown a recirculated mass flow ratio of 1.25 (equivalent to 55.5% product gases in ignition mixture) which is more favorable for distributed combustion conditions.

For colorless flame our experience has shown oxygen concentration in the ignition mixture should be approximately 8% or less [22]. Such low oxygen concentration is hard to achieve, as gas turbines operate in lean combustion (typical equivalence ratio of 0.6 or lower), and that the entrained flow (entrained reactive species) contain oxygen, so that at equivalence ratio of 0.6 and 85.7% product gas in ignition mixture, the oxygen concentration will be about 10%. Any increase in recirculation does not

yield significant reduction in oxygen concentration. Consequently, this value will be used as a favorable value for seeking distributed reactions.

The recirculation and entrainment is the focus here as this the first parameter in the DI. A simple relation is proposed here for the recirculation portion  $f(\text{entrainment})$ , wherein the product gases and reactive species in the ignition mixture is normalized by the value required for optimum performance, resulting in optimum distributed reaction condition at a value of 1.

$$f(\text{entrainment}) = \frac{\text{recirculated mass flow rate \%}}{\text{ideal recirculated mass flow rate \%}} \quad (\text{Equation 8-6})$$

Following this definition, using ideal recirculated mass flow rate of 85.7%, configuration “N” would have a  $f(\text{ent})$  of 0.33, while configuration AT would have a  $f(\text{ent})$  value of 0.6414.

### 8.3.2. Air Injection Velocity

Two different injection velocities were employed and the resultant flowfield examined using particle image velocimetry to determine the impact of injection velocity on flow behavior. Also the pollutants emission at 6 different velocities has been measured. Using the PIV data at two examined velocities, it was found that at injection velocity of 46m/s, the recirculation ratio was 1.25, which increased to 1.4375 with an injection velocity of 78 m/s. Thus, a percentage of reactive gases of 55.5% and 58.9% were achieved, leading to a  $f(\text{ent})$  value of 0.65 and 0.69 respectively as per equation (8-6). Now using these two values, a linear fit can be obtained, wherein the recirculation ratio can be plotted as a function of injection velocity as:

$$\text{Recirculation Ratio} = 0.0059 \times \text{Air injection velocity} + 0.9805$$

(Equation 8-7)

Using the approximation, a recirculation ratio for air injection velocity of 103 m/s can be calculated and was found to be 1.59 leading to a reactive gas percentage of 61.3% and  $f(\text{ent})$  value of 0.72.

Now for the velocity portion of the DI,  $f(\text{injection velocity})$ , it is desired to quantify the relationship between injection velocity and mixing time scale along with pollutants emission. Mixing time scale can be defined on integral scale as:

$$\tau_{flow} = l_o / v_{rms} \quad (\text{Equation 8-8})$$

where,  $l_o$  is the integral length scale (approximated to  $d_{jet}/10$ ),  $d_{jet}$  is the jet diameter, while  $v_{rms}$  is the turbulent velocity. Following this definition, the mixing time scale for the injection velocities of 46 m/s and 78 m/s were 0.0794 ms and 0.022 ms, respectively. These mixing time scales are small compared to the characteristic residence time in a gas turbine combustor of ~2-10 ms, and are below the values implemented by some researchers (about 0.08 ms) [2].

On the other hand, if we relate NO emissions with injection velocities, the impact of injection velocity on NO emission is evident as seen in Figure 8-2. From this plot, it can be seen that NO approaches a minimum value as the velocity increases. Such minimum value is envisioned to be dictated by NO formation routes other than the Zeldovich (thermal) mechanism, such as, prompt (Fenimore) mechanism. Consequently, the optimum injection velocity can be assumed to be around 100m/s. The same plot is obtained for experiments where preheated air was employed. The data

suggests that as the velocity approaches 200 m/s, a minimum of NO emissions is approached for this operational condition.

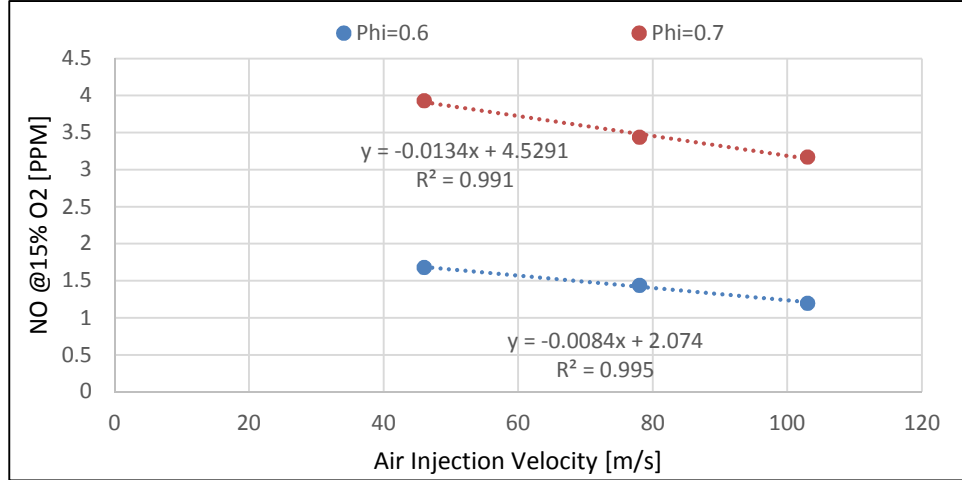


Figure 8-2 Effect of air injection velocity on NO emission

Using the above data, an expression is developed to show the impact of the injection velocity on distributed reaction. Optimum injection velocity is envisioned to be 100 m/s for normal air temperature and 200 m/s for 600K air injection temperature. Thus, an expression relating the actual velocity used to the optimum velocity can be formulated as:

$$f(\text{injection velocity}) = \frac{v_{\text{injection @ 300K}}}{100} \quad (\text{Equation 8-9})$$

where,  $v_{\text{injection @ 300K}}$  is the air injection velocity at 300 K. For injection at other temperatures, the velocity can be corrected through the following expression

$$v_{\text{injection @ 300K}} = v_{\text{injection @ T}} \times \frac{\rho @ T}{\rho @ 300K} \quad (\text{Equation 8-10})$$

### 8.3.3. Fuel Injection Location

The importance of mixture preparation for distributed combustion cannot be overstated. Mixing between freshly introduced air and hot recirculated reactive gases is governed by both the combustor geometry and the air injection velocity. The fuel introduction scheme plays an important role as well in forming the ready to ignite distributed mixture. Four different injection locations have been examined, ranging from 16D/3 away from the air injection point and moving further downstream.

As the fuel injection point moved further downstream, the reaction transformed into a diffusion mode reaction. This is evident through comparing NO emissions under different equivalence ratios at points downstream (AF2, AF3, and AF4), where NO emissions did not vary much. This is attributed to the fact that the fuel ignites as soon as it is injected in a diffusion mode flame, with equivalence ratio around unity, regardless of the global equivalence ratio. This behavior was not seen under configuration AF1, where NO significantly decreases with decreasing the equivalence ratio. Emissions obtained are shown in Figure 8-3.

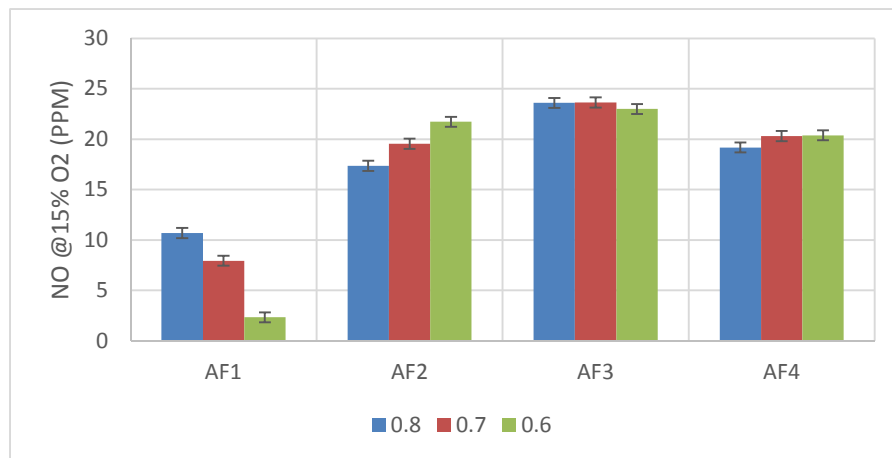


Figure 8-3 NO emission under different fuel injection locations

To further examine the effect of fuel injection location on combustion location, three different injection locations were also examined and compared to injection at location “1” as discussed in section 6.1. The previous experiments suggested that moving the fuel injector upstream yielded beneficial results. However, this was proven wrong when experiments were performed on configurations discussed in section 6.1. As the fuel injection point moved upstream, NO emissions dramatically increased (configuration CA, ATF0 compared to ATF1). The recorded NO emissions are shown in Figure 8-4.

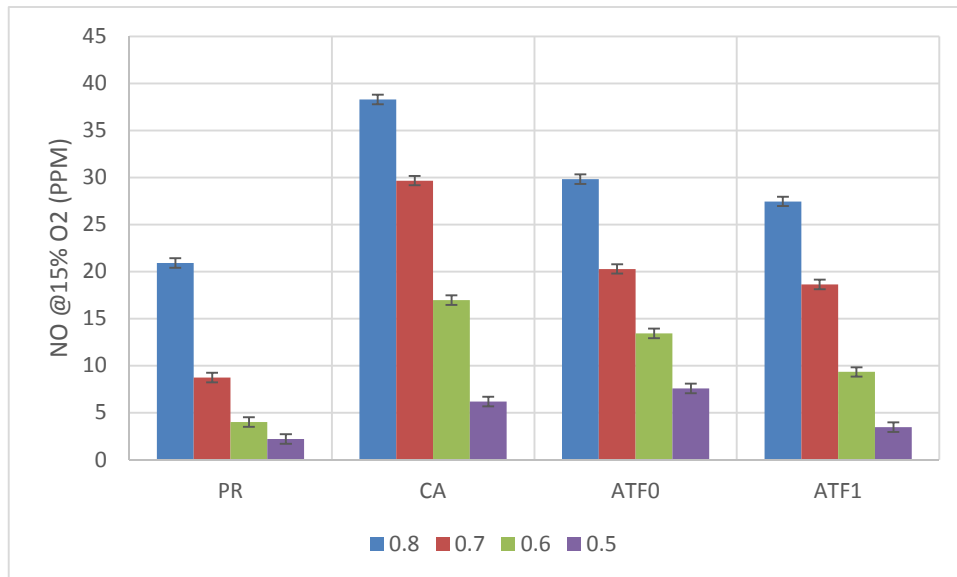


Figure 8-4 NO emissions for different fuel injection locations

The increase in NO emissions with upstream movement of the injection location was attributed to the ignition of the air and fuel mixture without the proper entrainment of hot recirculated reactive species to form a hot and diluted oxidizer – fuel mixture, necessary for distributed combustion conditions. This was confirmed through OH\* chemiluminescence marking the flame zone for these configurations coupled with numerical simulation. The only exception for this trend is the premixed injection case,

where air and fuel are readily premixed prior to injection. As the air and fuel are readily premixed, the global and local equivalence ratios are quite similar, leading to longer ignition delay as compared to diffusion flame that burns at stoichiometry, leading to longer time for hot recirculated reactive gases to mix in and foster distributed condition thus resulting in ultra low emissions.

Analyzing the data in Figure 8-3 and Figure 8-4, one can obtain a relation describing NO emissions with respect to NO emissions for the premixed case, as a function of the separation distance between air and fuel, with coaxial assigned distance of 0. The obtained data is plotted in Figure 8-5.

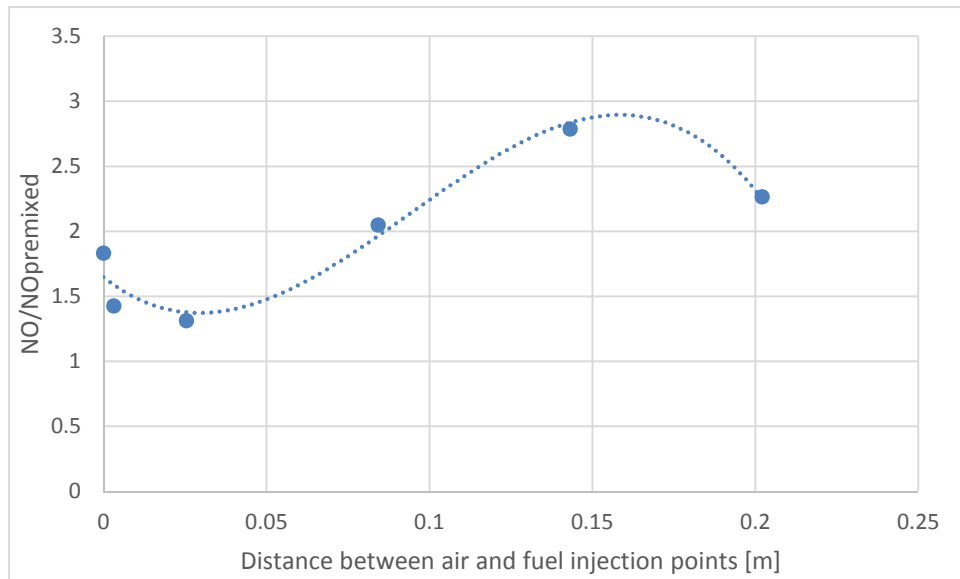


Figure 8-5 Normalized NO emission vs. air and fuel separation distance

The obtained data is plotted in Figure, and the data was curve fitted into a third degree polynomial as follows

$$\frac{NO}{NO_{premixed}} = -1422x^3 + 400.33x^2 - 19.871x + 1.648 \text{ (Equation 8-11)}$$

with  $R^2$  value of 0.9507, where  $x$  is the separation distance between air and fuel injection points.

Noting that premixed combustion resulted in lowest NO emissions, the mixing portion of the distribution index can be formulated as follows.

For Premixed combustion,  $f(\text{configuration}) = 1$ , otherwise,

$$f(\text{configuration}) = \frac{1}{-1422x^3 + 400.33x^2 - 19.871x + 1.648} \quad (\text{Equation 8-12})$$

#### 8.3.4. Equivalence Ratio

The fourth examined parameter was the equivalence ratio. Numerical simulations using CHEMKIN-PRO have been performed at different equivalence ratios with various inlet air temperatures. The obtained emissions have been normalized to the emissions at an equivalence ratio of 0.6. The obtained NO emissions and the normalized ones are shown in Figure 8-6.

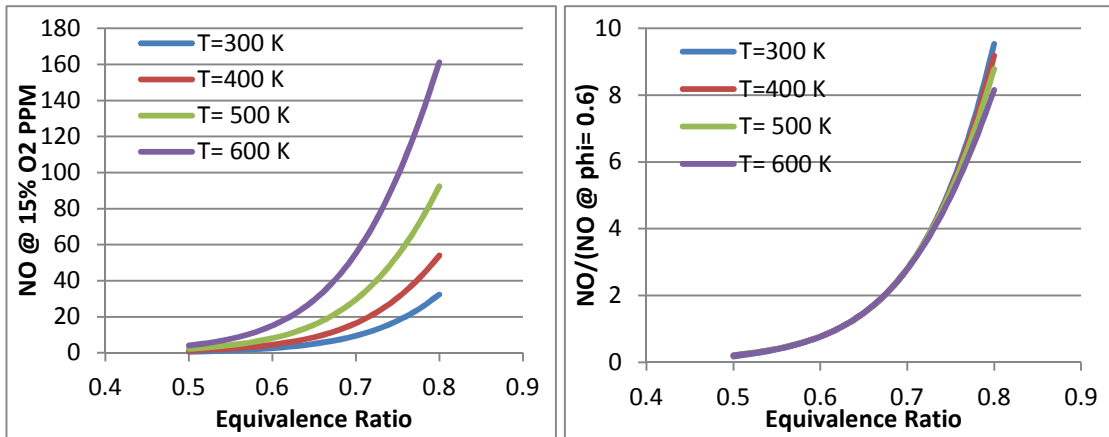


Figure 8-6 NO emission vs. Equivalence ratio

The following equation was obtained from the numerical simulation relating NO emission with equivalence ratios

$$NO/NO_{\phi=0.6} = 812.15\phi^4 - 1628.2\phi^3 + 1241.2\phi^2 - 422.93\phi + 54.121$$

(Equation 8-13)

with a coefficient of regression  $R^2=1$

Comparing the recorded experimental data with the equation obtained numerically, one can see that the experiments and the equations have the same trend, see Figure 8-7. The obtained equation tends to overestimate the emission at higher equivalence ratio (>0.7). This can be attributed to the fact that numerical simulations tends to overestimate pollutants emission at higher equivalence ratios, indicating the lack of adequate chemical mechanisms that correctly predict behavior of CDC mode. However, such higher equivalence ratios are outside the current gas turbine operational conditions.

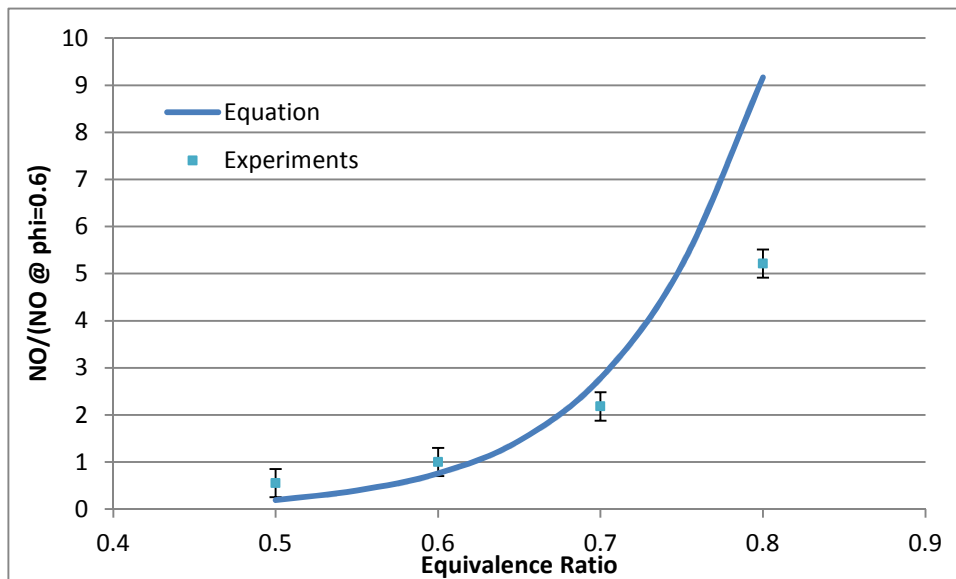


Figure 8-7 Experimentally measured NO emission as compared to the obtained equation

The emission data previously obtained suggest that the operating at an equivalence ratio of 0.6 offers the lowest combined NO and CO emissions. Consequently this will

be used as a baseline for developing an expression for the equivalence ratio effect on the Distribution Index (DI) which can be written as follows

$$f(\text{equivalence ratio}) = \frac{1}{812.15\phi^4 - 1628.2\phi^3 + 1241.2\phi^2 - 422.93\phi + 54.121} \quad (\text{Equation 8-14})$$

with  $R^2=0.9977$

### 8.3.5. Inlet Air Temperature

The effect of air preheats was quantified. Higher air preheats prior to combustion is expected to increase the flame temperature inside the combustor leading to higher  $\text{NO}_x$  emission, especially at higher equivalence ratios (0.7 – 0.8). Higher flame temperatures also aid in increasing combustion efficiency and ensuring full CO to  $\text{CO}_2$  conversion for fuel lean combustion. Numerical simulations have been performed using CHEMKIN-PRO and the full GRI3.0 mechanism. The obtained emissions have been normalized to an inlet air temperature of 300 K. The obtained NO emissions are shown in Figure 8-8 along with the normalized ones.

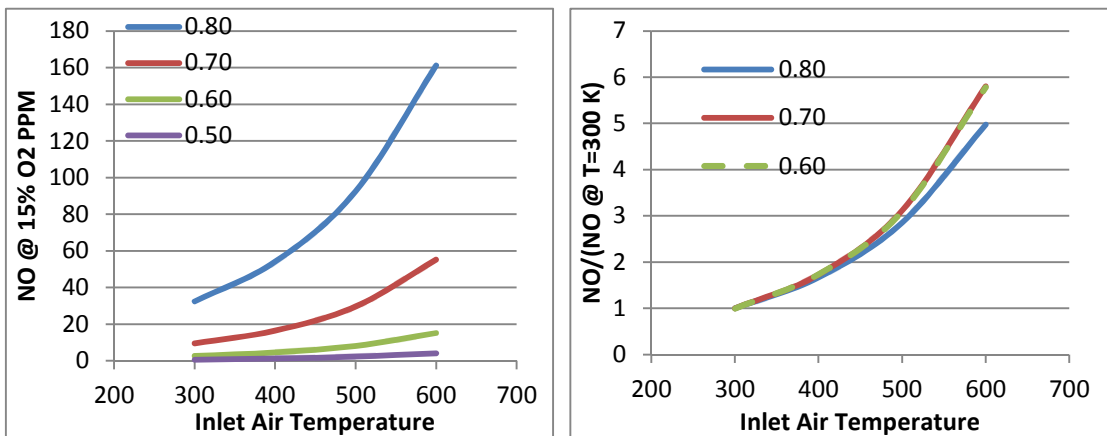


Figure 8-8 NO emission vs. inlet air temperature

The following equation was obtained from numerical simulations relating NO emissions to inlet air temperature:

$$NO/NO_{T=300} = 0.1749e^{0.0058T} \quad (\text{Equation 8-15})$$

With a coefficient of regression  $R^2=0.9993$

Comparing the recorded experimental data for inlet air temperature of 300 K with those recorded at inlet air temperature and corrected to 300 K using equation (8-15), one can see that the experiments and the equations agree favorably, see Figure 8-9.

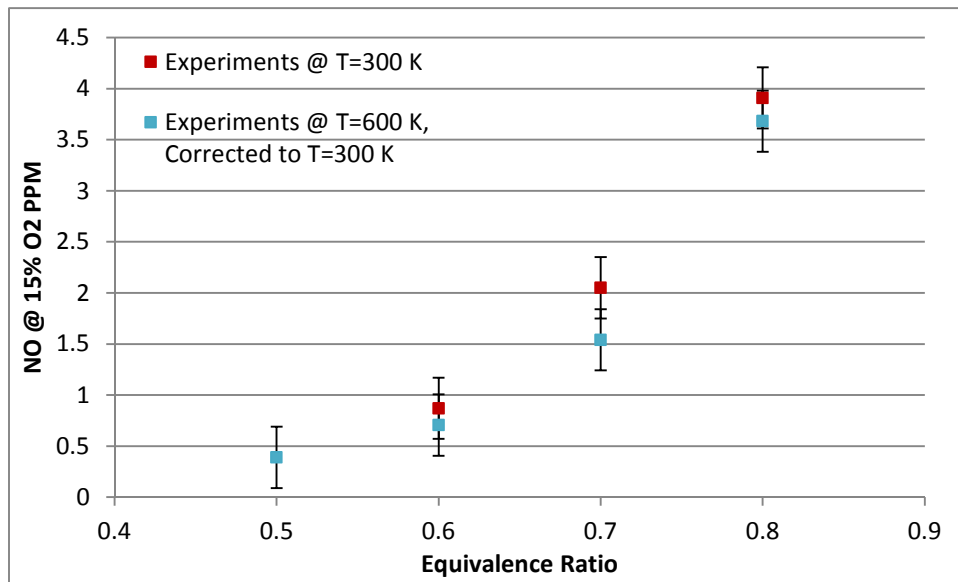


Figure 8-9 Experimentally measured NO emission as well as emission obtained from the developed relation

Similar to equivalence ratio, the impact of the preheat temperature on DI can be written as follows:

$$f(\text{inlet temperature}) = 5.7164e^{-0.0058T} \quad (\text{Equation 8-16})$$

with  $R^2=0.9993$

The impact of the operating conditions,  $f(\text{operating conditions})$ , can be expressed as the combination of  $f(\text{inlet temperature})$  and  $f(\text{equivalence ratio})$  such that

$$f(\text{operating conditions}) = f(\text{equivalence ratio}) \times f(\text{inlet temperature})$$

(Equation 8-17)

Another approach can be followed to develop an expression for the operating conditions portions of DI. Combining the above numerical simulations with experimental measurements provides an insight into the behavior of distributed combustion. The NO emission decreased with both equivalence ratio and inlet air temperature as predicted by the Zeldovich mechanism as a direct result of the flame temperature. The decrease of NO emission with these parameters comes to a plateau as the contribution of thermal NO to the total NO decreases with the major contribution of NO comes from prompt (Fenimore)  $\text{NO}_x$  (that is at low equivalence ratio and standard air intake temperature). This effect can be shown in Figure 8-10, where the contribution of thermal NO is obtained through CHEMKIN-PRO and plotted as a percentage of total NO.

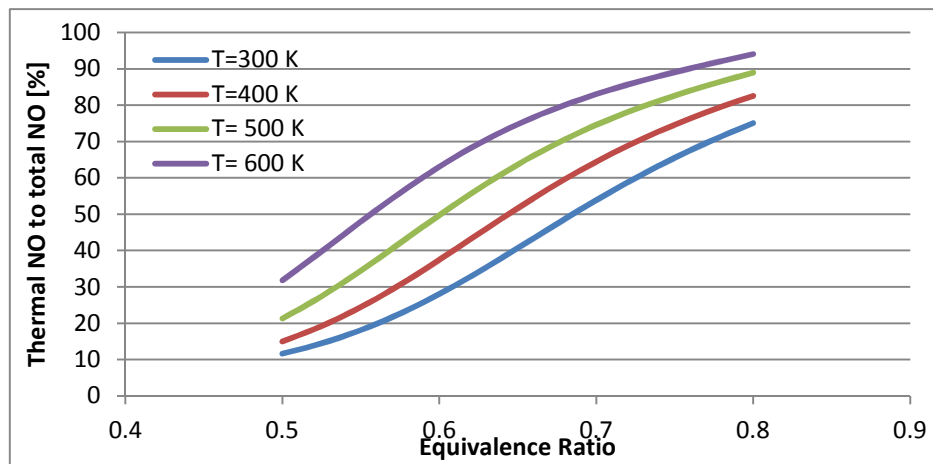


Figure 8-10 Contribution of thermal NO as a percent of total NO, CHEMKIN-PRO

The minimum level for NO based on the before mentioned numerical simulations is envisioned to be about 4 PPM at a phi of 0.6 and 2 PPM at a phi of 0.5. Such lean conditions are more relevant to gas turbine operational conditions. Consequently, using equations (8-13) and (8-15), NO emissions can be obtained and compared to the above mentioned values such that:

$$f(\text{operating condition}) = \frac{\text{Optimum NO Values}}{\text{NO values corrected to same condition}} \quad (\text{Equation 8-18})$$

where, the optimum NO values are 2 ppm and 4 ppm at equivalence ratios of 0.5 and 0.6, respectively. The NO values can be either directly measured or corrected to these optimum conditions using equations (8-13) and (8-15) and equation (8-18) is used instead of equations (8-14), (8-16), and (8-17).

### 8.3.6. DI Equation

Combining the previously discussed parameters, one can obtain an index that describes how well the reaction is distributed within the combustor. Such index has a maximum value of one and can be described, combining equations (8-5), (8-6), (8-9), (8-12) and (8-18) as follows:

$$DI = \left[ \frac{\text{recirculated mass flow rate \%}}{85.7\%} \right] \times \left[ \frac{v_{\text{injection @300K}}}{100} \right] \\ \times \left[ \frac{1}{-1422x^3 + 400.33x^2 - 19.871x + 1.648} \right] \\ \times \left[ \frac{\text{Optimum NO Values}}{\text{NO values corrected to same condition}} \right] \quad (\text{Equation 8-19})$$

## **9. Chapter Nine: Conclusions and Recommendations for Future Work**

### **9.1. Conclusions**

Design and development of a CDC combustor for high thermal intensity application requires careful examination of critical parameters such as gas recirculation, flowfield configuration, and fuel/oxidizer mixing to achieve desirable combustion characteristics. By systematic design of the combustor, ultra-low emissions of NO and CO were demonstrated with fuel flexibility. Direct injection of air and fuel in the combustion chamber at high velocity was employed and no flame stabilizer such as swirler or bluff body was used in the present work. Simple computational fluid dynamics as well as chemical kinetic computations were performed to help in designing the combustor as well as to understand the experimental results. The experimental database reported in this dissertation could also serve as a database to develop and validate computational models to predict combustion characteristics of CDC combustors. Following conclusions can be drawn based on the work performed in this dissertation that can be useful for designing a high thermal intensity CDC combustor.

#### **9.1.1. Effect of Flowfield Configuration**

Both swirling and non-swirling flow configurations were investigated and it was observed that the flame was more distributed under swirling configuration as indicated by OH\* chemiluminescence. Swirling configurations also resulted in significantly lower NO and CO emissions as compared to a non-swirling flow configuration. Particle image velocimetry indicated that swirling configuration had a higher internal

recirculation as compared to non-swirling configuration which fosters distributed reactions to provide ultra-low emissions. Also, extending the combustor exit into the combustion volume reduced CO emissions as a direct result of the enhanced residence time.

#### 9.1.2. Effect of Fuel Injection Location

Various fuel injection locations has been examined, ranging from coaxial injection to cross flow injection. The injection location was moved downstream to identify the role of air-fuel separation distance on emissions. Early injection (such as coaxial) resulted in high emissions due to the fact that air and fuel ignites without proper mixing with the hot recirculated reactive gases, critical to achieve CDC conditions. On the other hand, delayed injection led to high emissions as fuel ignites before it is properly mixed with the hot diluted oxidizer (formed through mixing air and hot recirculated reactive gases). Fuel injection midway provided minimal NO and CO emissions as compared to injection upstream or downstream of that point. This outlines the importance of mixing time scale with respect to ignition delay to provide the combustor with a well-mixed air/recirculated hot reactive gases/fuel mixture for distributed combustion.

#### 9.1.3. Temperature and Pressure Effect

Increasing air inlet temperature increased NO emissions as a result of the increased combustion temperature. However, increasing the air inlet temperature reduced CO emissions as a result of better CO to CO<sub>2</sub> conversion. Also higher temperature

stabilized the flame at lower equivalence ratio leading to extension of the operational limit.

Increasing the combustor pressure resulted in similar behavior with increased emissions. It is noteworthy that operating at higher pressure mandated increasing the heat load to keep the heat release intensity constant. Increasing the pressure in the combustor also extended the lean operational limit.

Increasing air temperature and/or combustion pressure resulted in a reduction in the combustion reaction zone as outlined by OH\* chemiluminescence. The reaction zone shifted upstream as the reaction was stabilized at higher flow velocities with increased air temperature. This can be seen as a direct result of the variation of flame speed with change in temperature and pressure. Emissions below 10 PPM of NO and CO were demonstrated for both premixed and non-premixed injection under elevated temperature and pressure conditions.

#### 9.1.4. Fuel Flexibility

Proper combustor design fostering distributed reactions led to increased fuel flexibility. Different fuels have been examined to evaluate the fuel flexibility of the combustor in terms of pollutants emission and stability. Emission less than 7.5 PPM of NO was demonstrated regardless of the fuel used with CO emissions below 40 PPM for heavier hydrocarbons, and less than 10PPM for methane based fuels without any modifications to the combustor used. Novel combustor design was able to handle different flame speeds such the slow flame speed of diluted methane to the much higher speed of hydrogen enriched methane. Methane dilution led to about 45% decrease in

NO emissions while enriched hydrogen methane extended the lean operational limit. No flame flashback or any combustion instabilities were observed. The increased emissions in heavier fuels (propane, kerosene, and JP-8) compared to methane can be related to less distributed nature of the reaction as the fuel is harder to mix as compared to methane. Increased CO emissions can be seen as a result of the increased carbon content in the fuel. No sooting was observed even with heavier hydrocarbons. The fuel flexibility range did not only include traditional gaseous and liquid fuels but also extended to include renewable fuels such as HRJ fuel and novel Butyl Nonanoate fuel.

#### 9.1.5. Injector Shape

The role of injector shape on emissions was examined. Elliptical nozzles resulted in higher emissions compared to circular nozzles. This was observed in both cases where the fuel jet was parallel to the elliptical long axis or short axis. Elliptical nozzles led to either decreased mixing with the hot recirculated gases (and less entrainment) or decreased mixing with fuel due to the change in jet momentum ratio, depending on the elliptical nozzle orientation.

#### 9.1.6. Air Injector Velocity

Increase in air injection velocity led to higher entrainment rates as shown by PIV isothermal flowfield measurements. The increased entrainment of hot recirculated reactive gases were expected to decrease emissions, which was verified as NO emissions were reduced by up to 45% with minimal impact on CO emissions. This emissions reduction was observed for both premixed and non-premixed injection

modes. The flame zone was observed to be further downstream with increased air velocity, leading to more time for the mixing process prior to ignition.

#### 9.1.7. Fuel Dilution Effects

Dilution of methane with air resulted in significant reduction in NO emission with non-premixed injection. Dilution of fuel with small amount of air, such that the fuel stream is above the rich flammability limit of fuel to avoid problem of flashback, could be used as a viable option to significantly reduce the NO<sub>x</sub> emissions. No emissions with fuel dilution demonstrated NO emissions near premixed values for the combustor discussed in this dissertation and in other ultra high intensity CDC combustor.

#### 9.1.8. Dual Injection

Dual air and fuel injection was examined to provide insight on combustor scaling up for practical gas turbine size. Dual injection demonstrated higher emissions compared to single injection. This can be attributed to flame to flame interaction between different reaction zones and improper temperature distribution inside the combustor. OH\* chemiluminescence outlined the fact that one of the reaction zone had higher intensity than the other. Careful manipulation of fuel distribution between nozzles led to decrease in emissions and even reaction zone intensity. Lowest emissions were observed with 55% of the fuel was injected in the first injector, were the recorded emissions were lower than those recorded under single injection mode. This outlines the possibility of manipulating fuel distribution in dual and multi injection combustors to control emissions.

#### 9.1.9. PLIF Experiments

PLIF data have indicated the presence of OH radicals at the air intake, outlining the role of recirculated hot reactive species in configurations ATP/ATF1 which demonstrated ultra-low emissions. Also PLIF data showed that OH is more distributed than shown through OH\* chemiluminescence, where OH occupied larger area as compared to the data obtained through chemiluminescence. OH was detected in the entry region of the combustor indicating the presence of hot reactive recirculated gases at the combustor inlet, a feature that was not present in OH\* chemiluminescence. PLIF also demonstrated the ability to measure temperature non-intrusively, where it was shown that the ratio indicating temperature had small fluctuations inside the combustor with no hot-spots visible.

#### 9.1.10. Distribution Index

The newly developed distribution index offers an inexpensive method to evaluate the reaction distribution within a given combustor based on design parameters of the combustor. The distributed index “DI” incorporated the role of hot reactive gases recirculation, air injection velocity, air/fuel mixing, and operational conditions with view to develop ultra-low emissions truly distributed reaction combustors. It was found that obtained expressions for DI agrees favorably with the different geometries/conditions examined in this dissertation.

## 9.2. Recommendations for Future Work

Colorless distributed combustion (CDC) have shown remarkable potential for further development and implementation in gas turbine combustors, for both stationary and aviation applications. However, in depth research is still required to gain insight on the fundamental process of combustion of fuel in hot and diluted conditions under high thermal intensity conditions. Improved design and testing is also essential to transfer the technology for practical gas turbine applications. Recommendation for future work is suggested below:

### 9.2.1. Examination of the Role of Hot Recirculated Reactive Gases

The role of internally recirculated hot reactive gases needs to be quantified to obtain the minimum requirement of recirculation. Hot reactive gases mix with air to form hot and diluted oxidizer that fosters distributed reactions. The impact of the amount of recirculated gases on flame structure and behavior needs to be investigated to outline the minimum required amount of recirculated gases that fosters distributed combustion to be used as a design target for future combustor designs.

### 9.2.2. Detailed Species and Temperature Distribution

Detailed reaction zone structure, species and temperature distribution can be obtained using advanced non-intrusive optical diagnostic techniques such as planar laser induced fluorescence (PLIF) for characterization of turbulent combustion regimes in both premixed and non-premixed combustion modes. NO formation regions could be identified and novel techniques could be used to further reduce the pollutant emissions. These detailed measurements can be used to develop much needed chemical

kinetics mechanisms that correctly predicts the behavior of distributed combustion. PLIF showed significant promise in measuring temperature in a non-intrusive way within the combustor, however, further work is required to overcome the hurdles of background noise and reflections to enhance the signal quality and minimize errors.

### 9.2.3. Quantification of Relevant Time Scales

Ignition delay and mixing time scales can be quantified and it can be confirmed that the mixing time scales are lower than ignition delay time scales. Ignition delay time is expected to be different under CDC conditions due to the different environment in which combustion occurs. The impact of the amount of recirculated gases on ignition delay shall be examined as well. Such quantification will ensure that the fuel/oxidizer mixture burns due to spontaneous ignition after a uniform mixture is achieved as well as it will provide understanding to further improve the combustor design to achieve even lower emissions.

### 9.2.4. Improved Fuel/Oxidizer Mixing

Fuel/oxidizer mixing could be further enhanced by considering novel ideas such as implementation of forced pulsations in the fuel stream. Fuel dilution effects were investigated in the present dissertation and it was observed that small amount of air addition to the fuel stream (much above the rich flammability limit to avoid flashback) could result in substantial reduction in NO emission level in non-premixed mode. This technique could be further explored to achieve ultra-low emission levels. Other injector geometries can be investigated to enhance entrainment of hot recirculated gases and mixing with fuel, such as Chevron shaped injectors.

#### 9.2.5. Characterization of Dynamic Performance

The dynamic stability of the combustor could be investigated in detail and the combustor can be characterized based on the dynamic response at lean operation. Pressure oscillations could be measured to understand the interaction of heat release oscillations with natural modes of the combustor. Forced pulsations from fuel or air streams could be used to understand the effect of perturbations on the dynamic stability of the combustor. The dynamic performance of the combustor using liquid fuels is also of interest to identify the response time of the combustor with sudden change in fuel flow conditions such as sudden increase in fuel flow that might not evaporate quickly enough to sustain the combustion.

#### 9.2.6. Multi-injection and Scaling of CDC Combustor

Scaling-up of CDC combustor from laboratory scale to practical combustors present many challenges such as maintaining similar turbulent mixing time scales, achieving sufficient mixing at large scale, achieving dynamic stability as well as desired pressure drop while maintaining similar ultra-low emissions and high thermal intensity. Dual injection experiments have been performed to provide insight for scaling up. Multi-injection and its impact on pollutants emission can be investigated for practical implementation of the CDC technology for gas turbine engines.

#### 9.2.7. Elevated Pressure Operation

Land based gas turbine combustors operate at elevated pressures at about 15 atm.. At these pressures the combustion chemistry can be very different as compared to normal pressure condition even though the aerodynamics might be similar.

Experiments have been performed at 2 atm. as discussed in this dissertation. However, investigation of CDC operation at much elevated pressure condition will give useful insight while designing a practical gas turbine combustor. Aircraft engines operate at pressure ratios up to 40 and hence performance of the combustor under elevated pressure is of extreme importance for this application. The elevated pressure not only will affect the mixture preparation in the combustor but also change the ignition delay of the mixture. Further studies need to include elevated pressure to pave the path for ultra-low emission operation at elevated pressures.

#### 9.2.8. Part Load Operation

The operational window for gas turbines with ultra low emissions is normally limited to the design load. However, the gas turbine combustors operate at part load conditions depending on the demand fluctuation and the operation between 50-100% load conditions is desirable. Aircraft combustors have even more different and demanding requirements ranging from taxi, takeoff climb, cruise, approach and landing and different operating conditions require different power level from the combustor which may range from 20-100%. Operation at elevated pressure is expected to increase the operational window of the combustor. Extension of operational window for CDC combustor could be pursued to increase the applicability of CDC combustors to practical engines. Further research is required to understand relight capability of CDC combustor in case of blow-off during combustor operation. Also examination of the stability limits under multi injection can provide wider operational range more suitable to the challenging gas turbine operating conditions

## Appendix A: List of Papers

### A.1 Published Journal Papers

1. Khalil, A.E.E., and Gupta, A.K., “Swirling Distributed Combustion for Clean Energy Conversion in Gas Turbine Applications”, Applied Energy, Vol. 88, 2011, pp. 3685-3693.
2. Khalil, A.E.E., and Gupta, A.K., “Distributed Swirl Combustion for Gas Turbine Application”, Applied Energy, Vol. 88, 2011, pp. 4898-4907
3. Arghode, V. K., Khalil, A.E.E., and Gupta, A. K., “Fuel Dilution and Liquid Fuel Operational Effects on Ultra-High Thermal Intensity Distributed Combustor”, Applied Energy, Vol. 95, 2012, pp. 132-138.
4. Khalil, A.E.E, Arghode, V.K., and Gupta, A.K., “Low Calorific Value Fuelled Distributed Combustion with Swirl for Gas Turbine Applications”, Applied Energy, Vol. 98, 2012, pp. 69-78
5. Khalil, A.E.E., Gupta, A.K., Bryden, M.K., and Lee, S.C., “Mixture Preparation Effects on Distributed Combustion for Gas Turbine Applications”, J. Energy Resour. Technol., Vol. 134 (3), 2012, 032201. **Awarded Melville medal for the best original paper published in the ASME Transactions**
6. Khalil, A.E.E., and Gupta, A.K., “Hydrogen Addition Effects on High Intensity Distributed Combustion”, Applied Energy, Vol. 104, 2013, pp. 71-78
7. Khalil, A.E.E., Arghode, V.K., and Gupta, A.K., “Novel Mixing for Ultra-High Thermal Intensity Distributed Combustor” Applied Energy, Vol. 105, 2013, pp.327-334
8. Khalil, A.E.E., and Gupta, A.K., “Fuel Flexible Distributed Combustion with Swirl for Gas Turbine Applications” Applied Energy, Vol. 109, 2013, pp.267-274
9. Khalil, A.E.E., and Gupta, A.K., “Dual Injection Distributed Combustion for Gas Turbine Application”, Journal of Energy Resources Technology, J. Energy Resour. Technol., Vol. 136 (1), 2014, 011601
10. Khalil, A.E.E., and Gupta, A.K., “Swirling Flowfield for Colorless Distributed Combustion”, Applied Energy, Vol. 113, 2014, pp.208-218
11. Khalil, A.E.E., and Gupta, A.K., “Butyl Nonanoate as a Future Biofuel for Clean Gas Turbine Engines”, Fuels, Vol. 116, 2014, pp.522-528

## **A.2 Journal Papers Under Review/In preparation**

1. Khalil, A.E.E., and Gupta, A.K., “Velocity and Turbulence Effect on Distributed Combustion for Clean Gas Turbine Engines”, Submitted, Applied Energy
2. Khalil, A.E.E., and Gupta, A.K., “Towards Distributed Combustion for Ultra Low Emission using Swirling and Non-Swirling Flowfields”, Submitted, Applied Energy

## **A.3 Peer Reviewed Conference Papers**

1. Khalil, A.E.E., Arghode, V. and Gupta, A.,” Colorless Distributed Combustion (CDC) With Swirl For Gas Turbine Application”, POWER2010-27309, Proceedings of ASME 2010 Power Conference, 13-15 July, 2010, Chicago, Illinois, USA. Doi:10.1115/POWER2010-27309.
2. Khalil, A.E.E., Arghode, V. and Gupta, A., “Swirl Effects On Distributed Combustion For Near Zero Emission Gas Turbine Application”, DETC2010-28136 Proceedings of the ASME 2010 International Design Engineering Technical Conference & Computers and Information in Engineering Conference IDETC/CIE 2010 15-18 August, 2010, Montreal, Canada. Doi:10.1115/DETC2010-28136.
3. Khalil, A.E.E., Arghode, V., and Gupta, A., “Distributed Combustion with Swirl for Gas Turbine Applications”, Paper # AIAA-2011-0064, 49th AIAA Aerospace Sciences Meeting including the New Horizons Forum and Aerospace Exposition. 4 - 7 January 2011, Orlando World Center Marriott, Orlando, Florida, USA.
4. Khalil, A.E.E. and Gupta, A., “Distributed Combustion With Swirl For Gas Turbine Engine Applications”, International Conference on Applied Energy (ICAE 2011), 16-18 May, 2011, Perugia, Italy.
5. Khalil, A.E.E. and Gupta, A., “Distributed Combustion with Swirl for Gas Turbine Application using Low Calorific Value Fuel”, POWER2011-55109, Proceedings of ASME 2011 Power Conference, 12-14 July, 2011, Denver, Colorado, USA. Doi:10.1115/POWER2011-55109
6. Khalil, A.E.E. and Gupta, A., “Swirl and Pressure Effects on Colorless Distributed Combustion For Gas Turbine Application”, Paper # AIAA-2011-5528, 9th International Energy Convention Engineering Conference, 31 July- 3 August 2011, San Diego Convention Center, San Diego, California, USA.
7. Khalil, A.E.E. and Gupta, A., “Colorless Distributed Combustion for Ultra Low Emission Gas Turbine Applications”, 20th International Symposium on Air

- Breathing Engines (ISABE) (2011), Paper # ISABE-2011-1127, 12-16 September 2011, Gothenburg, Sweden
8. Khalil Hasan, A.E.E., Gupta, A., Bryden K.M., and Lee, S.C., “Mixture Preparation Effects on Distributed Combustion for Gas Turbine Applications”, Paper # AIAA-2012-0930, 50th AIAA Aerospace Sciences Meeting including the New Horizons Forum and Aerospace Exposition. 9 - 12 January 2012, Gaylord Opryland Resort & Convention Center, Nashville, Tennessee, USA. **Best Terrestrial Energy Systems Paper Award**
  9. Khalil Hasan, A.E.E., Gupta, A., “Fuel Flexible Distributed Combustion for Gas Turbine Engines”, Paper # AIAA-2012-4033, 48th AIAA/ASME/SAE/ASEE Joint Propulsion Conference. 29 July-1 August 2012, Hyatt Regency Atlanta, Georgia, USA
  10. Khalil Hasan, A.E.E., Gupta, A., “Flowfield Effects on Distributed Combustion for Clean Gas Turbines”, 51st AIAA Aerospace Sciences Meeting including the New Horizons Forum and Aerospace Exposition. 7-10 January 2013, Gaylord Texan Hotel and convention Center, Grapevine (Dallas/Ft. Worth Region), Texas, USA
  11. Khalil Hasan, A.E.E., Gupta, A., “Characterization of swirling Distributed Combustion”, AIAA 11th International Energy Conversion Engineering Conference, 15 - 17 July 2013, San Jose Convention Center, San Jose, California
  12. Khalil, A.E.E. and Gupta, A., “Dual Injection Distributed Combustion For Gas Turbine Application”, POWER2013-98080, Proceedings of ASME 2013 Power Conference, 29 July- 1st August, 2013, Boston, MA, USA.

## Appendix B: Combustor Assembly

This section describes the design and fabrication of the swirling CDC combustor.

### B.1 Schematic of the Combustor

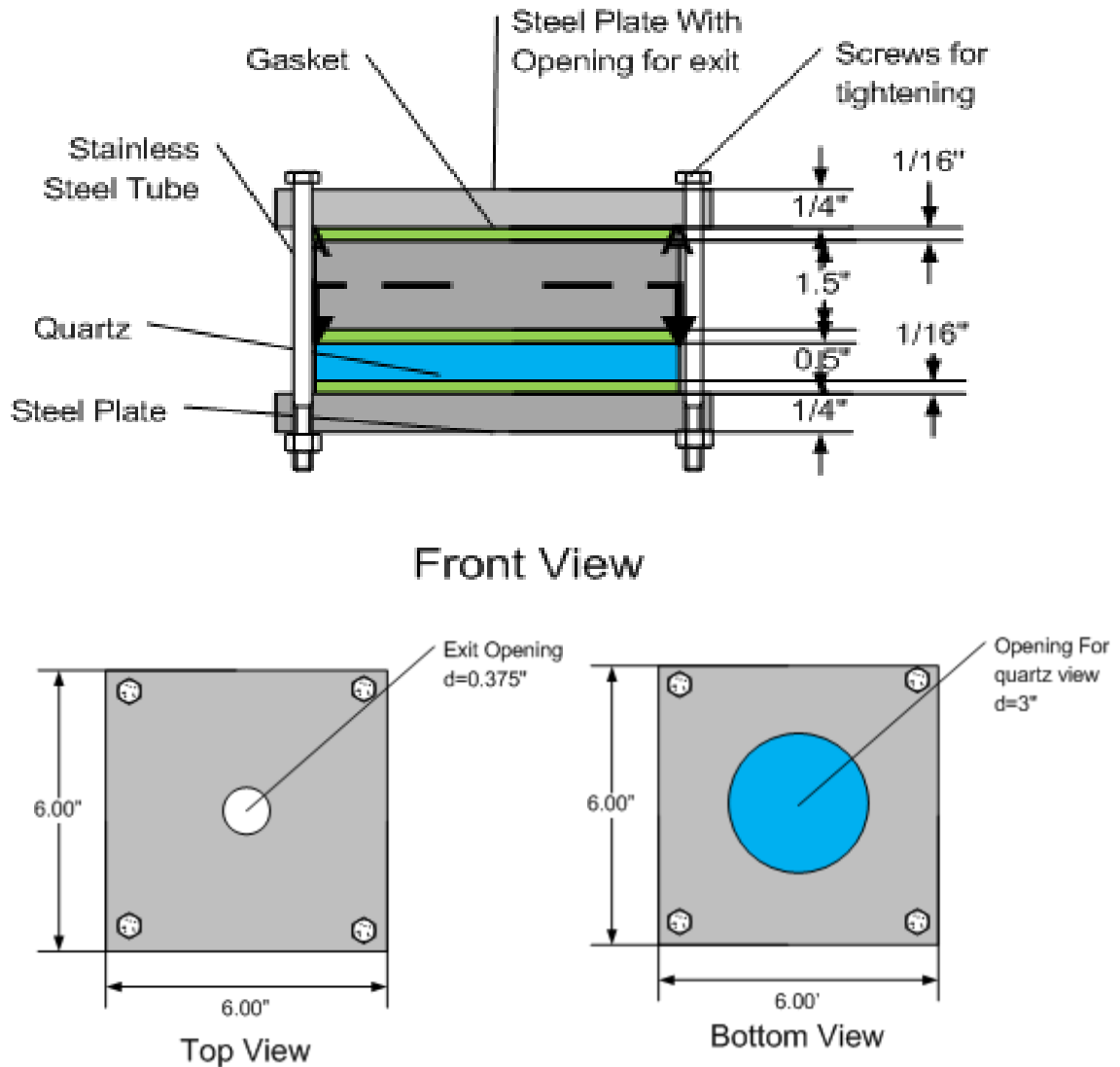


Figure B-1 Schematic of the assembled Combustor

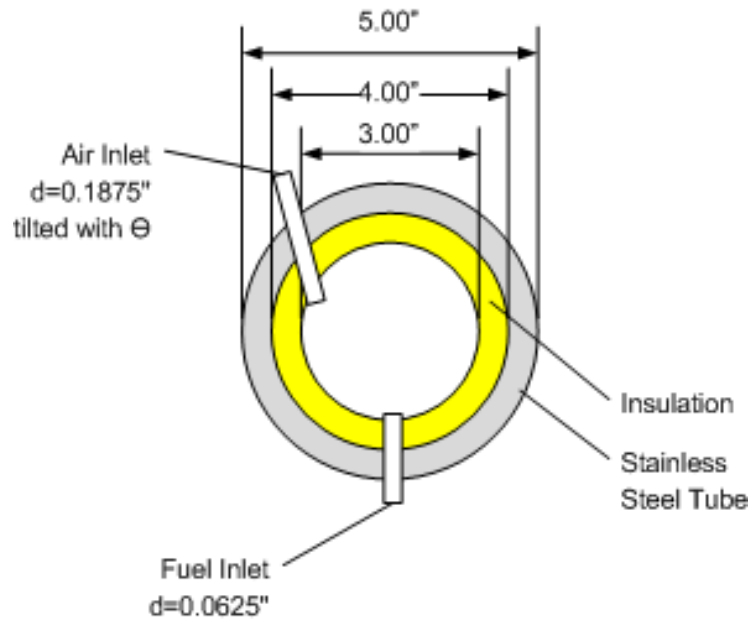


Figure B-2 Cut section into the combustor assembly

### B.2 Stainless Steel assembly

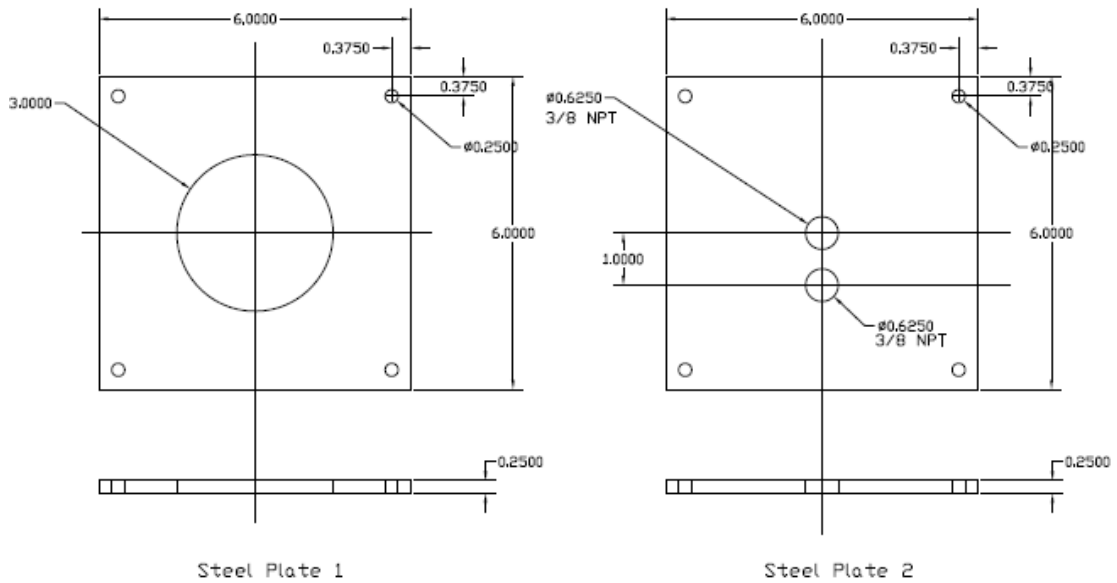


Figure B-3 End-Plates dimensions

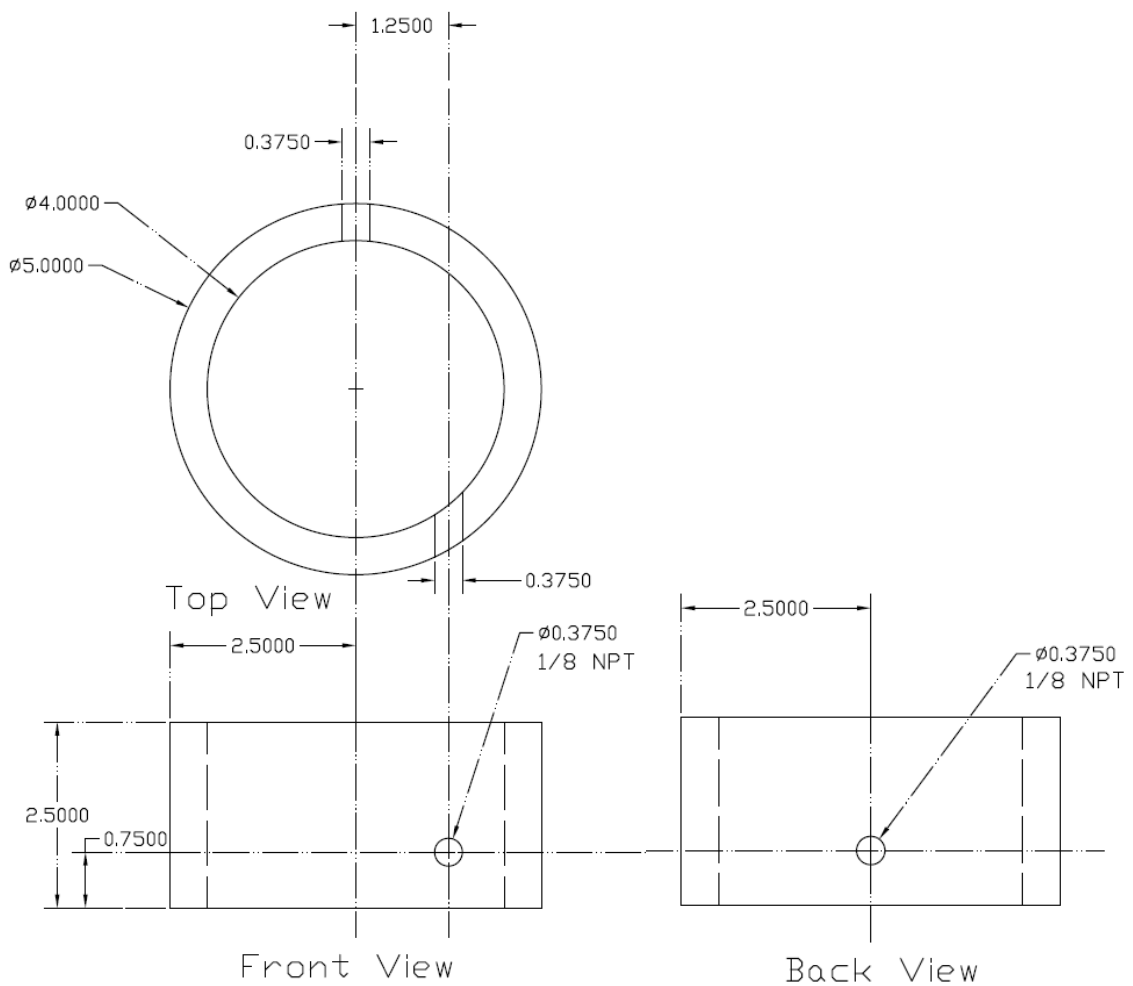


Figure B-4 Stainless Steel pipe dimensions

### B.3 Insulation

The combustor was internally insulated to minimize heat losses. The cylindrical walls were insulated with a  $1/2$  inch thick zirconia ceramics with the following composition:

Zircar Zirconia's Type ZYC: 85 wt%  $ZrO_2 + HfO_2$ , 10 wt%  $Y_2O_3$ , and 5%  $SiO_2$

The back wall of the combustor was insulated with 1 inch thick alumina insulation with the following composition: Zircar Ceramics ZAL-15: 85%  $\text{Al}_2\text{O}_3$ , 15%  $\text{SiO}_2$ .

Holes were drilled through the insulation to allow for air and fuel injection and product gases exit. Also an ignition port was drilled. The insulation was then treated with a zircar zirconia rigidizer to prevent erosion of the insulation.

#### **B.4 Extended Axial Exit**

An alumina tube was extended inside the combustor to enhance residence time. Alumina was chosen as it can withstand extreme temperatures without any damage or transformation.



Figure B-5 Inner insulation with extended axial exit at center

## **B.5 Injectors and Exit Assembly**

Air and fuel injectors were made from stainless steel tubes with internal diameter matching the required diameter. The injectors were connected to the combustor by using “Swage Lok” connectors to eliminate any leakage. The combustion products were guided to a manifold where the sampling line was installed along with a thermocouple before exiting to the exhaust system. A valve was added to this manifold to choke the combustor which allowed operation at pressures higher than atmospheric pressure.

## **Appendix C: Geometrical Variations**

In chapter 4 we have investigated different geometrical combustor configuration and their impact on the flowfield and emission characteristics of the combustor. In this appendix we will discuss other geometrical variations that do not necessarily change the flowfield behavior in a profound way but rather modify it. The effect of each of these variations on the combustor behavior has been studied experimentally to further enhance reaction distribution and achieve ultra low pollutants emission as discussed herein.

### **C.1 Combustor Length Variation**

The first parameter studied was the length (depth) of the combustor. All the previous investigations were performed with the combustor having a depth of 8D (1.5"). Figure C-1 shows the combustor schematic where the depth was changed. Two experiments have been performed with the combustor having a length of 5.33D (1") and 10.66D (2"). Changing the combustor length changed the overall energy release intensity from 36 MW/m<sup>3</sup>-atm to 48 MW/m<sup>3</sup>-atm (5.33D) and 24 MW/m<sup>3</sup>-atm (10.66D). Change in the energy release intensity is expected to affect both the residence time in the combustor and the combustor pollutants emissions.

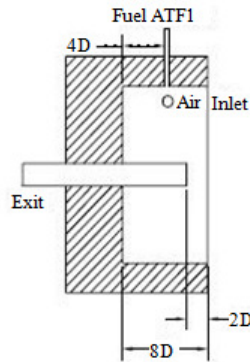


Figure 0C-1 Schematic of the Combustor with depth change (8D)

Figure C-2 shows the obtained emission with different combustor length for non-premixed combustion. NO emissions did not change with the combustor depth of 8D and 5.33D. However, for the case of 10.66D depth, NO emission increased dramatically to more than double the original emissions. On the other hand, CO emissions were highest for the 5.33D case which can be related to the reduced combustor volume and residence time. On the other hand, CO emissions were lowest for the case of 8D, not 10.66D as one might think. Though the residence time is higher in the 10.66D depth case, which should lead to lower CO emissions, the combustion was observed to be less distributed. This is also supported by the high NO emission. This behavior indicates that as the combustor volume starts to get larger, for the same heat load, the mixture preparation is harder to achieve due to the fact that the freshly injected reactants and recirculated hot reactive species are not close enough to each other to achieve enhanced mixing and distributed reactions.

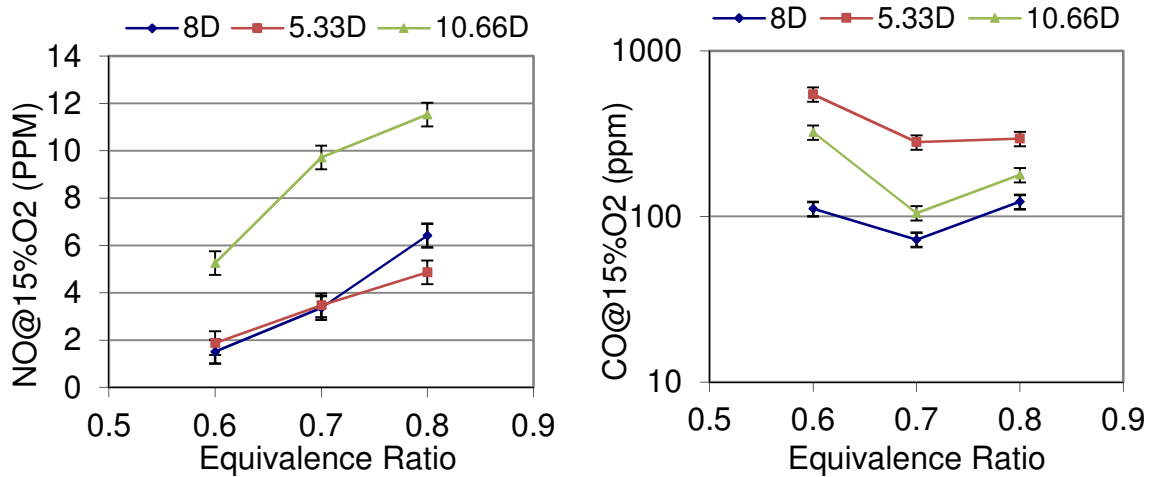


Figure C-2 NO and CO emissions for different combustor depth

## C.2 Combustor Exit Clearance

The second parameter studied was the clearance between the extended exit tube and the end of the combustor as shown in Figure C-1. In all the previous experiments the distance between the end of the tube and the end of the combustor was 2D (0.375”), this was reduced to 1D (0.1875”). Decreasing the depth of the clearance for hot products exit is expected to enhance the residence time inside the combustor. On the other hand, the reduction will make it harder for the gasses to exit leading to an increase in the pressure drop. The recorded emissions showed an increase in NO emissions for both premixed and non-premixed combustion modes (ATP and ATF1) with minimal decrease in CO emissions. However, the pressure drop across the combustor was increased by 30% outlining the unfavorable effect of reducing this clearance. The experiments were performed with both standard air temperature and preheated air temperature. The recorded emissions for preheated air experiments are shown in Figure C-3.

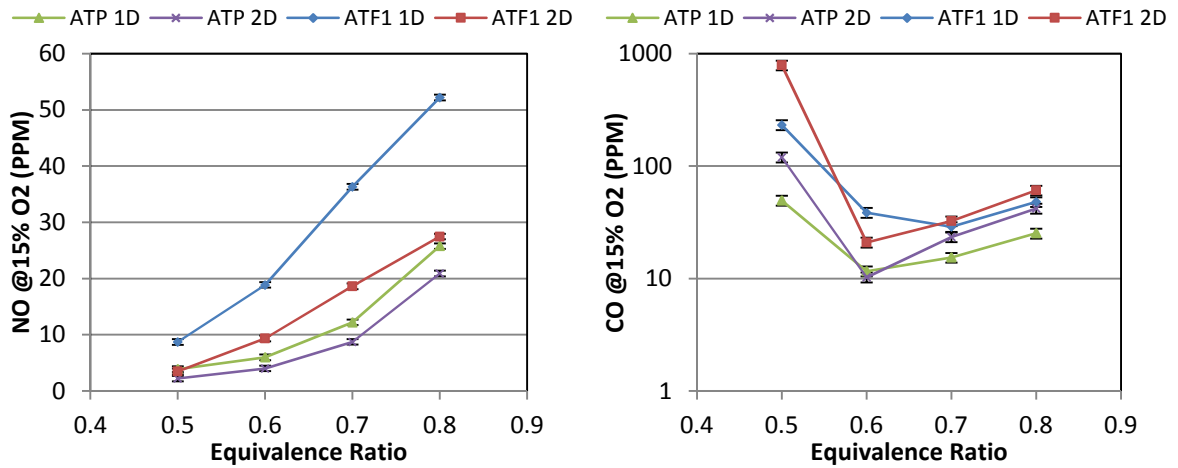


Figure C-3 NO and CO emissions for different exit clearances and air intake temperature of 600K

Further investigations of the examined configuration showed that the higher emissions of NO under the condition of 1D exit clearance can result from the less distributed nature of the reaction occurring under this condition. OH\* chemiluminescence has been recorded for this configuration and the images are shown in Figure C-4 Comparing the intensity distribution with that obtained under 2D exit clearance outlines the difference in reaction distribution were the reaction was found to be less distributed.

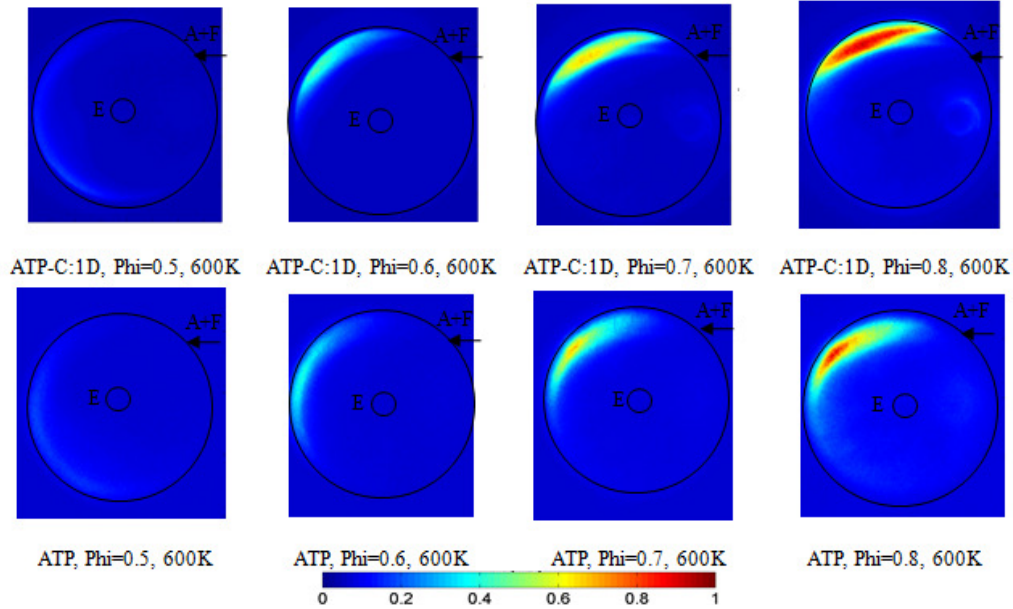


Figure C-4 OH\* Chemiluminescence for 1D exit clearance and the base case for premixed combustion with air preheat temperature of 600K

### C.3 Injection Plane Location

The third parameter investigated was the air and fuel injection plane with respect to the combustor depth. For all the experiments performed, air and fuel were injection at the mid depth of the combustor. In this section, the injection plane is moved deeper into the combustor at a depth of 2D rather than 4D as shown in Figure C-5.

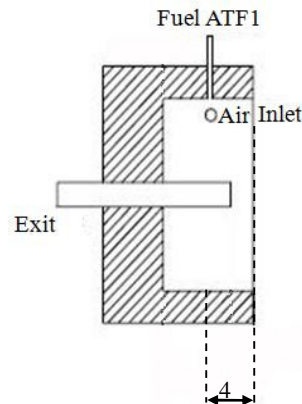


Figure C-5 Air/Fuel injection plane location

The injection plane was not moved to the other side as that would have led to some of the fresh reactants directly escaping prior to combustion as the new mixture will be injected at the extended tube under that configuration (injection at 6D).

The obtained emissions for injection at 2D are shown and compared to the results obtained with injection at mid plane in Figure C-6. For both premixed and non-premixed combustion NO emissions were found to increase. NO emissions increased by about 20% with the injection at 2D. The increase in NO emissions was much higher in the non-premixed case (50% increase). On the other hand, CO emissions were reduced for both premixed and non-premixed by about 20% or more. Though the reduction in CO is beneficial, but it is outweighed by the substantial increase in NO emissions from the combustor.

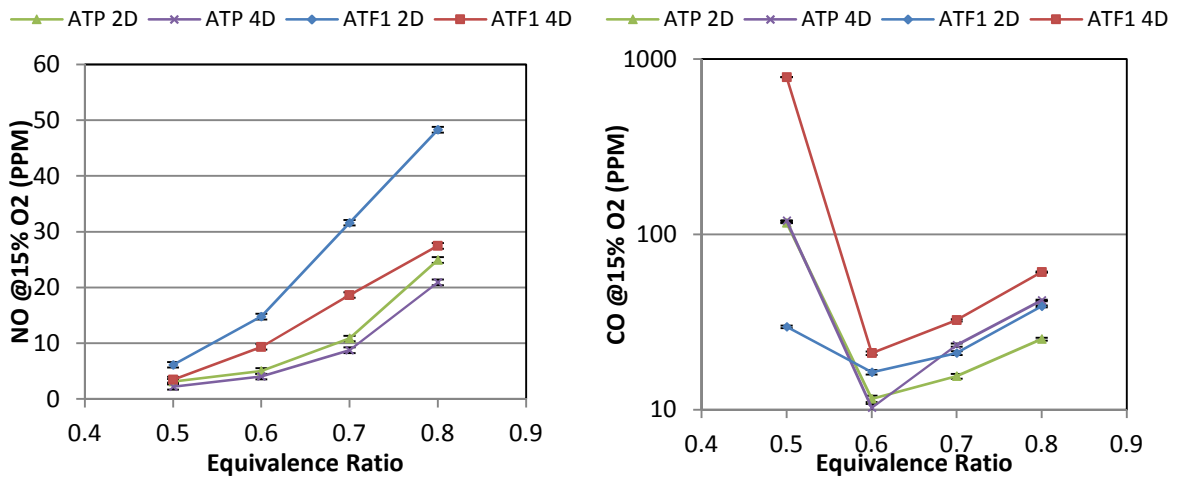


Figure C-6 NO and CO emissions for different injection planes

Further investigations of the examined configuration showed that the higher emissions of NO air and fuel injection plane at 2D can be related to the less distributed nature of the reaction occurring under this condition. OH\* chemiluminescence has been

recorded for this configuration and the images are shown in Figure C-7. For injection at 2D (ATP-I:2D), the combustor was inverted to accommodate that change, consequently the obtained images are mirrored compared to the base case. Comparing the intensity distribution with that obtained under 2D exit clearance outlines the difference in reaction distribution were the reaction was found to be less distributed and areas of high OH\* intensity was found to be higher under this condition.

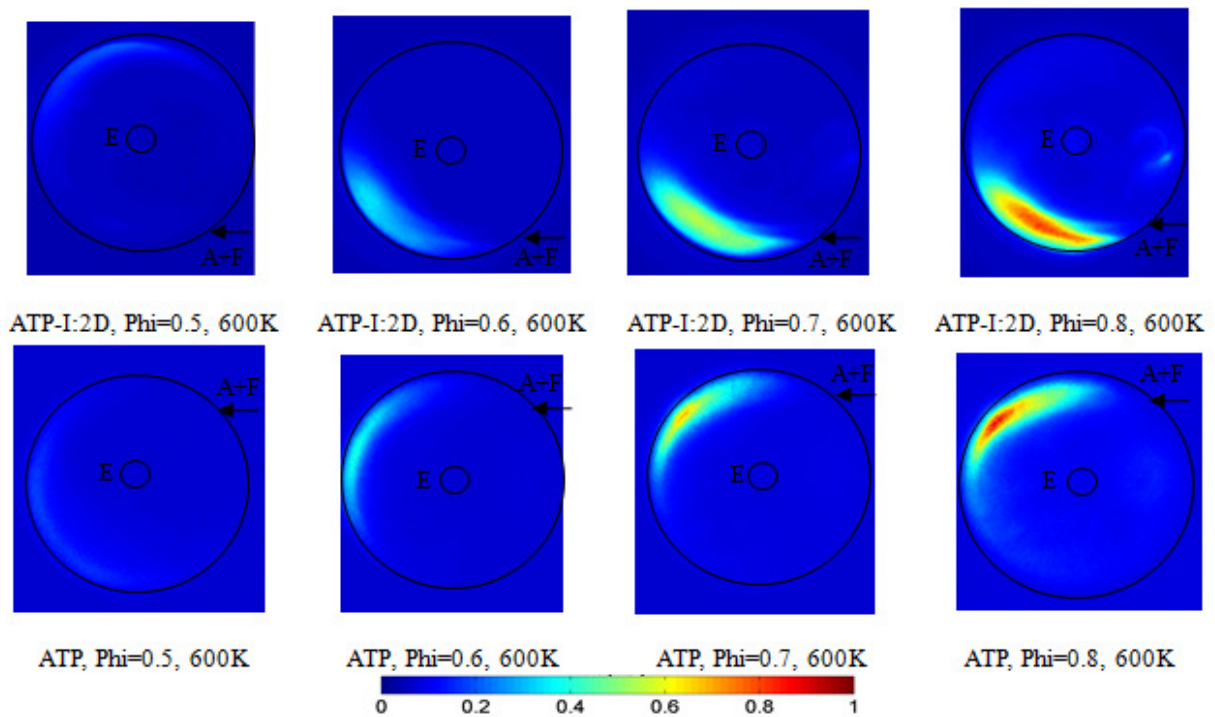


Figure C-7 OH\* Chemiluminescence for 2D injection plane and the base case for premixed combustion with air preheat temperature of 600K

#### C.4 Combustor Diameter Effect

The fourth parameter examined was the combustor diameter, where the combustor diameter was reduced from 16D to 13D. Reducing the combustor diameter will reduce the combustor volume offering less residence time for combustion. However, that reduction is expected to affect the combustor pollutants emissions differently than what

was encountered in the first set of experiments regarding combustor length. This is due to the helical nature of the flow inside the combustor.

Figure C-8 shows the recorded NO and CO emissions for the two examined diameters. For premixed combustion, it can be seen that the change in NO was minimal. On the other hand, for non-premixed combustion, NO increased dramatically, suggesting improper mixing inside the combustor. To achieve ultra low emissions, mixture preparation has to be performed adequately to result in a distributed mixture for spontaneous ignition.

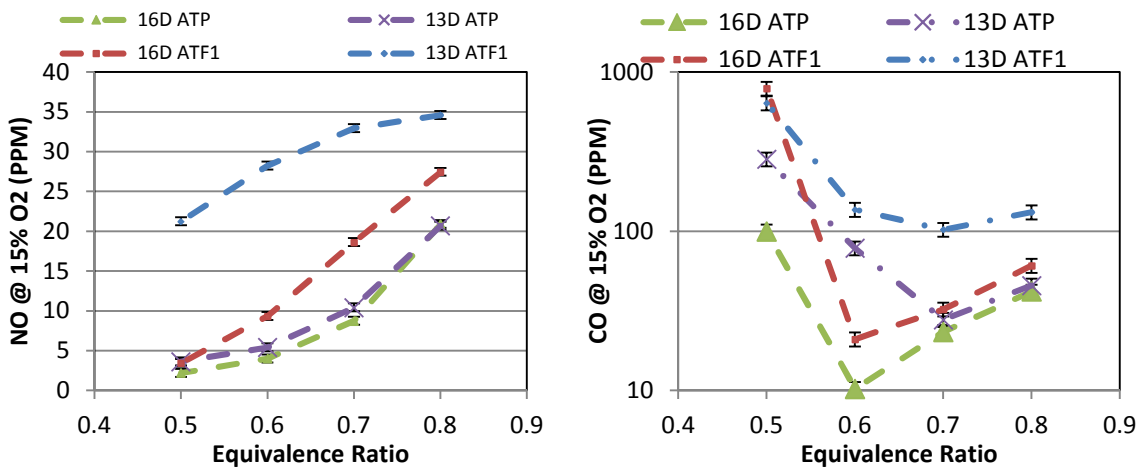


Figure C-8 NO and CO emissions for different combustor diameters

CO emission trend was consistent with what was encountered when the combustor length was reduced. Smaller diameter led to lower residence time, resulting in higher CO emissions as demonstrated in Figure C-8.

## **Appendix D: Novel Mixing for Ultra-High Thermal Intensity**

Air and fuel dilution with flue gasses have been studied with emphasis on the effect of air dilution versus fuel dilution on nitric oxides emissions [142]. It was concluded that the greater effectiveness of fuel dilution as compared to air dilution in practical applications results from enhanced turbulent mixing and heat transfer. Dilution of fuel with inert gases and lower heating value fuel has been investigated for combustor operation with ultra-low emission. Nitrogen addition has been shown to decrease NO emissions by 50% to achieve emissions of 2 PPM of NO 12 PPM of CO [143]. The same trend was observed with air and carbon dioxide dilution [144] leading to an overall enhanced performance. The decrease in pollutants emission is attributed to the fuel jet having higher jet momentum (due to the added diluents). Also, the added mass acts as a thermal sink that lowers the overall combustor temperature which significantly lowers the thermal NO<sub>x</sub> through Zeldovich mechanism [9].

In this appendix, fuel dilution effects with different amounts of air (and also air dilution effects with different amounts of fuel) are investigated with emphasis on achieving ultra-low emissions comparable to or less than those from novel premixed combustion in distributed combustion without encountering any flashback or combustion instabilities. The combustor used in this investigation is characterized by ultra-high thermal heat release intensity (270-420 MW/m<sup>3</sup>-atm). Such heat release intensities are much higher than those used in modern gas turbine engines.

## D.1 Geometry

Figure D(a) shows a schematic of the CDC combustor examined here. The combustor was of rectangular cross section to facilitate complete optical access through quartz windows from front and back side. Air was injected from the exit side and fuel was either injected in cross-flow in non-premixed/direct-injection mode (Figure D(b)) or thoroughly mixed with the combustion air in premixed mode (Figure D(c)).

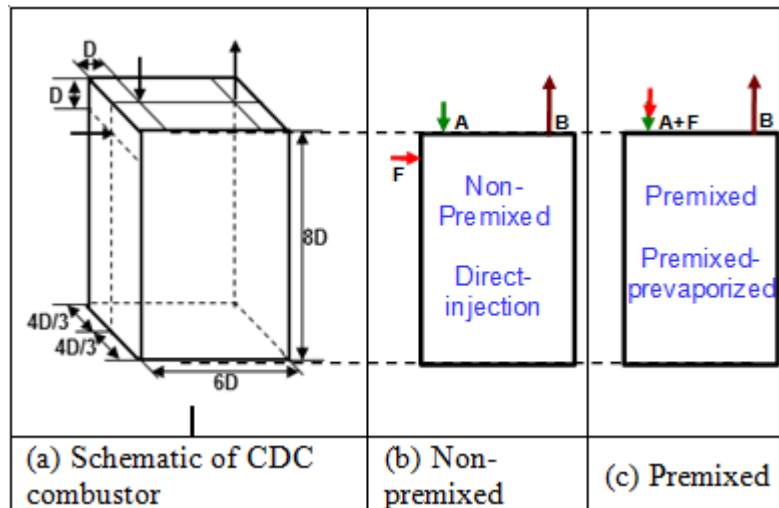


Figure D-1 Ultra-high thermal intensity CDC combustor (a) schematic, (b) non-premixed mode, and (c) premixed mode

The premixed combustion mode was expected to provide minimum thermal  $\text{NO}_x$  and hence it can be considered as a baseline case for comparison with the non-premixed and other novel fuel/air dilution modes. In novel fuel/air dilution modes, small amount of air was introduced into the fuel jet, diluting it and increasing its jet momentum. Also, fuel was introduced into the air stream to reduce mixing process inside the combustor. For all the cases discussed here, the equivalence ratio for each of the streams was kept well outside the flammability limits reported for methane to prevent the possibility of

flame flashback [4]. The total air and fuel flow rates were kept constant with a heat load of 6.25 kW resulting in thermal intensity of 420 MW/m<sup>3</sup>-atm at equivalence ratio of 0.8. This equivalence ratio is much higher than that used in current gas turbine engines. It is expected that future gas turbine engines will operate at higher equivalence ratios approaching the high equivalence ratios examined here.

## **D.2 Numerical**

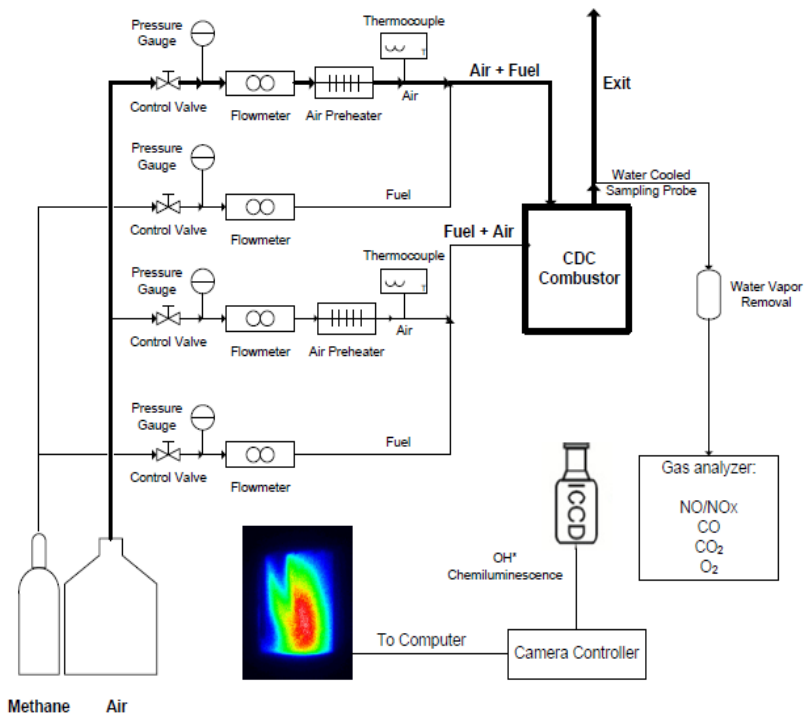
The flow field pattern prediction under non-reacting condition is aimed at providing an understanding of the mixing process inside the combustor to seek for novel mixture preparation cases. The mass flow rates of air and fuel correspond to heat load of 6.25 kW at equivalence ratio of 0.8 using methane as the fuel. Heat load of 6.25 kW corresponds to ultra-high thermal intensity of 420 MW/m<sup>3</sup>-atm. Under novel mixing conditions small amount of fuel is mixed with the air stream as well as fuel is diluted with small amount of air in the cross fuel stream introduced into the combustor. The temperature of air (top) stream and fuel (cross) stream was 600 K and 300 K, respectively, and the combustor operated at 1 atm. pressure.

The flow field was solved using a steady state, implicit, finite volume based method and SIMPLE algorithm was used for pressure velocity coupling. Full hexahedral grid was used and appropriate refinement of grid was performed in the regions with higher gradients. Geometrical symmetry was used to reduce the computational time so that only one-half of the geometry with grid size of about 0.85 million cells was used. The grid refinement effects on calculations performed showed negligible effect on the results for the conditions examined here. Inlet turbulence intensity of 5% was used for

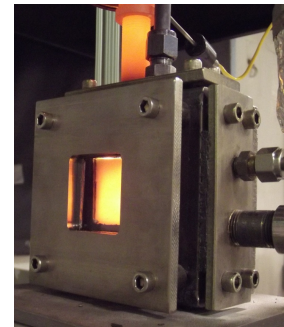
both air and fuel jets and inlet length scale was 0.07 times the hydraulic diameter for both the air and fuel jets. Realizable k- $\epsilon$  model was used to model the turbulence. Second order upwind scheme was used to discretize the convective terms. Convergence was obtained when the normalized residuals for all the variables were found to be less than  $10^{-4}$ . Commercial FLUENT software was used for the simulations.

### **D.3 Experimental**

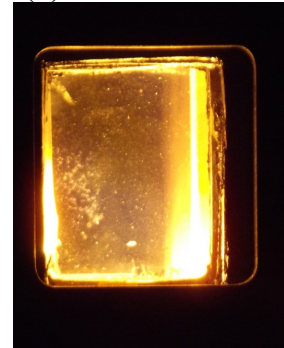
The combustor was operated at a heat load range of 3.9-6.25 kW for equivalence ratio variation from 0.5-0.8, with ultra-high thermal intensity of 270-420 MW/m<sup>3</sup>-atm using methane as the fuel. The combustion chamber was made of a stainless steel that is insulated from the inside with a thick ceramic insulation to reduce heat losses from the combustor. Quartz windows were installed at the combustor sides to allow full optical access in the combustion chamber. Holes were drilled through the steel assembly to accommodate injection of air and fuel into the combustion chamber, and to allow hot combustion gases to exit. A pilot flame was used for initial ignition of the mixture and then transitioned to the CDC mode. Figure D shows a schematic diagram of the experimental test facility along with the combustor.



(a) Schematic drawing of the experimental facility



(b) CDC Combustor



(c) Combustor optical access

Figure D-2 Ultra-high intensity CDC (a) experimental facility, (b) CDC combustor, and (c) the combustor optical access.

For non-premixed case, fuel was injected at ambient temperature of 300 K. Air was injected at elevated temperature of 600 K to simulate the heating due to the compressor in a gas turbine engine. Details of operating conditions for different cases investigated here with methane in premixed, non-premixed and dilution modes are given in Table D-1.

Table D-1 Different cases presented ( $\Phi = 0.8$ , heat load = 6.25 kW,  $T_{top} = 600$  K,  $T_{cross} = 300$  K)

Case	Air (Top) Stream			Fuel (Cross) Stream			Momentum Ratio (air stream/Cross fuel stream)
	Air flow (SLPM)	CH <sub>4</sub> flow (SLPM)	$\Phi$	Air flow (SLPM)	CH <sub>4</sub> flow (SLPM)	$\Phi$	
Premixed	137	11.55	0.8	-	-	-	-
Non-Premixed	137	-	-	-	11.55	-	44.88
1	129.6	2.7	0.2	8.4	8.85	10	13.36
2	119.9	2.55	0.2	17.1	9	5	4.65
3	127.3	1.3	0.1	9.7	10.25	10	9.56
4	130	4.1	0.3	7	7.45	10	19.84

The combustor was allowed to run for about 20 minutes in each configuration so as to reach steady state condition before taking the experimental data. The exhaust gas sample was collected using a water-quenched sampling probe. The NO concentration was measured using chemiluminescent NO/NO<sub>x</sub> analyzer, CO concentration was measured using non-dispersive infrared method and O<sub>2</sub> concentration (used to correct the NO and CO emissions at standard 15% oxygen concentration) was measured using the galvanic cell method. Unburned hydrocarbon (UHC) was measured using a heated flame ionization detector (HFID). The emission readings were observed to stabilize within 3 minutes for any change in experimental condition (here change in equivalence ratio for the same configuration). The experiments were repeated at least three times for each configuration and the uncertainty was estimated to be about  $\pm 0.5$  PPM for NO,  $\pm 10$  PPM for CO emissions for gaseous fuel cases, and  $\pm 1$  PPM for the UHC. The chemiluminescence intensity from OH\* radicals in the flame was obtained using an ICCD camera coupled with a narrow band interference filter (OH\* at 307 nm) with

camera f-stop setting of f-4.5, exposure time of 50 ms and gain of 70 for all the conditions.

## **D.4 Results and Discussion**

### D.4.1 Flow field and mixing

Results from the numerical simulation on flow field and methane mass fraction distribution for the five cases examined here are shown in Figure D and Figure D. The flow field is obtained in only non-reacting condition and the computational domain for the simulations is shown in Figure D(a). Note that in reacting condition the flow field will be different; however, investigation in non-reacting condition gives insight to better understand the flow physics and mixing characteristics in the combustor. The objective here was to help assist in determining the role of various cases on global features of the flow field and mixing. For the premixed flow case the air jet is observed to decay along the length of the combustor but the combustor length seems to be insufficient for complete decay of air jet and high velocity jet hits the bottom portion of the combustor and turns towards the exit end (see Figure D(b)). Flow field is affected with injection of methane fuel in cross flow of the air (top) jet (see non-premixed case, Table D-1) and the air jet is observed to deflect slightly due to injection of fuel in cross-flow as shown in Figure D(c). However, the global features of the flow field are similar to that observed for the premixed case.

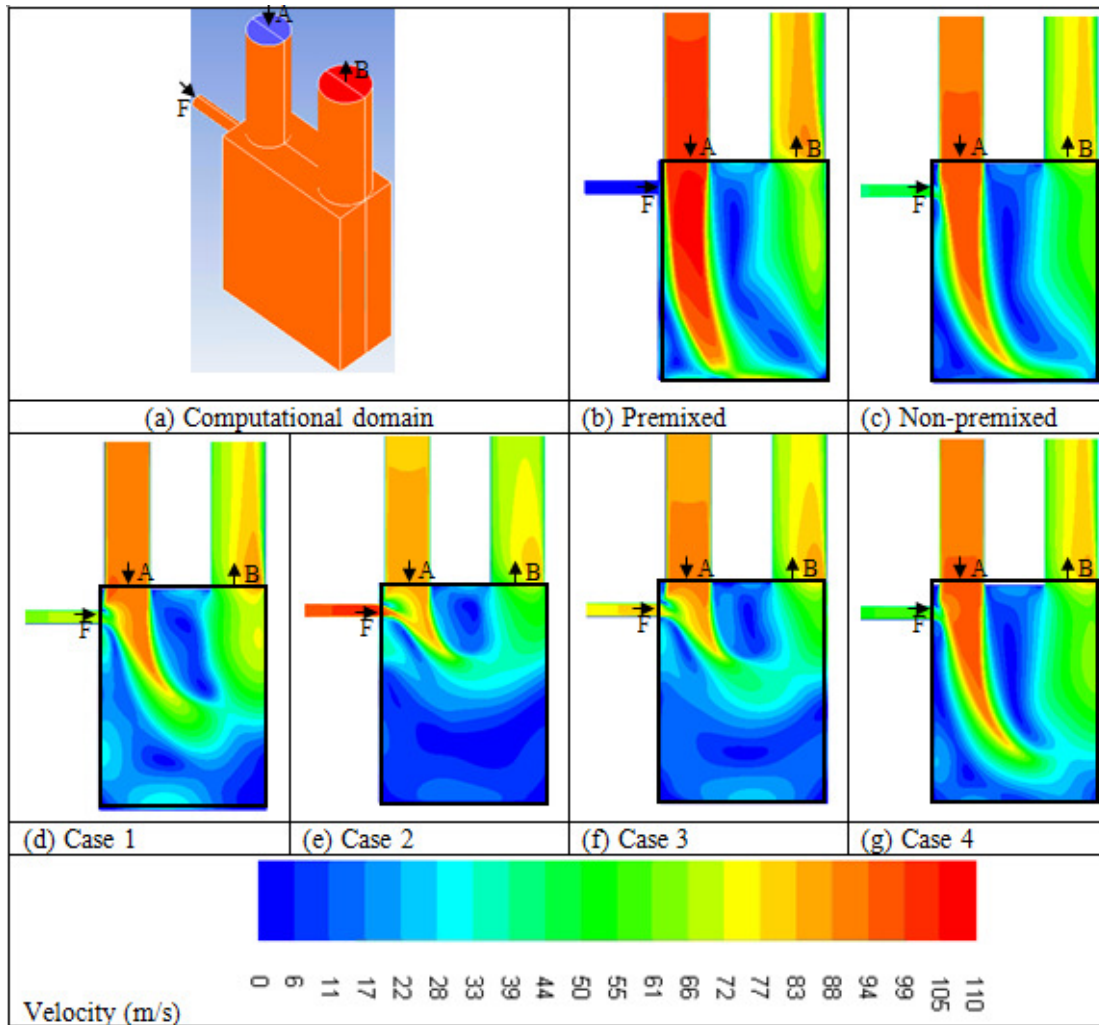


Figure D-3 Velocity magnitude contours at the symmetrical plane for various cases presented

Flow field is significantly affected for the cases where methane fuel is diluted with air (case 1-4, Table D-1). The fuel (cross) jet significantly distorts the air (top) jet profile and the flow field features inside the combustor. For these cases the air jet is pushed away from the combustor walls (see Figure D(d-g)). This can be attributed to higher momentum of the cross flowing jet as compared to the non-premixed case where only methane is used as fuel. It may be noted that the fuel (cross) stream of methane diluted with air has higher mass flow rate as well as higher velocity as compared to the

non-premixed case. Hence the momentum ratio (top/cross) is much smaller as compared to the non-premixed case (see Table D-1). Due to higher momentum of cross flowing stream the flow field inside the combustor is severely distorted for the diluted methane case.

Case 2 with lowest momentum ratio (top/cross) shows maximum distortion of the air jet and most of the flow turns towards the exit without fully penetrating towards the bottom side of the combustor (see Figure D (e)). This may result in confinement of the reaction zone in upper portion of the combustor only without fully occupying the combustor volume. Case 4 has much larger momentum ratio (top/cross) and hence this case shows the flow field features to be closer to the non-premixed case (see Figure D(g)). Higher momentum of fuel (cross) jet though distorts the flow field significantly, it can lead to better mixing between fuel and air and hence appropriate flow field control is required to achieve optimum performance.

Figure D shows the methane mass fraction contours for the cases discussed here to understand the mixing behavior inside the combustor. The maximum value of contour is fixed as 0.045 which corresponds to fully mixed state at equivalence ratio of 0.8. The contours above the methane mass fraction value of 0.045 are not shown in the plot. For the non-premixed case, mixing is delayed and the unmixed air stream is observed to reach near the bottom side of the combustor (see Figure D(a)). However, for the Case 2 which has the lowest momentum ratio (top/cross), very rapid mixing of methane and air is observed with lower methane mixture fraction region confined to the top portion of the combustor (see Figure D(b)). This may be because of higher momentum of fuel jet also which may result in increased fuel jet penetration and enhanced mixing. Case

4 shows mixing characteristics closer to the non-premixed case (see Figure D(e)) due to higher momentum ratio (top/cross) while Case 3 shows mixing characteristics closer to Case 2 due to lower momentum ratio (top/cross).

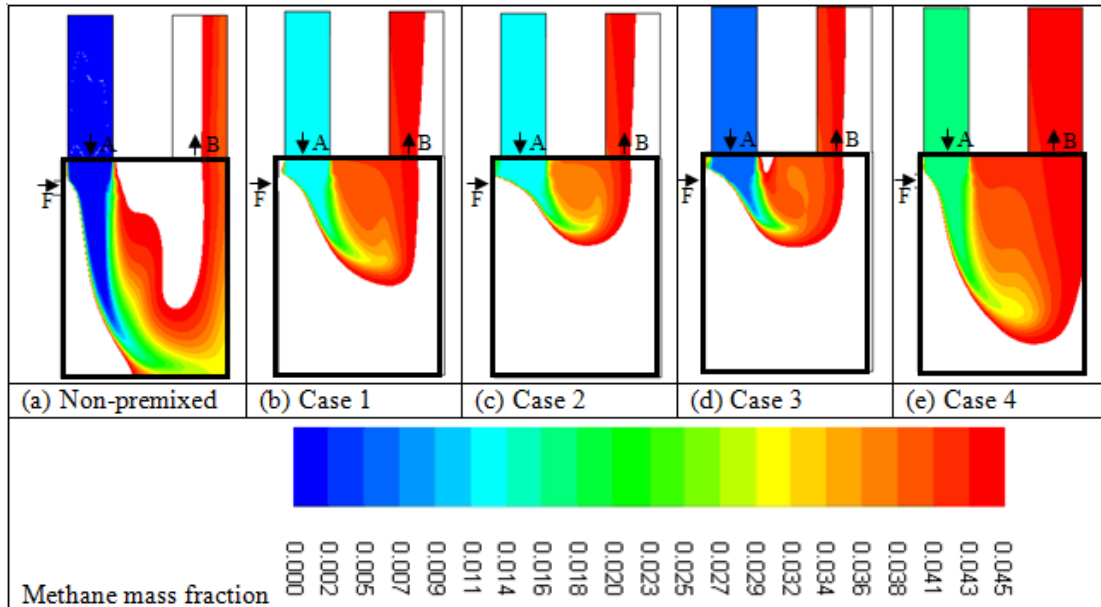


Figure D-4 Methane mass fraction contours at the symmetrical plane for various cases presented

#### D.4.2 Premixed and Non-Premixed Operation

The initial experimental investigations were aimed at evaluating the combustor performance with specific focus on pollutants emission and operational range. The combustor was operated in both premixed and non-premixed combustion mode using methane as the fuel. The equivalence ratio was varied from 0.5 to 0.8 resulting in thermal intensity range of 270 to 420 MW/m<sup>3</sup>-atm. Air flow rate was kept constant for these cases. Figure D shows the measured pollutants emission for both premixed and non-premixed combustion modes.

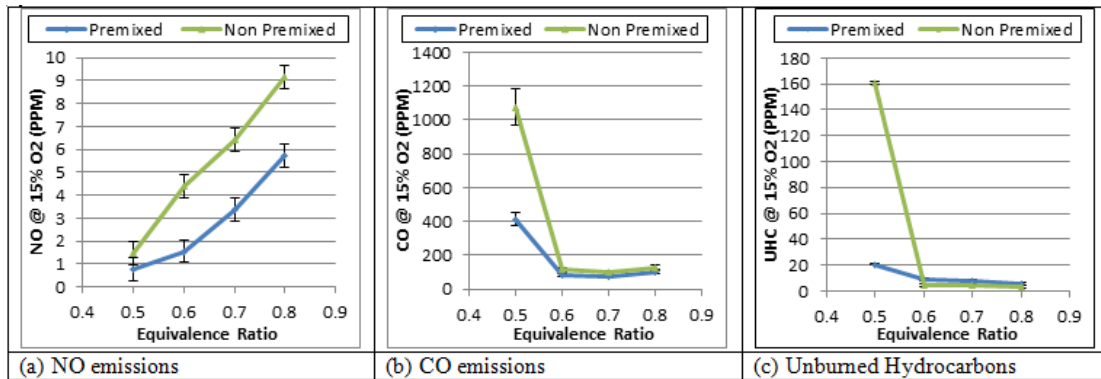


Figure D-5 NO, CO, and unburned hydrocarbons emission for premixed and non-premixed combustion modes with methane as the fuel

The combustor demonstrated ultra-low NO emissions for both premixed and non-premixed combustion modes. NO emission of less than 2 PPM was obtained for premixed combustion at an equivalence ratio of 0.6 at thermal intensity of  $317 \text{ MW/m}^3\text{-atm}$ . For non-premixed mode of combustion, at the same operational conditions, the NO emission was less than 5 PPM. CO emissions were about 100 PPM for both the operational modes which is ultra-low given the size and the thermal intensity of the combustor operation. Previous investigations on a relatively low thermal intensity combustor operation of  $200 \text{ MW/m}^3\text{-atm}$  demonstrated similar ultra-low pollutants emission levels [144]; however, in the present investigation the thermal intensity is significantly higher as compared to previous studies. This suggests good performance in terms of both NO and CO emissions of the CDC combustor even at much higher thermal intensity. Recorded unburned hydrocarbon emissions were below 10 PPM for both modes of operation at equivalence ratios between 0.6 and 0.8 emphasizing that the complete combustion is present with high efficiency. Higher UHC and CO emissions

were encountered at equivalence ratio of 0.5 as the combustor approaches its lean operational limit (see Figure D).

The  $\text{OH}^*$  chemiluminescence intensity distribution at equivalence ratio of 0.8 is shown in Figure D in both non-premixed and premixed flow mode. The results show that for both combustion modes, the reaction zone occupies most of the combustor volume. In the premixed mode, the reaction zone is spread over large portion of the combustor with the region extending from and around the air jet injection location and adjacent to the bottom portion of the combustor (see, Figure D(a)). However, in non-premixed mode the reaction zone is somewhat smaller as part of the combustor (upper left region) utilizes mixture preparation (see, Figure D(b)). Delayed mixing of methane with the air stream can also be observed from Figure D(a). It can also be noted that the  $\text{OH}^*$  chemiluminescence intensity is low near the combustor exit suggesting that all the heat released is from inside the combustor to achieve ultra-high thermal intensity with complete combustion as supported by the lower unburned hydrocarbon emissions.

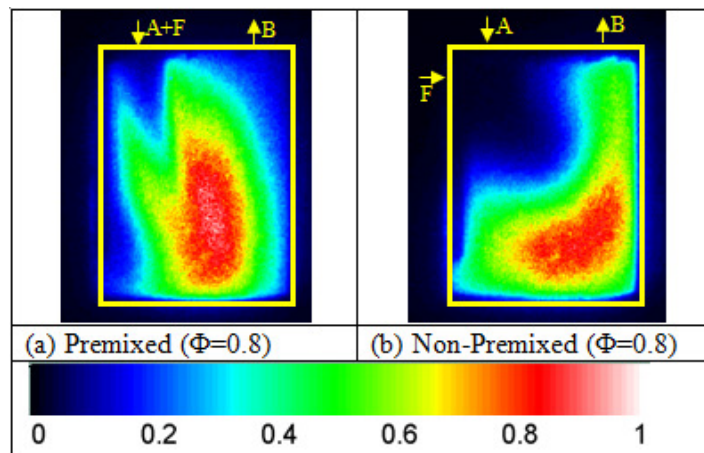


Figure D-6  $\text{OH}^*$  distribution (equivalence ratio = 0.8) for premixed and non-premixed mode with methane as the fuel.

#### D.4.3 Novel Mixture Preparation

Novel mixture preparation effects on combustion performance in the non-premixed mode are investigated for ultra-high thermal intensity CDC combustor. In this case air and fuel flow rates are split into two streams. The main “top stream” injects most of the air flow rate, while the other “cross stream” injects most of the fuel. Fuel is added to the “top stream” and air is added to the “cross stream” such that the equivalence ratio for each streams is well outside of the flammability limits for methane-air combustion. Such mixing method is expected to yield favorable results as the mixing required inside the combustor is less compared to the non-premixed combustion case. Also, the higher cross stream momentum is expected to affect the turbulence inside the combustor, significantly enhancing the mixing process; however, it may also distort the flow field as observed from Figure D and Figure D. Four different cases are studied to evaluate different local equivalence ratio in the jets and their effect on combustion as detailed in Table D-1. The top stream equivalence ratio is varied between 0.1 and 0.3, while the cross stream equivalence ratio was kept at 10 (cases 1, 3 and 4, Table D-1). The cross stream equivalence ratio was also varied (5 and 10) with the top stream equivalence ratio kept at 0.2 (cases 1 and 2, Table D-1).

Figure D shows the measured pollutants emission for the cases discussed here, normalized with respect to premixed mode of combustor operation. For cases 1, 3 and 4, where the top stream equivalence ratio was changed between 0.1 and 0.3, the obtained NO and CO emissions were equivalent to those obtained from non-premixed combustion mode which is relatively high compared to those of premixed combustion mode. On the other hand, case 2 produced favorable pollutants emissions, with NO

emission close to that of premixed combustion. Case 2 was characterized by high cross stream momentum which significantly affected the turbulence mixing inside the combustor leading to better mixing.

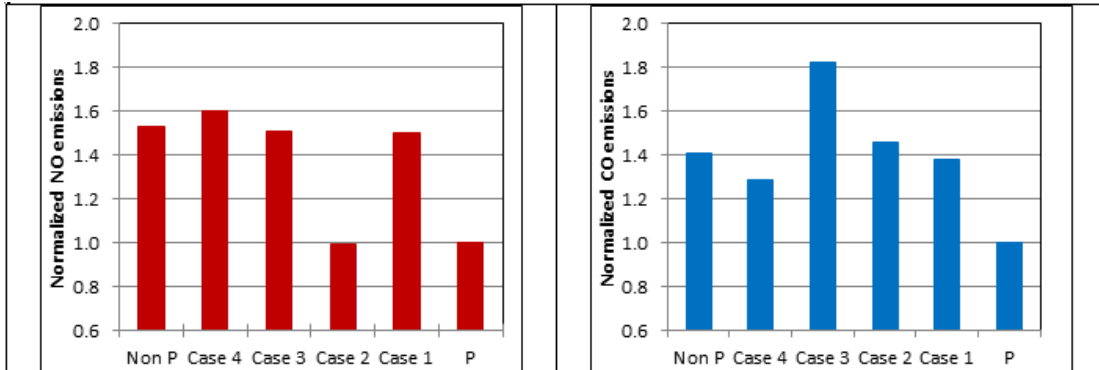


Figure D-7 NO and CO emission for different mixing cases, normalized by premixed emissions (Non P = non-premixed, P = premixed)

The  $\text{OH}^*$  chemiluminescence images are shown in Figure D for the cases investigated. It can be seen that, for all the novel mixing cases investigated, the ignition started earlier than what was encountered in non-premixed combustion case. Also, the  $\text{OH}^*$  intensity distribution was significantly affected by the cross stream as the reaction zone was lifted away from the bottom of the combustor compared to the non-premixed combustion mode. This can be explained from Figure D and Figure D wherein the higher momentum of fuel (cross) stream prevents the air (top) stream to penetrate the bottom regions of the combustor. Note that for case 2 which had the lowest momentum ratio (top/cross) the reaction zone is only confined to top portion of the combustor. Also note that the movements of the reaction zone closer to the combustor exit may result in lower residence time of the hot gases that can result in higher CO emissions. Case 4

which has momentum ratio (top/cross) closer to the non-premixed case also shows reaction zone characteristics closer to the non-premixed case (see discussion for Figure D and Figure D). The difference in the  $\text{OH}^*$  intensity distribution between the different cases examined here outlines the importance of mixture preparation and injection jets momentum effects to form the reaction zone.

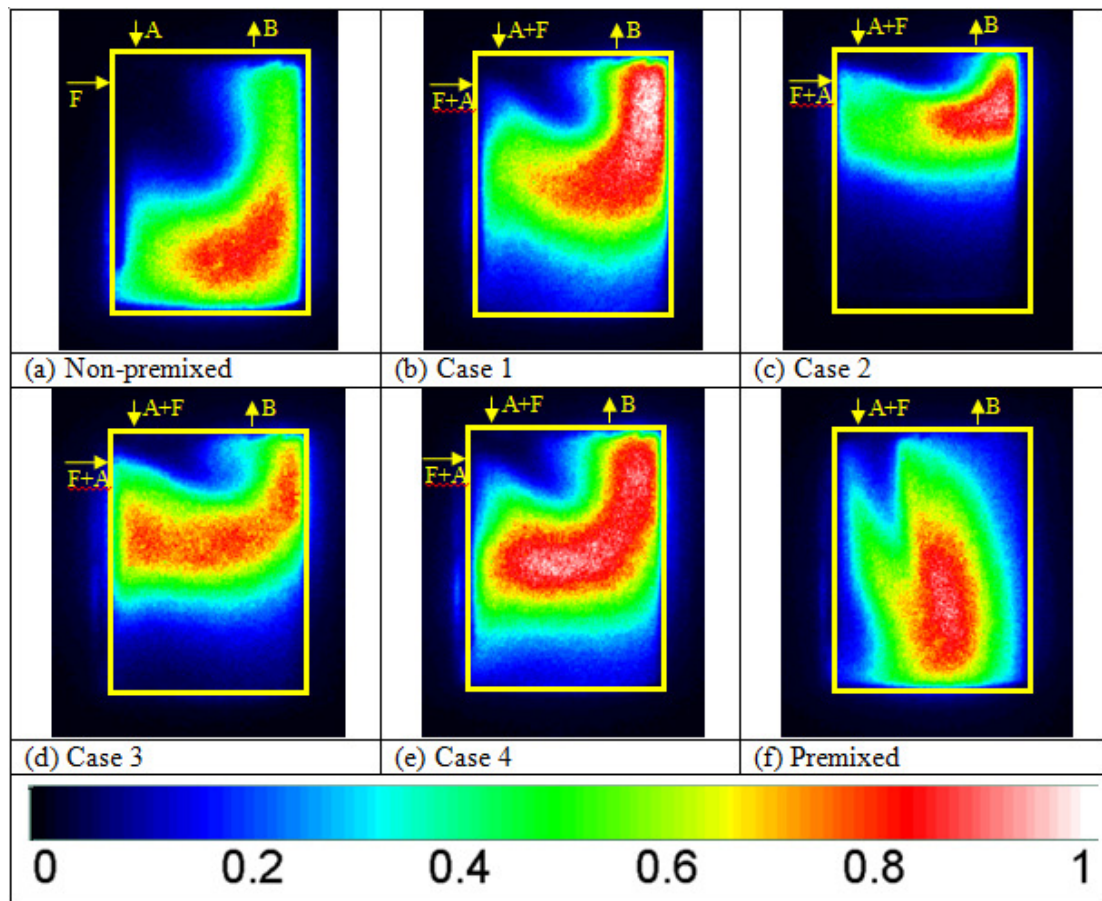


Figure D-8  $\text{OH}^*$  distribution (equivalence ratio = 0.8) for different cases presented

## D.5 Conclusions

Development of ultra-high thermal intensity colorless distributed combustion (CDC) for gas turbine applications requires careful examination on the role of various input and operational parameters for ultra-low NO<sub>x</sub> and CO emission and high performance. This research has successfully extended the previous research on distributed combustion to ultra-high thermal intensities that are much higher than that used in present day gas turbine engine combustors used in stationary or aviation engine applications. The combustor operating at ultra-high thermal intensity range of 270-420 MW/m<sup>3</sup>-atm produced NO emission level of about 5 PPM in non-premixed mode and 2 PPM in novel premixed mode at rather high equivalence ratio of  $\Phi=0.6$ . The CO emission levels of about 100 PPM were observed in both the non-premixed and premixed modes. The combustor demonstrated ultra-low unburned hydrocarbon emission (<10 PPM) for the operational conditions discussed here. The OH\* chemiluminescence intensity distribution showed the reaction zone to occupy most of the combustor zone indicating higher utilization of combustor volume that supports our goals of ultra-high thermal intensity.

Novel air and fuel mixing, where fuel is diluted with air while portion of the fuel is introduced in the main air jet, has demonstrated NO emission comparable to those encountered in premixed combustion mode. The NO emission was highly dependent on the mixing and the flow momentum of each jet. One case, characterized by high cross jet momentum, demonstrated NO emission comparable to premixed mode of combustion operation. Such novel mixing technique eliminates the possibility of flame flashback as the equivalence ratio in the jets is outside the methane air flammability

limit.  $\text{OH}^*$  intensity distribution showed that the combustion zone is affected by the cross jet momentum and equivalence ratio. The ability of this mixing technique to demonstrate near zero emission suggests very good performance even at such ultra-high thermal intensities with pollutants emission equivalent to that of premixed combustion without any of the premixed combustion drawbacks, such as, flame flashback and combustion instability.

## References

- [1] U.S. Energy Information Administration, "Annual Energy Outlook 2012," DOE/EIA, 2012.
- [2] V. K. Arghode, *Development of Colorless Distributed Combustion for Gas Turbine Application*, University of Maryland, College Park, 2011.
- [3] A. H. Lefebvre, *Gas Turbine Combustion*, Philadelphia: Taylor & Francis, 1999.
- [4] S. R. Turns, *An Introduction to Combustion: Concepts and Application*, Boston: McGraw-Hill, 2006.
- [5] Environmental Protection Agency, *Standards of Performance for Stationary Combustion Turbines; Final Rule*, vol. 71, Federal Register, 2006.
- [6] E. T. Vincent, *The Theory and Design of Gas Turbines and Jet Engines*, New York: McGraw-Hill, 1950.
- [7] C. L. Vandervort, "9 ppm NO<sub>x</sub>/CO Combustion System for "F" Class Industrial Gas Turbines," *Journal of Engineering for Gas Turbines and Power*, vol. 123, pp. 317-321, 2001.
- [8] T. Lieuwen and V. Yang, "Combustion Instabilities in Gas Turbine Engines," *Progress in Astronautics and Aeronautics*, vol. 210, 2005.
- [9] S. M. Correa, "A Review of NO<sub>x</sub> Formation Under Gas Turbine Combustion Conditions," *Combustion Science and Technology*, vol. 87, pp. 329-362, 1992.
- [10] M. C. Drake and R. J. Blint, "Calculations of NO<sub>x</sub> Formation Pathways in Propagating Laminar, High Pressure Premixed CH<sub>4</sub>/Air Flames," *Combustion Science and Technology*, vol. 75, pp. 261-285, 1991.
- [11] M. C. Drake and R. J. Blint, "Relative Importance of Nitric Oxide Formation in Laminar Opposed-Flow Diffusion Flames," *Combustion and Flame*, vol. 83, pp. 185-203, 1991.
- [12] M. Nishioka, S. Nakagawa, Y. Ishikawa and T. Takeno, "NO Emission Characteristics of Methane-Air Double Flame," *Combustion and Flame*, vol. 98, pp. 127-138, 1994.
- [13] R. K. Hanson and S. Salimian, "Survey of Rate Constants in H/N/O Systems," in *Combustion Chemistry*, New York, Springer-Verlag, 1984, pp. 361-421.
- [14] C. P. Fenimore, "Formation of Nitric Oxide in Premixed Hydrocarbon Flames," *Thirteenth Symposium (International) on Combustion*, vol. 13, pp. 373-380, 1971.
- [15] A. H. Lefebvre, "The Role of Fuel Preparation in Low-Emission," *Journal of Engineering for Gas Turbines and Power*, vol. 117, no. 4, pp. 617-654, 1995.
- [16] Q. P. Zheng, A. K. Jasuja and A. H. Lefebvre, "Influence of Air and Fuel Flows on Gas Turbine Sprays at High Pressures," *Twenty Sixth (International) Symposium on Combustion*, vol. 26, pp. 2757-2762, 1996.

- [17] J. S. Chin and A. H. Lefebvre, "Influence of Fuel Chemical Properties on Soot Emissions from Gas Turbine Combustors," *Combustion Science and Technology*, vol. 73, no. 1-3, pp. 479-486, 1990.
- [18] M. B. Hilt and J. Waslo, "Evolution of NO<sub>x</sub> Abatement Techniques Through Combustor Design for Heavy-Duty Gas Turbines," *Journal of Engineering for Gas Turbines and Power*, vol. 106, no. 4, pp. 825-832, 1984.
- [19] C. Wilkes and B. Gerhold, "NO<sub>x</sub> Reduction from a Gas Turbine Combustor Using Exhaust Gas Recirculation," in *Joint Power Conference*, Phoenix, AZ, 1980.
- [20] G. Leonard and J. Stegmaier, "Development of an Aeroderivative Gas Turbine Dry Low Emissions Combustion System," *Journal of Engineering for Gas Turbines and Power*, vol. 116, no. 3, pp. 542-546, 1994.
- [21] H. Tsuji, A. K. Gupta, T. Hasegawa, M. Katsuki, K. Kishimoto and M. Morita, *High Temperature Air Combustion: from Energy conservation to Pollution Reduction*, Bacoratan: CRC Press, 2003.
- [22] A. K. Gupta, "Thermal Characteristics of Gaseous Fuel Flames using High Temperature Air," *Journal of Engineering for Gas Turbines and Power*, vol. 126, no. 1, pp. 9-19, 2004.
- [23] A. K. Gupta, S. Bolz and T. Hasegawa, "Effect of Air Preheat and Oxygen Concentration on Flame Structure and Emission," *Journal of Energy Resources Technology*, vol. 121, pp. 209-216, 1999.
- [24] J. A. Wunning and J. G. Wunning, "Flameless Oxidation to Reduce Thermal NO Formation," *Progress in Energy and Combustion Science*, vol. 23, pp. 81-94, 1997.
- [25] A. F. Colorado, B. A. Herrera and A. A. Amell, "Performance of a Flameless Combustion Furnace using Biogas and Natural Gas," *Bioresources Technology*, vol. 101, pp. 2443-2449, 2010.
- [26] R. Luckerath, W. Meier and M. Aigner, "FLOX Combustion at High Pressure with Different Fuel Compositions," *Journal of Engineering for Gas Turbines and Power*, vol. 130, no. 1, pp. 011505-1-7, 2008.
- [27] O. Lammel, H. Schutz, G. Schmitz, R. Luckerath, M. Stohr, B. Noll, M. Aigner, M. Hase and W. Krebs, "FLOX Combustion at High Power Density and High Flame Temperature," *Journal of Engineering for Gas Turbine and Power*, vol. 132, p. 121503, 2010.
- [28] A. S. Verrissimo, A. M. Rocha and M. Costa, "Operational Combustion and Emission Characteristics of a Small Scale Combustor," *Energy and Fuels*, vol. 25, pp. 2469-2480, 2011.
- [29] A. Cavaliere and M. Joannon, "Mild Combustion," *Progress in Energy and Combustion Science*, vol. 30, pp. 329-366, 2004.
- [30] I. B. Ozdemir and N. Peters, "Characteristics of the Reaction Zone in a Combustor Operating at Mild Combustion," *Experiments in Fluids*, vol. 30, pp. 683-695, 2001.

- [31] R. Weber, J. P. Smart and W. vd Kamp, "On the (MILD) Combustion of Gaseous, Liquid, and Solid Fuels in High Temperature Preheated Air," *Proceedings of the Combustion Institute*, vol. 30, pp. 2623-2629, 2005.
- [32] S. Kumar, P. J. Paul and H. S. Mukunda, "Studies on a New High-Intensity Low-Emission Burner," *Proceedings of the Combustion Institute*, vol. 29, pp. 1131-1137, 2002.
- [33] M. K. Bobba, P. Gopalakrishnan, K. Periagaram and J. M. Seitzman, "Flame Structure and Stabilization Mechanisms in a Stagnation-point Reverse-Flow Combustor," *Journal of Engineering for Gas Turbine and Power*, vol. 130, no. 3, pp. 031505-1-8, 2008.
- [34] P. Gopalakrishnan, M. K. Bobba and J. M. Seitzman, "Controlling Mechanisms for Low NO<sub>x</sub> Emissions in a Non-Premixed stagnation Point Reverse Flow Combustor," *Proceedings of the Combustion Institute*, vol. 31, pp. 3401-3408, 2007.
- [35] V. K. Arghode, A. K. Gupta and M. Bryden, "High Intensity Colorless Distributed Combustion for Ultra Low Emissions and Enhanced Performance," *Applied Energy*, vol. 92, pp. 822-830, 2012.
- [36] A. E. Khalil and A. K. Gupta, "Distributed swirl Combustion For Gas Turbine Application," *Applied Energy*, vol. 88, pp. 4898-4907, 2011.
- [37] A. E. Khalil and A. K. Gupta, "Swirling Distributed Combustion For Clean Energy Conversion In Gas Turbine Applications," *Applied Energy*, vol. 88, pp. 3685-3693, 2011.
- [38] K. Y. Hsu, L. P. Goss and W. M. Roquemore, "Characteristics of a Trapped Vortex Combustor," *Journal of Propulsion and Power*, vol. 14, pp. 57-65, 1998.
- [39] M. J. Melo, J. M. Sousa, M. Costa and Y. Levy, "Experimental Investigation of a Novel Combustor Model for Gas Turbines," *Journal of Propulsion and Power*, vol. 25, pp. 609-617, 2009.
- [40] D. L. Straub, K. H. Casleston, R. E. Lewis, T. G. Sidwell, D. J. Maloney and G. A. Richards, "Assesment of Rich-Burn, Quick-Mix, Lean Burn Trapped Vortex Combustor for Stationary Gas Turbines," *Journal of Engineering for Gas Turbines and Power*, vol. 127, pp. 36-41, 2005.
- [41] J. Zelina, D. T. Shouse and R. D. Hancock, "Ultra-Compact Combustors for Advanced Gas Turbine Engines," in *ASME Turbo Expo 2004: Power for Land, Sea, and Air (GT2004)*, June 14-17, 2004, Vienna, Austria , 2004.
- [42] R. A. Yetter, I. Glassman and H. C. Gabler, "Asymmetric Whirl Combustion: a New Low NO<sub>x</sub> Approach," *Proc. of the Combustion Institute*, vol. 28, pp. 1265-1272, 2000.
- [43] T. Rutar and P. C. Malte, "NO<sub>x</sub> Formation in High Pressure Jet Stirred Reactors with Significance to Lean-Premixed Combustion Turbines," *Journal of Engineering for Gas Turbines and Power*, vol. 124, pp. 776-783, 2002.

- [44] Environmental Protection Agency, "Alternative Control Techniques Document - NO<sub>x</sub> Emissions from Stationary Gas Turbines," North Carolina, 1993.
- [45] A. Sobiesiak, S. Rahbar and H. A. Becker, "Performance Characteristics of the Novel Low-NO<sub>x</sub> CGRI Burner for Use with High Air Preheat," *Combustion and Flame*, vol. 115, pp. 93-125, 1998.
- [46] Y. He, Flameless Combustion of Natural Gas in SJ/WJ Furnace, PhD Dissertation - Queen's University, 2008.
- [47] J. Mi, P. Li, B. B. Dally and R. A. Craig, "Importance of Initial Momentum Rate and Air-Fuel Premixing on Moderate or Intense Low Oxygen Dilution (MILD) Combustion in a Recuperative Furnace," *Energy and Fuels*, vol. 23, pp. 5349-5256, 2009.
- [48] B. B. Dally, E. Riesmeier and N. Peters, "Effect of Fuel Mixture on Moderate and Intense Low Oxygen Dilution Combustion," *Combustion and Flame*, vol. 137, pp. 418-431, 2004.
- [49] X. Xing, B. Wang and Q. Lin, "Structure of Reaction Zone of Normal Temperature Air flameless Combustion in a 2 ton/h Coal-Fired Boiler Furnace," *Journal of Power and Energy*, vol. 221, pp. 473-480, 2007.
- [50] G. G. Szego, B. B. Dally and G. J. Nathan, "Scaling of NO<sub>x</sub> Emissions from a Laboratory Scale Mild Combustion Furnace," *Combustion and Flame*, vol. 154, pp. 281-295, 2008.
- [51] E. W. Grandmaison, I. Yimer, H. A. Becker and A. Sobiesiak, "The Strong-Jet/Weak-Jet Problem and Aerodynamic Modeling of the CGRI Burner," *Combustion and Flame*, vol. 114, pp. 381-396, 1998.
- [52] P. Li, B. B. Dally, J. Mi and F. Wang, "MILD Oxy-combustion of Gaseous Fuels in a Laboratory-scale Furnace," *Combustion and Flame*, vol. 160, no. 5, pp. 933-946, 2013.
- [53] M. Derudi and R. Rota, "Experimental Study of the MILD Combustion of Liquid Hydrocarbons," *Proceedings of the Combustion Institute*, vol. 33, no. 2, pp. 3325-3332, 2011.
- [54] S. Kumar, P. J. Paul and H. S. Mukunda, "Investigations of the Scaling Criteria for a MILD Combustion Burner," *Proceedings of the Combustion Institute*, vol. 30, pp. 2613-2621, 2005.
- [55] J. G. Wunning and J. A. Wunning, "Combustion Chamber with Flameless Oxidation". United States of America Patent 7,062,917, 2006.
- [56] H. Schütz, R. Lücknerath, T. Kretschmer, B. Noll and M. Aigner, "Analysis of the Pollutant Formation in the FLOX Combustion," *Journal of Engineering for Gas Turbines and Power*, vol. 130, no. 1, p. 011503, 2008.
- [57] P. Gopalakrishnan, Effects of the Reacting Flowfield on Combustion Process in a Stagnation Point Reverse Flow Combustor, PHD Dissertation-Georgia Institute of Technology, 2008.

- [58] M. K. Bobba, Flame Stabilization and Mixing Characteristics in a Stagnation Point Reverse Flow Combustor, PhD Dissertation - Georgia Institute of Technology, 2007.
- [59] B. T. Zinn, Y. Neumeier, J. M. Seitzman, J. Jagoda and B. Hashmonay, "stagnation Point Reverse Flow Combustor for a Combustion system". United States of America Patent 7,168,949, 2007.
- [60] T. R. Shuman, NO<sub>x</sub> and CO Formation for LEan-Premixed Methane-Air combustion in a Jet-Stirred Reactor Operated at Elevated Pressure, PHD Dissertation University of Washington, 2000.
- [61] R. G. Edmonds, J. T. Williams, R. C. Steele, D. L. Straub, K. H. Casleton and A. Bining, "Low NO<sub>x</sub> Advanced Vortex Combustor," *Journal of Engineering for Gas Turbine and Power*, vol. 130, no. 3, p. 034502, 2008.
- [62] D. Kendrick, S. P. Lawlor and R. C. Steele, "Trapped Vortex Combustor". United States of America Patent 7,003,961, 2006.
- [63] S. Kostka, R. D. Branam, M. W. Renfro, P. J. Lakusta, J. R. Gord and S. Roy, "Laser-Induced Fluorescence Measurements of Product Penetration within an Ultracompact Combustor," *Journal of Propulsion and Power*, vol. 28, no. 3, pp. 617-624, 2012.
- [64] T. J. Erdmann, D. L. Blunck, D. Shouse, C. Neuroth, A. Lynch, A. Caswell, D. Richardson and A. Briones, "Rayleigh Pressure Loss Analysis and Mitigation in Ultra-Compact Combustors," in *51st AIAA Aerospace Sciences Meeting*, Grapevine (Dallas/Ft. Worth Region), Texas, 2013.
- [65] T. Hasegawa, S. Mochida and A. K. Gupta, "Development of Advanced Industrial Furnace using Highly Preheated Combustion Air," *Journal of Propulsion and Power*, vol. 18, no. 2, pp. 233-239, 2002.
- [66] M. Katsuki and T. Hasegawa, "The Science and Technology of Combustion in Highly Preheated Air," *Proceedings of the Twenty Seventh Symposium (Intl) on Combustion*, vol. 27, pp. 3135-4146.
- [67] Y. Suzukawa, S. Sugiyama, Y. Hino, M. Ishioka and I. Mori, "Heat Transfer Improvement and NO<sub>x</sub> Reduction by Highly Preheated Air Combustion," *Energy Conversion and Management*, vol. 38, no. 10-13, pp. 1061-1071, 1997.
- [68] K. Kitagawa, N. Konishi, N. Arai and A. K. Gupta, "Temporally Resolved 2-D Spectroscopic Study on the Effect of Highly Preheated and Low Oxygen Concentration Air on Combustion," *Journal of Engineering for Gas Turbines and Power*, vol. 125, pp. 326-331, 2003.
- [69] M. Mortberg, W. Blasiak and A. K. Gupta, "Experimental Investigation of Flow Phenomena of a single Fuel Jet in Cross-Flow During Highly Preheated Air Combustion Conditions," *Journal of Engineering for Gas Turbine and Power*, vol. 129, pp. 556-564, 2007.
- [70] M. Mortberg, Study of Gas Jet Burning in Low Oxygen Content and High Temperature Oxidizer, PHD Dissertation Royal Institute of Technology, 2005.

- [71] M. Mortberg, W. Blasiak and A. K. Gupta, "Combustion of Normal and Low Calorific Fuels in High Temperature and Oxygen Deficiency Environment," *Combustion Science and Technology*, vol. 178, pp. 1345-1372, 2006.
- [72] S. Lille, W. Blasiak and M. Jewartowski, "Experimental Study of the Fuel Jet Combustion in High Temperature and Low Oxygen Content Exhaust Gases," *Energy*, vol. 30, pp. 373-384, 2005.
- [73] W. Yang and W. Blasiak, "chemical Flame Length and Volume in Liquefied Propane Gas Combustion using High-Temperature and Low Oxygen Concentration Oxidizer," *Energy and Fuels*, vol. 18, pp. 1329-1335, 2004.
- [74] B. B. Dally, A. N. Karpetis and S. R. Barlow, "Structure of Turbulent Non-Premixed Jet Flames in a Diluted Hot Coflow," *Proceedings of the Combustion Institute*, vol. 29, pp. 1147-1154, 2002.
- [75] G. M. Choi and M. Katsuki, "New Approach to Low Emission of Nitric Oxides from Furnaces using Highly Pre-heated Air Combustion," *Journal of the Energy Institute*, vol. 73, pp. 18-24, 2000.
- [76] F. P. Ricou and D. B. Spalding, "Measurements of Entrainment by Axisymmetrical Turbulent Jets," *Journal of Fluid Mechanics*, vol. 11, no. 1, pp. 21-32, 1961.
- [77] D. Han and M. G. Mungal, "Direct Measurement of Entrainment in Reacting/Nonreacting Turbulent Jets," *Combustion and Flame*, vol. 124, pp. 370-386, 2001.
- [78] W. Yang and W. Blasiak, "Flame entrainments Induced by a Turbulent Reacting Jet using High Temperature and Oxygen Deficient Oxidizer," *Energy and Fuels*, vol. 19, pp. 1473-1483, 2005.
- [79] A. K. Gupta, D. G. Lilley and N. Syred, *Swirl Flows*, Tunbridge Wells: Abacus Press, 1984.
- [80] I. W. Leuckel and N. Fricker, "The Characteristics of Swirl Stabilized Natural Gas Flames," *Journal of Institute of Fuel*, vol. 49, pp. 103-112, 1976.
- [81] S. C. Li and F. A. Williams, "Reaction Mechanisms for Methane Ignition," *Journal of Engineering for Gas Turbines and Power*, vol. 124, pp. 471-480, 2002.
- [82] B. D. Pratte and W. D. Baines, "Profiles of the Round Turbulent Jet in a Cross Flow," *Journal of Hydraulic Engineering*, vol. 92, pp. 53-64, 1967.
- [83] S. H. Smith and M. G. Mungal, "Mixing structure and Scaling of the Jet in Crossflow," *Journal of Fluid Mechanics*, vol. 357, pp. 83-122, 1998.
- [84] J. Andreopoulos and I. Rodi., "Experimental Investigation of Jets in a Crossflow," *Journal of Fluid Mechanics*, vol. 138, pp. 93-127, 1984.
- [85] G. P. Smith, D. M. Golden, M. Frenklach, N. W. Moriarty, B. Eiteneer, M. Goldenberg, C. T. Bowman, R. K. Hanson, S. Song, W. C. Gardiner, V. V. Lissianski and Z. Qin, *GRI 3.0 Mechanism*, [http://www.me.berkeley.edu/gri\\_mech/](http://www.me.berkeley.edu/gri_mech/).

- [86] V. K. Arghode and A. K. Gupta, "Effect of Flow Field for Colorless Distributed Combustion (CDC) for Gas Turbine Combustion," *Applied Energy*, vol. 87, no. 5, pp. 1631-1640, 2010.
- [87] V. K. Arghode and A. K. Gupta, "Investigation of Forward Flow Distributed Combustion for Gas Turbine Application," *Applied Energy*, vol. 88, pp. 29-49, 2010.
- [88] V. K. Arghode and A. K. Gupta, "Development of High Intensity CDC Combustor for Gas Turbine Engines," *Applied Energy*, vol. 88, no. 3, pp. 963-973, 2011.
- [89] E. D. Baluev and Y. V. Troyankin, "The Effect of Design Parameters on the Aerodynamics of Cyclone Chambers," *Thermal Engineering*, vol. 14, no. 2, pp. 67-71, 1967.
- [90] B. P. Ustimenko and M. A. Bukhman, "Turbulent Flow Structure in a Cyclone Chamber," *Thermal Engineering*, vol. 15, no. 2, pp. 64-67, 1968.
- [91] R. B. Xiang and K. W. Lee, "Numerical Study of Flow field in Cyclones of Different Height," *Chemical Engineering and Processing*, vol. 44, pp. 877-883, 2005.
- [92] A. J. Hoekstra, J. J. Derksen and H. Van Der Akker, "An Experimental and Numerical Study of Turbulent Swirling Flow in Gas Cyclones," *Chemical Engineering Science*, vol. 54, pp. 2055-2065, 1999.
- [93] M. Elia, M. Ulinski and M. Metgalchi, "Laminar Burning Velocity of Methane-Air-Diluent Mixtures," *Journal of Energy Resources Technology*, vol. 123, pp. 190-196, 2001.
- [94] Z. Al-Hamamre, S. Diezinger, P. Takuldar, F. Van Issendorff and D. Trimis, "Combustion of Low Calorific Gases from Landfills and Waste Pyrolysis Using Porous Medium Burner Technology," *Process Safety and Environmental Protection*, vol. 84, pp. 297-308, 2006.
- [95] W. Qin, F. N. Egofoopoulos and T. T. Tsotsis, "Fundamental and Environmental Aspects of Landfill Gas Utilization for Power Generation," *Chemical Engineering Journal*, vol. 82, pp. 157-172, 2001.
- [96] W. T. Tsai, "Bioenergy from Lanfill Gas (LPG) in Tawiwan," *Renewable and Sustainable Energy Reviews*, vol. 11, pp. 331-344, 2007.
- [97] F. Caresana, G. Comodi, L. Pelagalli, P. Pierpaoli and S. Vagni, "Energy Production from Landfill Biogas: an Italian Case," *Biomass and Bioenergy*, vol. 35, pp. 4331-4339, 2011.
- [98] R. Stone, A. Clarke and P. Beckwith, "Correlations for the Laminar-Burning Velocity of Methans/Diluent/Air Mixtures Obtained in Free-Fall Experiments," *Combustion and Flame*, vol. 114, pp. 546-555, 1998.
- [99] H. S. Kim, A. H. Lim and K. Y. Ahn, "Study on the Combustion Characteristics of a Lean Premixed Combustor," *Journal of Korean Society of Combustion*, vol. 9, pp. 25-31, 2004.

- [100] A. R. Choudhuri and S. R. Gollahali, "Combustion Characteristics of Hydrogen-Hydrocarbon Hybrid Fuels," *International Journal of Hydrogen Energy*, vol. 25, pp. 451-462, 2000.
- [101] A. R. Choudhuri and S. R. Gollahali, "Characteristics of Hydrogen-Hydrocarbon Composite Fuel Turbulent Jet Flame," *International Journal of Hydrogen Energy*, vol. 28, pp. 445-454, 2003.
- [102] G. A. Karim, I. Wierzba and Y. Al-Alousi, "Methane-hydrogen Mixtures as Fuels," *International Journal of Hydrogen Energy*, vol. 21, pp. 625-631, 1996.
- [103] M. Karbasi and I. Wierzba, "The Effect of Hydrogen Addition on the Flame Stability Limits of Methane Jet Diffusion Flames," *International Journal of Hydrogen Energy*, vol. 23, pp. 123-129, 1997.
- [104] R. W. Schefer, D. M. Wickall and A. K. Agrawal, "Combustion of Hydrogen-Enriched Methane in Lean Premixed Swirl Stabilized Burner," *Proc. of the Combustion Institute*, vol. 29, pp. 843-851, 2002.
- [105] R. W. Schefer, "Hydrogen Enrichment for Improved Lean Flame Stability," *International Journal of Hydrogen Energy*, vol. 28, pp. 1131-1141, 2003.
- [106] N. Wu, G. P. McTaggart-Cowan, W. K. Bushe and M. H. Davy, "Effects of Hydrogen Addition on High-Pressure Nonpremixed Natural Gas Combustion," *Combustion Science and Technology*, vol. 183, pp. 20-42, 2011.
- [107] H. S. Kim, V. K. Arghode and A. K. Gupta, "Flame Characteristics of Hydrogen-Enriched Methane-Air Premixed Swirling Flames," *International Journal of Hydrogen Energy*, vol. 34, pp. 1063-1073, 2009.
- [108] T. Lieuwen, V. McDonell, E. Petersen and D. Santavicca, "Fuel Flexibility Influence on Premixed Combustor Blowout, Flashback, Autoignition, and Stability," *Proceedings of the ASME Turbo Expo: Power for Land, Sea and Air*, pp. GT2006-90770, 2006.
- [109] D. R. Noble, Q. Zhang and T. Lieuwen, "Hydrogen Effects upon Flashback and Blowout," *Proceedings of the International Colloquium on Environmentally Preferred Advanced Power Generation*, pp. ICEPAG2006-24012, 2006.
- [110] B. Dam, N. Love and A. Choudhuri, "Flashback Propensity of Syngas Fuels," *Fuel*, vol. 90, no. 2, pp. 618-625, 2011.
- [111] V. K. Arghode and A. K. Gupta, "Hydrogen Addition Effects on Methane-Air Colorless Distributed Combustion Flames," *International Journal of Hydrogen Energy*, vol. 36, pp. 6292-6302, 2011.
- [112] M. Ilbas, A. P. Crayford, I. Yilmaz, P. J. Bowen and N. Syred, "Laminar-Burning Velocities of Hydrogen-Air and Hydrogen-Methane-Air Mixtures: an Experimental Study," *International Journal of Hydrogen Energy*, vol. 31, pp. 1768-1779, 2006.
- [113] J. Schornick, R. Farr and J. Dicampili, "Liquid Biofuels in the Aeroderivative Gas Turbine," in *World Energy 21st Congress 11-16 September*, Montreal, Canada, 2010.

- [114] N. Leplat, P. Dagaut, C. Togbe and J. Vandooren, "Numerical and Experimental Study of Ethanol Combustion and Oxidation in Laminar Premixed Flames and in Jet Stirred Reactor," *Combustion and Flame*, vol. 158, no. 4, pp. 705-725, 2011.
- [115] M. Cetin, F. Yuksel and H. Kus, "Emission Characteristics of a Converted Diesel Engine Using Ethanol as Fuel," *Energy for sustainable Development*, vol. 13, no. 4, pp. 250-254, 2009.
- [116] P. Dagaut and M. Cathonnet, "The Ignition, Oxidation, and Combustion of Kerosene: a Review of Experimental and Kinetic Modelling," *Progress in energy and Combustion Sciences*, vol. 32, no. 1, pp. 48-92, 2006.
- [117] W. P. Jones, S. Lyra and A. Navarro-Martinez, "Numerical Investigation of Swirling Kerosene Spray Flames Using Large Eddy Simulation," *Combustion and Flame*, vol. 159, no. 4, pp. 1539-1561, 2012.
- [118] W. A. Sirignano, T. K. Pham and D. Dunn-Rankin, "Miniature-scale Liquid-Fuel-Film Combustor," *Proc. of the Combustion Institute*, vol. 29, no. 1, pp. 925-931, 2002.
- [119] C. M. Vagelopoulos, F. N. Egolfopoulos and C. K. Law, "Further Considerations on the Determination of Laminar Flame Speeds with the Counterflow Twin Flame Technique," *Proceedings of the Combustion Institute*, vol. 25, pp. 1341-1347, 1994.
- [120] E. Hu, Z. Huang, J. He, C. Jin and J. Zheng, "Experimental and Numerical Study on Laminar Burning Characteristics of Premixed Methane-Hydrogen-Air Flames," *International Journal of Hydrogen Energy*, vol. 34, pp. 4876-4888, 2009.
- [121] E. Varea, V. Modica, A. Vandel and B. Renou, "Measurements of Laminar Burning Velocity and Markstein Length Relative to Fresh Gases Using a New Postprocessing Procedure: application to Laminar Spherical Flames for Methane, ethanol, and Isooctane/Air Mixtures," *Combustion and Flame*, vol. 159, no. 2, pp. 577-590, 2012.
- [122] K. Kumar and C. Sung, "Laminar Flame Speeds and Extinction Limits of Preheated n-Decane/O<sub>2</sub>/N<sub>2</sub> and n-Dodecane/O<sub>2</sub>/N<sub>2</sub> Mixtures," *Combustion and Flame*, vol. 151, no. 1-2, pp. 209-224, 2007.
- [123] J. I. Hileman, R. W. Stratton and P. E. Donohoo, "Energy Content and Alternative Jet Fuel Viability," *Journal of Propulsion and Power*, vol. 26, no. 6, pp. 1184-1195, 2010.
- [124] A. A. Boateng, C. A. Mullen and N. M. Goldberg, "Producing Stable Pyrolysis Liquids from the Oil-Seed Presscakes of Mustard Family Plants: Pennycress (*Thlaspi arvense* L.) and Camelina (*Camelina sativa*)," *Fuels & Energy*, vol. 24, no. 12, pp. 6624-6632, 2010.
- [125] L. Rye, S. Blakey and C. W. Wilson, "Sustainability of supply or the planet: a review of potential drop-in alternative," *Energy & Environmental Science*, vol. 3, no. 1, pp. 17-27, 2010.

- [126] S. Blakey, L. Rye and C. W. Wilson, "Aviation gas turbine alternative fuels: A review," *Proceedings of the Combustion Institute*, vol. 33, pp. 2863-2885, 2011.
- [127] N. A. Carter, R. W. Stratton, M. K. Bredehoeft and J. I. Hileman, "Energy and Environmental Viability of Select Alternative Jet Fuel Pathways," in *47th AIAA/ASME/SAE/ASEE Joint Propulsion Conference*, San Diego, CA, 2011.
- [128] E. Corporan, M. J. Dewitt, C. D. Klingshirn, R. Striebich and M. Cheng, "Emissions Characteristics of Military Helicopter Engines with JP-8 and Fischer-Tropsch Fuels," *Journal of Propulsion and Power*, vol. 26, no. 2, pp. 317-324, 2010.
- [129] D. R. Shonnard, L. Williams and T. N. Kalnes, "Camelina-Derived Jet Fuel and Diesel: Sustainable Advanced Biofuels," *Environmental Progress & Sustainable Energy*, vol. 29, no. 3, pp. 382-392, 2010.
- [130] V. H. Tran, C. D. Morton, R. N. Parthasarathy and S. R. Gollahalli, "Combustion Characteristics of Petroleum and Biofuel Spray Flames in a Furnace," in *51st AIAA Aerospace Sciences Meeting*, Grapevine (Dallas/Ft. Worth Region), TX, 2013.
- [131] E. Corporan, R. Reich, O. Monroig, M. J. DeWitt, V. Larson, T. Aulich, M. Mann and W. Seames, "Impacts of Biodiesel on Pollutant Emissions of a JP-8-Fueled Turbine Engine," *Journal of Air & Water Management Association*, vol. 55, no. 7, pp. 940-949, 2005.
- [132] S. Kim, Y. Yoon and I. Jeung, "Nitrogen Oxides Emissions in Turbulent Hydrogen Jet Nonpremixed Flames: Effect of Coaxial Air and Flame Radiation," *Proc. of the Combustion Institute*, vol. 28, pp. 463-471, 2000.
- [133] E. Villermaux and D. H. Rehab, "Mixing in Coaxial Jets," *Journal of Fluid Mechanics*, vol. 425, pp. 161-185, 2000.
- [134] G. Singh, T. Sundararajan and K. A. Bhaskaran, "Mixing and Entrainment Characteristics of Circular and Noncircular Confined Jets," *Journal of Fluids Engineering*, vol. 125, pp. 835-842, 2003.
- [135] K. Zaman, "Spreading Characteristics and Thrust of Jets From Asymmetric Nozzles," in *AIAA 34th Aerospace Science Meeting and Exhibit*, Reno, NV, 1996.
- [136] E. J. Gutmark and F. F. Grinstein, "Flow Control with Noncircular Jets," *Annual Review of Fluid Mechanics*, vol. 31, pp. 239-272, 1999.
- [137] E. Gutmark, K. C. Schadow, T. P. Parr, D. M. Hanson-Parr and K. J. Wilson, "Noncircular Jets in Combustion Systems," *Experiments in Fluids*, vol. 7, pp. 248-258, 1989.
- [138] J. Mi, G. J. Nathan and R. E. Luxton, "Centerline Mixing Characteristics of Jets from Nine Differently Shaped Nozzles," *Experiments in Fluids*, vol. 28, pp. 93-94, 2000.

- [139] A. R. Choudhuri, S. P. Luna and S. R. Gollahalli, "Elliptic Coflow Effects on a Circular Gas Jet Flame," *Journal of Propulsion and Power*, vol. 18, no. 3, pp. 686-695, 2002.
- [140] R. Chen and F. Driscoll, "Nitric Oxide Levels of Jet Diffusion Flames: Effect of Coaxial Air and Other Mixing Parameters," *Proc. of the Combustion Institute*, vol. 23, pp. 281-288, 1990.
- [141] A. S. Verissimo, A. M. A. Rocha and M. Costa, "Importance of the Inlet Air Velocity on the Establishment of Flameless Combustion in a Laboratory Combustor," *Experimental Thermal and Fluid Science*, vol. 44, pp. 75-81, 2013.
- [142] J. J. Feese and S. R. Turns, "Nitric Oxide Emissions from Laminar Diffusion Flames: Effect of Air-Side versus Fuel-Side Diluent Addition," *Combustion and Flames*, vol. 113, pp. 66-78, 1998.
- [143] A. E. Khalil, V. K. Arghode, A. K. Gupta and S. Lee, "Low Calorific Value Fuelled Distributed Combustion with Swirl for Gas Turbine Applications," *Applied Energy*, vol. 98, pp. 69-78, 2012.
- [144] V. K. Arghode, A. E. Khalil and A. K. Gupta, "Fuel Dilution and Liquid fuel Operation Effects on Ultra-High Thermal Intensity Distributed Combustor," *Applied energy*, vol. 95, pp. 132-138, 2012.
- [145] A. E. Khalil, V. K. Arghode and A. K. Gupta, "Novel Mixing for Ultra-High Thermal Intensity Distributed Combustor," *Applied Energy*, vol. 105, pp. 327-334, 2013.
- [146] J. A. Cole, T. P. Parr, N. C. Widmer, K. J. Wilson, K. C. Schadow and W. R. Seeker, "Scaling Criteria for the Development of an Acoustically Stabilized Dump combustor," *Proceedings of the Combustion Institute*, vol. 28, pp. 1297-1304, 2000.
- [147] A. C. Eckberth, *Laser Diagnostics for Combustion Temperature and Species*, 3rd ed., Amsterdam: Overseas Publishers Association, 1996.
- [148] K. Kohse-Hoinghaus, "Laser techniques for the quantitative detection of reactive intermediates in combustion systems," *Progress in Energy and Combustion Science*, vol. 20, no. 3, pp. 203-279, 1994.
- [149] C. H. Dieke and H. M. Crosswhite, "The Ultraviolet Bands of OH," *J. Quant. Spectrosc. Radiat. Transfer*, vol. 2, no. 2, pp. 97-199, 1962.
- [150] J. Luque and D. R. Crosley, "LIFBASE: Database and spectral simulation (version 1.5)," SRI International Report MP 99-009, 1999.
- [151] A. R. Choudhuri and S. R. Gollahalli, "Laser Induced Fluorescence Measurements of Radical Concentration in Hydrogen-Hydrocarbon Hybrid Gas Fuel Flames," *International Journal of Hydrogen Energy*, vol. 25, pp. 1119-1127, 2000.
- [152] U. E. Meier, D. Wolff-Gabmann and W. Stricker, "LIF Imaging and 2D Temperature Mapping in a Model Combustor at Elevated Pressure," *Aerospace Sci. Technol.*, vol. 4, pp. 403-414, 2000.

- [153] R. Giezendanner-Thoben, U. Meier, W. Meier and M. Aigner, "Phase-Locked Temperature Measurements by Two-Line OH PLIF Thermometry of a Self-Excited combustion Instability in a Gas Turbine Model Combustor," *Flow, Turbulence and Combustion*, vol. 75, pp. 317-333, 2005.
- [154] S. Tedder and Y. Hicks, "OH Planar Laser Induced Fluorescence (PLIF) Measurements for the Study of High Pressure Flames: An Evaluation of a New Laser and a New Camera System," Glenn Research Center, Cleveland, 2012.
- [155] M. Birouk and A. K. Gupta, "Structure of Lean Premixed Swirling Flames using PLIF Imaging," *Journal of Flow Visualization and Image Processing*, vol. 8, pp. 341-353, 2001.
- [156] R. K. Hanson, J. M. Seitzman and P. H. Paul, "Planar Laser Fluorescence Imaging of Combustion Gases," *Applied Physics B*, vol. 50, pp. 441-454, 1990.
- [157] R. J. Cattolica and S. R. Vosen, "Two Dimensional Measurements of the [OH] in a Constant Volume Combustion Chamber," *20th Symposium (Intl) on combustion*, vol. 20, pp. 1273-1282, 1984.
- [158] R. Sadanandan, M. Stohr and W. Meier, "Simultaneous OH-PLIF and PIV measurements in a Gas Turbine Model Combustor," *Applied Physics B*, vol. 90, pp. 609-618, 2008.
- [159] T. R. Meyer, S. Roy, V. M. Belovich, E. Corporan and J. R. Gord, "Simultaneous Planar Laser-Induced Incandescence, OH Planar Laser-Induced Fluorescence, and Droplet Mie Scattering in a Swirl Stabilized Spray Flames," *Applied Optics*, vol. 44, no. 3, pp. 445-454, 2005.
- [160] A. Katoh, H. Oyama, K. Kitagawa and A. Gupta, "Visualization of OH Radical Distribution in a Methane Hydrogen Mixture Flame By Isotope Shift/ Planar Laser Induced Fluorescence Spectroscopy," *Combustion Science and Technology*, vol. 178, no. 12, pp. 2061-2074, 2006.
- [161] R. P. Lucht, N. M. Laurendeau and D. W. Sweeney, "Temperature Measurement by Two-line Laser-saturated OH Fluorescence in Flames," *Applied Optics*, vol. 21, no. 20, pp. 3729-3735, 1982.
- [162] J. M. Seitzman and R. K. Hanson, "Two-line Planar Fluorescence for Temporally Resolved Temperature Imaging in a Reacting Supersonic Flow over a Body," *Applied Physics B*, vol. 57, pp. 385-391, 1993.
- [163] P. J. Lakusta, *Laser-Induced Fluorescence and Performance Analysis of the Ultra Compact Combustor*, Air Force Institute of Technology, Wright-Patterson Air Force Base, Ohio, 2008.
- [164] B. E. Battles, J. M. Seitzman and R. K. Hanson, "Quantitative Planar Laser-Induced Fluorescence Imaging of Radical Species in High Pressure Flames," in *32nd Aerospace Sciences Meeting & Exhibit*, Reno, NV, 1994.
- [165] B. E. Battles and R. K. Hanson, "Laser-Induced Fluorescence Measurements of NO and OH Mole Fraction in Fuel-Lean High Pressure (1-10 atm) Methane Flames: Fluorescence Modeling and Experimental Validation," *Journal of*

*Quantitative Spectroscopy and Radiative Transfer*, vol. 54, no. 3, pp. 521-537, 1995.

- [166] M. G. Allen, K. R. McManus, D. M. Sonnenfroh and P. H. Paul, "Planar Laser-Induced-Fluorescence Imaging Measurements of OH and Hydrocarbon Fuel Fragments in High-Pressure Spray-Flame Combustion," *Applied Optics*, vol. 34, no. 27, pp. 6287-6300, 1995.